Development of Copper(I) Frameworks: Photophysical Properties and Chemiresistive Gas Sensing Performances

Ph.D. Thesis

By

Dilip Pandey

DISCIPLINE OF CHEMISTRY

INDIAN INSTITUTE OF TECHNOLOGY INDORE

DECEMBER 2024

Development of Copper(I) Frameworks: Photophysical Properties and Chemiresistive Gas Sensing Performances

A THESIS

Submitted in partial fulfillment of the
requirements for the award of the degree
of
DOCTOR OF PHILOSOPHY

by

Dilip Pandey

DISCIPLINE OF CHEMISTRY
INDIAN INSTITUTE OF TECHNOLOGY INDORE
DECEMBER 2024

INDIAN INSTITUTE OF TECHNOLOGY INDORE

I hereby certify that the work which is being presented in the thesis entitled **Development of Copper(I) Frameworks: Photophysical properties and Chemiresistive Gas Sensing Performance** in the partial fulfillment of the requirements for the award of the degree of **DOCTOR OF PHILOSOPHY** and submitted in the **DEPARTMENT OF CHEMISTRY, Indian Institute of Technology Indore**, is an authentic record of my own work carried out during the time period from January 2020 to December 2024 under the supervision of **Dr. Abhinav Raghuvanshi**, Assistant Professor, Indian Institute of Technology Indore.

The matter presented in this thesis has not been submitted by me for the award of any other degree of this or any other institute.

दिलीप पाण्डेय 23/05/25

Signature of the student with date

Dilip Pandey

This is to certify that the above statement made by the candidate is correct to the best of my/our knowledge.

23/5/2025

Signature of Thesis Supervisor with date

Dr. ABHINAV RAGHUVANSHI

Dilip Pandey has successfully given his/her Ph.D. Oral Examination held on **23.05.2025**.

23/5/2025

Signature of Thesis Supervisor with date

Dr. ABHINAV RAGHUVANSHI

ACKNOWLEDGEMENTS

My Ph.D. journey at **IIT Indore** has been an incredibly meaningful chapter in my life. I am profoundly grateful to the remarkable individuals I've met along the way, whose insights and support have enriched my experiences and expanded my understanding.

Pursuing a career in research has long been a dream of mine, and this journey would not have been possible without the invaluable support of my supervisor, **Dr. Abhinav Raghuvanshi**. His mentorship throughout my Ph.D. at IIT Indore has been instrumental; his thoughtful feedback has sharpened my ideas, inspiring me to think critically and independently. His patience and balanced guidance provided the freedom I needed to grow.

I extend my gratitude to my PSPC members, **Dr. Dipak Kumar Roy** and **Dr. Umesh A. Kshirsagar**, for their constructive feedback, which has greatly enhanced my research over the past five years. I am also grateful to **Prof. Shaibal Mukherjee** and **Dr. Dhirendra K. Rai**, whose collaboration and expertise have been instrumental in my work. Special thanks to **Dr. Chandrabhan Patel** and **Dr. Mayank Singh** for their contributions to the gas sensing and electrochemical studies that were pivotal to our collaborative projects.

My gratitude extends to my family, especially my uncles, **Shri Vijay Shankar Pandey** and **Shri Kripa Shankar Pandey**. I owe immense gratitude for their encouragement, which has been my source of motivation since the beginning. I am profoundly grateful to my parents, **Mrs. Shimla Pandey** and **Mr. Gauri Shanker Pandey**, whose sacrifices and unwavering faith have been the foundation of my success. My brother, **Mr. Sandeep Pandey**, **Mr. Pradeep Pandey**, and My sister **Mrs. Ruchi Chaubey** have been a continuous source of support, helping me to achieve my goals with ease.

I am fortunate to have shared this journey with my lab members and friends: **Mr. Shivendu Mishra**, **Mr. Kharabe Laxman Sarjerao**, **Mr. Gopal Singh**, **Mr. Rajaneesh Kumar Yadav**, **Mr. Trivedi Samarth**, **Mr. Anrudh Mishra**, **Mr. Sarvesh Kumar Maurya**, **Dr. Anupam Mishra**, **Mr. Vinod Kumar Yadav**, **Dr. Ashish Kushwaha**, **Mr. Harsh Kumar**, **Mr. Rahul Kumar Yadav**, **Mr. Abhishek Ojha**, **Ms. Darakshan Praveen**, **Dr. Sayantan Sarkar, Mr. Abhinay Chillal**, **Mr. Vijay Kumar Simhadri, Dr. Anshu Sahoo, Dr. Vikesh Kumar, Dr. Shrish Nath Upadhyay, Mr. Arpit Singh** and **Mr. Rajesh Tabaji Bhavale**. Their companionship and support made this journey enriching and enjoyable. My appreciation also extends to **Prof. Preeti A. Bhobe**, **Prof. Michael Knorr**, **Dr. Lydie Viau**, **Dr. Neeraj K. Jaiswal**, **Dr. Srimanta Pakhira**, **Mr. Kulbhushan Mishra**, **Mr. Bikas Sahoo**, **Mr. Suresh Chandra Baral**, and **Mr. Ponvijayakanthan L** for their generous help and insights with analytical, experimental, and computational aspects of my work.

I am appreciative of the dedicated staff in the Department of Chemistry, especially **Mr. Manish Kushwaha**, **Mrs. Vinita Kothari**, **Mr. Shouvik Debnath**, and **Mr. Rameshwar Dauhare**, for their essential support in administrative and departmental matters. My thanks also go to **Mr. Kinny Pandey**, **Mr. Ghanshyam Bhavsar**, **Dr. Ravinder**, and **Mr. Nitin Upadhyay** for their expertise in various characterizations, and to **Mr. Tapesh Parihar** and **Mr. Rahul Srivas** for their assistance with academic issues. IIT Indore’s financial support has been crucial, and I am deeply grateful for it.

I attribute my gratitude to "**Lord Shiva and Lord Hanuman**" for the immense generosity I feel, as it is they and only they who have bestowed it upon me.

DEDICATED TO MY,

LATE

GRANDPARENTS

Synopsis

Introduction

The advancement of efficient materials in the detection of toxic gases and volatile organic compounds (VOCs) is crucial for both environmental protection and public health. The sensing materials could be useful in monitoring air quality, managing industrial processes, ensuring food safety, and facilitating the early diagnosis of some diseases. In this context, organic-inorganic frameworks, comprising metal nodes (ions or clusters) and organic linkers, have emerged as strong candidates for high-performance sensing applications. These frameworks offer significant advantages, such as large surface areas, tunable pore size, and functionalisable active sites, which make them particularly well-suited for detecting various gases and VOCs. Additionally, their intrinsic properties, including electrical conductivity, luminescence, and chromism, further enhance their utility in advanced sensor technologies. The high porosity of these frameworks enables strong interactions with analytes, leading to observable and measurable responses when exposed to gases and VOCs. While recent studies have focused heavily on luminescent sensors based on organic-inorganic frameworks, there remains a lack of comprehensive investigation of their chemiresistive gas sensing potential *[1–5]*.

Copper(I) complexes have emerged as key contenders for the development of efficient chemiresistive gas sensors. The redox-active nature of copper, coupled with the use of multidentate N and S donor ligands, offers intriguing possibilities for tuning both electrical conductivity and sensing properties. The presence of distinct secondary building units (SBUs) and framework dimensionality plays a crucial role in influencing the material's ability to conduct electricity and interact with target gases, thereby enhancing its detection capabilities *[6–10]*. By employing copper(I) frameworks with varied dimensionalities and ligand architectures, this thesis aims to develop novel sensor materials with enhanced performance for gas sensing applications. An extensive investigation has been carried out to explore the potential applications of newly developed Cu(I) frameworks for gas sensing. The key findings and a summary of the thesis chapters are outlined as follows:

Chapter 1. General Introduction

This chapter addresses the critical challenges in current gas sensing technologies, emphasizing the necessity for advanced materials that can meet evolving environmental and industrial demands. Further, different types of sensing methods, the importance of chemiresistive sensing and the terminologies used in this field are discussed. The chapter further explores the benefits of using electrically conductive frameworks, focusing on the improved detection sensitivity, selectivity, and stability they can offer for gas sensing. The next part discusses the Cu(I) coordination polymers, their structural features and their effect on the photophysical and conducting properties. This foundational overview sets the stage for the subsequent chapters, where these materials' synthesis, structural characterization, and application in gas sensing are explored in detail.

Chapter 2. Solvatochromic behavior of cyclic dithioether-functionalized triphenylamine ligands and their mechano-responsive Cu(I) coordination polymers

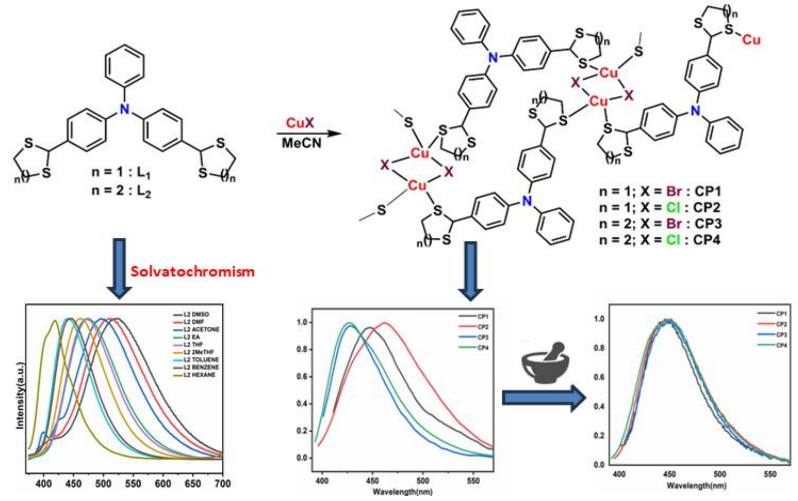

This study focuses on synthesizing emissive materials that offer an environment-friendly and cost-effective foundation for creating diverse functional materials and sensors. Besides the characteristics of the metal center, organic ligands significantly influence the emissive properties of coordination polymers. Herein, the synthesis of dithiane- and dithiolane-substituted triphenylamine ligands $\mathbf{L_1}$ and $\mathbf{L_2}$ has been reported. These ligands were found to be emissive both in the solid state and in solution. In addition, these ligands exhibit solvatochromic behavior due to the twisted intramolecular charge transfer (TICT) phenomenon. Next, coordination behavior of these ligands was explored with Cu(I)X salts (X = Br and Cl) and four new 1D coordination polymers $[\{Cu(\mu_2\text{-}X)_2Cu\}(\mu_2\text{-}\mathbf{L})]_n$, **CP1** (X = Br, L = $\mathbf{L_1}$), **CP2** (X = Cl, L = $\mathbf{L_1}$), **CP3** (X = Br, L = $\mathbf{L_2}$), and **CP4** (X = Cl, L = $\mathbf{L_2}$) were synthesized and crystallographically characterized. The emission behavior of all the CPs suggests ligand-centered transitions. On mechanical grinding, emission maxima (λ_{em}) for **CP1** and **CP2** were blue-shifted, whereas for **CP3** and **CP4** red-shifts were observed. All CPs were found to emit at 448 nm with increased intensity after grinding. Grinding is supposed to be responsible for a change in the spatial arrangement (dihedral angles) of the phenyl groups of Ph_3N, causing the observed emission shifts.

Chapter 3. Two-dimensional Cu(I)-MOF with mesoporous architecture towards chemiresistive NO_2 sensing

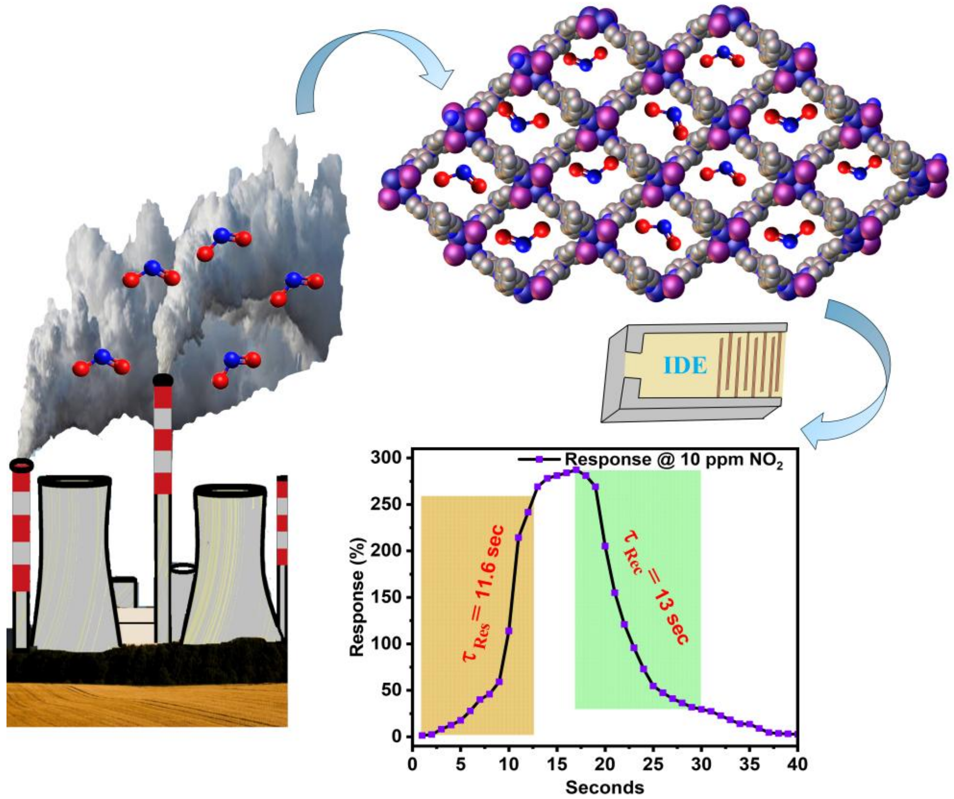

This work presents a semiconducting copper(I)-MOF (**Cu-MOF**) formed by the self-assembly of CuI and N-phenyl-N-(pyridin-4-yl)pyridin-4-amine (**L_3**). The **Cu-MOF** consists of a 2D network comprising Cu_4I_4 secondary building units, which forms an intercalating 3D structure driven by multiple weak interactions. The semiconducting nature and mesoporous structure motivated the exploration of its chemiresistive gas sensing capabilities. The chemiresistive device fabricated with **Cu-MOF** displays high selectivity and efficient room temperature NO_2 sensing with a lower limit of detection (3.5 ppb) and a swift response/recovery times (~11/13s), fastest among the reported state-of-the-art MOF-based NO_2 sensors. Experimental and theoretical analysis reveals that the adsorption of NO_2 on **Cu-MOF** withdraws electrons from the Cu(I) center, leading to a change in electrical response.

Chapter 4. Semiconducting 2D Copper(I) Framework for Ammonia Sensing

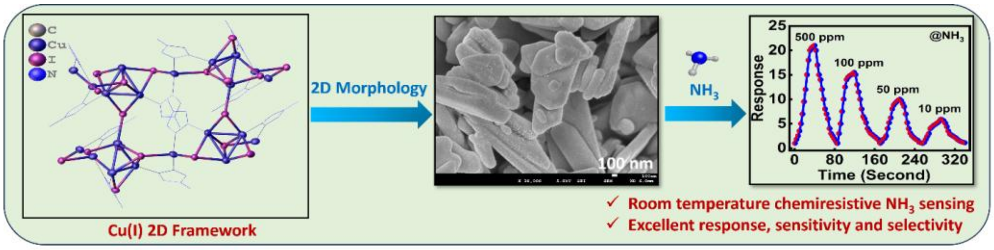

In this work, two distinct CuI coordination polymers, 2D **CuTz1** and 1D **CuTz2**, were synthesized from 4-amino-1,2,4-triazole and CuI under similar conditions but in varying ratios. Remarkably, 2D **CuTz1** features a unique Cu_4I_4 secondary building unit (SBU) while **CuTz2** has a rhomboid Cu_2I_2 SBU. The 2D **CuTz1** was found to be green emissive, semiconducting and exhibiting 2D nano-flakes-like morphology. **CuTz1** not only shows the change in emission color from green to yellow-orange in the presence of aqueous ammonia vapor but also the chemiresistive sensor derived from **CuTz1** shows exceptional ammonia sensing capabilities. The sensor exhibits a remarkable response of 21 at 500 ppm, coupled with rapid response and recovery times (29.5 s/39.5 s) and very high sensitivity (LOD, 73 ppb; LOQ, 243 ppb) for ammonia vapors at room temperature. Excellent sensitivity and selectivity, accompanied by fast dynamic response/recovery time at room temperature, positions **CuTz1** as the most promising material among the reported MOF/CP-based ammonia sensors.

Chapter 5. Semiconducting Cu(I) framework for room temperature NO_2 sensing via efficient charge transfer

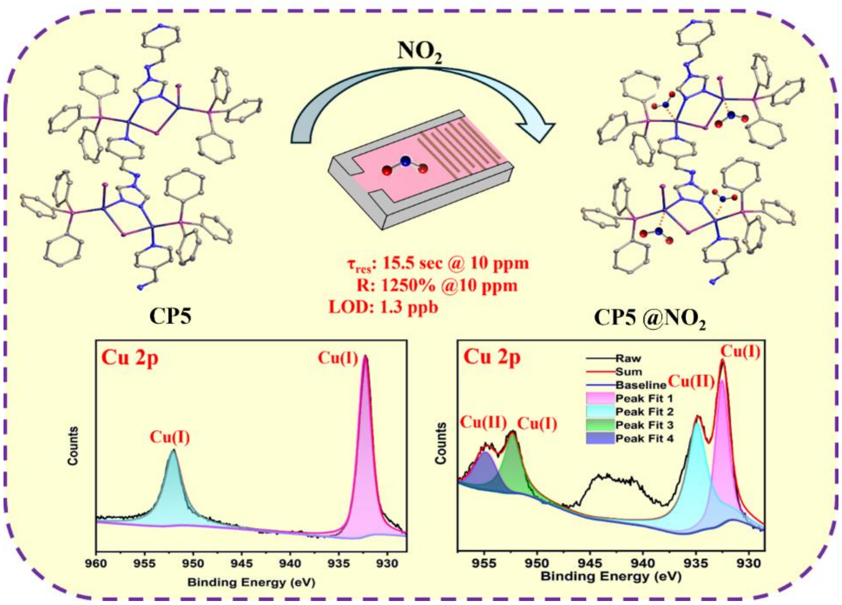

Previous studies have suggested that the presence of an electron-rich metal center is beneficial for effective charge transfer to the analyte which increases the gas-sensing properties. For this work, PPh_3 is used as an auxiliary ligand to synthesize electron-rich Cu(I) CP. Two new one-dimensional CPs $[Cu_2X_2(PPh_3)_2(\mathbf{L_5})]_n$, **CP5** (X = I) and **CP6** (X = Br) synthesized using CuI, (pyridin-4-yl)-N-(4H-1,2,4-triazol-4-yl)methanimine (**L**$_5$) and triphenylphosphine. These CPs were crystallographically characterized and found to have unique structural arrangements of secondary building units. Due to their semiconducting properties, both CPs were fabricated into conventional interdigitated electrodes by drop-casting. Benefitting from the higher electron density of Cu(I) center, **CP6** demonstrates selective sensing for NO_2 gas with excellent sensitivity and reversibility. The material offers one of the best room temperature NO_2 chemiresistive sensing performances among the MOF/CP-based materials with ultrafast response time (15.5 sec @10 ppm). Additionally, convenient synthesis and ease of device fabrication for sensing give our material a distinct advantage. The experimental and theoretical findings collectively suggest that the adsorption of NO_2 on the material's surface and the concomitant effective charge transfer between Cu(I) and NO_2 are key to its efficacious gas sensing capabilities.

Conclusions

This thesis presents the photophysical and gas sensing properties of some copper-based coordination polymers (CPs) and metal-organic frameworks (MOFs). By leveraging the tunable structural and electronic properties of copper(I) frameworks, the research demonstrates these materials' multifunctionality and high performance in sensor applications, particularly for NO_2 and NH_3 detection. This work establishes Cu(I) CPs as a promising material for gas sensing and also provides a way for future research aimed at environmental monitoring and industrial safety applications.

List of publications

(A) Outcomes from Ph.D. thesis work:

A1. In referred journals:

Papers published/unpublished:

1. **Dilip Pandey**, Gopal Singh, Shivendu Mishra, Lydie Viau, Michael Knorr and Abhinav Raghuvanshi

   Solvatochromic behaviour of cyclic dithioether-functionalized triphenylamine ligands and their mechano-responsive Cu(I) coordination polymers. *Dalton Trans.*, 2023, **52**, 14151-14159. ***(Impact Factor = 3.4)***

2. **Dilip Pandey**, Chandrabhan Patel, Shivendu Mishra, Shaibal Mukherjee and Abhinav Raghuvanshi

   Semiconducting 2D Copper(I) Framework for Sub-ppb-Level Ammonia Sensing. *ACS Appl. Nano Mater*. 2024, **7**, 15833–15840. ***(Impact Factor = 5.3)***

3. **Dilip Pandey**, Chandrabhan Patel, Shivendu Mishra, Lokesh Yadav, Dikeshwar Halba, Srimanta Pakhira, Shaibal Mukherjee and Abhinav Raghuvanshi

   Semiconducting Cu(I) framework for room temperature ultrafast NO_2 sensing via efficient charge transfer. *Small, 2025, **21**, 2409553* ***(Impact Factor = 13.3)***

4. **Dilip Pandey**, Trivedi Samarth, Vikash Kumar Verma, Chandrabhan Patel, L Ponvijayakanthan, Neeraj K. Jaiswal, Shaibal Mukherjee and Abhinav Raghuvanshi

   Two-dimensional Cu(I)-MOF with mesoporous architecture towards chemiresistive NO_2 sensing *J. Mater. Chem. A, 2025, **13**, 11416-11424.* ***(Impact Factor = 10.7)***

Other outcomes outside of Ph.D. thesis work:

B1. In referred journals:

1. **Dilip Pandey**, Mayank K. Singh, Shivendu Mishra, Dhirendra K. Rai and Abhinav Raghuvanshi

   2D Layered Semiconducting $(LCu_3I_3)_n$ Coordination Polymer for Energy Storage through Dual Ion Intercalation. *J. Mater. Chem. A*, 2024, **12**, 27355–27363. ***(Impact Factor = 10.7)***

2. **Dilip Pandey**, Anrudh Mishra, Laxman Sarjerao Kharabe, Sarvesh Kumar Maurya and Abhinav Raghuvanshi

   Semiconducting Copper (I) Iodide 2D-Coordination Polymers for Efficient Sunlight-Driven Photocatalysis in Dye Degradation. *Cryst. Growth Des.*, 2024, **14**, 6051–6059. ***(Impact Factor = 3.2)***

3. **Dilip Pandey**, Trivedi Samarth, Laxman Sarjerao Kharabe, Anrudh Mishra, Anupam Mishra and Abhinav Raghuvanshi

   Manifesting the multi-stimuli-responsive behaviour of triazole-substituted triphenylamine. *Luminescence*, 2024, **39**, 4876–4882. ***(Impact Factor = 3.2)***

4. Shivendu Mishra, **Dilip Pandey**, Kulbhushan Mishra, Lydie Viau and Abhinav Raghuvanshi

Copper(I) coordination polymers with triazole substituted pyridine ligands: Photophysical and electrical conductivity properties. *New J. Chem.*, 2023, **47**, 19751–19759. ***(Impact Factor = 3.4)***

5. Anrudh Mishra†, **Dilip Pandey**†, Sarvesh Kumar Maurya, Abhinav Raghuvanshi

   Sunlight-driven photocatalytic degradation of organic dyes using Cu(I) coordination polymers: an efficient and recyclable solution for wastewater remediation. *CrystEngComm, 2025,* ***27****, 2462-2469* ***(Impact Factor = 2.8)***

6. Shivendu Mishra, Mayank K. Singh, **Dilip Pandey**, Dhirendra K. Rai and Abhinav Raghuvanshi

   Two-dimensional conducting Cu(I)-CN coordination polymer for binder and conductive additive-free supercapattery. *J. Mater. Chem. A*, 2024, **12**, 4534–4543. ***(Impact Factor = 10.7)***

7. Shivendu Mishra, Chandrabhan Patel, **Dilip Pandey**, Shaibal Mukherjee and Abhinav Raghuvanshi

   Semiconducting 2D Copper(I) Iodide Coordination Polymer as a Potential Chemiresistive Sensor for Methanol. *Small*, 2024, **20**, 2311448. ***(Impact Factor = 13.3)***

8. Laxman Sarjerao Kharabe, Tanushree Ghosh, **Dilip Pandey**, Rajesh Kumar and Abhinav Raghuvanshi

   Heteroleptic Cu(I) complex with vapochromism and its application as electrochromic material. *Appl. Organomet Chem.* 2024, e7451. ***(Impact Factor = 3.7)***

9. Shivendu Mishra, Chandrabhan Patel, **Dilip Pandey**, L. Ponvijayakanthan, Harshini V. Annadata, Neeraj K. Jaiswal, Shaibal Mukherjee and Abhinav Raghuvanshi

   Two-dimensional ionic conducting Copper (I) metal-organic framework in chemiresistive sensing of NO_2. ***(Under Revision)***

LIST OF CONFERENCES ATTENDED

1. Poster presentation in International Conference on Frontiers in Materials Engineering (ICFME)-2022, Department of Metallurgy Engineering and Materials Science, IIT Indore.
2. Poster Presentation in In-House Symposium Chem-2021, Department of Chemistry, IIT Indore.
3. Poster presentation in International Conference on Modern Trends in Inorganic Chemistry (MTIC-XX), Department of Chemistry, Indian Institute of Science, Bangalore, 2023.

References:

1. López-Molino, J., and Amo-Ochoa, P. (2020). Gas Sensors Based on Copper-Containing Metal-Organic Frameworks, Coordination Polymers, and Complexes. ChemPlusChem *85*, 1564–1579. (DOI: 10.1002/cplu.202000428)

2. Li, H.-Y., Zhao, S.-N., Zang, S.-Q., and Li, J. (2020). Functional metal-organic frameworks as effective sensors of gases and volatile compounds. Chem. Soc. Rev. *49*, 6364–6401. (DOI: 10.1039/C9CS00778D)

3. Campbell, M.G., and Dincă, M. (2017). Metal-Organic Frameworks as Active Materials in Electronic Sensor Devices. Sensors *17*, 1108. (DOI: 10.3390/s17051108)

4. Yang, G.G., Kim, D.-H., Samal, S., Choi, J., Roh, H., Cunin, C.E., Lee, H.M., Kim, S.O., Dincă, M., and Gumyusenge, A. (2023). Polymer-Based Thermally Stable Chemiresistive Sensor for Real-Time Monitoring of NO_2 Gas Emission. ACS Sens. *8*, 3687–3692. (DOI: 10.1021/acssensors.3c01530)

5. Roh, H., Kim, D., Cho, Y., Jo, Y., Del Alamo, J.A., Kulik, H.J., Dincă, M., and Gumyusenge, A. (2024). Robust Chemiresistive Behavior in Conductive Polymer/MOF Composites. Adv. Mater. *36*, 2312382. (DOI: 10.1002/adma.202312382)

6. Kobayashi, A., Fujii, M., Shigeta, Y., Yoshida, M., and Kato, M. (2019). Quantitative Solvent-Free Thermal Synthesis of Luminescent Cu(I) Coordination Polymers. Inorg. Chem. *58*, 4456–4464. (DOI: 10.1021/acs.inorgchem.8b03641)

7. Schlachter, A., Tanner, K., and Harvey, P.D. (2021). Copper halide-chalcogenoether and -chalcogenone networks: Chain and cluster motifs, polymer dimensionality and photophysical properties. Coord. Chem. Rev. *448*, 214176. (DOI: 10.1016/j.ccr.2021.214176)

8. Conesa-Egea, J., Zamora, F., and Amo-Ochoa, P. (2019). Perspectives of the smart Cu-Iodine coordination polymers: A portage to the world of new nanomaterials and composites. Coord. Chem. Rev. *381*, 65–78. (DOI: 10.1016/j.ccr.2018.11.008)

9. Troyano, J., Zamora, F., and Delgado, S. (2021). Copper(I)–iodide cluster structures as functional and processable platform materials. Chem. Soc. Rev. *50*, 4606–4628. (DOI: 10.1039/D0CS01470B)

10. Chen, J., Zhou, K., Li, J., Xu, G., Hei, X., and Li, J. (2024). Strongly photoluminescent and radioluminescent copper(i) iodide hybrid materials made of coordinated ionic chains. Chem. Sci. (DOI: 10.1039/D4SC06242F)

TABLE OF CONTENTS

Chapter 1: Introduction

Chapter 3: Two-dimensional Cu(I)-MOF with mesoporous architecture towards chemiresistive NO_2 sensing

Chapter 4: Semiconducting 2D Copper(I) Framework for Ammonia Sensing

Chapter 5: Semiconducting Cu(I) framework for room temperature NO_2 sensing via efficient charge transfer

Chapter 6:

LIST OF FIGURES

LIST OF TABLES

LIST OF SCHEMES

ABBREVIATIONS

Å	Angstrom
℃	Degree Celsius
θ	Diffraction angle
W	Watt
α	Alpha
mg	Milligram
mmol	Millimole
h	Hour
µL	Microliter
mL	Milliliter
m	Multiplet
V/V	Volume/volume
Hz	Hertz
s	Second
δ	Chemical shift
cm	Centimetre

r.t.	Room temperature
K	Kelvin
eV	Electron Volt
nm	Nanometer
τ	Angular Index
π	Pi
MHz	Megahertz
T	Temperature
µm	Micrometer
λ	Wavelength
λem	Emission wavelength
λex	Excitation wavelength
λmax	Emission maximum
min	Minute
ms	Millisecond
µs	Microsecond
Φ	Quantum yield
S	Siemen
GPa	Gigapascal
V	Volt
°	Degree
σ	Conductivity
ppm	Parts per million
ppb	Parts per billion
Ω	Ohm
χ	Oscillation
k	Wavenumber of photo electron
e	Electron
E_{ads}	Energy of adsorption
C	Coulomb

g	Gram
F	Farade
kW	Kilowatt
Kg	Kilogram
MHz	Megahertz
kHz	Kilohertz
mV	Millivolt
I	Current
A	Ampere

ACRONYMS

$CDCl_3$	Chloroform-d
$CHCl_3$	Chloroform
DCM	Dichloromethane
CP/MAS	Cross polarization magic angle spinning
DMSO	Dimethyl sulfoxide
DMF	Dimethyl formamide
ACN	Acetonitrile
FTIR	Fourier transform infrared Spectroscopy
MeOH	Methanol
NMR	Nuclear magnetic resonance
PXRD	Powder X-ray diffraction
SEM	Scanning electron microscope
UV-Vis	UV-Visible spectroscopy
TGA	Thermogravimetric analysis
VOC	Volatile organic compounds
CP	Coordination polymer
MOF	Metal-organic framework

IDE	Inter-digitated electrode
FET	Field-effect transistors
SC	Supercapacitor
SBU	Secondary building unit
KI	Potassium iodide
1D	One-dimensional
2D	Two-dimensional
3D	Three-dimensional
MLCT	Metal-ligand charge transfer
XLCT	Halide-ligand charge transfer
TADF	Thermally activated delayed fluorescence
HE	High energy
LE	Low energy
Tz	Triazole
CC	Cluster centered
AIE	Aggregation induced emission

Chapter 1

Introduction

1.1 Introduction

1.1.1. Motivation

In today's rapidly advancing technological landscape, the primary goal is to enhance and simplify various aspects of human life, with a particular focus on safety, security, surveillance, and environmental monitoring. Many individuals frequently work in hazardous environments where exposure to combustible, flammable, or toxic gases is a serious health risk. Since human olfactory senses are limited in detecting such gases, exposure often leads to immediate health consequences. This highlights the critical need for gas sensor technology as a solution for detecting harmful gases *[1–3]*. Gas sensors provide a compact, cost-effective alternative to sophisticated gas analyzers like gas chromatography, optical spectroscopy, and mass spectrometry, which analyze gases and volatile organic compounds (VOCs) based on molecular properties. These sensors are essential in a wide array of industries, including fuel production, automotive, chemical processing, food safety, and even domestic applications *[4–6]*.

Historically, the need for gas sensors emerged from the necessity to protect workers in hazardous environments, such as coal mines, from the dangers of flammable gases, toxic fumes, and oxygen deprivation. Early methods, including using open flame lamps and canary birds, were inadequate and posed their own risks. Significant progress came in 1927 when Dr. Oliver Johnson developed a commercial gas sensor using a platinum catalyst *[7]*, and in 1962, when Seiyama et al. introduced semiconducting metal-oxide-based sensors *[8]*. Since then, research has evolved, with Taguchi's commercialization of metal-doped tin oxide sensors in 1969, contributing significantly to safety in industrial settings *[9]*. Over the decades, the gas sensor market has expanded beyond safety applications to encompass fields such as environmental monitoring, food quality control, and healthcare diagnostics. The focus of recent research has shifted toward miniaturization, improved selectivity, and the development of cost-effective sensors capable of operating in complex, real-world conditions. Real-world applications where humidity, temperature, and gas concentrations vary significantly pose major challenges for accurate detection. For example, human breath contains over 900 VOCs, making the detection of specific biomarkers like acetone or ammonia challenging for disease diagnostics. Similarly, plants emit various VOCs when under stress, and the ability to detect these emissions can improve agricultural efficiency. To address these challenges, modern gas sensors must be capable of accurately detecting target gases in complex environments *[10–12]*.

1.1.2. Type of Gas Sensors

The fundamental principle of a gas sensor lies in the interaction between gas species and the surface of the sensor material (receptor) and the subsequent conversion of this chemical energy into an electrical signal (transducer). Depending on the specific receptor and transducer principles, the variations in electrical signals can be monitored through various means, including changes in resistance, capacitance, or optical properties. Gas sensors are classified based on the type of electrical and optical signal as follows:

1.1.2.1 Thermoelectric sensors

Thermoelectric sensors are also known as thermal-conductivity sensors. They operate as a result of adsorption of the target analyte/gas followed by the Seebeck effect. According to this principle, the change in the electric voltage of the sensing material is measured based on the difference in the temperature arising out of two contact points in the presence of the target analyte. The sensor device consists of two main parts, one is a thermoelectric film and the other is the sensing material *[13,14]*. For instance, a bismuth-telluride thermoelectric film consisting of $Pt/\gamma\text{-}Al_2O_3$ sensing element was used to sense 3 vol.% of H_2/Air with a temperature difference of 55 °C *[15]*. Another example of detection of volatile organic compounds (VOCs) like acetone with a limit of detection (LoD) of 28 ppm, was studied by developing films of chromium metal and tin oxide *[16]*. Although the simplicity of thermoelectric sensors may be a boon, these sensors have major drawbacks of temperature fluctuations and longer response times that may affect the overall sensitivity *[17]*.

1.1.2.2. Optical sensors

The basic principle involved in an optical sensor is the measurement of the optical properties (absorption/emission scattering) caused by the scattering of the target analyte molecule when in contact with the optical sensing element. An optical sensor consists of four parts, that include a light-emitting diode, a photodetector, the sensing material and a phosphorescence/fluorescence detector *[18]*. For example, a hydrogen gas sensor was developed by coating a WO_3 thin film on silica core of the optical fiber *[19]*. Although the sensors were effective at room temperature, the declining durability of the sensor should not be overlooked. Infrared sensors can also be categorized under optical sensors. An infra-red sensor consists of an infra-red source (to produce an incandescent light), an optical fiber (mostly a non-dispersive), a gas cell and an infra-red detector to convert the electromagnetic radiation to electrical readout signals. Non-dispersive infrared (NDIR) gas sensors have commonly been explored for the detection of CO_2 gas *[17]*.

1.1.2.3. Surface acoustic wave sensors (SAWs)

Surface Acoustic Wave (SAW) sensors operate by utilizing mechanical waves that propagate along the surface of a piezoelectric substrate, such as quartz or lithium niobate. These waves are generated by applying an alternating voltage to interdigital transducers (IDTs) on the substrate, which creates vibrations through the piezoelectric effect. As the surface acoustic waves travel across the substrate, they interact with a sensing layer or directly with the environment, causing changes in the wave's properties such as velocity, amplitude, phase, or frequency. These changes arise from alterations in surface characteristics, such as mass, stress, temperature, or chemical adsorption, induced by the target analyte or environmental factor. The modified waves are detected by an output IDT, which converts them back into electrical signals for analysis. SAW sensors are highly sensitive to surface interactions and are widely used in gas and chemical sensing, biosensing, temperature and pressure monitoring, and structural stress detection *[17]*. SAW sensors, though versatile, have limitations such as sensitivity to environmental factors, dependence on stable sensing layers, and temperature-induced signal drift. Their surface-confined range, fragile substrates, complex fabrication, and weak output signals requiring amplification hinder the performance *[20]*.

1.1.2.4. Piezoelectric sensors

Piezoelectric sensors in some cases are also known as acoustic wave sensors since both can operate on the phenomenon of piezoelectric effect. The basic criterion for this effect is the presence of a piezoelectric material that can convert any mechanical stress (ex. external pressure, acoustic wave) into an electrical signal. Quartz crystal microbalance and microcantilever are also categorized as piezoelectric gas sensors *[21,22]*. Common examples of piezoelectric materials are quartz crystal and lithium tantalate ($LiTaO_3$) *[23]*. Another example is HKUST-1 microcantilever which was developed for the detection of 400 ppb p-xylene *[24]*. Although devices of piezoelectric materials can be very sensitive for gas sensing, thicker films can result in a decline in sensitivity. This makes the device fabrication of piezoelectric sensors trickier.

1.1.2.5. Chemicapacitance sensors

Chemicapacitance sensors detect analytes by measuring changes in capacitance caused by interactions between the analyte and a dielectric layer, typically made of polymers, metal oxides, or functionalized materials, sandwiched between two electrodes. These changes correspond to the analyte's concentration or presence. For instance, a film of Cu-BTC (back electrode) with Ag spots (top electrode) on its top was used to detect ethanol and methanol *[26]*. The chemicapacitance sensors are widely used in gas detection, humidity monitoring, and biosensing due to their high sensitivity, low power consumption, and real-time response. However, they face challenges such as environmental sensitivity, limited selectivity leading to cross-interference, material degradation over time, and weak signals requiring precise instrumentation. Additionally, the fabrication of consistent dielectric layers and miniaturization for compact devices remain complex and costly *[17,25]*.

1.1.2.6. Impedance sensors

Impedance sensors operate by measuring changes in the electrical impedance of a sensing material when exposed to an analyte. Impedance, which encompasses resistance and reactance, is influenced by factors such as charge transfer, ion mobility, or dielectric properties of the material. These sensors typically consist of electrodes and a sensing layer, which interacts with the target analyte. The interaction can alter the conductivity, permittivity, or both, resulting in a measurable impedance change that correlates with the analyte's presence or concentration. Impedance sensors are widely used in chemical, biological, and environmental applications due to their high sensitivity and capability for real-time monitoring *[27]*. Achmann et al. demonstrated Fe-BTC (BTC= 1,3,5 benzene tricarboxylic acid) coated on an interdigitated electrode for sensing of water over ethanol and methanol target analytes *[28]*. Impedance sensors face limitations such as sensitivity to environmental conditions (e.g., temperature, humidity), poor selectivity leading to cross-interference, and complex signal processing requirements. Long-term material stability may degrade under environmental exposure, and miniaturization or integration into portable devices can be costly and technically challenging *[17]*.

1.1.2.7. Chemiresistive sensors

Chemiresistive sensing (a combination of chemical interactions to cause a modification in the electrical resistance of the overall material) is one of the simplest and most affordable ones. The principle is simply based on the change in electrical resistance on contact with the target analyte/ gas. The nature of the sensing material and the target gas property decides the change in resistance (increase/decrease). These sensors offer significant advantages, including low-cost fabrication, ease of miniaturization, and straightforward integration into electronic devices, making them highly attractive for practical applications *[29,30]*.

1.3.1. Sensing Measurements

5N purity gases are employed to measure the sensing performance of the fabricated sensor. The flow rate of these gases is precisely controlled by using an advanced mass flow controller (model: Alicat, MC1^1 slpm, USA). The concentration of these test gases is varied by mixing the synthetic air (99.999 Purity) into the mixing chamber before exposing on the sensor surface. The resistance change of the sensing layer during test gas exposure is continuously monitored on the Keithley-2612A source meter by applying a constant voltage of +1 V.

To improve the practical applicability of a gas sensor, a chemiresistive sensor was fabricated from the CPs/MOFs. First, it is blended with an ethanol solution. Subsequently, 5µL of this mixture is drop-casted onto the active area of the device using a micropipette. The active area of the device is constructed with Ti/Pt (20/200 nm) interdigitated electrodes (IDEs) on a glass substrate measuring (5.5 mm × 6 mm) (**Fig. 1.1**). Following this, the device undergoes a drying process in a hot air oven for 24 hours at 70 °C to remove any moisture content present in the sensing material. The sensing performance of the fabricated sensor is investigated under a dynamic flow gas sensing setup (**Fig. 1.2**).

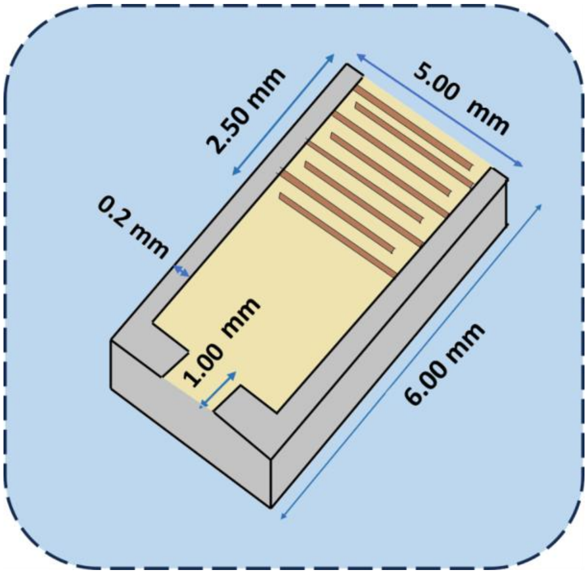

Fig. 1.1 Schematic representation of IDE device**.**

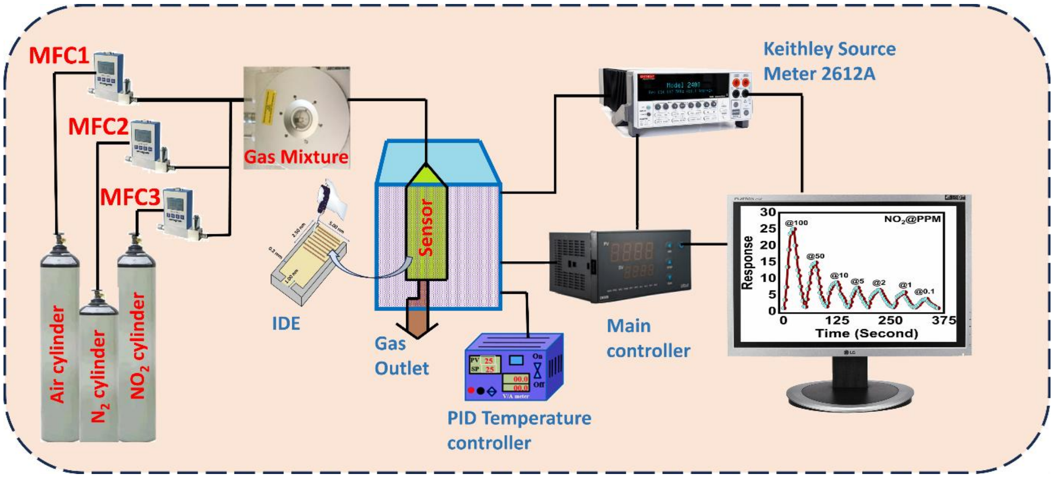

Fig. 1.2 Illustration of the dynamic flow gas sensing setup

1.3.2. Gas Sensing Terminology

Before exploring the details of semiconductor gas sensors, it's important to define the key parameters that apply to all gas sensors. These fundamental terms include:

1.3.2.1. Response (R)

Sensor response is the measure of the change in the sensor's baseline resistance when transitioning from an open-air environment to exposure to a test gas under stable conditions. It can be expressed as:

Response (R) = $| R_{\text{baseline}} - R_{\text{gas}} / R_{\text{baseline}} | \times 100\ \%$

Or

$R = R_{\text{baseline}} / R_{\text{gas}}$ or $R = R_{\text{gas}} / R_{\text{baseline}}$

Where; R_{baseline} and R_{gas} represent the sensor's resistance in open air and in the presence of the test gas, respectively.

1.3.2.2. Selectivity (S)

Selectivity is the sensor's ability to detect a specific gas in the presence of other gases. It is determined by comparing the sensor's response to different test gases.

1.3.2.3. Reversibility

Reversibility refers to the sensor's capacity to return to its original state once the test gas is removed from the environment.

1.3.2.4. Response Time (τ_{Res})

Response time is the duration it takes for the sensor's output to shift from 0% to 90% of its maximum response after being exposed to the test gas.

1.3.2.5. Recovery Time (τ_{Rec})

Recovery time is the time required for the sensor’s output to decrease from its maximum response to 10% after the test gas has been removed.

1.3.2.6. Repeatability

Repeatability describes the sensor’s ability to consistently provide the same response across multiple cycles of exposure to and withdrawal of the test gas.

1.3.2.7. Long-term Stability

Long-term stability is the sensor's ability to maintain consistent performance and response characteristics over an extended period of time.

1.4. Materials utilized for chemiresistive gas sensing:

Metal oxides have long been regarded as promising candidates for gas sensing due to their versatile functionalization capabilities. In particular, heterojunctions, which incorporate catalysts and filtering layers, have been shown to improve sensor performance by either activating target gases or filtering out interferences *[31–33]*. However, these materials often require high operational temperatures, leading to significant power consumption and limiting their portability. Despite their established status as highly sensitive chemiresistive materials, metal oxides still face significant challenges, particularly in achieving selective detection of target gases in complex environments. This is because metal oxides primarily rely on surface reactions with chemisorbed oxygen, making it difficult to distinguish between different analytes when multiple gases are present. Consequently, achieving high selectivity, sensitivity, and stability remains a challenge in real-world applications. Although metal oxides offer higher response levels than many other materials, they are hindered by issues such as low selectivity and baseline drift caused by their high-temperature operation. Carbon-based materials, which can function at room temperature and feature high surface areas, suffer from low sensitivity, poor selectivity, and limited reproducibility. Likewise, 2D transition metal dichalcogenides (TMDs), while showing promise, are prone to oxidation when exposed to air, which limits their practical use. Despite ongoing efforts by researchers to address these challenges in conventional sensing materials, significant advancements are still required *[34–38]*.

Conductive metal-organic frameworks (MOFs) and coordination polymers (CPs) present an exciting alternative for gas sensing. These materials hold the potential to revolutionize gas sensor technology by offering low power consumption, enhanced selectivity, and increased sensitivity. Furthermore, post-synthetic modifications of conductive MOFs/CPs can produce derivatives with unique porous structures such as hollow, hierarchical, or multi-dimensional forms resulting in high-performance gas-sensing materials. By leveraging these advancements, researchers can develop next-generation gas sensors that overcome the limitations of conventional materials, paving the way for novel, efficient, and selective gas-sensing technologies *[39–43]*.

1.5. Electrical conductivity, Electrically Conductive CPs/MOFs and their applications in chemiresistive gas sensing:

Electrical conductivity is a crucial property of materials, representing their ability to conduct an electric current under specific conditions such as temperature, pressure, and applied current. Conductivity is often explained through Ohm’s law, where the voltage (V) across a material is proportional to the current (I) flowing through it, with the proportionality constant being the resistance (R):

$$V = R \times I$$

To measure electrical conductivity, one can directly determine the resistance by applying a known current and measuring the resulting voltage. However, since resistance depends on the material's geometry, measurements are typically expressed in terms of resistivity (ρ), a more intrinsic property of the material. Resistivity is defined by the formula:

$$\rho = R \times (A/l)$$

Where: R is the resistance of the material, A is the cross-sectional area (calculated as width a times thickness d), and l is the distance between the points where the voltage is measured. Resistivity is generally reported in units of ohm-centimeters ($\Omega \cdot cm$). The inverse of resistivity is conductivity (σ), given by:

$$\sigma = 1/\rho$$

and is measured in Siemens per centimeter ($S \cdot cm^{-1}$).

Though Ohm's law provides a straightforward approach to measuring conductivity, it does not apply universally. Semiconductors and many low-dimensional materials often deviate from Ohm's law, especially at higher currents. Even metals, which are generally good conductors, only obey Ohm's law within certain current or voltage ranges. As a result, when reporting conductivity or resistivity values, it is essential to specify the current or voltage range under which these values were measured to provide context for the measurement. Thermal Dependence and Conductivity Mechanisms In addition to room temperature measurements, it is vital to assess the thermal variation of resistivity, as this can provide insight into the material's electronic properties and behavior. For example, the thermal dependence of resistivity can help differentiate between metallic, semiconducting, or insulating behaviors *[44,45]*.

Historically, coordination polymers (CPs) and metal-organic frameworks (MOFs) were considered electrical insulators, leading research to primarily explore their host-guest interactions in areas like catalysis, molecular separations, and molecular recognition. However, recent advances in design and synthesis, such as the incorporation of redox-active building blocks and transition metals, have shifted the focus toward their potential as electrically conductive materials. Conductivity in CPs and MOFs can emerge through various mechanisms, including continuous conductive inorganic channels held together by organic ligands, molecular stacks with photoactive or redox-active ligands, or internal charge transfer via proper electronic alignment between metal nodes and ligands. Enhanced orbital overlap can facilitate π-electron delocalization throughout the structure. Additionally, the intrinsic porosity and well-defined cavities of CPs and MOFs enable the integration of electroactive guest molecules or conductive phases, further boosting electrical performance. This progress has led to the development of electroactive CPs and MOFs with potential applications across diverse fields *[46–50]*. In the context of chemiresistive gas sensing, conductive CPs/MOFs have emerged as promising materials. Their ability to selectively adsorb gas molecules in well-defined cavities facilitates strong host-guest interactions, leading to changes in their electrical properties upon exposure to specific gases. These changes, driven by mechanisms such as charge transfer between gas molecules and the framework or modification of charge carrier pathways, enable sensitive and selective detection. For example, conductive MOFs with redox-active or π-conjugated ligands can exhibit enhanced responses to gases such as NH_3, NO_2, H_2S, etc *[51–55]*. Among electrically conductive MOFs, 2D frameworks exhibit the highest conductivity, attributed to in-plane charge delocalization and extended π-conjugation facilitated by electronic communication through metal nodes *[56,57]*. Notable examples are $Cu_3(HHTP)_2$, $Cu_3(HITP)_2$, and $Ni_3(HITP)_2$ (HITP = 2,3,6,7,10,11-hexaiminotriphenylene, and HHTP = 2,3,6,7,10,11-hexahydroxytriphenylene), reported by Dincă and coworkers as one of the most conductive microporous MOFs (**Fig 1.3**). These findings highlight the potential of 2D MOFs, especially those featuring linkages such as o-phenylenediamine, dithiolene, or o-semiquinone, as advanced functional

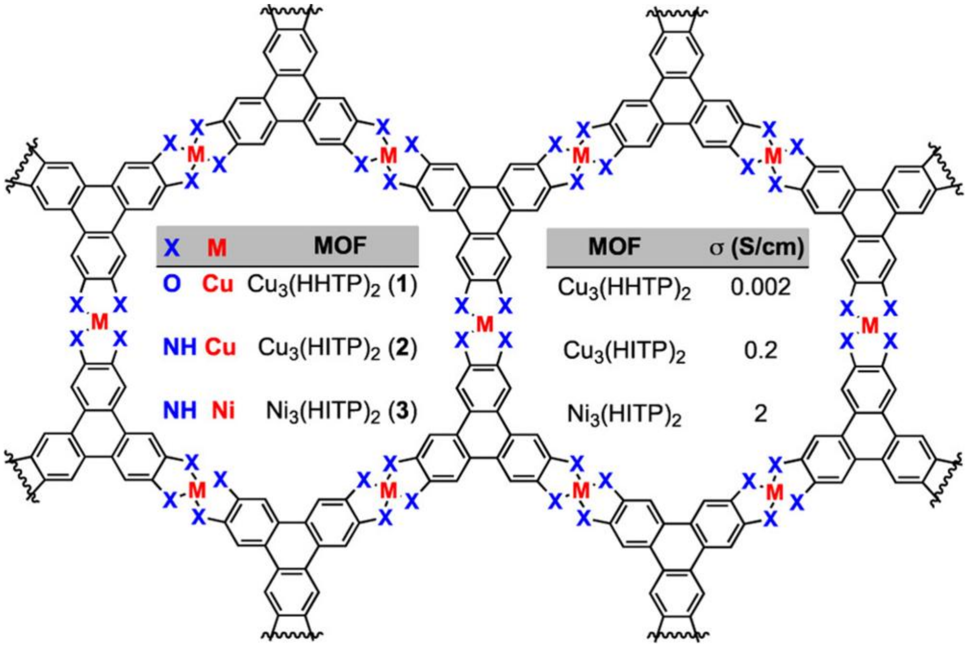

Fig. 1.3 Chemical structures of the conductive 2D MOFs, reproduced with permission from the American Chemical Society, ref *[58]*.

materials for various applications *[52,58,59]*. Expanding on this, Dincă and coworkers pioneered the use of these MOFs in chemiresistive sensing. A Cu-based 2D MOF demonstrated a reversible "turn-on" response to sub-ppm levels of ammonia vapor, with the response being linearly proportional to ammonia concentration (**Fig 1.4**). This enabled reliable, quantitative detection under ambient conditions and high humidity. Further investigations explored the impact of systematically replacing Ni with Cu in the $Ni_3(HITP)_2$ framework. The resulting $Cu_3(HITP)_2$ maintained high electrical conductivity while exhibiting significantly enhanced sensitivity to ammonia vapor. Unlike the "turn-off" response commonly observed in carbon nanotube (CNT) and conductive polymer-based sensors, $Cu_3(HITP)_2$ displayed a "turn-on" response similar to metal chalcogenide sensors. This unique behavior, combined with its linear response to ammonia concentration, positions $Cu_3(HITP)_2$ as an effective material for quantitative sensing. Its sensitivity rivals cutting-edge materials like pristine CNTs, PEDOT-based polymers, and MoS_2 transistors, meeting detection requirements for air quality monitoring and agricultural applications. In contrast, $Ni_3(HITP)_2$ showed no detectable response to ammonia under identical conditions. Theoretical studies attribute this difference to the substitution of Ni with Cu, a metal with a higher d-electron count, which raises the Fermi level energy and modifies the electronic structure, thereby enhancing chemiresistive performance. This stark contrast underscores the critical role of metal center selection in tuning MOF properties *[52]*.

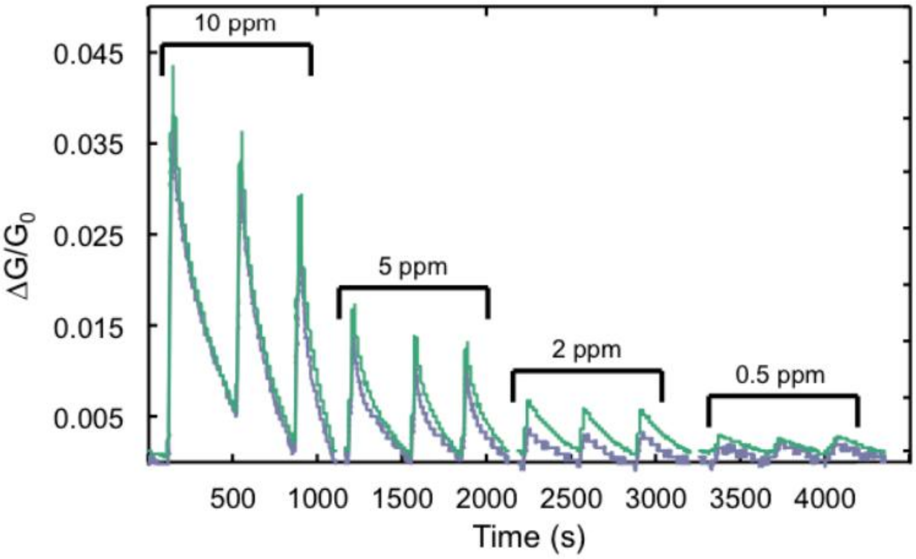

Fig. 1.4 Relative response of $Cu_3(HITP)_2$ devices to various concentrations of ammonia diluted with nitrogen gas, reproduced with permission from the John Wiley and Sons, ref *[52]*.

Thus, $Cu_3(HITP)_2$ not only surpasses $Ni_3(HITP)_2$ in ammonia sensitivity but also exhibits distinctive and practical response characteristics, making it a promising candidate for advanced sensing applications. This comparative analysis underscores the potential of rationally designed MOFs to enable next-generation chemiresistive sensors with tailored functionalities.

1.6. Copper(I) CPs/MOFs:

The quest for novel materials with exceptional optoelectronic and electrical properties has led to the discovery of a wide array of chromophores and semiconductors, with coordination complexes standing out as particularly promising. These materials offer a versatile platform for developing advanced applications due to their highly tailored molecular structures, superior environmental stability, and a broad range of electronic properties arising from their coordinated metal centers. Among these, Copper(I) compounds have gained considerable attention. Unlike noble metals or rare earth elements, copper is both abundant and affordable, with low toxicity, making Cu(I)-based compounds ideal candidates for large-scale applications across numerous fields, particularly in optoelectronics and sensor technologies *[60–62]*.

One of the most attractive features of Cu(I) compounds is the ease with which their structural frameworks can be modified through simple changes in reaction conditions. This flexibility allows for the creation of materials that not only exhibit tunable phosphorescence at room temperature but also possess long luminescence lifetimes lasting several microseconds. These emission characteristics can be further modulated by external factors such as temperature, pressure or chemical interactions, making Cu(I) complexes especially useful for developing materials that display dynamic optical behaviors. This versatility has propelled them into the spotlight for applications in optoelectronic devices, where materials with stimuli-responsive properties are in high demand *[63–68]*.

The pioneering work of Ford and collaborators on luminescent cubane-shaped $Cu_4I_4L_4$ clusters and their derivatives (L = N- or P-donor ligands) laid the foundation for extensive research into copper halide-based materials. These studies prompted numerous research groups to explore a broader range of $Cu_xX_xL_y$ species, where X represents halides (Cl, Br, and I), x varies from 2 to 8, and y ranges between 4 and 8. Among these, copper iodide-based materials stood out for their intense luminescent properties, which facilitated the development of diverse functional materials, including stimuli-responsive and smart systems. These materials encompass discrete clusters and complexes (0D) as well as coordination polymers with 1D, 2D, or 3D architectures. In coordination polymers, the Cu_xX_x cores, often termed secondary building units (SBUs), play a central role in their structural and functional properties.

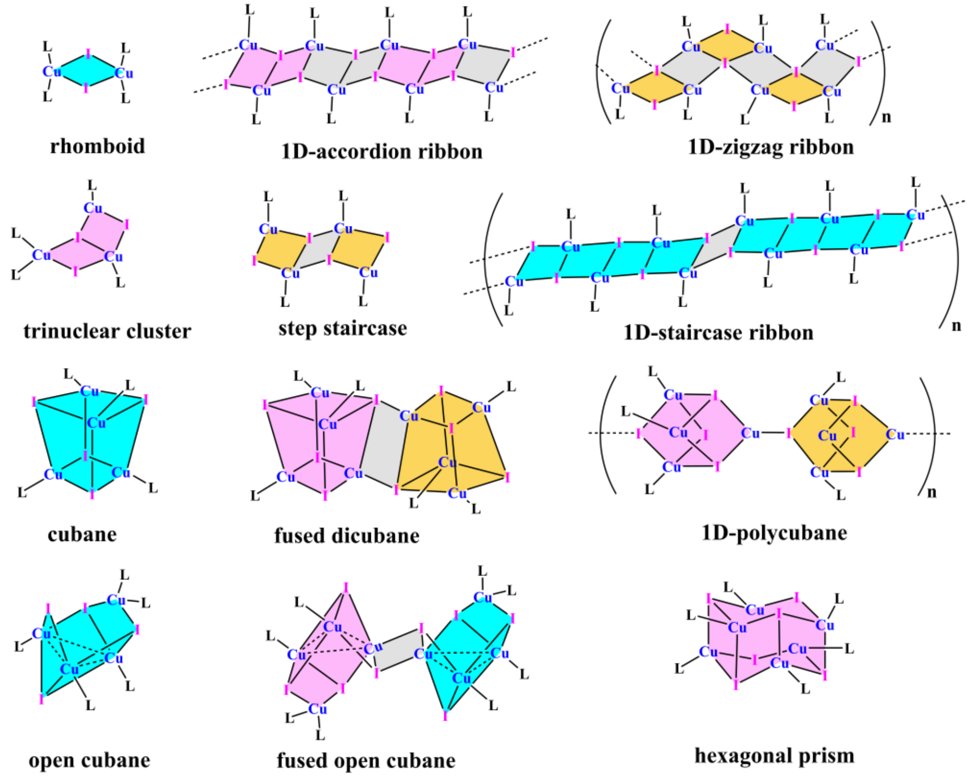

Fig. 1.5 Structures of the various SBUs or 0D complexes encountered for neutral $Cu_xI_xL_y$ motifs (L = N, P or S-donor ligands); top, quasi-planar, bottom, globular. Note that this list is not exhaustive, reproduced with permission from the Royal Society of Chemistry, ref *[64]*.

Structural surveys have shown that $Cu_xX_xP_y$ (X = Cl, Br, I) species predominantly form 0D complexes, while $Cu_xX_xN_y$ and $Cu_xX_xS_y$ species are typically found in coordination polymers, particularly in 1D and 2D structures (**Fig 1.5**). These differences in SBU geometries and network structures lead to distinct solid-state properties, such as variations in electrical conductivity and mechanical behavior. These modern Cu(I)-based materials exhibit rich electronic, optoelectronic, redox, and mechanical properties, with significant advancements reported in the last decade *[69–75]*. The resulting materials have demonstrated have multifunctional application like tunable emission, optical sensing, energy storage, gas sensing, photocatalysis and electroluminescence (**Fig. 1.6**) *[69–73]*. Consequently, the continued exploration of $Cu_xX_xL_y$ materials, across diverse ligand systems and structural formats, holds immense potential for the development of next-generation functional materials with broad applications in optoelectronics and beyond.

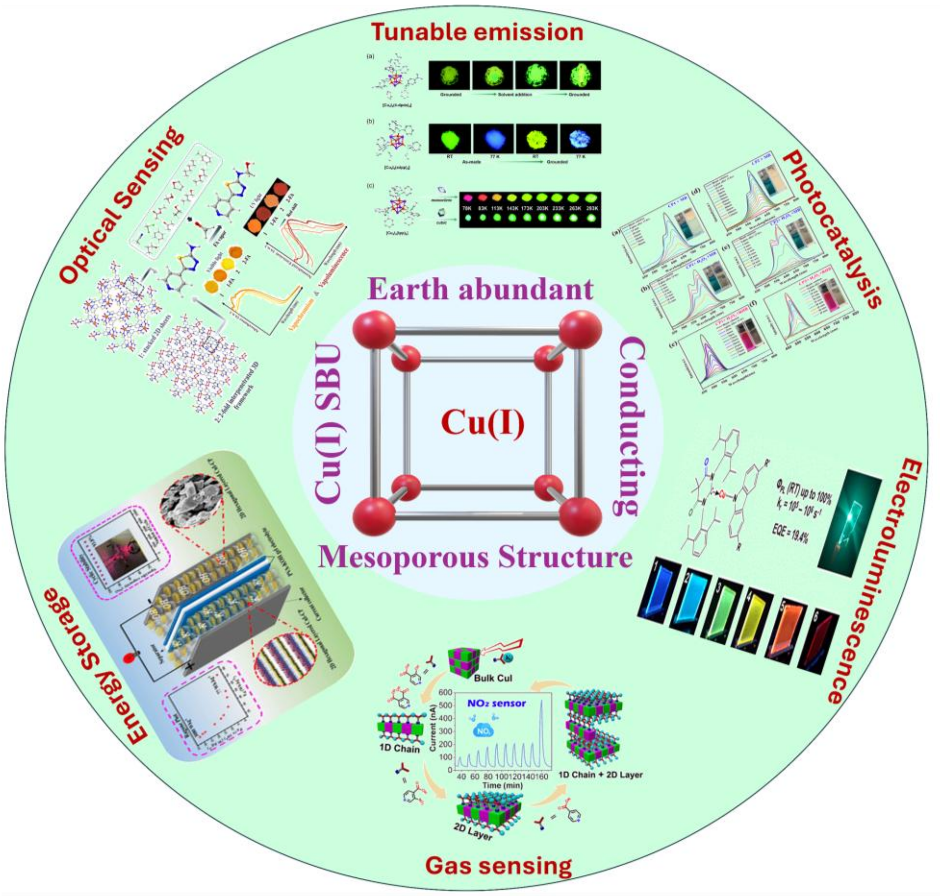

Fig. 1.6 Schematic illustration of various CuX nanocluster-based CPs/MOFs applications. Images taken from ref *[64,69,70,73, and 88].*

A key feature of these systems is their stimuli-responsive luminescence, which can be triggered by changes in temperature or pressure. This behavior is closely linked to structural adaptability, particularly variations in Cu···Cu distances. For instance, the $Cu_4I_4L_4$ clusters exhibit two extreme geometries stair-case and closed cubane tetramer and are directly associated with distinct photophysical properties. Stimuli-responsive luminescence in these systems extends to light-, solvent-, vapor-, and mechano-chromic effects. In coordination polymers, such responses may involve solid-to-solid phase transitions, further enhancing their versatility *[74,77]*.

1.6.1. Mechanochromic behaviour of Cu(I) frameworks:

Mechanochromic luminescent materials, which exhibit switchable luminescence in response to external mechanical forces, have garnered significant interest for applications in strain detection, optical recording, data storage, and anti-counterfeiting. A key advantage of these materials is the ease of detecting emission changes through simple, non-invasive spectroscopic methods or even visually. Despite the growing number of compounds with luminescent mechanochromism reported over the past decade, detailed studies on their underlying mechanisms remain limited. Such investigations are crucial for advancing fundamental understanding and guiding the design of materials with optimized stimuli-responsive properties *[78–81]*. Copper iodide clusters, including non-cubane geometries such as chair-like isomers, have demonstrated notable mechanochromic luminescence *[82–84]*. For example, the $[Cu_4I_4(PPh_3)_4]\cdot 2CHCl_3$ compound undergoes a mechanically induced structural isomerization from chair to cubane geometry upon grinding, resulting in a dramatic emission shift from blue to yellow (**Fig 1.7**). This transition involves the formation of additional Cu–I bonds and Cu–Cu interactions, as confirmed by photophysical and structural data supported by DFT calculations. The mechanism depends on weak intermolecular interactions and labile solvent molecules in the crystalline structure, enabling geometric flexibility *[85]*. In contrast, robust hydrogen bonding networks, as observed in $[Cu_4I_4(PPh_2\text{-}C_6H_4CO_2H)_4]$, inhibit such transitions *[86]*. Other examples of mechanochromic copper iodide systems include double cubane $[Cu_8I_8(PPh_2C_6H_4\text{-}N(CH_3)_2)_4]$ *[86]* clusters and butterfly-shaped $[Cu_4I_4(PPh_2py)_2]$ *[87]* clusters, where mechanochromism is attributed to changes in Cu–Cu distances or intermolecular interactions.

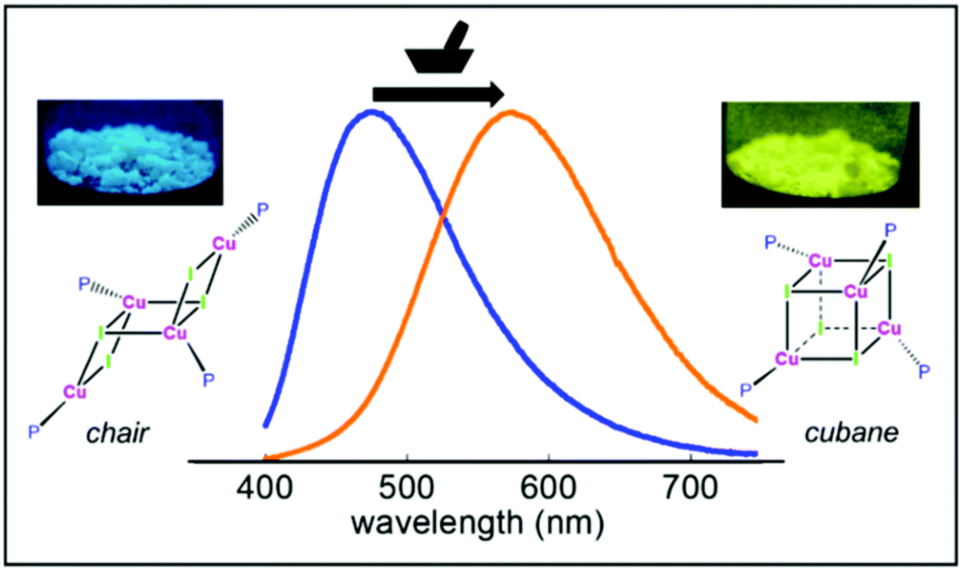

Fig. 1.7 Mechanochromism of $[Cu_4I_4(PPh_3)_4]\cdot 2CHCl_3$ with photographs of the powder before and after grinding and associated emission spectra with representations of the two chair and cubane isomers, reproduced with permission from the Royal Society of Chemistry, ref *[83]*.

1.6.2. Vapochromic behaviour of Cu(I) frameworks:

Vapochromism forms the very basis for the sensing properties of these coordination polymers. Several examples of small molecule-responsive coordination polymers built upon copper halide-thioether and -thione networks have been reported during the past few years. For example, Boonmak et al. prepared new amino-functionalized iodo-based 2D Cu(I) coordination polymers of $[CuI(pyt\text{-}NH_2)]_n$ (1) and (2) (where pyt-NH_2 = 2-amino-5-(4-pyridinyl)-1,3,4-thiadiazole). They possess densely diverse crystalline architectures decorated by uncoordinated amino groups as a binding site. Remarkably, 1 and 2 undergo the change of color and naked-eye solid-state luminescence in response to formaldehyde (FA) vapor, demonstrating simultaneous vapochromism and vapoluminescence *[73]*. FA-exposed 1 and 2 (1-FA and 2-FA) display an extension of absorption spectral edge to a longer wavelength around 570 nm, which is consistent with the orange color. The luminescent signals of 1 and 2 are also altered by FA vapor, which demonstrates red-shifted emission bands from 567 to 587 nm for 1-FA and from 551 to 590 nm for 2-FA, corresponding to the emission color change from orange to red-orange under UV light (**Fig. 1.8**).

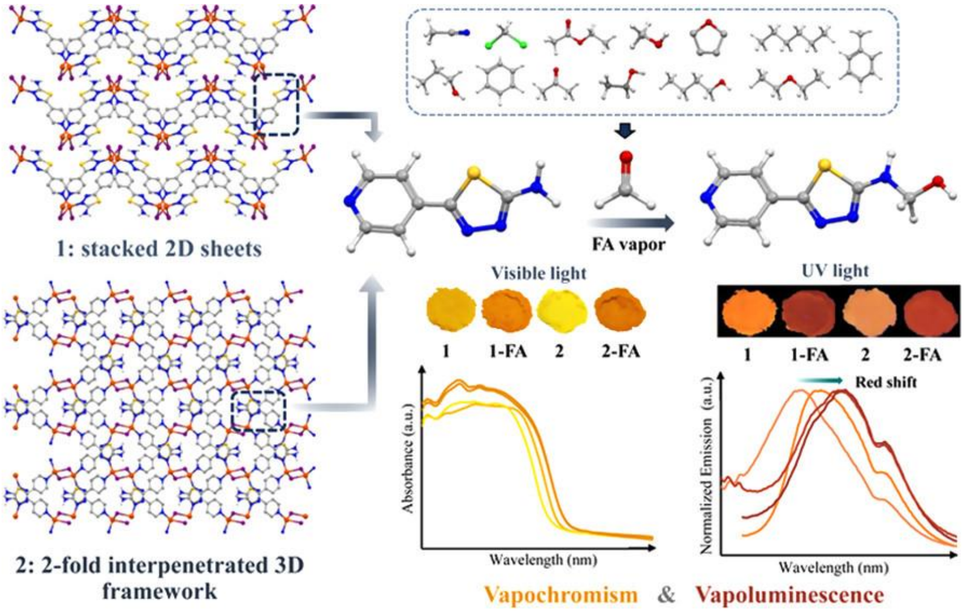

Fig. 1.8 Amino-functionalized chromic Cu(I)-CPs undergo color and naked-eye luminescent change in selective response to formaldehyde (FA) vapor, demonstrating simultaneous vapochromism and vapoluminescence, reproduced with permission from the American Chemical Society, ref *[73]*.

1.6.3. Cu(I) CPs/MOFs in chemiresistive and optical gas sensing:

Beyond optoelectronic applications, Cu(I)-based coordination frameworks are emerging as highly effective materials for gas sensing technologies. Monitoring gases such as hydrocarbons, VOCs and several toxic gases such as ammonia (NH_3), and nitrogen dioxides (NO_2) is crucial for both environmental protection and public health. Toxic gases can contribute to serious environmental issues like acid rain, smog, and the greenhouse effect, while even non-toxic gases like oxygen and water vapor are critical for various industrial processes. For instance, oxygen-free environments are essential in the metallurgical and chemical industries, while humidity control is vital in sectors ranging from agriculture to home comfort systems. Cu(I)-based materials, with their sensitivity and selectivity to different gas molecules, provide a promising solution for these monitoring needs. The integration of Cu(I) coordination compounds into gas sensor technologies takes advantage of the unique optical and chemical properties of these materials *[2,3]*.

Recent advancements in Cu(I)-based coordination polymers (CPs) and hybrid materials have demonstrated significant potential for high-performance sensing applications. In 2023, Jing Li and collaborators developed CuI-based hybrids featuring tunable 1D or 2D CuI modules stabilized within potassium isonicotinic acid (HINA) frameworks and its derivatives. The dimensionality of the CuI modules critically influenced their properties, with 2D-CuI structures achieving photoconductivity up to five orders of magnitude higher than 1D counterparts. These materials also marked the debut of CuI-based hybrid NO_2 chemiresistive sensors, with sensitivity exceeding pristine CuI by several orders of magnitude (**Fig 1.9**). Notably, the CuI-K-INA hybrid, integrating both 1D and 2D CuI modules, performed comparably to the best NO_2 chemiresistors reported to date *[88]*.

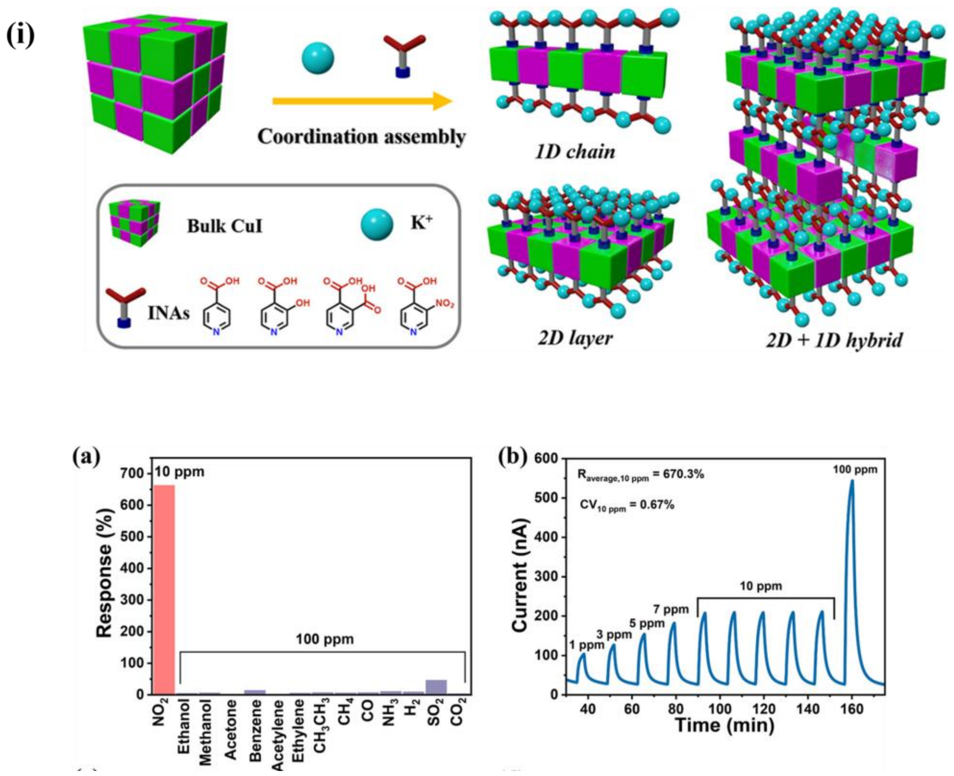

Fig. 1.9 (i) Schematic illustration of the confinement of 1D chain and/or 2D layered CuI modules assembled in K-INA-R CPs. (a) Responses of CuI-K-INA as a sensor to 10 ppm NO_2 with other different 100 ppm gases. (b) Response and recovery curve of CuI-K-INA toward NO_2 with varied concentrations at RT, reproduced with permission from the American Chemical Society, ref *[88]*.

Further, Mishra and coworkers in 2024 synthesized a 2D semiconducting CP via a one-pot method, achieving a conductivity of 2.02×10^{-7} $S \cdot cm^{-1}$. Structural analysis revealed Cu_2I_2 SBUs bridged by 1,4-TzB through the triazole ring's nitrogen atoms. The resulting sensor exhibited exceptional selectivity for methanol vapor over other VOCs, with an impressive response (R_g/R_a) of 66.7, ultra-fast response and recovery times (17.5/34.2 seconds), and ppb-level sensitivity at room temperature (**Fig 1.10**). Furthermore, the device demonstrated excellent repeatability without requiring external stimuli *[72]*.

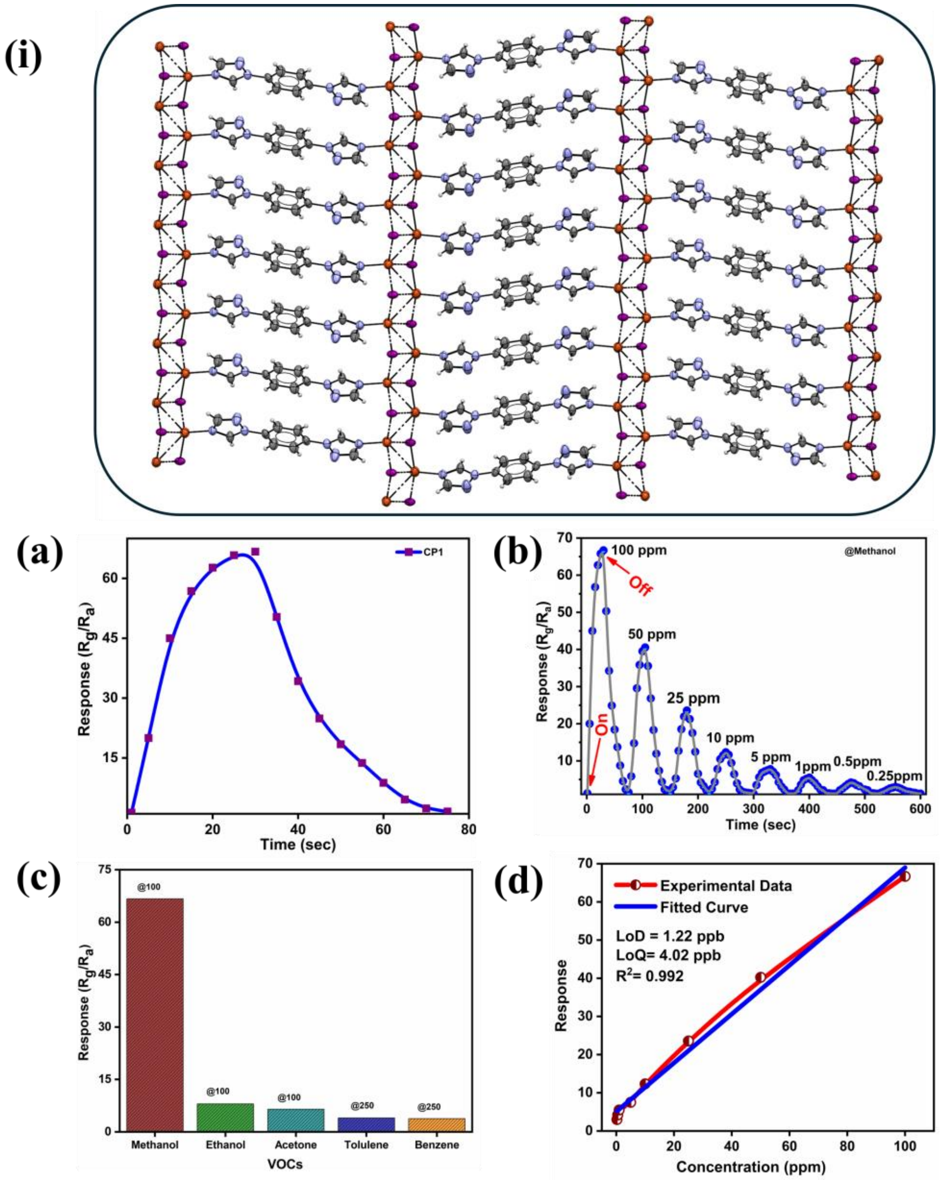

Fig. 1.10 (i) Molecular structure of 2D CP (a) response of CP (b) (d) response and recovery of methanol at different concentrations, (c) selectivity analysis for the CP sensor with interfering VOCs. (d) LoD and LoQ for the CP sensor, reproduced with permission from John Wiley and Sons, ref *[72]*.

Together, these advancements highlight the transformative role of integrating semiconducting CuI modules with CPs and MOFs. The synergy between tunable electronic properties, enhanced conductivity, and selective gas sensitivity bridges the gap between fundamental material innovation and practical sensing technologies. The intrinsic porosity and conductive pathways in these hybrid systems pave the way for next generation chemiresistive sensors and optoelectronic devices, underscoring the interplay between inorganic frameworks and organic coordination scaffolds.

This thesis aims to develop and investigate copper(I)-based CPs/MOFs as advanced materials for chemiresistive gas sensing applications. This thesis focuses on synthesizing novel copper-based frameworks with varied dimensionalities and ligand architectures to optimize their sensitivity, selectivity, and stability. Special attention is given to two-dimensional 2D frameworks, which are known for their superior conductivity and enhanced gas sensing capabilities due to their high surface area and accessible active sites. The study explores the role of electron-rich copper(I) centers in facilitating charge transfer interactions with analytes, thus improving the sensing performance. By integrating the concepts of framework conductivity with rational design of Cu(I)-based CPs and MOFs, this thesis aims to address key challenges in real-world applications, including room-temperature operation, rapid response times, and long-term stability. Ultimately, this research contributes to the development of efficient, scalable, and reliable gas sensor materials tailored for environmental monitoring, industrial safety, and related fields.

1.7. References

1. Hu, Z., Deibert, B.J., and Li, J. (2014). Luminescent metal–organic frameworks for chemical sensing and explosive detection. Chem Soc Rev *43*, 5815–5840. (DOI: 10.1039/C4CS00010B)

2. López-Molino, J., and Amo-Ochoa, P. (2020). Gas Sensors Based on Copper-Containing Metal-Organic Frameworks, Coordination Polymers, and Complexes. ChemPlusChem *85*, 1564–1579. (DOI: 10.1002/cplu.202000428)
3. Li, H.-Y., Zhao, S.-N., Zang, S.-Q., and Li, J. (2020). Functional metal–organic frameworks as effective sensors of gases and volatile compounds. Chem. Soc. Rev. *49*, 6364–6401. (DOI: 10.1039/C9CS00778D)
4. Lustig, W.P., Mukherjee, S., Rudd, N.D., Desai, A.V., Li, J., and Ghosh, S.K. (2017). Metal–organic frameworks: functional luminescent and photonic materials for sensing applications. Chem. Soc. Rev. *46*, 3242–3285. (DOI: 10.1039/C6CS00930A)
5. Yang, G., Jiang, X., Xu, H., and Zhao, B. (2021). Applications of MOFs as Luminescent Sensors for Environmental Pollutants. Small *17*, 2005327. (DOI: 10.1002/smll.202005327)
6. Olorunyomi, J.F., Geh, S.T., Caruso, R.A., and Doherty, C.M. (2021). Metal–organic frameworks for chemical sensing devices. Mater. Horiz. *8*, 2387–2419. (DOI: 10.1039/D1MH00609F)
7. Weppner, W. (1987). Solid-state electrochemical gas sensors. Sens. Actuators *12*, 107–119. (DOI: 10.1016/0250-6874(87)85010-2)
8. Seiyama, T., Kato, A., Fujiishi, K., and Nagatani, M. (1962). A New Detector for Gaseous Components Using Semiconductive Thin Films. Anal. Chem. *34*, 1502–1503. (DOI: 10.1021/ac60191a001)
9. Sakai, G., Matsunaga, N., Shimanoe, K., and Yamazoe, N. (2001). Theory of gas-diffusion controlled sensitivity for thin film semiconductor gas sensor. Sens. Actuators B Chem. *80*, 125–131. (DOI: 10.1016/S0925-4005(01)00890-5)
10. Hakeem Anwer, A., Saadaoui, M., Mohamed, A.T., Ahmad, N., and Benamor, A. (2024). State-of-the-Art advances and challenges in wearable gas sensors for emerging applications: Innovations and

future prospects. Chem. Eng. J. *502*, 157899. (DOI: 10.1016/j.cej.2024.157899)

11. Trung, T.Q., and Lee, N. (2016). Flexible and Stretchable Physical Sensor Integrated Platforms for Wearable Human-Activity Monitoring and Personal Healthcare. Adv. Mater. *28*, 4338–4372. (DOI: 10.1002/adma.201504244)
12. Singh, E., Meyyappan, M., and Nalwa, H.S. (2017). Flexible Graphene-Based Wearable Gas and Chemical Sensors. ACS Appl. Mater. Interfaces *9*, 34544–34586. (DOI: 10.1021/acsami.7b07063)
13. Shin, W., Matsumiya, M., Izu, N., and Murayama, N. (2003). Hydrogen-selective thermoelectric gas sensor. Sens. Actuators B Chem. *93*, 304–308. (DOI: 10.1016/S0925-4005(03)00225-9)
14. Shin, W., Matsumiya, M., Qiu, F., Izu, N., and Murayama, N. (2004). Thermoelectric gas sensor for detection of high hydrogen concentration. Sens. Actuators B Chem. *97*, 344–347. (DOI: 10.1016/j.snb.2003.08.029)
15. Huang, H., Luan, W., Zhang, J.-S., Qi, Y.-S., and Tu, S.-T. (2008). Thermoelectric hydrogen sensor working at room temperature prepared by bismuth–telluride P–N couples and Pt/γ-Al2O3. Sens. Actuators B Chem. *128*, 581–585. (DOI: 10.1016/j.snb.2007.07.060)
16. Anuradha, S., and Rajanna, K. (2006). Development of Thermoelectric Gas Sensors for Volatile Organic Compounds. In 2006 5th IEEE Conference on Sensors (IEEE), pp. 716–718. (DOI: 10.1109/ICSENS.2007.355561)
17. Panda, S., Mehlawat, S., Dhariwal, N., Kumar, A., and Sanger, A. (2024). Comprehensive review on gas sensors: Unveiling recent developments and addressing challenges. Mater. Sci. Eng. B *308*, 117616. (DOI: 10.1016/j.mseb.2024.117616)

18. McDonagh, C., Burke, C.S., and MacCraith, B.D. (2008). Optical Chemical Sensors. Chem. Rev. *108*, 400–422. (DOI: 10.1021/cr068102g)

19. Okazaki, S., Nakagawa, H., Asakura, S., Tomiuchi, Y., Tsuji, N., Murayama, H., and Washiya, M. (2003). Sensing characteristics of an optical fiber sensor for hydrogen leak. Sens. Actuators B Chem. *93*, 142–147. (DOI: 10.1016/S0925-4005(03)00211-9)

20. Lim, C., Wang, W., Yang, S., and Lee, K. (2011). Development of SAW-based multi-gas sensor for simultaneous detection of CO2 and NO_2. Sens. Actuators B Chem. *154*, 9–16. (DOI: 10.1016/j.snb.2010.02.057)

21. Tressler, J.F., Alkoy, S., and Newnham, R.E. (1998). Piezoelectric Sensors and Sensor Materials. J. Electroceramics *2*, 257–272. (DOI: 10.1023/A:1009926623551)

22. Torad, N.L., Zhang, S., Amer, W.A., Ayad, M.M., Kim, M., Kim, J., Ding, B., Zhang, X., Kimura, T., and Yamauchi, Y. (2019). Advanced Nanoporous Material–Based QCM Devices: A New Horizon of Interfacial Mass Sensing Technology. Adv. Mater. Interfaces *6*, 1900849. (DOI: 10.1002/admi.201900849)

23. Korotcenkov, G. (2013). Materials for Piezoelectric-Based Gas Sensors. In Handbook of Gas Sensor Materials: Properties, Advantages and Shortcomings for Applications Volume 1: Conventional Approaches, G. Korotcenkov, ed. (Springer), pp. 307–328. (DOI: 10.1007/978-1-4614-7165-3-13)

24. Venkatasubramanian, A., Lee, J.-H., Houk, R.J., Allendorf, M.D., Nair, S., and Hesketh, P.J. (2010). Characterization of HKUST-1 Crystals and Their Application to MEMS Microcantilever Array Sensors. ECS Trans. *33*, 229. (DOI: 10.1149/1.3484126)

25. Asri, M.I.A., Hasan, Md.N., Fuaad, M.R.A., Yunos, Y.Md., and Ali, M.S.M. (2021). MEMS Gas Sensors: A Review. IEEE Sens. J. *21*, 18381–18397. (DOI: 10.1109/JSEN.2021.3091854)
26. Hosseini, M.S., Zeinali, S., and Sheikhi, M.H. (2016). Fabrication of capacitive sensor based on Cu-BTC (MOF-199) nanoporous film for detection of ethanol and methanol vapors. Sens. Actuators B Chem. *230*, 9–16. (DOI: 10.1016/j.snb.2016.02.008)
27. Rheaume, J.M., and Pisano, A.P. (2011). A review of recent progress in sensing of gas concentration by impedance change. Ionics *17*, 99–108. (DOI: 10.1007/s11581-010-0515-1)
28. Achmann, S., Hagen, G., Kita, J., Malkowsky, I.M., Kiener, C., and Moos, R. (2009). Metal-Organic Frameworks for Sensing Applications in the Gas Phase. Sensors *9*, 1574–1589. (DOI: 10.3390/s90301574)
29. Majhi, S.M., Mirzaei, A., Kim, H.W., Kim, S.S., and Kim, T.W. (2021). Recent advances in energy-saving chemiresistive gas sensors: A review. Nano Energy *79*, 105369. (DOI: /10.1016/j.nanoen.2020.105369)
30. Srinivasan, P., Ezhilan, M., Kulandaisamy, A.J., Babu, K.J., and Rayappan, J.B.B. (2019). Room temperature chemiresistive gas sensors: challenges and strategies—a mini review. J. Mater. Sci. Mater. Electron. *30*, 15825–15847. (DOI: 10.1007/s10854-019-02025-1)
31. Barsan, N., Koziej, D., and Weimar, U. (2007). Metal oxide-based gas sensor research: How to? Sens. Actuators B Chem. *121*, 18–35. (DOI: 10.1016/j.snb.2006.09.047)
32. Dey, A. (2018). Semiconductor metal oxide gas sensors: A review. Mater. Sci. Eng. B *229*, 206–217. (DOI: 10.1016/j.mseb.2017.12.036)
33. Li, Z., Li, H., Wu, Z., Wang, M., Luo, J., Torun, H., Hu, P., Yang, C., Grundmann, M., Liu, X., et al. (2019). Advances in designs and

mechanisms of semiconducting metal oxide nanostructures for high-precision gas sensors operated at room temperature. Mater. Horiz. *6*, 470–506. (DOI: 10.1039/C8MH01365A)

34. Koo, W.-T., Jang, J.-S., and Kim, I.-D. (2019). Metal-Organic Frameworks for Chemiresistive Sensors. Chem *5*, 1938–1963. (DOI: 10.1016/j.chempr.2019.04.013)
35. Jo, Y.-M., Jo, Y.K., Lee, J.-H., Jang, H.W., Hwang, I.-S., and Yoo, D.J. (2023). MOF-Based Chemiresistive Gas Sensors: Toward New Functionalities. Adv. Mater. *35*, 2206842. (DOI: 10.1002/adma.202206842)
36. Campbell, M.G., and Dincă, M. (2017). Metal–Organic Frameworks as Active Materials in Electronic Sensor Devices. Sensors *17*, 1108. (DOI: 10.3390/s17051108)
37. Yang, G.G., Kim, D.-H., Samal, S., Choi, J., Roh, H., Cunin, C.E., Lee, H.M., Kim, S.O., Dincă, M., and Gumyusenge, A. (2023). Polymer-Based Thermally Stable Chemiresistive Sensor for Real-Time Monitoring of NO_2 Gas Emission. ACS Sens. *8*, 3687–3692. (DOI: 10.1021/acssensors.3c01530)
38. Roh, H., Kim, D., Cho, Y., Jo, Y., Del Alamo, J.A., Kulik, H.J., Dincă, M., and Gumyusenge, A. (2024). Robust Chemiresistive Behavior in Conductive Polymer/MOF Composites. Adv. Mater. *36*, 2312382. (DOI: 10.1002/adma.202312382)
39. Yao, M.-S., Lv, X.-J., Fu, Z.-H., Li, W.-H., Deng, W.-H., Wu, G.-D., and Xu, G. (2017). Layer-by-Layer Assembled Conductive Metal–Organic Framework Nanofilms for Room-Temperature Chemiresistive Sensing. Angew. Chem. Int. Ed. *56*, 16510–16514. (DOI: 10.1002/anie.201709558)
40. Yan, X., Chen, J., Su, X., Zhang, J., Wang, C., Zhang, H., Liu, Y., Wang, L., Xu, G., and Chen, L. (2024). Redox Synergy: Enhancing Gas Sensing Stability in 2D Conjugated Metal–Organic Frameworks

via Balancing Metal Node and Ligand Reactivity. Angew. Chem. Int. Ed. *63*, e202408189. (DOI: 10.1002/anie.202408189)

41. Shan, Z., Xiao, J.-Z., Wu, M., Wang, J., Su, J., Yao, M.-S., Lu, M., Wang, R., and Zhang, G. (2024). Topologically Tunable Conjugated Metal–Organic Frameworks for Modulating Conductivity and Chemiresistive Properties for NH3 Sensing. Angew. Chem. Int. Ed. *63*, e202401679. (DOI: 10.1002/anie.202401679)
42. Su, X., Zhong, Z., Yan, X., Zhang, T., Wang, C., Wang, Y.-X., Xu, G., and Chen, L. (2023). Facile Synthesis of Metallosalphen-Based 2D Conductive Metal-Organic Frameworks for NO_2 Sensing: Metal Coordination Induced Planarization. Angew. Chem. Int. Ed. *62*, e202302645. (DOI: 10.1002/anie.202302645)
43. Benedetto, G., and Mirica, K.A. (2024). Conductive Framework Materials for Chemiresistive Detection and Differentiation of Toxic Gases. Acc. Chem. Res. *57*, 2775–2789. (DOI: 10.1021/acs.accounts.4c00319)
44. Givaja, G., Amo-Ochoa, P., Gómez-García, C.J., and Zamora, F. (2011). Electrical conductive coordination polymers. Chem. Soc. Rev. *41*, 115–147. (DOI: 10.1039/C1CS15092H)
45. Bredas, J.L., and Street, G.B. (1985). Polarons, bipolarons, and solitons in conducting polymers. Acc. Chem. Res. *18*, 309–315. (DOI: 10.1021/ar00118a005)
46. Li, W.-H., Deng, W.-H., Wang, G.-E., and Xu, G. (2020). Conductive MOFs. EnergyChem *2*, 100029. (DOI: 10.1016/j.enchem.2020.100029)
47. Xie, L.S., Skorupskii, G., and Dincă, M. (2020). Electrically Conductive Metal–Organic Frameworks. Chem. Rev. *120*, 8536–8580. (DOI: 10.1021/acs.chemrev.9b00766)
48. Xu, G., Zhu, C., and Gao, G. (2022). Recent Progress of Advanced Conductive Metal–Organic Frameworks: Precise Synthesis,

Electrochemical Energy Storage Applications, and Future Challenges. Small *18*, 2203140. (DOI: 10.1002/smll.202203140)

49. Sun, L., Campbell, M.G., and Dincă, M. (2016). Electrically Conductive Porous Metal–Organic Frameworks. Angew. Chem. Int. Ed. *55,* 3566–3579. (DOI: 10.1002/anie.201506219)
50. Liu, L., Xu, Q., and Zhu, Q.-L. (2021). Electrically Conductive Metal–Organic Frameworks for Electrocatalytic Applications. Adv. Energy Sustain. Res. *2,* 2100100. (DOI: 10.1002/aesr.202100100)
51. Yao, M.-S., Li, W.-H., and Xu, G. (2021). Metal–organic frameworks and their derivatives for electrically-transduced gas sensors. Coord. Chem. Rev. *426*, 213479. (DOI: 10.1016/j.ccr.2020.213479)
52. Campbell, M.G., Sheberla, D., Liu, S.F., Swager, T.M., and Dincă, M. (2015). Cu_3(hexaiminotriphenylene)$_2$: An Electrically Conductive 2D Metal–Organic Framework for Chemiresistive Sensing. Angew. Chem. Int. Ed. *54*, 4349–4352. (DOI: 10.1002/anie.201411854)
53. Sharma, A., Babu Eadi, S., Noothalapati, H., Otyepka, M., Lee, H.-D., and Jayaramulu, K. (2024). Porous materials as effective chemiresistive gas sensors. Chem. Soc. Rev. *53*, 2530–2577. (DOI: 10.1039/D2CS00761D)
54. Liu, C., Gu, Y., Liu, C., Liu, S., Li, X., Ma, J., and Ding, M. (2021). Missing-Linker 2D Conductive Metal Organic Frameworks for Rapid Gas Detection. ACS Sens. *6*, 429–438. (DOI: 10.1021/acssensors.0c01933)
55. Rubio-Giménez, V., Almora-Barrios, N., Escorcia-Ariza, G., Galbiati, M., Sessolo, M., Tatay, S., and Martí-Gastaldo, C. (2018). Origin of the Chemiresistive Response of Ultrathin Films of Conductive Metal–Organic Frameworks. Angew. Chem. *130,* 15306–15310. (DOI: 10.1002/ange.201808242)
56. Park, C., Baek, J.W., Shin, E., and Kim, I.-D. (2023). Two-Dimensional Electrically Conductive Metal–Organic Frameworks as

Chemiresistive Sensors. ACS Nanosci. Au *3*, 353–374. (DOI: 10.1021/acsnanoscienceau.3c00024)

57. Wang, Z., Bu, M., Hu, N., and Zhao, L. (2023). An overview on room-temperature chemiresistor gas sensors based on 2D materials: Research status and challenge. Compos. Part B Eng. *248*, 110378. (DOI: 10.1016/j.compositesb.2022.110378)
58. Campbell, M.G., Liu, S.F., Swager, T.M., and Dincă, M. (2015). Chemiresistive Sensor Arrays from Conductive 2D Metal–Organic Frameworks. J. Am. Chem. Soc. *137*, 13780–13783. (DOI: 10.1021/jacs.5b09600)
59. Smith, M.K., Jensen, K.E., Pivak, P.A., and Mirica, K.A. (2016). Direct Self-Assembly of Conductive Nanorods of Metal–Organic Frameworks into Chemiresistive Devices on Shrinkable Polymer Films. Chem. Mater. *28*, 5264–5268. (DOI: 10.1021/acs.chemmater.6b02528)
60. Lu, J.Y. (2003). Crystal engineering of Cu-containing metal–organic coordination polymers under hydrothermal conditions. Coord. Chem. Rev. *246*, 327–347. (DOI: 10.1016/j.cct.2003.08.005)
61. Kobayashi, A., Fujii, M., Shigeta, Y., Yoshida, M., and Kato, M. (2019). Quantitative Solvent-Free Thermal Synthesis of Luminescent Cu(I) Coordination Polymers. Inorg. Chem. *58*, 4456–4464. (DOI: 10.1021/acs.inorgchem.8b03641)
62. Schlachter, A., Tanner, K., and Harvey, P.D. (2021). Copper halide-chalcogenoether and -chalcogenone networks: Chain and cluster motifs, polymer dimensionality and photophysical properties. Coord. Chem. Rev. *448*, 214176. (DOI: 10.1016/j.ccr.2021.214176)
63. Conesa-Egea, J., Zamora, F., and Amo-Ochoa, P. (2019). Perspectives of the smart Cu-Iodine coordination polymers: A portage to the world of new nanomaterials and composites. Coord. Chem. Rev. *381*, 65–78. (DOI: 10.1016/j.ccr.2018.11.008)

64. Troyano, J., Zamora, F., and Delgado, S. (2021). Copper(i)–iodide cluster structures as functional and processable platform materials. Chem. Soc. Rev. *50*, 4606–4628. (DOI: 10.1039/D0CS01470B)

65. Chen, J., Zhou, K., Li, J., Xu, G., Hei, X., and Li, J. (2024). Strongly photoluminescent and radioluminescent copper(i) iodide hybrid materials made of coordinated ionic chains. Chem. Sci. (DOI: 10.1039/D4SC06242F)

66. Liu, W., Fang, Y., and Li, J. (2018). Copper Iodide Based Hybrid Phosphors for Energy-Efficient General Lighting Technologies. Adv. Funct. Mater. *28,* 1705593. (DOI: 10.1002/adfm.201705593)

67. Cariati, E., Lucenti, E., Botta, C., Giovanella, U., Marinotto, D., and Righetto, S. (2016). Cu(I) hybrid inorganic–organic materials with intriguing stimuli responsive and optoelectronic properties. Coord. Chem. Rev. *306*, 566–614. (DOI: 10.1016/j.ccr.2015.03.004)

68. Zheng, H.-W., Yang, D.-D., Liang, Q.-F., Liu, Y.-P., Shan, J.-H., Liu, Q.-Q., Tan, H.-W., Chen, L., and Zheng, X.-J. (2022). A diamond-like cuprous coordination polymer based on the $[Cu_8I_6]^{2+}$ cluster with multistimuli-responsive luminescence and iodine adsorption behavior. J. Mater. Chem. C *10*, 3901–3907. (DOI: 10.1039/D1TC05937H)

69. Pandey, D., K. Singh, M., Mishra, S., K. Rai, D., and Raghuvanshi, A. (2024). A 2D layered semiconducting $(LCu_3I_3)_n$ coordination polymer for energy storage through dual ion intercalation. J. Mater. Chem. A *12*, 27355–27363. (DOI: 10.1039/D4TA04301D)

70. Pandey, D., Mishra, A., Kharabe, L.S., Maurya, S.K., and Raghuvanshi, A. (2024). Semiconducting Copper(I) Iodide 2D-Coordination Polymers for Efficient Sunlight-Driven Photocatalysis in Dye Degradation. Cryst. Growth Des. *24*, 6051–6059. (DOI: 10.1021/acs.cgd.4c00699)

71. Mishra, S., K. Singh, M., Pandey, D., K. Rai, D., and Raghuvanshi, A. (2024). A two-dimensional semiconducting Cu(i)-MOF for binder

and conductive additive-free supercapattery. J. Mater. Chem. A *12*, 4534–4543. (DOI: 10.1039/D3TA04708C)

72. Mishra, S., Patel, C., Pandey, D., Mukherjee, S., and Raghuvanshi, A. (2024). Semiconducting 2D Copper(I) Iodide Coordination Polymer as a Potential Chemiresistive Sensor for Methanol. Small *20*, 2311448. (DOI: 10.1002/smll.202311448)
73. Tunsrichon, S., Chainok, K., Promarak, V., Nalaoh, P., Youngme, S., and Boonmak, J. (2022). Simultaneous Occurrence of Vapochromism and Vapoluminescence in Formaldehyde-Responsive Amino-Functionalized Copper(I) Polymorphic Coordination Polymers. Inorg. Chem. *61*, 11734–11745. (DOI: 10.1021/acs.inorgchem.2c01421)
74. Shan, X.-C., Zhang, H.-B., Chen, L., Wu, M.-Y., Jiang, F.-L., and Hong, M.-C. (2013). Multistimuli-Responsive Luminescent Material Reversible Switching Colors via Temperature and Mechanical Force. Cryst. Growth Des. *13*, 1377–1381. (DOI: 10.1021/cg400027u)
75. Bai, S.-Q., Jiang, L., Tan, A.L., Yeo, S.C., Young, D.J., and Hor, T.S.A. (2015). Assembly of photoluminescent [Cu_nI_n] (n = 4, 6 and 8) clusters by clickable hybrid [N,S] ligands. Inorg. Chem. Front. *2*, 1011–1018. (DOI: 10.1039/C5QI00030K)
76. Xie, M., Han, C., Zhang, J., Xie, G., and Xu, H. (2017). White Electroluminescent Phosphine-Chelated Copper Iodide Nanoclusters. Chem. Mater. *29*, 6606–6610. (DOI: 10.1021/acs.chemmater.7b01443)
77. Roppolo, I., Celasco, E., Fargues, A., Garcia, A., Revaux, A., Dantelle, G., Maroun, F., Gacoin, T., Boilot, J.-P., Sangermano, M., et al. (2011). Luminescence thermochromism of acrylic materials incorporating copper iodide clusters. J. Mater. Chem. *21*, 19106–19113. (DOI: 10.1039/C1JM13600C)

78. Dong, Y.Q., Lam, J.W.Y., and Tang, B.Z. (2015). Mechanochromic Luminescence of Aggregation-Induced Emission Luminogens. J. Phys. Chem. Lett. *6*, 3429–3436. (DOI: 10.1021/acs.jpclett.5b01090)

79. Penczner, S.H., Kumar, P., Patel, M., Bouchard, L.-S., Iacopino, D., and Patel, R. (2024). Innovations in mechanochemical synthesis: Luminescent materials and their applications. Mater. Today Chem. *39*, 102177. (DOI: 10.1016/j.mtchem.2024.102177)

80. Huang, G., Xia, Q., Huang, W., Tian, J., He, Z., Li, B.S., and Tang, B.Z. (2019). Multiple Anti-Counterfeiting Guarantees from a Simple Tetraphenylethylene Derivative – High-Contrasted and Multi-State Mechanochromism and Photochromism. Angew. Chem. *131*, 17978–17983. (DOI: 10.1002/ange.201910530)

81. He, J., Chen, H., Li, J., Wang, J., Xu, J., Zhao, Z., and Tang, B.Z. (2022). Aggregation-induced delayed fluorescence molecules with mechanochromic behaviors for efficient blue organic light-emitting diodes. Cell Rep. Phys. Sci. *3*. (DOI: 10.1016/j.xcrp.2021.100733)

82. Fang, Y., Liu, W., Teat, S.J., Dey, G., Shen, Z., An, L., Yu, D., Wang, L., O'Carroll, D.M., and Li, J. (2017). A Systematic Approach to Achieving High Performance Hybrid Lighting Phosphors with Excellent Thermal- and Photostability. Adv. Funct. Mater. *27*, 1603444. https://doi.org/10.1002/adfm.201603444.

83. Vogel, U., Nixon, J.F., and Scheer, M. (2007). Copper(I) mediated oligomerisation of a phosphaalkyne. Chem. Commun., 5055–5057. (DOI: 10.1039/B712161J)

84. Kobayashi, A., Yoshida, Y., Yoshida, M., and Kato, M. (2018). Mechanochromic Switching between Delayed Fluorescence and Phosphorescence of Luminescent Coordination Polymers Composed of Dinuclear Copper(I) Iodide Rhombic Cores. Chem. – Eur. J. *24*, 14750–14759. (DOI: 10.1002/chem.201802532)

85. Huitorel, B., El Moll, H., Cordier, M., Fargues, A., Garcia, A., Massuyeau, F., Martineau-Corcos, C., Gacoin, T., and Perruchas, S. (2017). Luminescence Mechanochromism Induced by Cluster Isomerization. Inorg. Chem. *56*, 12379–12388. (DOI: 10.1021/acs.inorgchem.7b01870)

86. Shan, X.-C., Jiang, F.-L., Chen, L., Wu, M.-Y., Pan, J., Wan, X.-Y., and Hong, M.-C. (2013). Using cuprophilicity as a multi-responsive chromophore switching color in response to temperature, mechanical force and solvent vapors. J. Mater. Chem. C *1*, 4339–4349. (DOI: 10.1039/C3TC30482E)

87. Neshat, A., Aghakhanpour, R.B., Mastrorilli, P., Todisco, S., Molani, F., and Wojtczak, A. (2018). Dinuclear and tetranuclear copper(I) iodide complexes with P and P^N donor ligands: Structural and photoluminescence studies. Polyhedron *154*, 217–228. (DOI: 10.1016/j.poly.2018.07.045)

88. Wu, Z.-F., Wang, C., Liu, X., Tan, K., Fu, Z., Teat, S.J., Li, Z.-W., Hei, X., Huang, X.-Y., Xu, G., et al. (2023). Confinement of 1D Chain and 2D Layered CuI Modules in K-INA-R Frameworks via Coordination Assembly: Structure Regulation and Semiconductivity Tuning. J. Am. Chem. Soc. *145*, 19293–19302. (DOI: 10.1021/jacs.3c05095)

Chapter 2

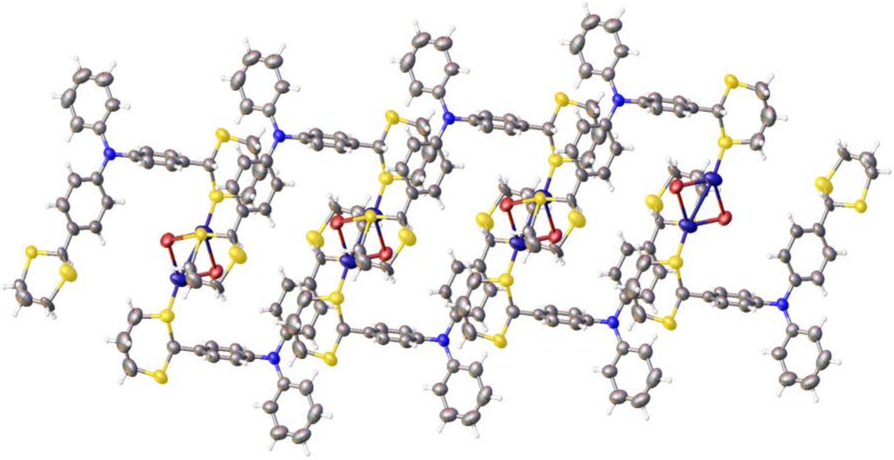

Solvatochromic behaviour of cyclic dithioether-functionalized triphenylamine ligands and their mechano-responsive Cu(I) coordination polymers

2.1. Introduction

External stimuli like light, pH, temperature, mechanical force and magnetic or electric fields can affect the luminescence behavior of various compounds *[1–3]*. Compounds with unique photoluminescent properties under different conditions are prominent materials for applications in sensing, detection, memory, display systems and others *[4–6]*. However, synthesizing materials that can respond in a controlled and desirable fashion under various external stimuli is challenging. Molecules with strong *π-π* interaction in the aggregated state lead to quenching of emission called aggregation-caused quenching (ACQ), whereas enhanced emission in the aggregated state is known as aggregation-induced emission (AIE). In order to design stimuli-responsive fluorescent materials, mostly tetraphenylethene, triphenylamine, pyrene and anthracene derivatives have been employed as fundamental building blocks, which could control the emission via ACQ or AIE phenomenon. Among this group of fluorophores, the triphenylamine (TPA) unit stands out as an optoelectronically active motif capable of adopting a range of conformations. Because of the non-planar propeller-shaped arrangement of three aryl groups around the nitrogen atom, TPA complexes usually show AIE. However, the occurrence of this phenomenon largely depends on the substituents present on the phenyl groups *[7–13]*. Several stimuli-responsive organic materials with TPA scaffold have been reported. However, examples of metal-organic frameworks (MOFs) and coordination polymers (CPs), composed of TPA ligands showing any response in the presence of external stimuli are significantly less known *[14–20]*. Bu *et al*. have reported a Cd(II) coordination network using tris(4-(pyridin-4-yl)phenyl)amine ligand that exhibits thermo and mechano-luminescence properties due to change in dihedral angles between the three phenyl rings of the TPA core *[20]*. To the best of our knowledge, this is the only example of a CP or MOF, where the dihedral angles between the three phenyls of TPA affect the emission.

Copper(I) halides-based CPs are known as efficient emissive materials that offer a versatile platform for developing various stimuli-responsive, electrically-conductive sensors, and other functional materials *[21–24]*. Different Cu_nX_n cluster cores or secondary building units (SBUs) present in these CPs may control the dimensionality of the material and thereby affect their behaviour and applications. These CPs may respond to various stimuli and show distinct changes in structural properties, mostly due to modification in Cu--Cu distance, cluster rearrangement, and solid-to-solid phase transitions. These structural changes could also alter various moderate and weak inter- and intra-molecular interactions, which significantly affect the luminescent properties of the CPs *[25–27]*. The development of Copper(I)-based CPs using polydentate organosulfur ligands has gained significant interest lately as they offer a large structural diversity *[28–34]*. In the last few years, we have designed different cyclic dithioethers, which are easily accessible by condensing an aldehyde and dithiols $HS(CH_2)_nSH$, and used them as a connecting unit to construct various Copper(I) CPs *[32–34]*. It was observed that the architecture of these CPs and the nuclearity of the SBU's depend on several factors, such as the nature of ligands, the metal-to-ligand ratio and the reaction conditions like solvent, temperature, and pressure.

In this work, we have extended our study and substituted two out of three phenyl rings of triphenylamine unit with 1,3-dithiane or 1,2-dithiolane. The substitution on the third ring was avoided intentionally to allow the free movement of a phenyl group even after CP formation, as it can control the photophysical properties of the TPA unit. The coordination behavior of these substituted triphenylamine ligands with Cu(I) halides has been explored to obtain CPs incorporating Cu_2X_2 SBUs. Since both organic and inorganic units possess unique photoluminescence properties, the objective was to study the combined effect on the resulting material's behavior.

2.2. Experimental Section:

2.2.1. General Information

2.2.1.1. Materials

All the chemicals were used as received from Sigma-Aldrich. All reactions were performed under nitrogen environment and checked by TLC using Merck 60 F254 pre-coated silica gel plate (0.25 mm thickness) and the products were revealed under a UV chamber.

2.2.2. Characterization methods

^{1}H NMR and ^{13}C{H}-NMR spectra were recorded on a Bruker 500 MHz NMR spectrometer (Bruker BioSpin AG, Faellanden, Switzerland), using $CDCl_3$ as solvent and known chemical shifts of residual proton signals of deuterated solvents (for ^{1}H-NMR) or carbon signals of deuterated solvents (for ^{13}C-NMR) as the internal standard. Liquid-chromatography mass spectrometer (LCMS) was determined with an Agilent Q-TOF 6510 mass spectrometer (Agilent Technologies, Santa Clara, CA, USA) using the direct injection method, and electrospray ionization (ESI) was used as an ionization technique A Fluoromax-4p spectrofluorometer from Horiba JobinYvon was used to record the luminescence spectra of all the compounds (model: FM-100). OriginPro 8.1 was used to evaluate each luminescence emission spectrum. The luminescence spectra were adjusted for the instrument's spectrum sensitivity. The temperature was kept constant throughout each experiment at 25 °C.

Single crystal X-ray data for structural analysis were obtained on dual source Super Nova CCD, Agilent Technologies (Oxford Diffraction) System using Mo-Kα= 0.71073 Å at 293 K. The structure solution was obtained by using OLEX software. The crystallinity and phase purity measurements of all three coordination polymers were performed on a Rigaku Smart X-ray diffractometer with monochromatic Cu Kα (0.1540 nm) radiation in 2θ range of 5-50 degrees. The thermogravimetric analysis was performed on Mettler Toledo TGA/DSC 1 star e-system in the temperature range of 30-800 °C.

2.3. Synthesis

2.3.1. Synthetic procedure for L_1, L_2, CP1, CP2, CP3 and CP4

2.3.1.1. Synthesis of L_1: Into a round bottom flask, bis(4-formylphenyl)phenylamine (0.1 g, 0.33 mmol) was dissolved in dichloromethane (1-2 mL). Concentrated HCl (1 mL) and 1,2-ethanedithiol (0.065 g, 0.696 mmol) were then added to the reaction mixture. The reaction mixture was stirred for 6h at room temperature. Water was added to the resulting mixture and product was extracted with dichloromethane. The organic phase was washed several times with water, dried over anhydrous Na_2SO_4, filtered and the solvent was evaporated under vacuum. The obtained crude was purified by column chromatography [C_6H_{14}: EtOAc—98: 2] to obtain pure **L_1** as a yellow solid. Yield 65%. MP 150-151 °C. **^{1}H NMR** (500 MHz, $CDCl_3$) δ (ppm) 7.38 (d, *J* = 8.7 Hz, 4H), 7.26 - 7.23 (m, 2H), 7.08 (d, *J* = 7.8 Hz, 2H), 7.04- 6.99 (m, 5H), 5.63 (s, 2H), 3.53 - 3.48 (m, 4H), 3.38 - 3.33 (m, 4H). **^{13}C{^{1}H} NMR** (126 MHz, $CDCl_3$) δ (ppm) 147.24, 133.7, 129.1, 128.7, 124.6, 123.1, 55.9, 40.2. **LCMS** (ESI) *m/z* calculated for $C_{24}H_{24}NS_4$ $[M+H]^+$ 454.0711, found 454.0786.

2.3.1.2. Synthesis of L_2: The pure product was obtained as a white crystalline solid following similar procedure as L_1, using 1,3-propane dithiol (0.071 g, 0.66 mmol) instead of 1,2-ethanedithiol. Yield 91%. MP 176-177 °C. **^{1}H NMR** (500 MHz, $CDCl_3$): δ (ppm) 7.32 (d, *J* = 8.6 Hz, 4H), 7.27-7.23 (m, 2H), 7.09 (d, *J* = 8.7 Hz, 2H), 7.05-7.00 (m, 5H), 5.13 (s, 2H), 3.09-3.03 (m, 4H), 2.93-2.89 (m, 4H), 2.18-2.14 (m, 2H), 1.96-1.87 (m, 2H); **^{13}C{^{1}H} NMR** (126 MHz, $CDCl_3$) δ (ppm) 147.9, 147.6, 133.4, 129.7, 129.0, 125.4, 124.1, 123.8, 51.3, 32.5, 25.4. **LCMS** (ESI) *m/z* calculated for $C_{26}H_{28}NS_4$ $[M+H]^+$ 482.1026, found 482.1099.

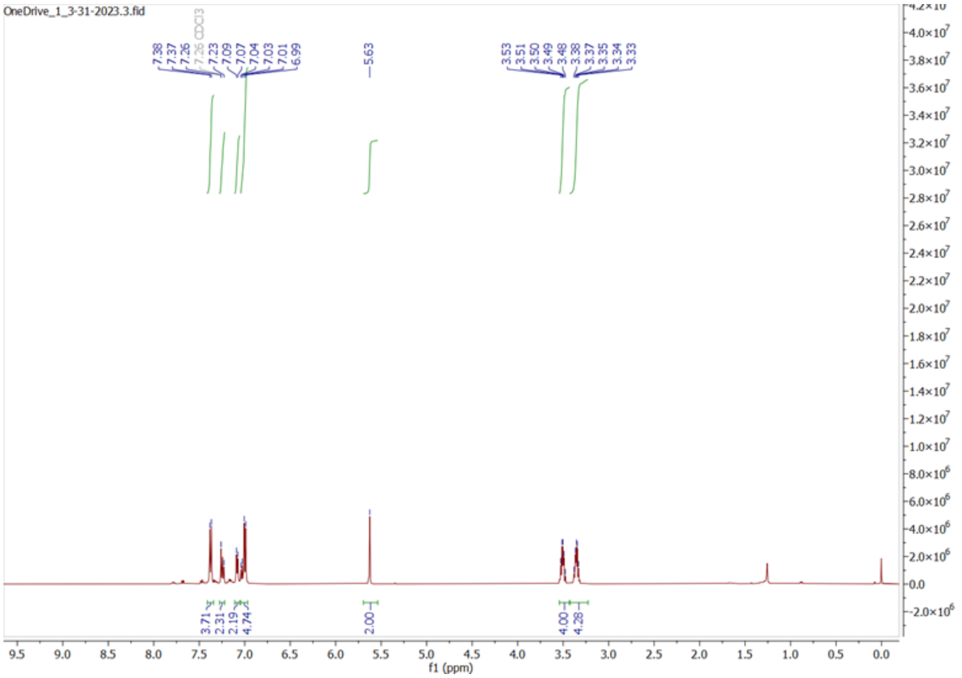

Fig. 2.1: ^{1}H NMR of **L$_1$**.

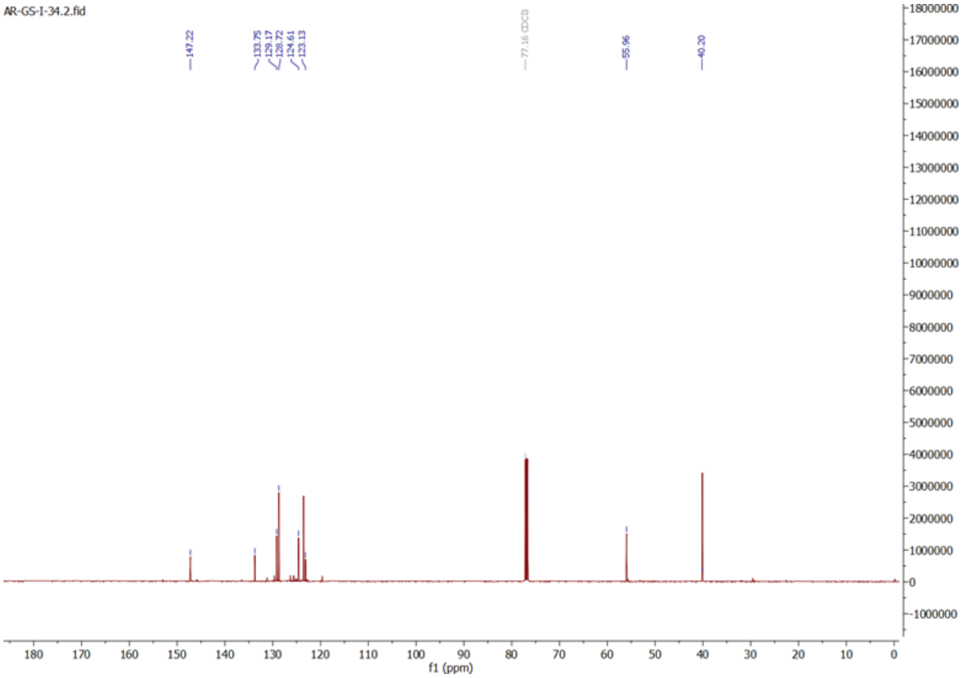

Fig. 2.2: ^{13}C{^{1}H} NMR of **L$_1$**.

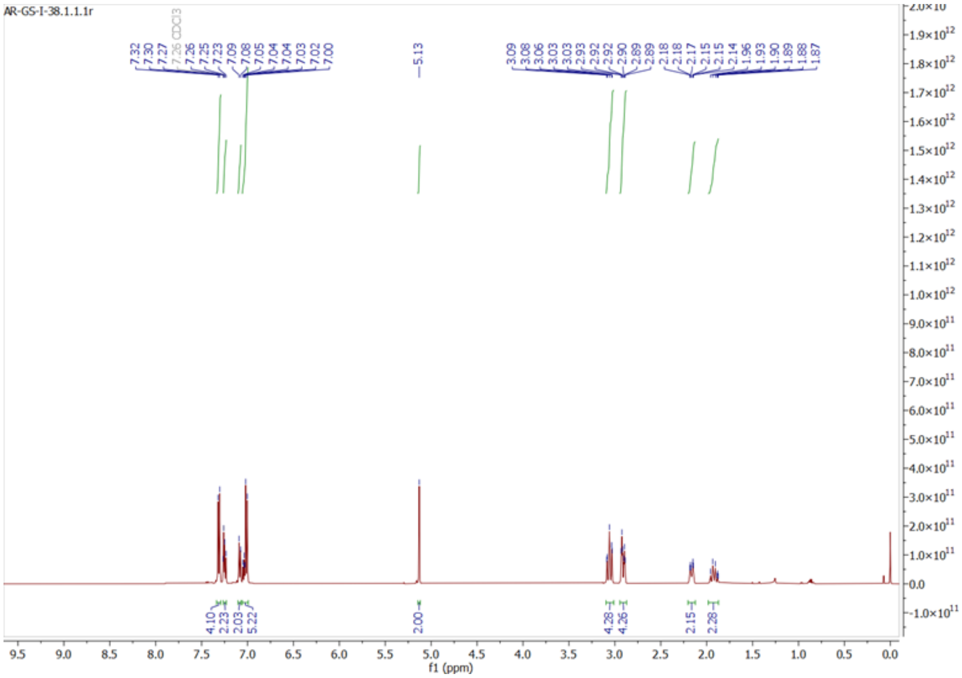

Fig. 2.3: ^{1}H NMR of **L2**.

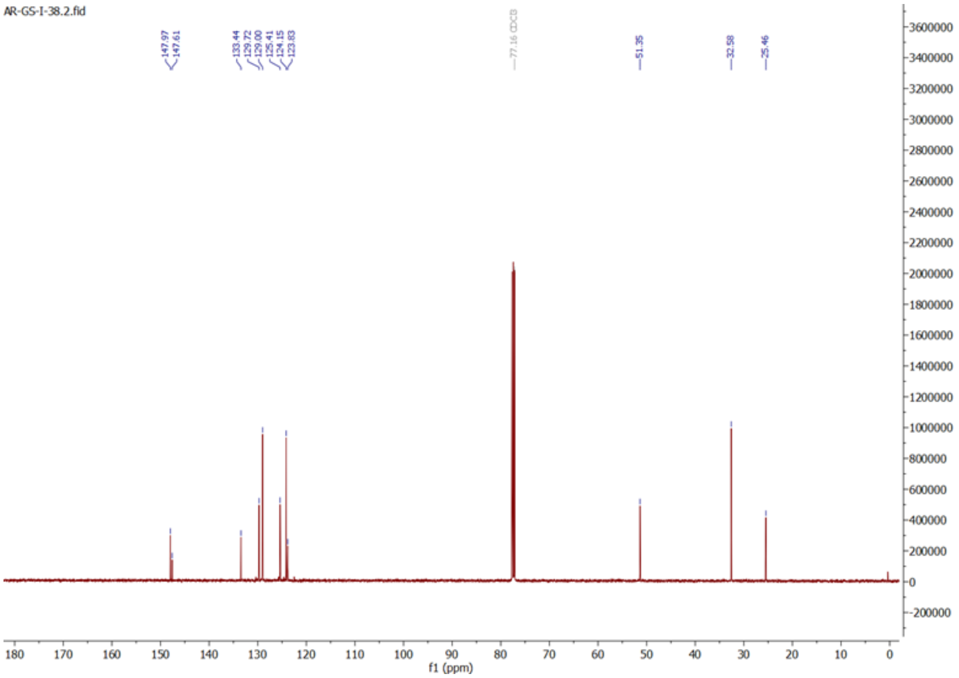

Fig. 2.4: ^{13}C{^{1}H} NMR of **L2**.

2.3.1.3. General Procedure for Preparation of CP1 - CP4:

In a 50 mL Schlenk tube, ligand **L_1** or **L_2** (1 eq.) was dissolved in acetonitrile and CuX (X = Br and Cl) (2 eq.) was separately dissolved in acetonitrile under N_2. A few drops of methanol were also added to the CuX solution to avoid Cu(I) oxidation. After that, CuX solution was added to the ligand solution and the reaction mixture was stirred for 6h at room temperature. The formation of off-white coloured products was observed after the completion of the reaction. Further workup was done in open air where the precipitate was filtered and washed with 5 mL dichloromethane (2-3 times) and 5 ml MeCN to remove the unreacted reactants.

CP1 yield is 83% (54.5 mg). When the 1:4 ratio of ligand **L_1** and CuBr was used up to 90% yield was observed. Anal. Calc. for $C_{24}H_{23}BrCuNS_4$ (597.14): C, 48.27; H, 3.88; N, 2.35; S, 21.48. Found: C, 48.35; H, 3.91; N, 2.37; S, 21.51%. **IR (ATR)**: 1584, 1496, 1415, 1304, 1263, 1173, 748, 690, 610, 525, 452 cm^{-1}.

CP2 yield is 79% (48.0 mg). When the 1:4 ratio of ligand **L_1** and CuBr was used up to 82% yield was observed. Anal. Calc. for $C_{24}H_{23}ClCuNS_4$ (552.169): C, 52.16; H, 4.19; N, 2.53; S, 23.20. Found: C, 52.13; H, 4.14; N, 2.49; S, 23.17%. **IR (ATR)**: 1586, 1479, 1415, 1300, 1263, 1167, 844, 749, 688, 530, 449 cm^{-1}.

CP3 yield is 69% (41.1 mg). When the 1:4 ratio of ligand **L_1** and CuBr was used up to 74% yield was observed. Anal. Calc. for $C_{26}H_{27}BrCuNS_4$ (625.19): C, 49.95; H, 4.35; N, 2.24; S, 20.51. Found: C, 49.92; H, 4.31; N, 2.19; S, 20.47%. **IR (ATR)**: 1588, 1491, 1413, 1275, 1171, 754, 678, 610, 528, 452 cm^{-1}.

CP4 yield is 52% (25.7 mg). When the 1:4 ratio of ligand **L_1** and CuBr was used up to 55% yield was observed. Anal. Calc. for $C_{26}H_{27}ClCuNS_4$ (580.74): C, 53.77; H, 4.69; N, 2.41; S, 22.08. Found: C, 53.73; H, 4.67;

N, 2.39; S, 22.04%. **IR (ATR)**: 1590, 1506, 1323, 1271, 1167, 825, 762, 696, 513, cm^{-1}.

2.4. Results and Discussion

2.4.1. Characterisations of CPs

Ligands **L$_1$** and **L$_2$** were synthesized by reacting the equimolar ratio of bis(4-formylphenyl)phenylamine with 1,2-ethanedithiol and 1,3-propanedithiol, respectively, in concentrated HCl at room temperature (**Scheme 2.1(a)**). After work-up, both ligands were obtained as yellow solids in good yields. NMR spectroscopy and Mass spectrometry were used to characterize the resulting organosulfur compounds.

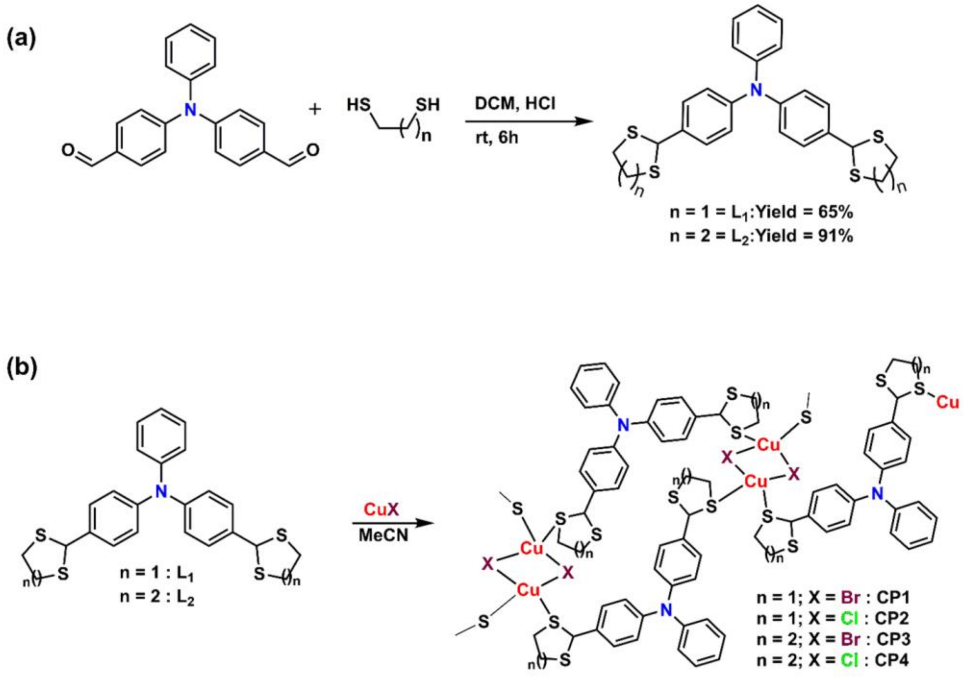

Scheme 2.1: General synthesis of ligands and copper (I) CPs.

In addition to the aromatic protons, the distinctive ^{1}H NMR (**Fig. 1 and Fig. 3**) signals for the two methine protons at 5.63 and 5.13 ppm confirm the formation of the 1,3-dithiolane and 1,3-dithiane moieties on TPA.

Moreover, the $^{13}C\{^1H\}$ peak in the aliphatic region confirms the formation of the ligands (**Fig. 2.2 and Fig. 2.4**) The structure of **L$_2$** was further authenticated by single-crystal X-ray analysis. Subsequently, **CP1** and **CP2** of composition $[\{Cu(\mu_2\text{-}Br)_2Cu\}(\mu_2\text{-}\mathbf{L_1})]_n$, and $[\{Cu(\mu_2\text{-}Cl)_2Cu\}(\mu_2\text{-}\mathbf{L_1})]_n$, respectively, were synthesized by reacting ligand **L$_1$** with CuBr and CuCl in acetonitrile (MeCN) solution at room temperature using a 1:2 molar ratio. The products were obtained as off-white solids with 83% yield for **CP1** and 79% yield for **CP2**. Similarly, **CP3** and **CP4** were synthesized by reacting **L$_2$** with CuBr and CuCl in a 1:2 molar ratio. The final compounds were obtained as white microcrystalline powders with 69% and 52% yields for **CP3** and **CP4**, respectively (**Scheme 2.1b**). Attempts to modify the dimensionality or SBUs of these CPs using different ligands/metal ratios in different solvents and mixtures of solvents, including EtCN, CH_3CN:DCM, CH_3CN:MeOH, and CH_3CN:DMF has not been conclusive and led to the same CPs (confirmed by PXRD analysis), though a higher ratio of Copper(I) salts provide better yield of CPs.

2.4.2. Description of the crystal structures of L$_2$ and CP1-CP4

Crystals suitable for single crystal X-ray diffraction (SCXRD) analysis of **L$_2$** were obtained by slow evaporation of a dichloromethane solution. **L$_2$** crystallizes in the monoclinic $P2_1/c$ space group (**Fig. 2.5**). The crystal structure suggests that the TPA unit is positioned in a propeller-like arrangement where the dihedral angles between the three phenyl planes are 89, 47 and 81°. Two of the three benzene rings are substituted with 1,3-dithiolane units at the *para*-position and both 1,3-dithiane units are arranged in a most stable chair conformation. All CPs were found insoluble in most of the common organic solvents but partially soluble in acetonitrile, propionitrile and DMF. In order to obtain suitable crystals for SCXRD analysis, the precipitates obtained after reactions were redissolved in boiling acetonitrile and left to evaporate at room temperature. Hexagon-shaped crystals of **CP1**, **CP2**, and **CP3**, and plate-shaped crystals for **CP4** were obtained after a few days. SCXRD data were collected at room temperature and crystallographic details are provided in **Tables 2.4-2.5**. The coordination polymers **CP1** and **CP2** crystallize in the triclinic $P\bar{1}$ space group, whereas **CP3** and **CP4** crystallize in the monoclinic $P2_1/n$ space group. Single crystal analysis of **CP1-CP4** reveals the formation of 1D coordination polymers with centrosymmetric $Cu(\mu_2\text{-}X)_2Cu$ (X = Br, Cl) rhomboid cores as SBUs confirming a 1:1 metal/ligand ratio (**Fig. 2.6-2.9**). Each Cu is coordinated to two sulfur atoms stemming from different ligands and two bridging halide atoms. Out of the two sulfur atoms in the dithiolane/dithiane rings, only one coordinate with the metal. However, since the sulfur atoms of different rings coordinate to different Cu centers, ribbon-like 1D coordination polymers form in all cases.

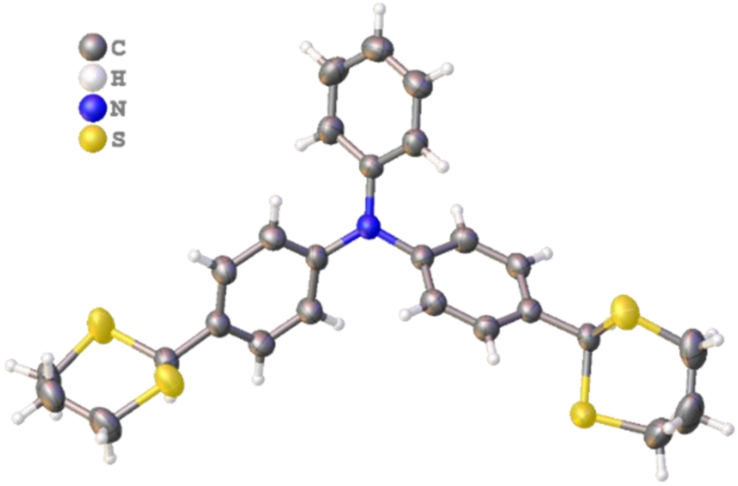

Fig. 2.5: Molecular structure of **L**$_2$

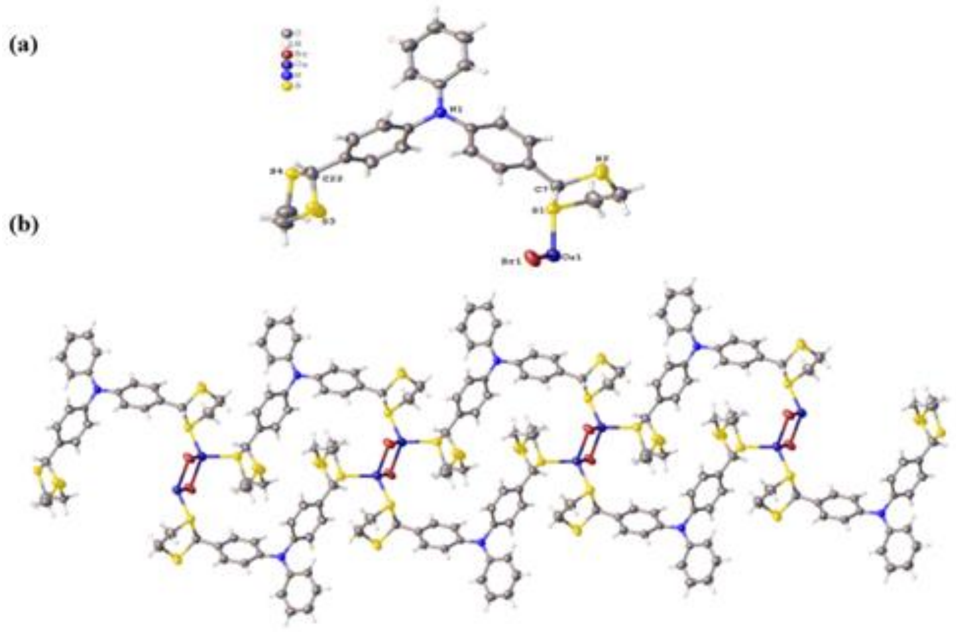

Fig. 2.6: (a) Individual motif of **CP1** (b) View of the 1D ribbon of [{Cu(μ$_2$-Br)$_2$Cu}(μ$_2$-**L$_1$**)]$_n$ (**CP1**) running along the *a* axis. Symmetry transformations used to generate equivalent atoms: ^{1}-x,1-y,1-z; ^{2}+x,+y,1+z; ^{1}+x,+y,-1+z ^{1}+x,+y,-1+z ^{1}+x,+y,-1+z; ^{1}+x,+y,-1+z.

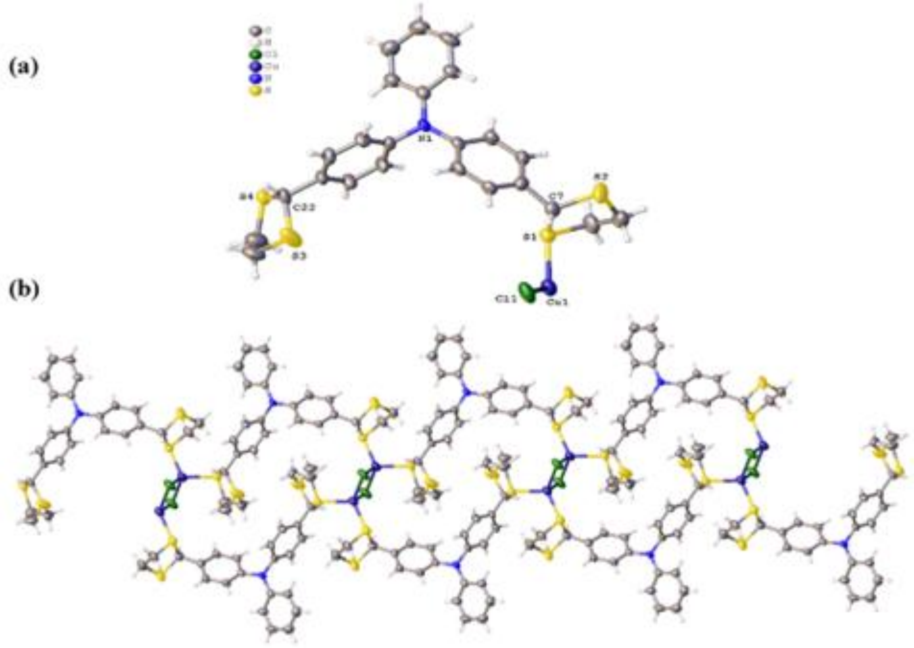

Fig. 2.7: (a) Individual motif of **CP2** (b) View of the 1D ribbon of $[\{Cu(\mu_2\text{-}Cl)_2Cu\}(\mu_2\text{-}\mathbf{L_1})]_n$ (**CP2**) running along the *a* axis. Symmetry transformations used to generate equivalent atoms: ^{1}*-x,1-y,2-z;* ^{2}*+x,+y,1+z;* ^{1}*-x,1-y,2-z;* ^{2}*+x,+y,1+z;* ^{3}*+x,+y,-1+z;* ^{1}*+x,+y,-1+z.*

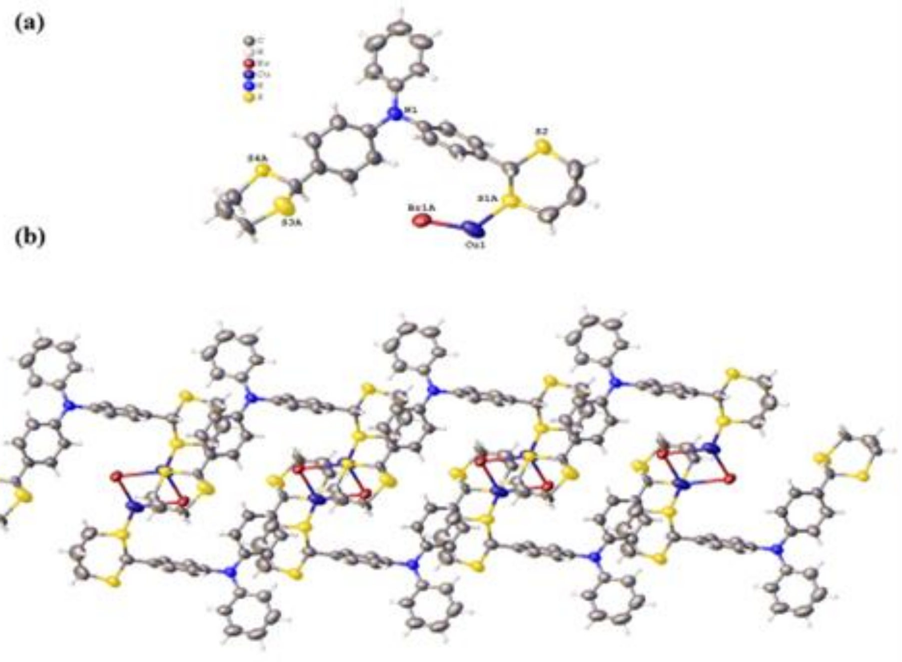

Fig. 2.8: (a) Individual motif of **CP3** (b) View of the 1D ribbon of $[\{Cu(\mu_2\text{-}Br)_2Cu\}(\mu_2\text{-}\mathbf{L_2})]_n$ (**CP3**) running along the *a* axis. Symmetry transformations used to generate equivalent atoms: ^{1}*1-x,1-y,1-z;* ^{2}*1+x,+y,+z;* ^{1}*1-x,1-y,1-z;* ^{2}*1+x,+y,+z;* ^{3}*-1+x,+y,+z;* ^{1}*-1+x,+y,+z.*

The geometric parameters for these CPs agree well with the values found in the similar-reported Cu(I) halide CPs having S-coordinated Cu_2X_2 units *[31–34]*. However, there is a significant deviation in structure for **CP1** to **CP4**. A comparison of the more relevant average bond lengths and average bond angles of all four CPs are summarized in **Tables 2.1-2.2**. **CP2** and **CP4** incorporating a $Cu(\mu_2\text{-}Cl)_2Cu$ unit have similar Cu···Cu distances (~2.92 Å) but **CP1** and **CP3** having $Cu(\mu_2\text{-}Br)_2Cu$ unit feature slightly different Cu···Cu distances (2.97 Å for **CP1** and 2.91 Å for **CP3**). Since these Cu···Cu separations are clearly beyond the van der Waals radii of two copper atoms (2.8 Å), one may exclude any cuprophilic bonding interaction *[35]*.

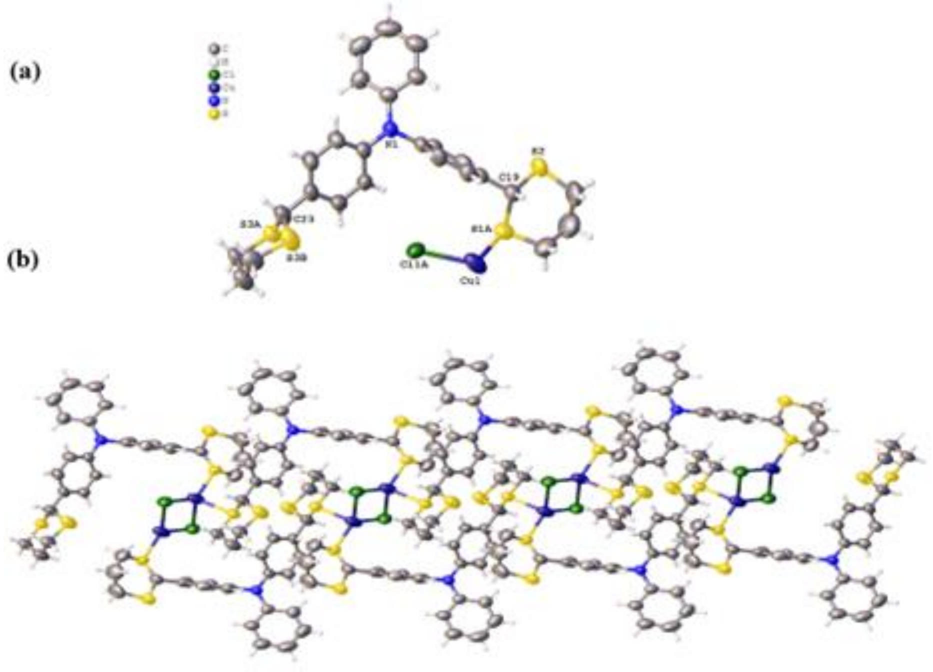

Fig. 2.9: (a) Individual motif of **CP4** (b) View of the 1D ribbon of [{Cu(μ_2-Cl)$_2$Cu}(μ_2-**L$_2$**)]$_n$ (**CP4**) running along the *a* axis. Symmetry transformations used to generate equivalent atoms: *^{1}1-x,1-y,1-z; ^{2}1+x,+y,+z; ^{1}1-x,1-y,1-z; ^{2}1+x,+y,+z; ^{3}-1+x,+y,+z; ^{1}-1+x,+y,+z.*

Examples of other 1D materials featuring Cu(μ_2-X)$_2$Cu SBUs with Cu···Cu contacts in a similar range are [{Cu(μ_2-Br)$_2$Cu}{μ_2-PhS(CH$_2$)$_3$SPh}$_2$]$_n$ *[36]* [{Cu(μ_2-Br)$_2$Cu}(bis(phenylthio)methane)$_2$]$_n$*[37]* and [{Cu(μ_2-Cl)$_2$Cu}(μ_2-2-methyl-1,3-dithiane)$_2$]$_n$.*[38]* Because of different Cu···Cu distances, the Cu—Br—Cu angle is more acute in **CP3** (71.67°) in comparison to **CP1** (74.18°). The average Cu−Br distance is 2.46 Å and the average Cu−Cl distance is 2.35 Å, which is similar to the previously reported examples *[35–38]*. In addition, CPs formed by 1,2-ditholane have shorter Cu−S bond lengths compared to CPs formed by 1,3-dithiane ((~ 2.29 *vs.* ~ 2.36 Å).). The average S−Cu−X angle is close to 107° for **CP1** and **CP3** (X = Br), whereas this angle is close to 113° for **CP2** and **CP4** (X = Cl). Further, the packing arrangement of these CPs indicates multiple intermolecular C–H···π interactions between the 1D chains and some intramolecular C–H···π interactions ranging from 2.75 to 3.15 Å (**Fig. 2.10-2.13**). In all four CPs, the coordination leads to the formation of 32-membered macrocycles with a maximum distance of approximately 12.5 Å between the centroids of the phenyl groups of different TPA units in a cycle (**Fig. 2.14-2.17**). From the crystal structures, it can be seen that the planes of the phenyl rings are oriented at different angles with respect to each other (**Table 2.3**).

Table 2.1. Selected bond lengths (Å) for **CP1-CP4**.

Compounds	**Average Cu−Cu**	**Average Cu−X**	**Average Cu−S**
CP1	2.97	2.46	2.29
CP2	2.92	2.35	2.28
CP3	2.91	2.47	2.36
CP4	2.92	2.35	2.35

Table 2.2. Selected bond angles (°) for **CP1-CP4**.

Compounds	**Average Cu−X−Cu**	**Average S−Cu−X**	**Average S−Cu−S**
CP1	74.18	107.31	110.40
CP2	76.65	113.21	111.49
CP3	71.67	107.66	111.62
CP4	75.93	112.50	111.46

Table 2.3. The dihedral angle between the planes of different phenyl rings (Ph_S – substituted phenyl and Ph_f – free phenyl).

Compounds	**Ph_S – Ph_f**	**Ph_S – Ph_S**	**Ph_S – Ph_f**
CP1	85.45	86.60	55.95
CP2	84.06	85.15	57.14
CP3	81.88	88.35	44.82
CP4	81.57	88.34	44.28

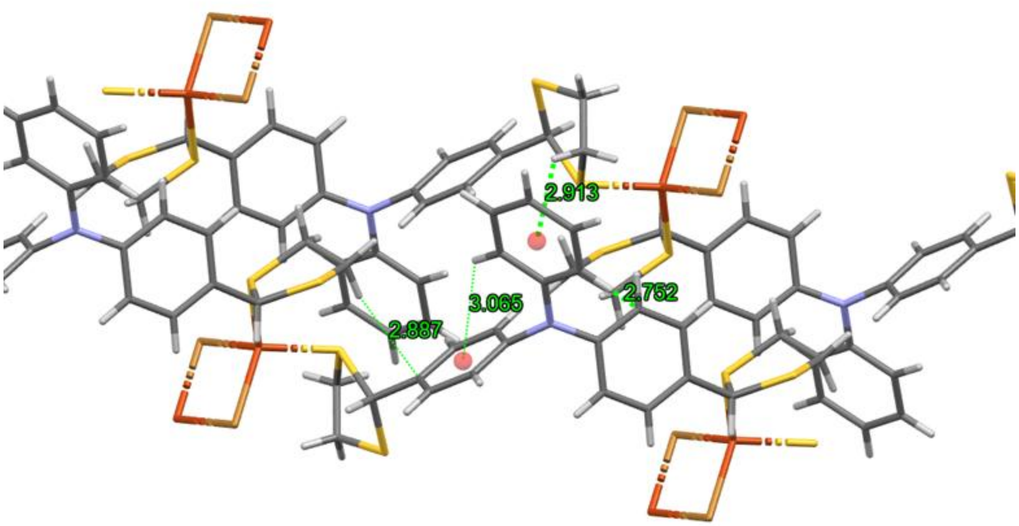

Fig. 2.10: Molecular packing of **CP1** indicating inter- and intramolecular C–H···π interactions. Symmetry transformations used to generate equivalent atoms: $^{1}-x,1-y,1-z$; $^{2}+x,+y,1+z$ $^{1}+x,+y,-1+z$ $^{1}+x,+y,-1+z$ $^{1}+x,+y,-1+z$ $^{1}+x,+y,-1+z$

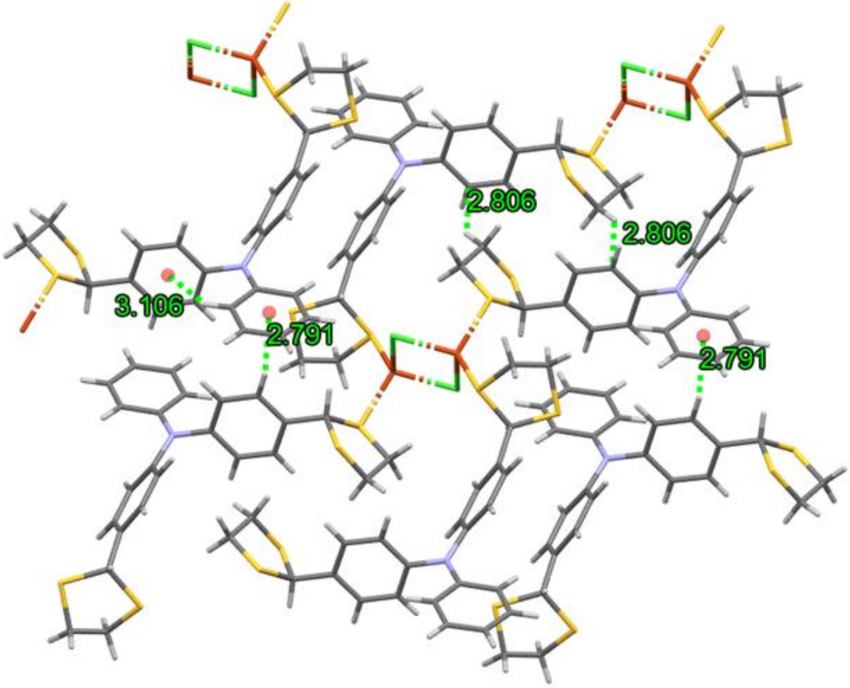

Fig. 2.11: Molecular packing of **CP2** with C–H···π interactions. Symmetry transformations used to generate equivalent atoms: ^{1}*-x,1-y,2-z*; ^{2}*+x,+y,1+z* ; ^{1}*-x,1-y,2-z*; ^{2}*+x,+y,1+z*; ^{3}*+x,+y,-1+z* ^{1}*+x,+y,-1+z*

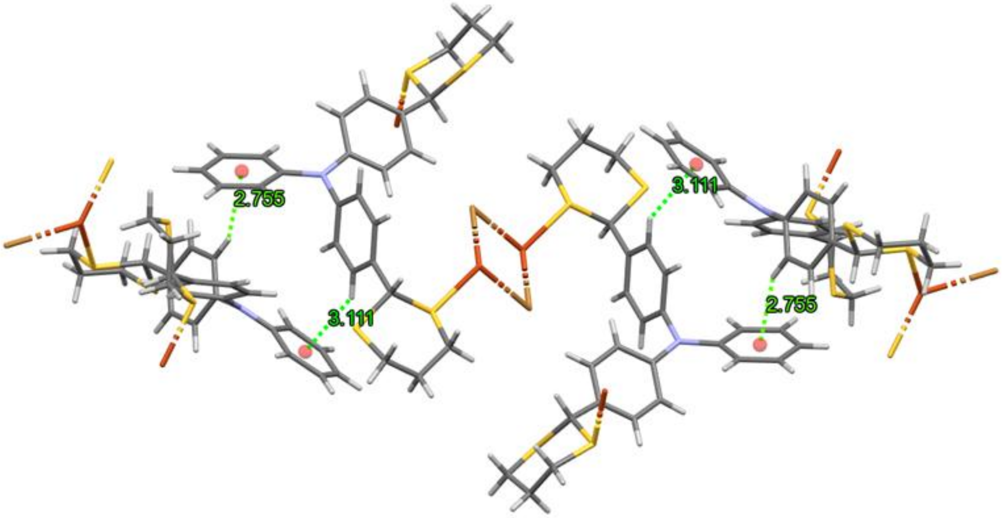

Fig. 2.12: Molecular packing of **CP3** with C–H···π interactions. Symmetry transformations used to generate equivalent atoms: ^{1}*1-x,1-y,1-z*; ^{2}*1+x,+y,+z* ; ^{1}*1-x,1-y,1-z*; ^{2}*1+x,+y,+z*; ^{3}*-1+x,+y,+z* ; ^{1}*-1+x,+y,+z*

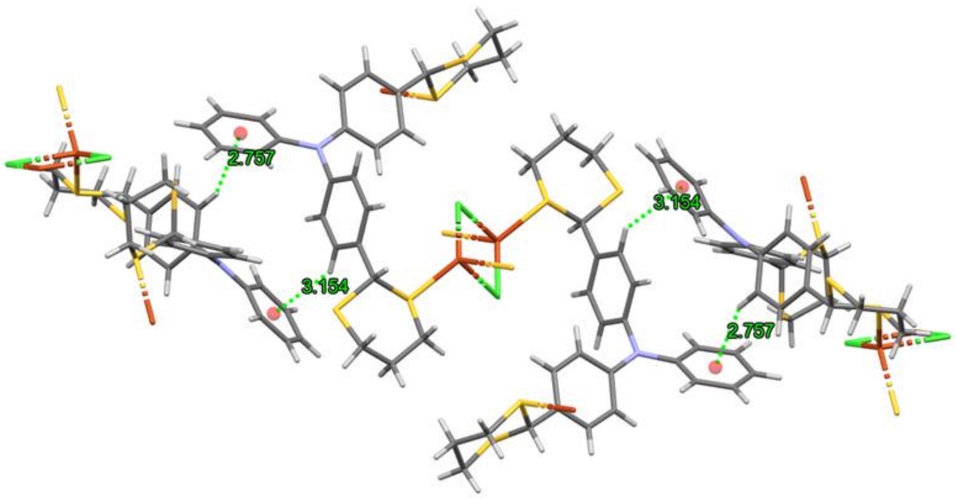

Fig. 2.13: Molecular packing of **CP4** with C–H···π interactions. Symmetry transformations used to generate equivalent atoms: ^{1}*1-x,1-y,1-z;* ^{2}*1+x,+y,+z ;* ^{1}*1-x,1-y,1-z;* ^{2}*1+x,+y,+z;* ^{3}*-1+x,+y,+z ;* ^{1}*-1+x,+y,+z.*

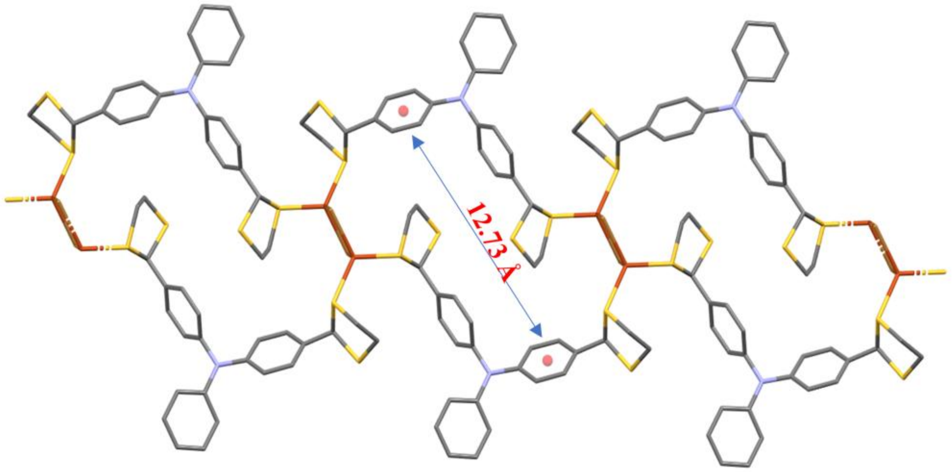

Fig. 2.14: Macrocyclic 32-member ring of **CP1**.

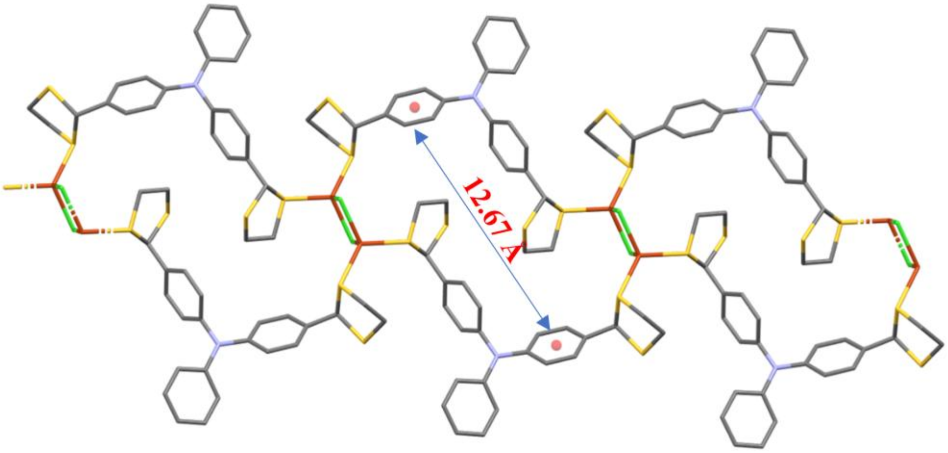

Fig. 2.15: Macrocyclic 32-member ring of **CP2**.

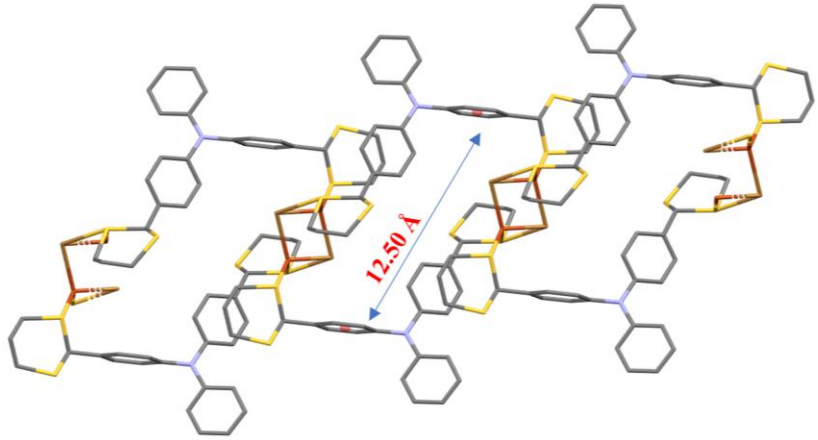

Fig. 2.16: Macrocyclic 32-member ring of **CP3**.

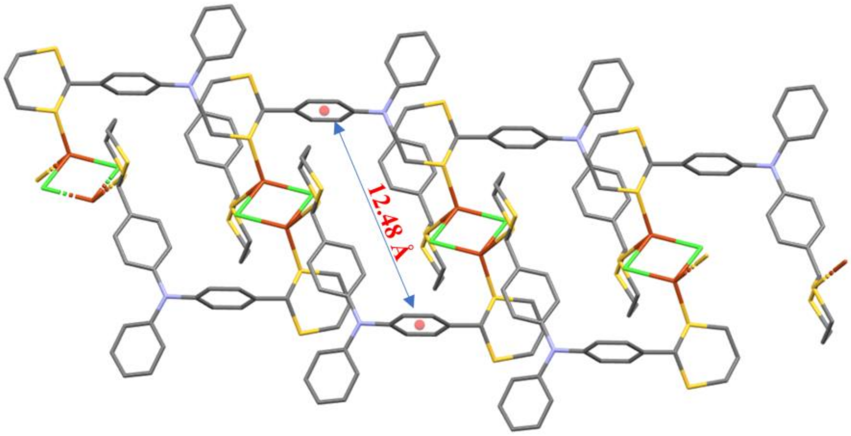

Fig. 2.17: Macrocyclic 32-member ring of **CP4**.

Table 2.4. Crystallographic data of **CP1**, **CP2**, and ligand **L₂**

Compound	**L_2**	**CP1**	**CP2**
CCDC No	2242123	2242124	2242127
Formula	$C_{26}H_{27}NS_4$	$C_{24}H_{23}BrCuNS_4$	$C_{24}H_{23}ClCuNS_4$
Formula weight	481.72	597.12	552.66
Wavelength (Å)	0.71073	0.71073	0.71073
Crystal system	monoclinic	triclinic	triclinic
Space group	$P2_1/c$	P-1	P-1
a/Å	11.4918(6)	9.1864(5)	9.1410(5)
b/Å	19.6484(8)	10.4799(10)	10.4411(9)
c/Å	11.7522(7)	13.0998(10)	13.0328(8)
α/°	90	99.642(7)	100.066(6)
β/°	111.656(6)	103.110(5)	103.938(5)
γ/°	90	97.023(6)	95.714(6)
V/ $Å^3$	2466.3(2)	1193.94(16)	1175.54(14)
Z	4	2	2
ρ_{calcd} (g/cm^3)	1.297	1.661	1.561
Temperature/K	293.00	293.00	293.00
GOF	1.049	1.005	0.982
2θ range for data collection	7.016 to 49.996	6.28 to 49.992	6.35 to 49.998
Reflections collected	12620	9205	8170
Independent reflections	4189 [R_{int} = 0.0386]	4203 [R_{int} = 0.0747]	4094 [R_{int} = 0.1140]
Completeness to θ = 25.242	99.7	99.7	98.8
Final R indices [I>2σ(I)]	R_1 = 0.0485, wR_2 = 0.1138	R_1=0.0491, wR_2 =0.1206	R_1=0.0640, wR_2 = 0.1603
Final R indices [all data]	R_1 = 0.0635, wR_2 = 0.1229	R_1= 0.0673, wR_2 = 0.1294	R_1 = 0.1045, wR_2 = 0.1927
Largest diff. peak/hole/ eÅ^{-3}	0.36/-0.34	0.84/-0.73	0.69/-0.64

Table 2.5. Crystallographic data of **CP3**, and **CP4**

Compound	**CP3**	**CP4**
CCDC No.	2242128	2242129
Formula	$C_{26}H_{27}BrCuNS_4$	$C_{26}H_{27}ClCuNS_4$
Formula Weight	625.17	580.71
Wavelength	0.71073 Å	0.71073 Å
Crystal System	monoclinic	monoclinic
Space group	$P2_1/n$	$P2_1/n$
a/Å	10.1179(4)	10.1508(3)
b/ Å	9.9871(4)	10.0144(3)
c/ Å	26.3324(8)	25.8556(6)
α /°	90	90
β/°	97.071(3)	96.520(2)
γ/°	90	90
V/ $Å^3$	2640.61(17)	2611.33(13)
Z	4	4
ρ_{calcd} (g/cm^3)	1.573	1.477
Temperature/K	293.00	293.00
2θ range for data collection	6.09 to 49.998	5.824 to 49.994
Reflections collected	28346	18333
Independent reflections	4620 [R_{int} =0.0660]	4573 [R_{int} = 0.0554]
Completeness to θ=25.242	99.7	99.9
Final R indices [I>2σ(I)]	R_1 = 0.0498, wR_2 = 0.1221	R_1 = 0.0600, wR_2 = 0.1643
Final R indices [all data]	R_1 = 0.0733, wR_2 = 0.1341	R_1 = 0.0923, wR_2 = 0.1843
Largest diff. peak/hole/ e $Å^{-3}$	0.58/-0.71	0.81/-0.68

Powder X-ray diffraction (PXRD) studies were performed at room temperature and a comparison of experimental PXRD data with simulated ones obtained from single-crystal X-ray analysis confirm~~s~~ the bulk identity of the samples (**Fig. 2.18-2.19**). All four CPs were found to be stable at room temperature in open vials for several months. Moreover, thermogravimetric analysis **(**TGA) was performed on all the compounds, confirming their stability up to 200 °C (**Fig. 2.20**). As already observed with coordination polymers containing dithiane ligand and Cu_2Br_2 or Cu_2Cl_2 rhomboids, the decomposition is a complicated phenomenon that implies at least three steps during which both ligands and halide ion decompose in the temperature range of 200 to 700 °C *[34]*. Finally, there is the formation of CuO which is confirmed by comparing experimental and theoretical values, which matches well except for **CP4** (experimentally observed 18%, 22%, 20% and 33% calculated 21%, 24%, 20% and 23%, respectively for **CP1**, **CP2** **CP3** and **CP4**).

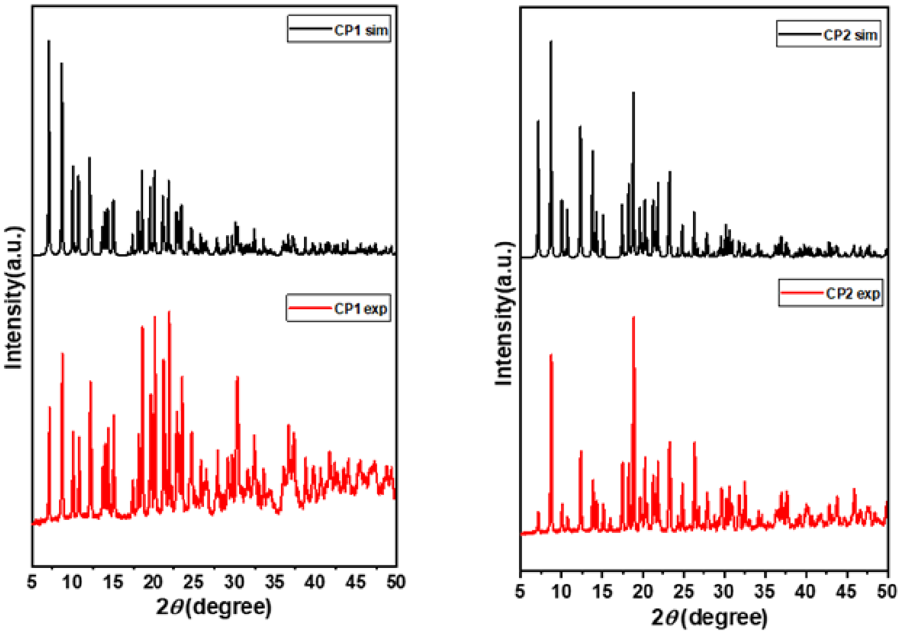

Fig. 2.18: Comparison of simulated and experimental PXRD patterns of **CP1** and **CP2**.

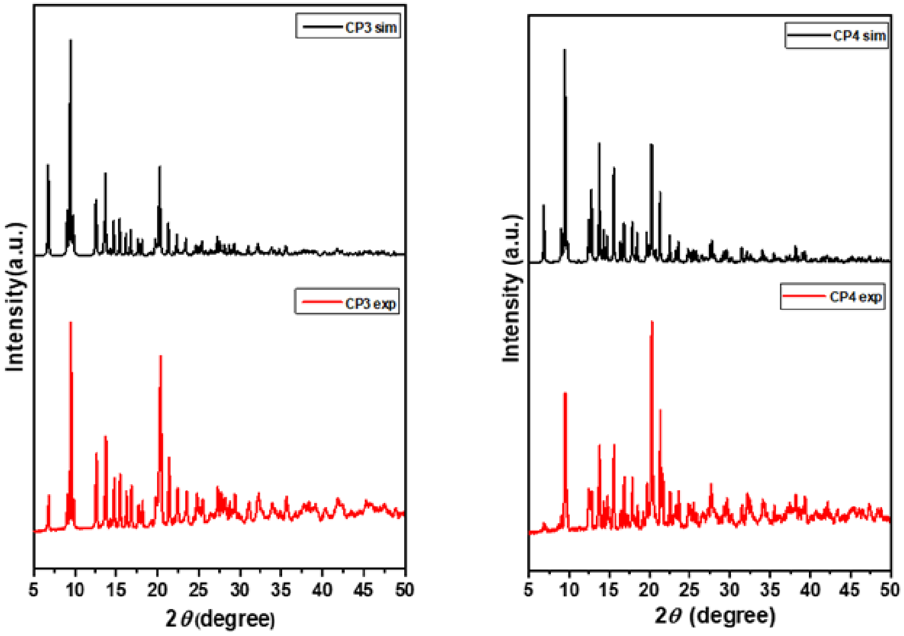

Fig. 2.19: Comparison of simulated and experimental PXRD patterns of **CP3** and **CP4**

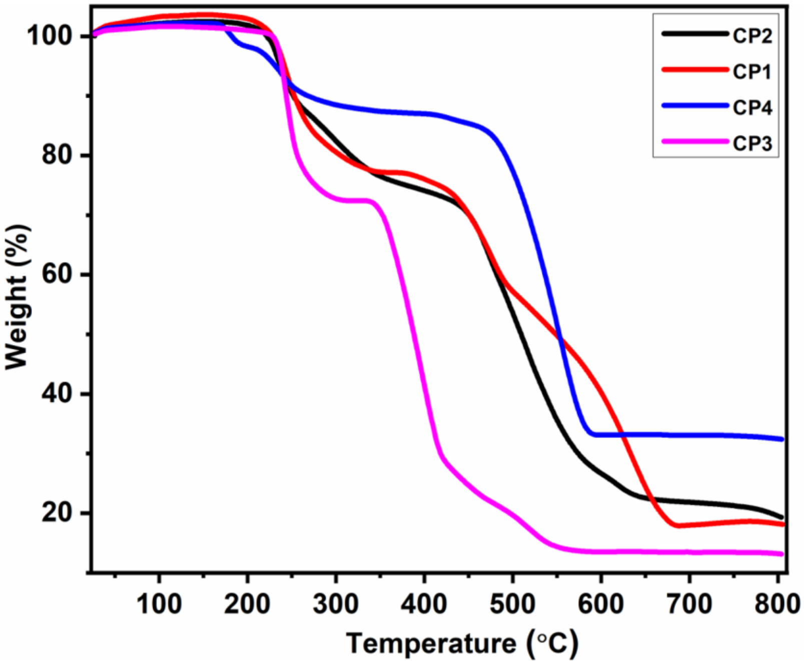

Fig. 2.20: TGA curve of **CP1**, **CP2, CP3** and **CP4**.

2.5. Photophysical studies and solvatochromic behavior of ligands

Triphenylamine-based luminogens are known to be quite sensitive in response to solvent polarity and show exceptional solvatochromic properties *[39–41]*. We recorded the luminescence of the synthesized ligands in different solvents and found that both ligands **L_1** and **L_2** are solvate-fluorochromes (**Fig. 2.21**). Both ligands show similar emission behavior in different solvents. The excitation maxima (365 nm) were constant across the solvent types, while the emission maxima were red-shifted when increasing the polarity of the solvent (the parameters for solvent polarity expressed as $E_T(30)$ values are reported in **Table 2.6** *[42]*. The highest energy emission bands are observed at 415 (**L_1**) and 418 nm (**L_2**) in hexane, while the lowest energy band at 524 and 526 nm appear in DMSO for **L_1** and **L_2**, respectively.

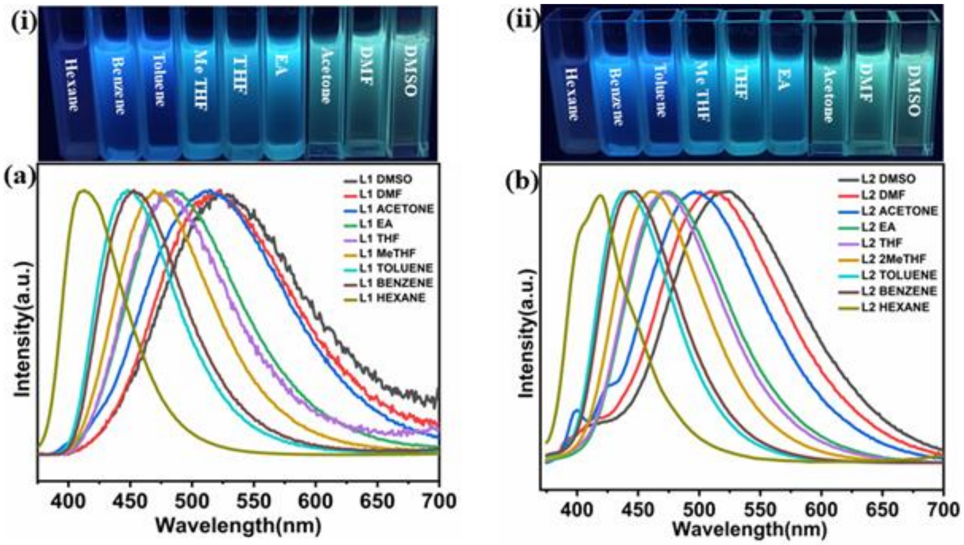

Fig. 2.21: (i) Photographs taken under UV lamp (~365 nm) for **L_1**, (ii) photographs taken under UV lamp (~365 nm) for **L_2**, (a) emission spectra of ligand **L_1** in different organic solvents, (b) emission spectra of ligand **L_2** in different organic solvents.

Similar solvatochromic effects in triphenylamine derivatives have already been observed and were explained by the involvement of a higher energy locally excited (LE) state that favors a coplanar conformation and a low energy twisted state *[43–46]*. The excited luminogens planar conformation can be stabilized in nonpolar solvents, producing a high energy and short-wavelength emission of the LE state. The structure of luminogen rotates intramolecularly in polar solvents, changing its state from LE to twisted intramolecular charge transfer (TICT) and accelerating the intramolecular transfer of electrons from donor to acceptor moieties. We propose a similar TICT phenomenon with our ligands that results in a red-shifted emission of ligands in polar solvents. Further to confirm the TICT phenomenon we have recorded the emission spectra of both the ligands **L_1** and **L_2** in the THF/Hexane mixture by gradually increasing the hexane fraction (f_{hex}) in THF solution (**Fig. 2.22**). Upon decreasing the polarity of the solution by the addition of hexane up to f_{hex} = 95%, a blue shift of 52 nm and 40 nm was observed for **L_1** and **L_2**, respectively, suggesting the occurrence of TICT phenomenon in both ligands.

Table 2.6. Excitation λ_{abs} and emission λ_{em} maxima for **L_1** and **L_2** in different solvents

Solvents	$E_T(30)$ / kcal mol^{-1}	λ_{abs}/ nm	λ_{em}/ nm (L_1)	λ_{em}/ nm (L_2)
DMSO	45.1	365	524	526
DMF	43.2	365	519	512
Acetone	42.2	365	513	499
Ethyl Acetate	38.1	365	484	475
THE	37.4	365	480	473
2-Me-THF	36.5	365	469	461
Benzene	34.3	365	454	445
Toluene	33.9	365	450	442
Hexane	31.0	365	415	418

E_T(30): Parameter of solvent polarity λ_{abs}- wavelength at electronic absorption maximum λ_{em}: wavelength at emission maximum**.**

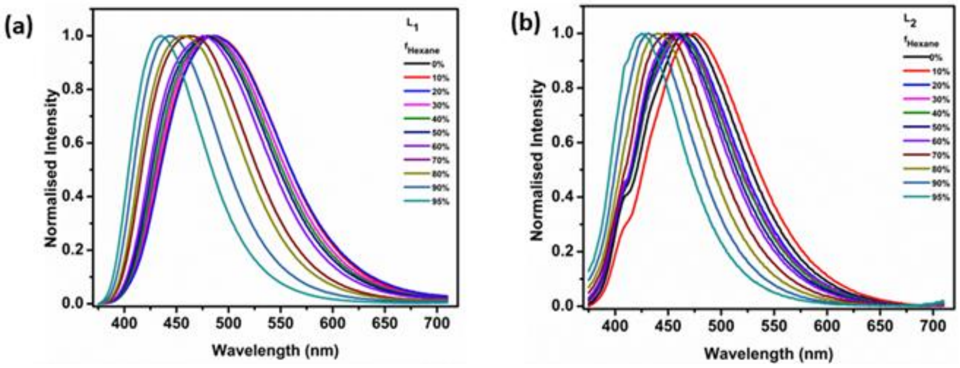

Fig. 2.22: Emission spectra of **L_1** (a) and (b) **L_2** in THF and THF/hexane mixtures (c = 1mM) with increasing fractions of hexane; formation of TICT state.

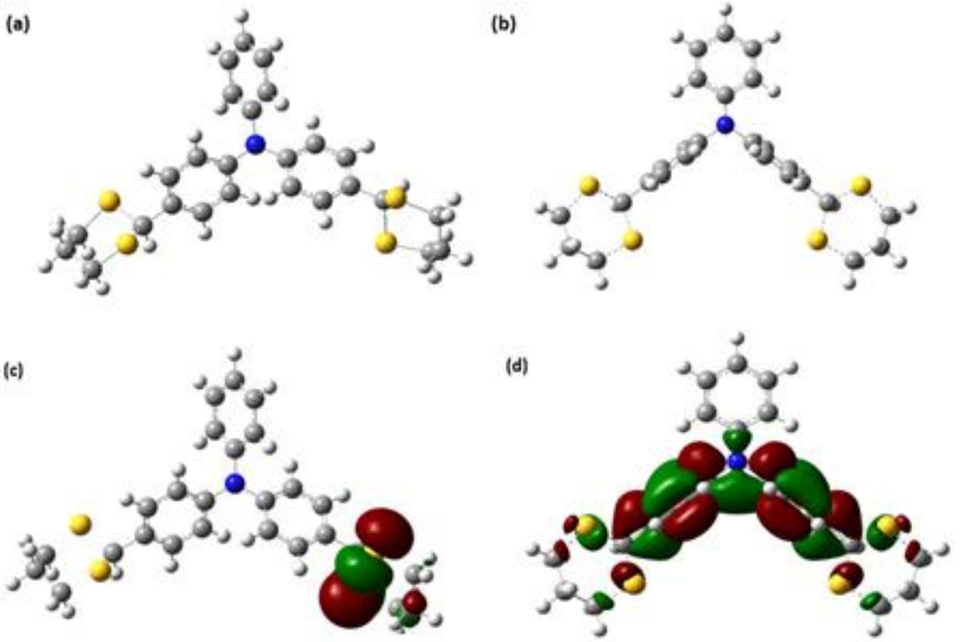

Fig. 2.23: Calculated molecular structures of **L_2** by DFT (a) Ground state (b) Excited state (c) HOMO in the ground state (d) LUMO excited state.

density was found to be at 1,3-dithiolan-2-yl. To get an insight into the luminescence behavior, *ab initio* calculations based on Density-Function

Theory (DFT) at the B3LPY/6-31+G(d,p) level have been performed with the Gaussian 09 program on **L$_2$** *[47]*. It was found that the excited state LUMO density was more heavily weighted toward the substituted phenyl moiety of TPA, while the ground state HOMO. Moreover, the unsubstituted phenyl and substituted phenyl moieties are substantially twisted in the excited states (**Fig. 2.23**). This observation is similar to previously reported systems and suggests TICT in the excited states of ligands *[43–46]*.

2.6. Photophysical studies and mechanochromic behaviour of CPs

All the compounds are off-white solids under ambient light and show cyan-blue luminescence under UV light (~365 nm) (**Fig. 2.24**). Solid-state photoluminescent properties were recorded for all the synthesized CPs at room temperature (**Fig. 2.26(i)**). It was observed that upon excitation at 382 nm, **CP1** and **CP2** emit at lower energy (452 and 463 nm) compared to **CP3** and **CP4** (426 & 427 nm). In order to understand the origin of the emission, luminescence spectra of **L$_1$** and **L$_2$** have also been recorded in the solid state. The emission maxima for **L$_1$** and **L$_2$** were observed at 448 and 427 nm, which is close to the emission of respective CPs and suggests that the ligand-centered transitions are responsible for the emission in the CPs.

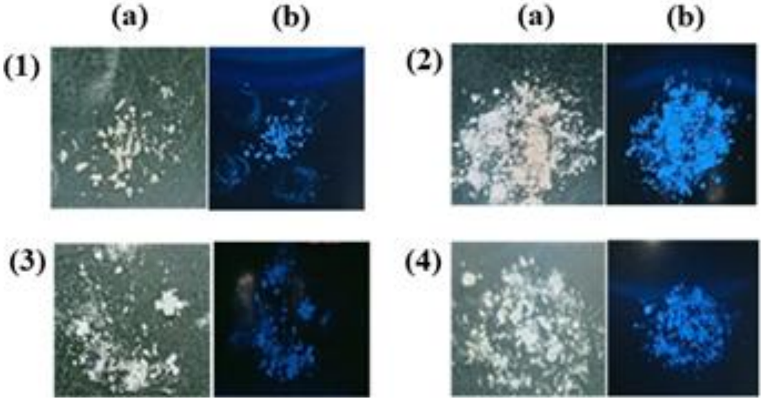

Fig. 2.24: Photoluminescent images of (1). **CP1** (2). **CP2** (3). **CP3** and (4). **CP4**; (a): under ambient light, (b): under UV lamp (~365 nm).

We observed that all CPs show interesting mechanochromic behavior. Mechanical grinding of **CP1** and **CP2** causes a small blue shift in emission from 452 and 463 nm to 448 nm with a significant increase in intensity (**Fig. 2.25**). Contrary to this, **CP3** and **CP4** display a red shift in emission from 426 and 427 nm to 448 nm with increased intensity (**Fig. 2.25**). Interestingly, after grinding, emission maxima for all the CPs were found at the same wavelength (**Fig. 2.26** and **Table 2.7**). Note that a similar occurrence of mechanochromism phenomenon was not observed with the ligands.

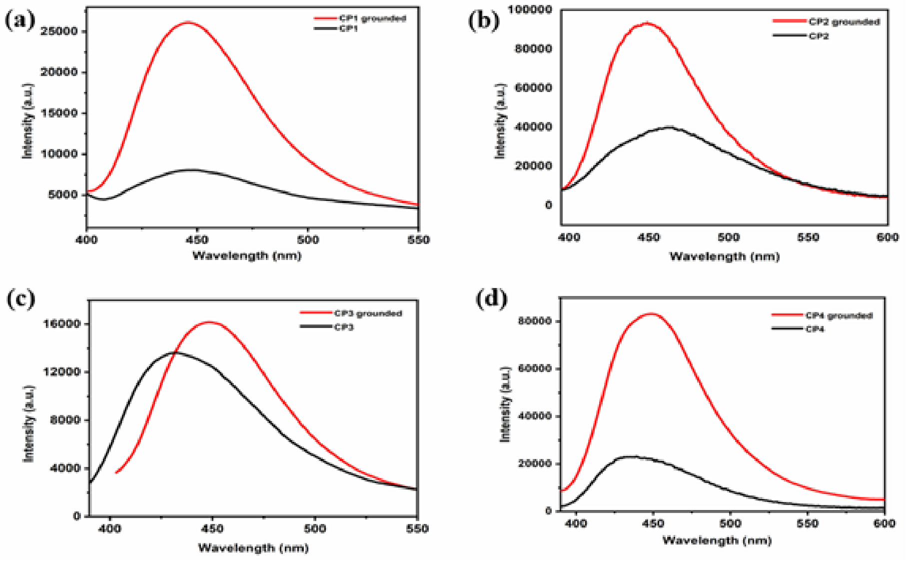

Fig. 2.25: Emission spectra of CPs with the grounded sample at an excitation wavelength of 382 nm (a) **CP1** (b) **CP2** (c) **CP3** (d) **CP4**.

Table 2.7. Change in emission λ_{em} of all CPs after grinding.

Compounds	**λ_{abs} (nm)**	**λ_{em} (nm)**	
		Pristine solid	**Ground**
CP1	382	452	448
CP2	382	463	448
CP3	382	426	448
CP4	382	427	448

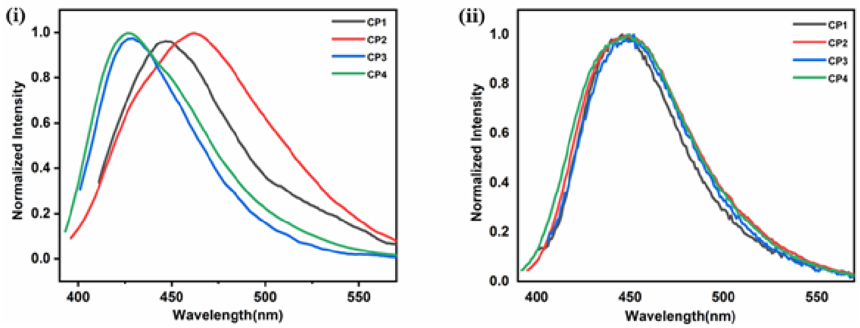

Fig. 2.26: (i) Normalized emission spectra of pristine **CP1**, **CP2**, **CP3** and **CP4**, (ii) luminescence emission spectra of grounded **CP1**, **CP2**, **CP3** and **CP4**.

It has been reported that the dihedral angles between the planes of phenyl groups of TPA affect the emission behaviour of TPA-derived compounds *[7,20]*. To gain further insight, we checked the crystal structure and found that **CP1** and **CP2** have similar dihedral angles between the planes of phenyl groups of TPA which is significantly different from **CP3** and **CP4** (**Table 2.3**). In the case of **CP1** and **CP2**, the dihedral angles between the plane of the phenyl ring of TPA are approximately 85°, 86° and 56° while in **CP3** and **CP4**, these angles are approximately 82°, 88° and 44°. The unusual blue shift and red shift observed after grinding could be attributed to the conformational twisting of the aromatic rings. Probably after PXRD the samples, the angles between the plane of the phenyl rings orient somewhere in between and are similar in all CPs, resulting in the same emission.

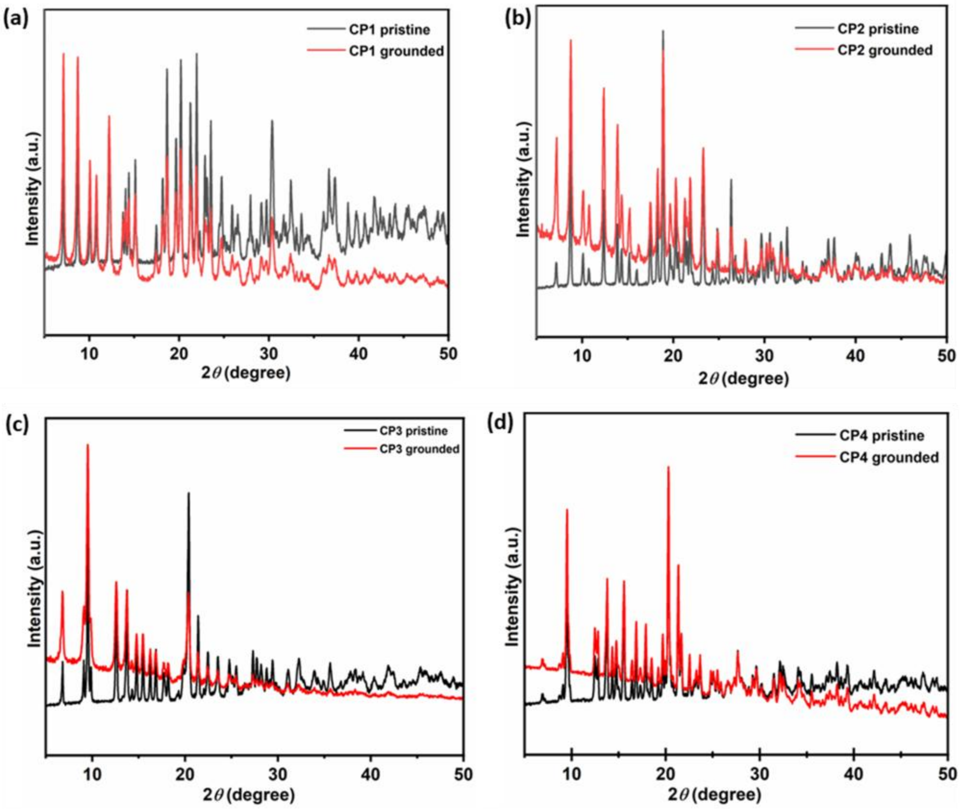

Fig. 2.27: PXRD patterns of pristine and ground CPs.

In addition to the shifting, also an increased emission intensity was observed after grinding the CPs. We further checked the geometric structures and packing arrangements of the CPs. No π–π interactions were observed between the phenyl group of the ligands in the crystal structures. However, as shown in (**Fig. 2.10-2.13**), multiple C–H···π inter- and intra-molecular interactions, with distances ranging from 2.75 to 3.15 Å, were found between different H-atoms and π-cloud of the phenyl rings of Ph_3N units. These multiple C–H···π interactions probably contribute to an increase of intermolecular non-radiative transitions, causing an effect similar to ACQ *[19]*. On grinding, these C–H···π interactions could be partially removed;

as a result, intramolecular radiative transitions are enhanced, thereby increasing emission intensity *[2,48–50]*. To approve this hypothesis, we have recorded the PXRD of all four CPs after grinding. By comparison with the data of pristine solid, a loss in crystallinity is suggested to some extent (**Fig. 2.27**). Further, the presence of solvent vapors could eliminate or decrease the weak inter- and intramolecular interactions in a similar way. In order to verify this, we have recorded the emission of CPs in the presence of solvent vapors. When the solid product was exposed to DMF vapors for 12 hours, a significant increase in the emission intensity was observed, similar to that observed after mechanical grinding (**Fig. 2.28**), confirming a phenomenon similar to the ACQ in all four CPs presented in this work.

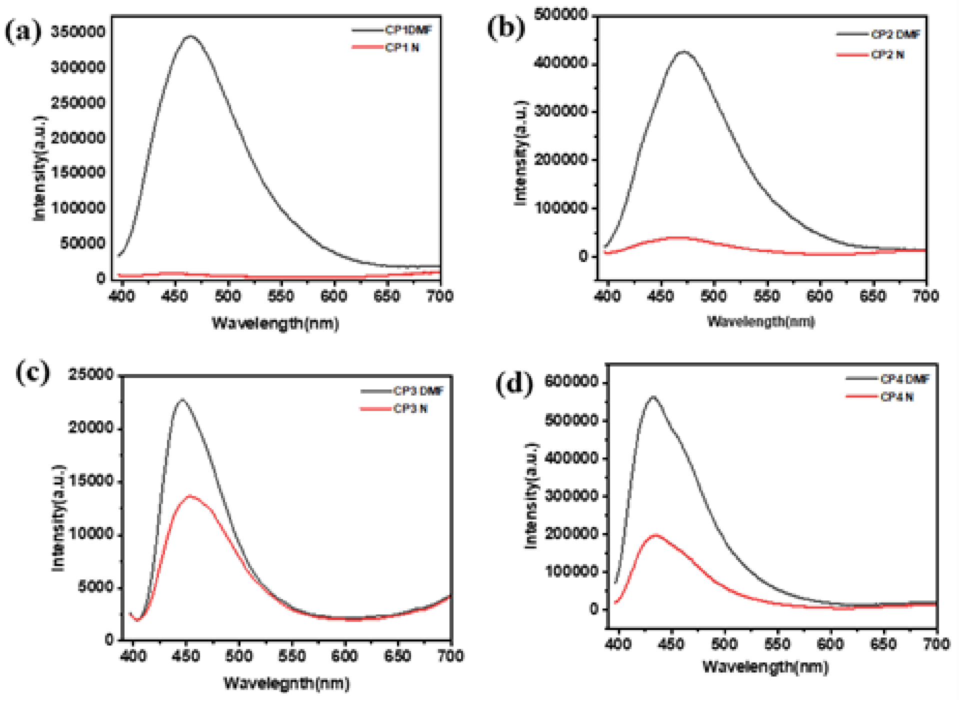

Fig. 2.28: Emission spectra of CPs in the presence of DMF solvent at an excitation wavelength of 382 nm.

2.7. Summary

This study investigates the structural characteristics and photophysical behaviour of the triphenylamine-based ligands **L_1** and **L_2**, and their Cu(I) coordination polymers. It was observed that both ligands **L_1** and **L_2** display solvato-fluorochromic properties due to the TICT phenomenon. With a Cu_2X_2 (X = Br and Cl) rhomboid cluster as SBU, four 1-D polymeric chains were synthesized, which exhibit mechanochromic properties as well. Grinding the CPs results in two phenomena: (*i*) a shift in emission maxima and (*ii*) an increase in emission intensity. The former effect results from the change in the angle between the free and coordinated phenyl groups that leads to the same λ_{em} for all the CPs. The later effect was observed due to the relaxation of C–H···π interactions leading to enhanced intensity. This was further confirmed by emission intensity enhancement in the presence of solvent vapors.

In conclusion, the variation in the ligand backbone around cyclic dithioethers and their coordination product could lead to the development of functional materials for different applications. We are currently investigating the coordination behaviour of triphenylamine ligand with dithioether substitution on all three phenyls in anticipation of getting a luminescent MOF-like structure for sensing applications.

2.8. References

1. Nakamura, K., Kanazawa, K., and Kobayashi, N. (2022). Electrochemical photoluminescence modulation of functional materials and their electrochemical devices. J. Photochem. Photobiol. C Photochem. Rev. 50, 100486. (DOI: 10.1016/j.jphotochemrev.2022.100486)
2. Xue, P., Ding, J., Wang, P., and Lu, R. (2016). Recent progress in the mechanochromism of phosphorescent organic molecules and

metal complexes. J. Mater. Chem. C 4, 6688–6706. (DOI: 10.1039/C6TC01503D)

3. Li, B., Fan, H.-T., Zang, S.-Q., Li, H.-Y., and Wang, L.-Y. (2018). Metal-containing crystalline luminescent thermochromic materials. Coord. Chem. Rev. 377, 307–329. (DOI: 10.1016/j.ccr.2018.09.004)
4. Stavila, V., Talin, A.A., and Allendorf, M.D. (2014). MOF-based electronic and opto-electronic devices. Chem Soc Rev 43, 5994–6010. (DOI: 10.1039/C4CS00096J)
5. Liu, J.-Q., Luo, Z.-D., Pan, Y., Kumar Singh, A., Trivedi, M., and Kumar, A. (2020). Recent developments in luminescent coordination polymers: Designing strategies, sensing application and theoretical evidences. Coord. Chem. Rev. 406, 213145. (DOI: 10.1016/j.ccr.2019.213145)
6. Givaja, G., Amo-Ochoa, P., Gómez-García, C.J., and Zamora, F. (2012). Electrical conductive coordination polymers. Chem. Soc. Rev. 41, 115–147. (DOI: 10.1039/C1CS15092H)
7. Gayathri, P., Pannipara, M., Al-Sehemi, A.G., and Anthony, S.P. (2020). Triphenylamine-based stimuli-responsive solid state fluorescent materials. New J. Chem. 44, 8680–8696. (DOI: 10.1039/D0NJ00588F)
8. Liang, Q.-F., Zheng, H.-W., Yang, D.-D., and Zheng, X.-J. (2022). A triphenylamine derivative and its Cd(ii) complex with high-contrast mechanochromic luminescence and vapochromism. CrystEngComm 24, 543–551. (DOI: 10.1039/D1CE01319J)
9. Ning, Z., Chen, Z., Zhang, Q., Yan, Y., Qian, S., Cao, Y., and Tian, H. (2007). Aggregation-induced Emission (AIE)-active Starburst Triarylamine Fluorophores as Potential Non-doped Red Emitters for Organic Light-emitting Diodes and Cl_2 Gas Chemodosimeter. Adv. Funct. Mater. 17, 3799–3807. (DOI: 10.1002/adfm.200700649)

10. Zhang, Y., Feng, Y.-Q., Wang, J.-H., Han, G., Li, M.-Y., Xiao, Y., and Feng, Z.-D. (2017). Moiety effect on the luminescent property of star-shaped triphenylamine (TPA) derivatives as mechanochromic materials. RSC Adv. 7, 35672–35680. (DOI: 10.1039/C7RA03123H).
11. Hu, W., Yang, W., Gong, T., Zhou, W., and Zhang, Y. (2019). Multi-stimuli responsive properties switch by intra- and inter-molecular charge transfer constructed from triphenylamine derivative. Cryst EngComm 21, 6630–6640. (DOI: 10.1039/C9CE01217F)
12. V. Bünau, G. (1970). J. B. Birks: Photophysics of Aromatic Molecules. Wiley-Interscience, London 1970. 704 Seiten. Preis: 210s. Berichte Bunsenges. Für Phys. Chem. 74, 1294–1295. (DOI: 10.1002/bbpc.19700741223)
13. Huang, B., Jiang, D., Feng, Y., Chen, W.-C., Zhang, Y., Cao, C., Shen, D., Ji, Y., Wang, C., and Lee, C.-S. (2019). Mechanochromic luminescence and color-tunable light-emitting devices of triphenylamine functionalized benzo[d , e]benzo[4,5]imidazo[2,1-a]isoquinolin-7-one. J. Mater. Chem. C 7, 9808–9812. (DOI: 10.1039/C9TC02592H)
14. Hu, L.-X., Gao, M., Wen, T., Kang, Y., and Chen, S. (2017). Synthesis of Halide-Modulated Cuprous(I) Coordination Polymers with Mechanochromic and Photocatalytic Properties. Inorg. Chem. 56, 6507–6511. (DOI: 10.1021/acs.inorgchem.7b00598)
15. Du, X.-S., Yan, B.-J., Wang, J.-Y., Xi, X.-J., Wang, Z.-Y., and Zang, S.-Q. (2018). Layer-sliding-driven crystal size and photoluminescence change in a novel SCC-MOF. Chem. Commun. 54, 5361–5364. (DOI: 10.1039/C8CC01559G)
16. Liu, S., Yuan, S., Hu, T., and Sun, D. (2014). Retracted: A 3D Luminescent Metal-organic Framework Constructed from Cu_4I_4

Cubane Clusters and Triangular Imidazole Ligand. Z. Für Anorg. Allg. Chem. 640, 2030–2034. (DOI: 10.1002/zaac.201400071).

17. Shi, Z., Pan, Z., Jia, H., Chen, S., Qin, L., and Zheng, H. (2016). Zn(II)/Cd(II) Terephthalate Coordination Polymers Incorporating Bi-, Tri-, and Tetratopic Phenylamine Derivatives: Crystal Structures and Photoluminescent Properties. Cryst. Growth Des. 16, 2747–2755. (DOI: 10.1021/acs.cgd.6b00056)

18. Hua, C., Turner, P., and D'Alessandro, D.M. (2015). Facile redox state manipulation in Cu(i) frameworks by utilisation of the redox-active tris(4-(pyridin-4-yl)phenyl)amine ligand. Dalton Trans. 44, 15297–15303. (DOI: 10.1039/C5DT01233C)

19. Wu, B., Guo, Z., Li, G., Zhao, J., Liu, Y., Wang, J., Wang, H., and Yan, X. (2021). Synergistic combination of ACQ and AIE moieties to enhance the emission of hexagonal metallacycles. Chem. Commun. 57, 11056–11059. (DOI: 10.1039/D1CC03787K)

20. Yao, Z., Xu, J., Zou, B., Hu, Z., Wang, K., Yuan, Y., Chen, Y., Feng, R., Xiong, J., Hao, J., et al. (2019). A Dual-Stimuli-Responsive Coordination Network Featuring Reversible Wide-Range Luminescence-Tuning Behavior. Angew. Chem. Int. Ed. 58, 5614–5618. (DOI: 10.1002/anie.201900190)

21. Cariati, E., Lucenti, E., Botta, C., Giovanella, U., Marinotto, D., and Righetto, S. (2016). Cu(I) hybrid inorganic–organic materials with intriguing stimuli responsive and optoelectronic properties. Coord. Chem. Rev. 306, 566–614. (DOI:10.1016/j.ccr.2015.03.004)

22. Schlachter, A., Tanner, K., and Harvey, P.D. (2021). Copper halide-chalcogenoether and -chalcogenone networks: Chain and cluster motifs, polymer dimensionality and photophysical properties. Coord. Chem. Rev. 448, 214176. https://doi.org/10.1016/j.ccr.2021.214176.

23. Tsuge, K., Chishina, Y., Hashiguchi, H., Sasaki, Y., Kato, M., Ishizaka, S., and Kitamura, N. (2016). Luminescent copper(I) complexes with halogenido-bridged dimeric core. Coord. Chem. Rev. 306, 636–651. (DOI: 10.1016/j.ccr.2015.03.022)

24. Fang, Y., Liu, W., Teat, S.J., Dey, G., Shen, Z., An, L., Yu, D., Wang, L., O'Carroll, D.M., and Li, J. (2017). A Systematic Approach to Achieving High Performance Hybrid Lighting Phosphors with Excellent Thermal- and Photostability. Adv. Funct. Mater. 27, 1603444. (DOI: 10.1002/adfm.201603444)

25. Vinogradova, K.A., Shekhovtsov, N.A., Berezin, A.S., Sukhikh, T.S., Rogovoy, M.I., Artem'ev, A.V., and Bushuev, M.B. (2021). Coordination-induced emission enhancement in copper(i) iodide coordination polymers supported by 2-(alkylsulfanyl)pyrimidines. Dalton Trans. 50, 9317–9330. (DOI: 10.1039/D1DT00826A)

26. Wen, T., Zhang, D.-X., Liu, J., Lin, R., and Zhang, J. (2013). A multifunctional helical Cu(i) coordination polymer with mechanochromic, sensing and photocatalytic properties. Chem. Commun. 49, 5660. (DOI: 10.1039/c3cc42241k)

27. Schlachter, A., and Harvey, P.D. (2021). Properties and applications of copper halide-chalcogenoether and -chalcogenone networks and functional materials. J. Mater. Chem. C 9, 6648–(DOI: 10.1039/D1TC00585E)

28. Li, D., Shi, W.-J., and Hou, L. (2005). Coordination Polymers of Copper(I) Halides and Neutral Heterocyclic Thiones with New Coordination Modes. Inorg. Chem. 44, 3907–3913. (DOI: 10.1021/ic050209j)

29. Kim, T.H., Shin, Y.W., Jung, J.H., Kim, J.S., and Kim, J. (2008). Crystal-to-Crystal Transformation between Three Cu^{I} Coordination Polymers and Structural Evidence for Luminescence

Thermochromism. Angew. Chem. Int. Ed. 47, 685–688. (DOI: 10.1002/anie.200704349)

30. Conesa-Egea, J., Zamora, F., and Amo-Ochoa, P. (2019). Perspectives of the smart Cu-Iodine coordination polymers: A portage to the world of new nanomaterials and composites. Coord. Chem. Rev. 381, 65–78. (DOI: 10.1016/j.ccr.2018.11.008)

31. Harvey, P.D., and Knorr, M. (2016). Designs of 3-Dimensional Networks and MOFs Using Mono- and Polymetallic Copper(I) Secondary Building Units and Mono- and Polythioethers: Materials Based on the Cu–S Coordination Bond. J. Inorg. Organomet. Polym. Mater. 26, 1174–1197. (DOI: 10.1007/s10904-016-0378-7)

32. Raghuvanshi, A., Dargallay, N.J., Knorr, M., Viau, L., Knauer, L., and Strohmann, C. (2017). 1,3-Dithiolane and 1,3-Ferrocenyl-dithiolane as Assembling Ligands for the Construction of Cu(I) Clusters and Coordination Polymers. J. Inorg. Organomet. Polym. Mater. 27, 1501–1513. (DOI: 10.1007/s10904-017-0610-0)

33. Raghuvanshi, A., Knorr, M., Knauer, L., Strohmann, C., Boullanger, S., Moutarlier, V., and Viau, L. (2019). 1,3-Dithianes as Assembling Ligands for the Construction of Copper(I) Coordination Polymers. Investigation of the Impact of the $RC(H)S_2C_3H_6$ Substituent and Reaction Conditions on the Architecture of the 0D–3D Networks. Inorg. Chem. 58, 5753–5775. (DOI: 10.1021/acs.inorgchem.9b00114)

34. Viau, L., Knorr, M., Knauer, L., Brieger, L., and Strohmann, C. (2022). 2,2′-Ethylenebis(1,3-dithiane) as a polydentate μ_2-, μ_4- and μ_5 -assembling ligand for the construction of sulphur-rich Cu(i), Hg(ii) and heterometallic Cu(i)/Hg(ii) coordination polymers featuring uncommon network architectures. Dalton Trans. 51, 7581–7606. (DOI: 10.1039/D2DT00800A)

35. Harisomayajula, N.V.S., Makovetskyi, S., and Tsai, Y. (2019). Cuprophilic Interactions in and between Molecular Entities. Chem. – Eur. J. 25, 8936–8954. (DOI: 10.1002/chem.201900332)

36. Knorr, M., Guyon, F., Khatyr, A., Strohmann, C., Allain, M., Aly, S.M., Lapprand, A., Fortin, D., and Harvey, P.D. (2012). Construction of $(CuX)_{2n}$ Cluster-Containing (X = Br, I; n = 1, 2) Coordination Polymers Assembled by Dithioethers $ArS(CH_2)_m SAr$ (Ar = Ph, p -Tol; m = 3, 5): Effect of the Spacer Length, Aryl Group, and Metal-to-Ligand Ratio on the Dimensionality, Cluster Nuclearity, and the Luminescence Properties of the Metal–Organic Frameworks. Inorg. Chem. 51, 9917–9934. (DOI: 10.1021/ic301385u)

37. Knorr, M., Khatyr, A., Dini Aleo, A., El Yaagoubi, A., Strohmann, C., Kubicki, M.M., Rousselin, Y., Aly, S.M., Fortin, D., Lapprand, A., et al. (2014). Copper(I) Halides (X = Br, I) Coordinated to Bis(arylthio)methane Ligands: Aryl Substitution and Halide Effects on the Dimensionality, Cluster Size, and Luminescence Properties of the Coordination Polymers. Cryst. Growth Des. 14, 5373–5387. (DOI: 10.1021/cg500905z)

38. Raghuvanshi, A., Knorr, M., Knauer, L., Strohmann, C., Boullanger, S., Moutarlier, V., and Viau, L. (2019). 1,3-Dithianes as Assembling Ligands for the Construction of Copper(I) Coordination Polymers. Investigation of the Impact of the $RC(H)S_2C_3H_6$ Substituent and Reaction Conditions on the Architecture of the 0D–3D Networks. Inorg. Chem. 58, 5753–5775. (DOI: 10.1021/acs.inorgchem.9b00114)

39. Grabowski, Z.R., Rotkiewicz, K., and Rettig, W. (2003). Structural Changes Accompanying Intramolecular Electron Transfer: Focus on Twisted Intramolecular Charge-Transfer States and Structures. Chem. Rev. 103, 3899–4032. (DOI: 10.1021/cr940745l)

40. Zhang, J., He, B., Hu, Y., Alam, P., Zhang, H., Lam, J.W.Y., and Tang, B.Z. (2021). Stimuli-Responsive AIEgens. Adv. Mater. 33, 2008071. (DOI: 10.1002/adma.202008071).

41. Yu, Y., Zhao, R., Liu, H., Zhang, S., Zhou, C., Gao, Y., Li, W., and Yang, B. (2020). Highly efficient deep-blue light-emitting material based on V-Shaped donor-acceptor triphenylamine-phenanthro[9,10-d]imidazole molecule. Dyes Pigments 180, 108511. (DOI: 10.1016/j.dyepig.2020.108511)

42. Reichardt, C. (1994). Solvatochromic Dyes as Solvent Polarity Indicators. Chem. Rev. 94, 2319–2358. ((DOI: 10.1021/cr00032a005)

43. Mizuguchi, K., Kageyama, H., and Nakano, H. (2011). Mechanochromic luminescence of 4-[bis(4-methylphenyl)amino]benzaldehyde. Mater. Lett. 65, 2658–2661. (DOI: 10.1016/j.matlet.2011.05.068)

44. Hu, R., Lager, E., Aguilar-Aguilar, A., Liu, J., Lam, J.W.Y., Sung, H.H.Y., Williams, I.D., Zhong, Y., Wong, K.S., Peña-Cabrera, E., et al. (2009). Twisted Intramolecular Charge Transfer and Aggregation-Induced Emission of BODIPY Derivatives. J. Phys. Chem. C 113, 15845–15853. (DOI: 10.1021/jp902962h)

45. Sasaki, S., Drummen, G.P.C., and Konishi, G. (2016). Recent advances in twisted intramolecular charge transfer (TICT) fluorescence and related phenomena in materials chemistry. J. Mater. Chem. C 4, 2731–2743. (DOI: 10.1039/C5TC03933A)

46. Wang, C., Qiao, Q., Chi, W., Chen, J., Liu, W., Tan, D., McKechnie, S., Lyu, D., Jiang, X., Zhou, W., et al. (2020). Quantitative Design of Bright Fluorophores and AIEgens by the Accurate Prediction of Twisted Intramolecular Charge Transfer (TICT). Angew. Chem. Int. Ed. 59, 10160–10172. (DOI: 10.1002/anie.201916357)

47. 7 M. J. Frisch, G. W. Trucks, H. B. Schlegel, G. E. Scuseria, M. A. Robb, J. R. Cheeseman, G. Scalmani, V. Barone, B. Mennucci, G. A. Petersson et al., Gaussian 09, Revision A.02, Gaussian, Inc., Wallingford, CT, 2009.
48. Chan, C.Y.K., Lam, J.W.Y., Zhao, Z., Chen, S., Lu, P., Sung, H.H.Y., Kwok, H.S., Ma, Y., Williams, I.D., and Tang, B.Z. (2014). Aggregation-induced emission, mechanochromism and blue electroluminescence of carbazole and triphenylamine-substituted ethenes. J Mater Chem C 2, 4320–4327. (DOI: 10.1039/C4TC00097H)
49. Sun, Y., Lei, Z., and Ma, H. (2022). Twisted aggregation-induced emission luminogens (AIEgens) contribute to mechanochromism materials: a review. J. Mater. Chem. C 10, 14834–14867. (DOI: 10.1039/D2TC02512D)
50. Zhang, X., Chi, Z., Zhang, Y., Liu, S., and Xu, J. (2013). Recent advances in mechanochromic luminescent metal complexes. J. Mater. Chem. C 1, 3376-3390. (DOI: 10.1039/c3tc30316k)

Chapter 3

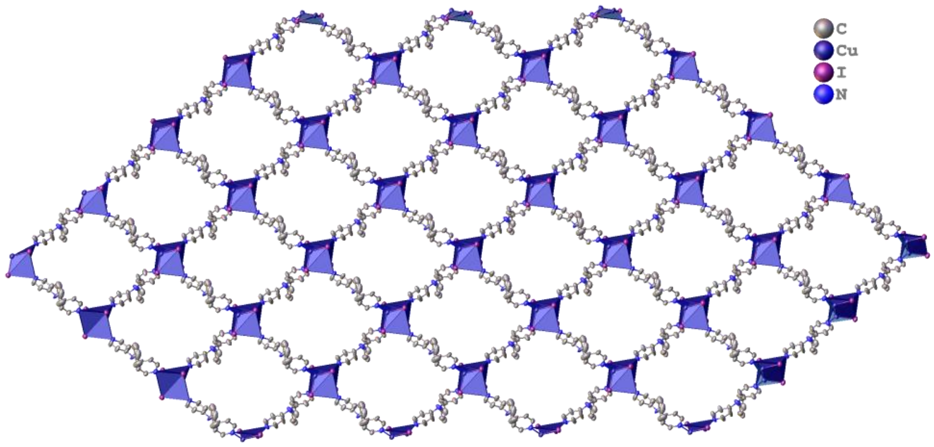

Two-dimensional Cu(I)-MOF with mesoporous architecture towards chemiresistive NO_2 sensing

3.1. Introduction

Metal-organic frameworks (MOFs) have gained significant interest due to their porosity along with chemical and structural diversity, leading to multifunctional properties. Although a majority of MOFs are electrical insulators, the past decade has witnessed the emergence of several electrically conductive MOFs (c-MOFs) *[1–3]*. c-MOFs are usually composed of π-conjugated ligands capable of effective charge delocalization and are highly attractive for various electronic applications, including electrocatalysis, sensing, energy storage, and quantum information *[4–10]*. In particular, 2D c-MOFs have emerged as promising candidates for the development of chemiresistive sensors. Their porous structures and electrical properties improve gas adsorption and interactions while maintaining high electrical conductivity under ambient conditions *[4,8,10–14]*. Moreover, The presence of diverse binding sites in these materials enables unique interactions with specific target molecules, significantly enhancing selectivity. Therefore, the incorporation of c-MOFs has significantly addressed the key limitations associated with the selectivity and room temperature operation of traditional sensing materials for some toxic gases *[15–19]*. Recently, semiconducting Cu(I) frameworks have attracted considerable attention in the field of chemiresistive gas sensing due to their potential for detecting a wide range of chemicals, including both volatile organic compounds and inorganic toxic gases such as NH_3, MeOH, and NO_2 *[18,20,21]*. The tendency of CuI salts to assemble into different high-nuclearity clusters such as [Cu_2I_2], [Cu_3I_3], [Cu_4I_4] etc., and their structural diversity makes attractive platforms for various applications *[22–26]*. These clusters contribute to the formation of semiconducting, robust frameworks, and tunable structures, enhancing their potential for sensing applications. Further, cost-effectiveness, low toxicity, and convenient synthesis make these materials even more attractive.

A significant discharge of industrial waste gases and automobile exhaust has caused considerable damage to the environment and human health. NO_2 is one of such commonly emitted toxic gas which can cause ground-level ozone formation, acid rain, eutrophication, reduced visibility, and climate change *[16,27]*. In addition, low-level NO_2 exposure can cause respiratory and cardiovascular issues, including bronchitis, pulmonary edema and olfactory paralysis, whereas prolonged exposure may lead to severe brain disorders such as Parkinson's disease, which can be life-threatening for humans *[28–31]*. Toxicity by NO_2 arises due to its reaction with hemoglobin to form methemoglobin, which is unable to carry oxygen *[32]*. Therefore, quick and real-time detection of NO_2 is essential for public health and environmental monitoring. Several materials have shown promising results for room temperature NO_2 sensing, but response time and reversibility are still a major challenge. The irreversibility is attributed to NO_2's strong tendency to extract electrons from metal nodes and form stable complexes *[33,34]*. Strategies such as photoactivation and high-temperature operation have been employed to address this issue, leading to additional power requirements in the device. The success of these approaches can not be undermined, but for real-world applications sensors that are user-friendly and can operate at room temperature would be more appropriate *[28,35]*.

In this study, we report a 2D **Cu-MOF,** synthesized from N-phenyl-N-(pyridin-4-yl)pyridin-4-amine and CuI. The **Cu-MOF** consists of a Cu_4I_4 secondary building unit (SBU). The semiconducting behavior and mesoporous structure intrigued us to explore its gas-sensing capabilities. The chemiresistive gas sensor fabricated from **Cu-MOF** demonstrated a high selectivity and response for NO_2 gas with an exceptionally fast response/recovery time of approximately 11/13 seconds at room temperature. The sensing mechanism is thoroughly investigated using experimental and theoretical studies.

3.2.1. General Information

3.2.1.1. Materials

Materials required for the synthesis of 4,4'-Dipyridylamine were purchased from Avra Chemicals. For ligand synthesis, TLC was used to monitor reaction progress using a Merck 60 F254 precoated silica gel plate (0.25 mm thickness), and the products were judged in a UV chamber. Unless otherwise specified, chemicals were used exactly as received. CuI (>99%) from Loba Chemie Pvt. Ltd., and used without further purification. Solvents like diphenyl ether, and acetonitrile (HPLC grade) were bought from Advent Chembio Pvt. Ltd.

3.2.1.2. Instruments

Powder X-ray diffraction (PXRD) data were recorded on Rigaku Smart X-ray diffractometer with monochromatic Cu Kα (0.1540 nm) radiation in 2θ range of 5-50 degrees. The attenuated total reflectance infrared spectroscopy (ATR-IR) was performed on Bruker Alpha II spectrophotometer of the powdered sample in the range of 4000-400 cm^{-1}. Both ^1H and $^{13}C\{^1H\}$ NMR spectra were collected using a Bruker 500 MHz spectrometer in DMSO-d_6. Data for proton NMR chemical shifts are shown in ppm downfield from tetramethyl silane and are mentioned in delta (δ) units. The ^1H NMR splitting patterns are singlet (s), doublet (d), triplet (t), and multiplet (m), and Mestre Nova processed the NMR data. We have used a field emission scanning electron microscope (FE-SEM) on JEOL JSM-7400F for morphological characterization and its elemental mapping. The thermogravimetric analysis was performed on Mettler Toledo TGA 1-star e-system in the temperature range of 30-700 °C.

3.2.1.3. Crystallographic details

Single crystal X-ray diffraction studies for **Cu-MOF** were carried out using Agilent technology (Oxford diffraction) super Nova CCD system, with monochromated Mo Kα radiation (λ=0.71073 Å). Unit cell determination, data collection and reduction, and empirical absorption correction were performed using the CrysAlisPro program.

3.3. Synthesis

3.3.1. Synthesis of *N-phenyl-N-(pyridine-4-yl)pyridine-4-amine* (L_3)

For the synthesis of $\mathbf{L_3}$, in a two-neck r.b., 4,4'-Dipyridylamine (DPA) (2000 mg, 11.7 mmol) was added with $CuSO_4$ (360 mg, 2.2 mmol), 18-crown-6 (120 mg, 0.05 mmol), potassium carbonate (3200 mg, 23.4 mmol) with bromobenzene (3.6 mL, 34.8 mmol) in diphenyl ether (15 mL). The reaction temperature was maintained at 450 K for two days in N_2. 2 days later, 200 mL of DCM and 200 mL of MeOH were added to the reaction mixture and passed through the celite pad. Most of the solvent was dried except diphenyl ether. Solvent and other impurities were removed and the compound was purified by column chromatography (Ph_2O and bromobenzene were removed by hexane as eluent and $\mathbf{L_3}$ was obtained in ethyl acetate as eluent). (Yield: 2000 mg, ~70%). **^{1}H NMR** (500 MHz, DMSO-d_6) δ 8.41 (s, 4H), 7.50 (t, *J* = 7.7 Hz, 2H), 7.37 (t, *J* = 7.6 Hz, 1H), 7.23 (d, *J* = 8.1 Hz, 2H), 6.95 (d, *J* = 4.7 Hz, 4H). **^{13}C{^{1}H} NMR** (126 MHz, DMSO-d_6) δ 150.99, 150.16, 143.03, 129.92, 127.17, 126.52, 115.52. **LCMS** (ESI) *m/z* calculated for $C_{16}H_{13}N_3$ $[M+H]^+$ 248.1182, found 248.1201.

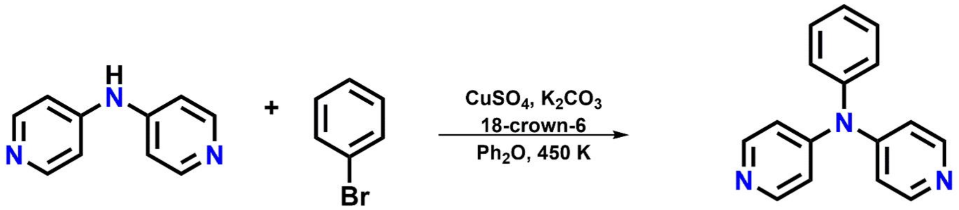

Scheme 3.1. Synthesis of $\mathbf{L_3}$

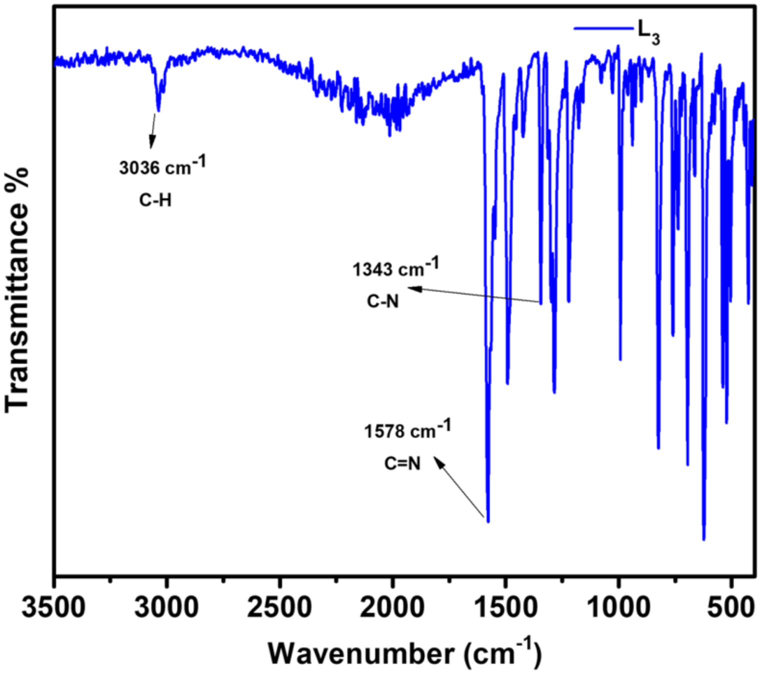

Fig. 3.1: IR spectra of **L₃**

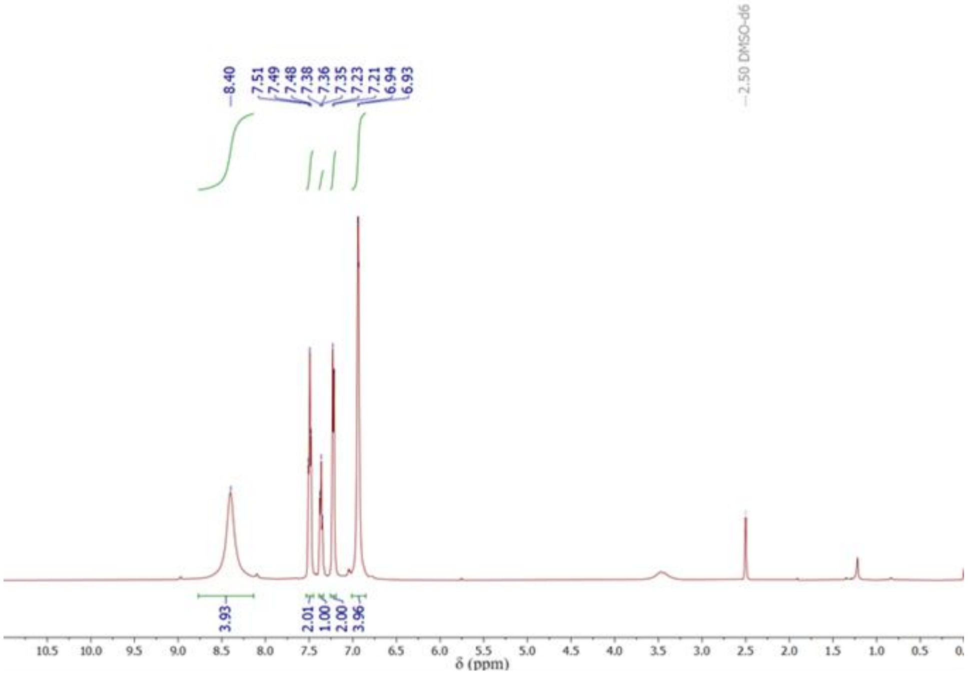

Fig. 3.2: ^{1}H NMR of **L₃**.

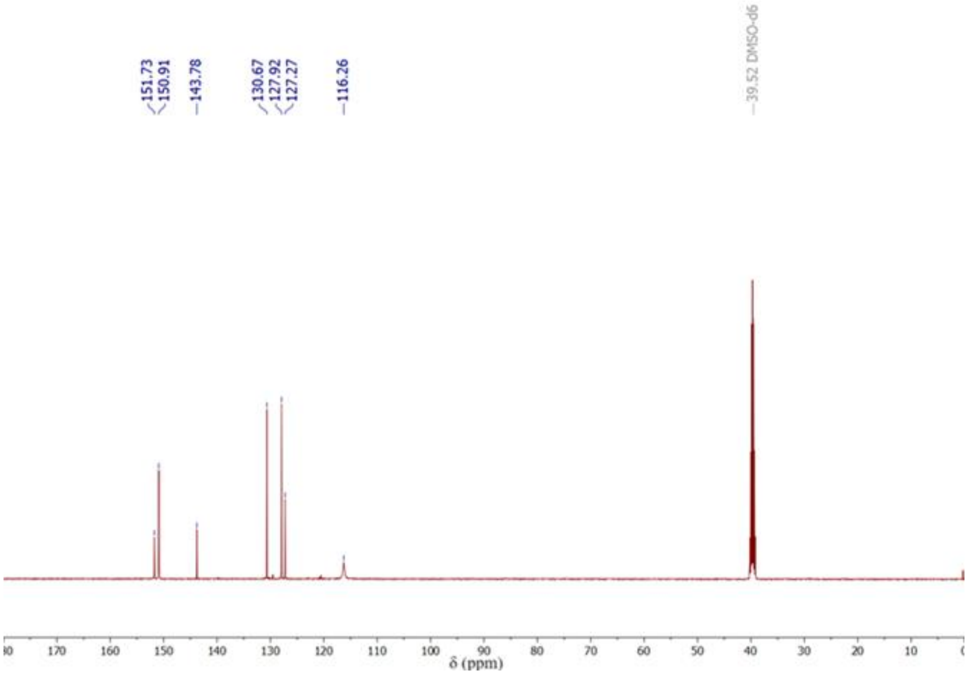

Fig. 3.3: ^{13}C{^{1}H} NMR of **L$_3$**

3.3.2. Synthesis of Cu-MOF

Into a 50 mL Schenk tube under N$_2$ condition, **L$_3$** (100 mg, 0.8 mmol) was dissolved in 2 ml DCM, to which CuI (153 mg, 1.6 mmol) dissolved in 10 mL ACN was added and resulted in instant white precipitates. The reaction mixture was stirred for 12 hours, after which the compound was dried and washed with ACN. (Yield: 200 mg, ~80%). Crystals were obtained by slow diffusion of CuI dissolved in ACN over ligand dissolved in DCM.

3.4. Results and Discussion

The ligand, **L$_3$** was synthesized in 70% yield by reacting 4,4'-dipyridylamine with bromobenzene (**Scheme 3.1**) and characterized with various spectroscopic techniques (**Fig. 3.1-3.3**).

The synthesized ligand was reacted with CuI in 1:2 ratio to obtain **Cu-MOF** as a white solid in 80 % yield (**Scheme 3.2**). The synthesized MOF was initially analyzed using Infrared spectroscopy, which showed slight shifts from the ligand spectrum, suggesting the coordination of the ligands with CuI (**Fig. 3.4**).

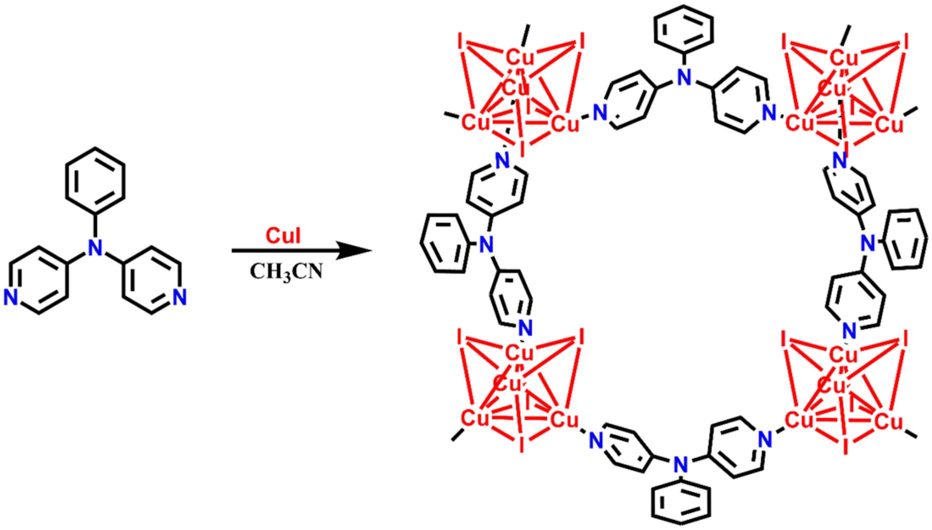

Scheme 3.2. Synthesis of **Cu-MOF**

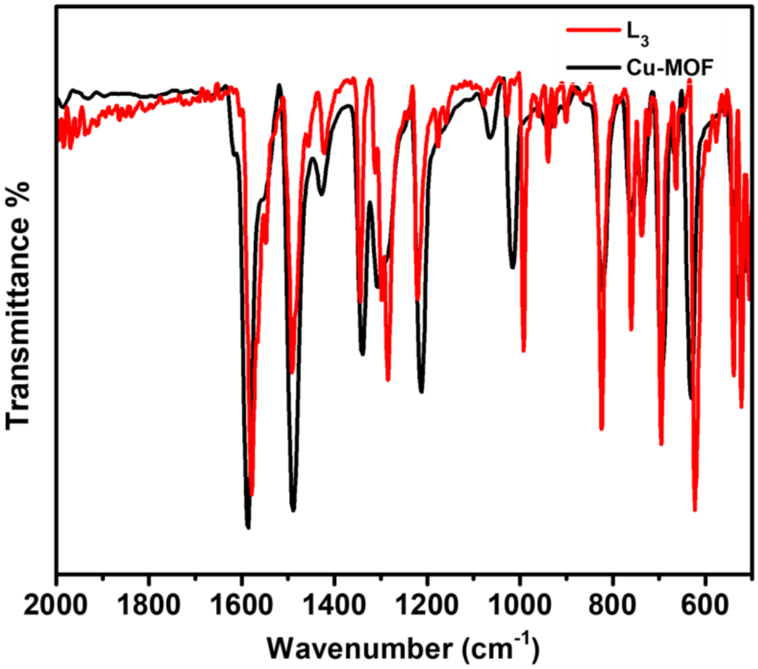

Fig. 3.4: Comparison of IR spectra of **L3** and **Cu-MOF**

Crystals suitable for single-crystal X-ray diffraction (SCXRD were obtained by slow diffusion of CuI in acetonitrile into a dichloromethane solution of the ligand over a week. **Cu-MOF** crystallizes in the monoclinic system with *Cc* space group. Other important crystallographic parameters are given in **Table 3.1**. The asymmetric unit consists of four copper, four iodides, and two units of ligand (**Fig. 3.6a**). The expanded structure reveals a new two-dimensional network with Cu_4I_4 distorted cubane tetrameric SBU. Each copper has distorted tetrahedral geometry and is bridged with μ^3-I and pyridyl nitrogens of ligand. Both pyridyl rings of ligand are coordinated to two different Cu_4I_4 clusters. These Cu_4I_4 SBUs are connected to adjacent Cu_4I_4 via the bridging of ligands, leading to the formation of a 2D framework with 44-membered metallacycle forming rectangular voids (F**ig. 3.5a** and **3.5b**). The distances between the centroid of adjacent clusters are 13.196 Å along vertical and 13.293 Å along horizontal axes (F**ig. 3.6b**). In Cu_4I_4 distorted cubane tetramer, Cu-I, Cu–N and Cu-Cu distances are in the range of 2.624-2.748 Å, 2.023–2.047 Å and 2.624-2.698 Å, respectively (F**ig. 3.7**). The angle of Cu-I-Cu is predominantly around 59°. These bond metrics are consistent with the previous reports on Cu(I) iodide frameworks having Cu_4I_4 SBU *[26,36,37]*. C-H---π interactions (2.805-2.898 Å) involving ortho and meta hydrogen of the phenyl ring lead to another entangled plane which is chemically equivalent to the 2D framework, partially filling the voids generated by the rhombus-grid structure. In addition, some solvent molecules are also found trapped in the cavity. Thus entangled planes and solvent molecules in the voids generated by the 2D network led to close packing in the crystal structure. Both sheets are nearly perpendicular to each other with a sliding angle of 77.75°. Such packing in crystal structures is relatively rare (F**ig. 3.5d**) *[38–40]*. Moreover, weak C-H---I (3.133 Å) interactions were also identified from para-hydrogen of the phenyl ring to Iodine, leading to parallel stacking of sheets with interplanar distances of 12.776 Å (F**ig. 3.5c**). Thus, there are infinitely parallelly 2D stacked sheets and 77.75° tilted 2D sheets forming a closely packed 2D-3D mixed network.

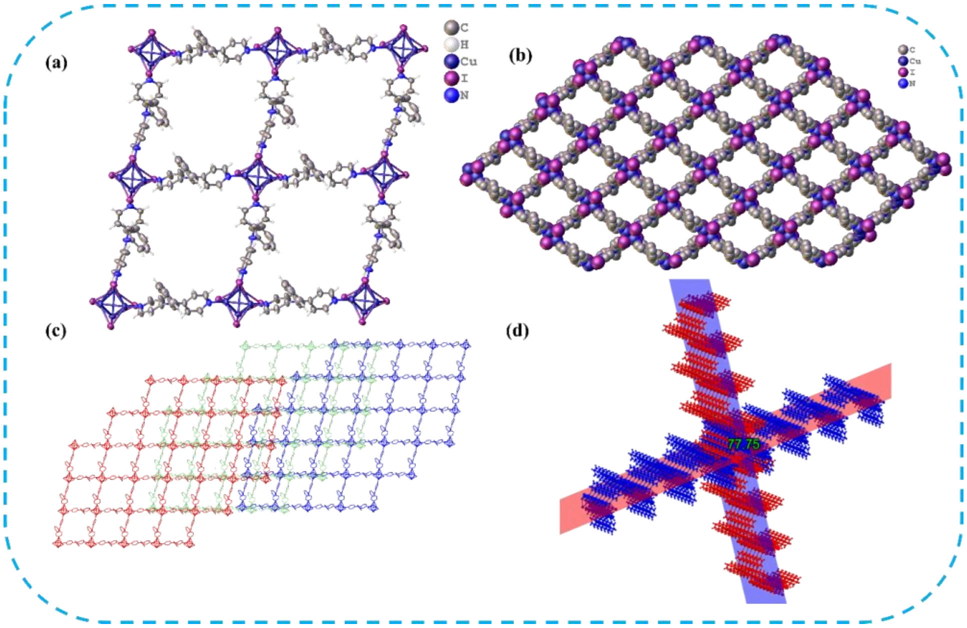

Fig. 3.5: (a) 2D sheet of rhombus grid network of **Cu-MOF** (b) Spacefilled model of 2D **Cu-MOF** (c) C-H---I interactions leading to parallel stacking of sheets (d) Interpenetration of two sheets.

The experimental powder X-ray diffraction (PXRD) patterns confirmed the phase purity of the bulk sample, which correlates well with the simulated pattern obtained from SCXRD analysis (F**ig. 3.8a**). **Cu-MOF** remains stable for several months under ambient conditions. The thermal stability of **Cu-MOF** was assessed using thermogravimetric analysis (TGA), (F**ig. 3.8b**), which suggests thermal stability till 250 °C. The Brunauer-Emmett-Teller (BET) analysis showed a type IV isotherm, with a surface area of 15.033 m²/g, indicating a mesoporous structure for **Cu-MOF** (F**ig. 3.9a**). Additionally, the pore size of **Cu-MOF** was determined to be 5.77 nm using the Barrett-Joyner-Halenda (BJH) method (F**ig. 3.9b**).

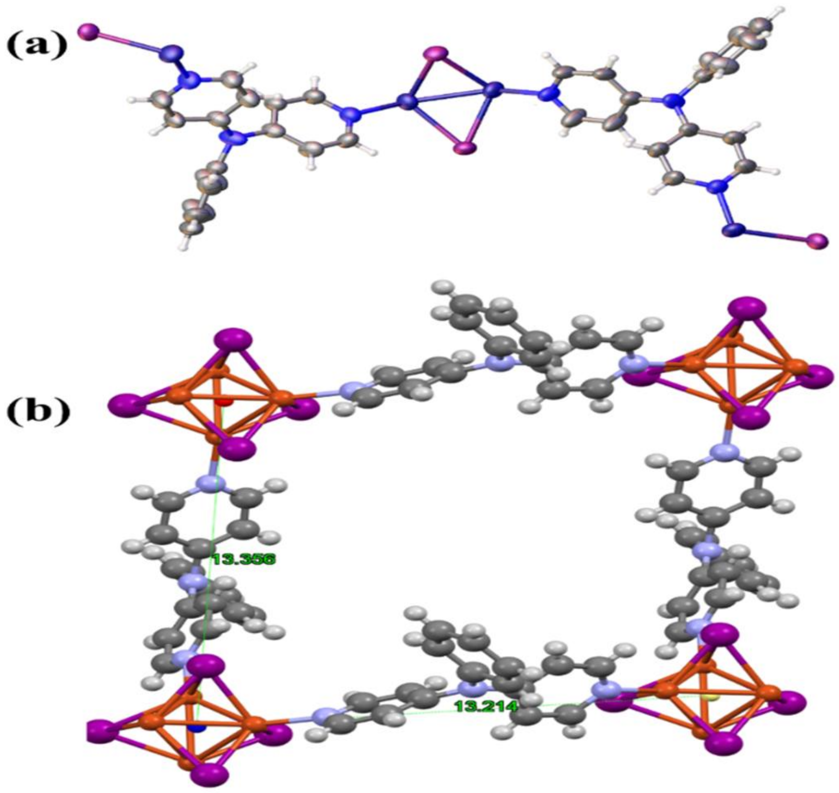

Fig. 3.6: (a) The asymmetric unit of **Cu-MOF** (b) different lengths across axes.

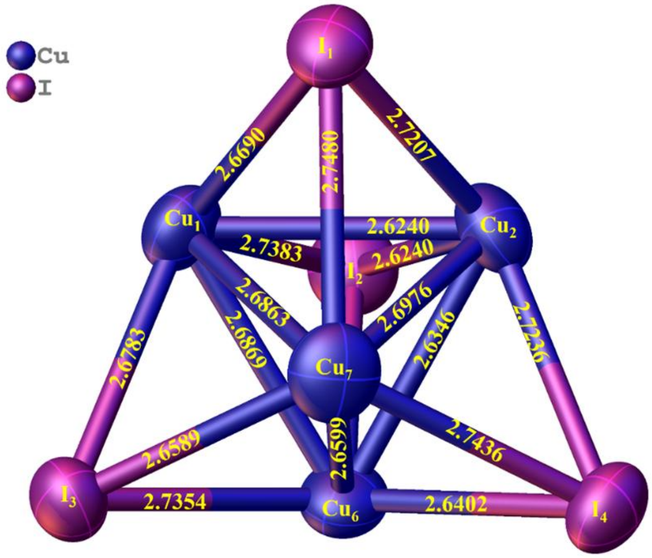

Fig. 3.7: Bond lengths of Cu-Cu and Cu-N in Cu_4I_4 SBU

The surface morphology of the synthesized MOF was assessed using a Field emission Scanning Electron Microscope (FE-SEM). FE-SEM images suggest the formation of irregular agglomerated petals (F**ig. 3.10**). These multiple petals pile up to form nanoflower structures of different sizes. These nanoflowers have curved ending sides while they seem to have grown over each other F**ig. 3.10a-3.10c**. Energy Dispersive X-ray (EDX) analysis confirms a uniform presence of Cu, C, N, and I elements in the appropriate portion in MOF (F**ig. 3.11**).

Table 3.1. Crystallographic parameters of **Cu-MOF**

Compound	**Cu-MOF**
CCDC No.	2385865
Formula	$C_{35}H_{31}Cl_2Cu_4I_4N_7$
Formula Weight	1382.33
Wavelength	0.71073 Å
Crystal System	monoclinic
Space group	*Cc*
a/Å	16.9593(2)
b/ Å	20.2694(2)
c/ Å	13.3565(2)
α /°	90
β/°	105.5110(10)
γ/°	90
V/ Å^3	4424.14(10)
Z	4
ρ_{calcd} (g/cm^3)	2.075
Temperature/K	298.00
GOF	1.034
2θ range for data collection	4.006 to 54.814
Reflections collected	70029

Independent reflections	9468 [R_{int} = 0.0377, R_{sigma} = 0.0283]
Completeness to θ=25.242	99.8
Final R indices [I>2σ(I)]	R_1 = 0.0345, wR_2 = 0.0766
Final R indices [all data]	R_1 = 0.0416, wR_2 = 0.0801
Largest diff. peak/hole/ e Å^{-3}	0.48/-0.52

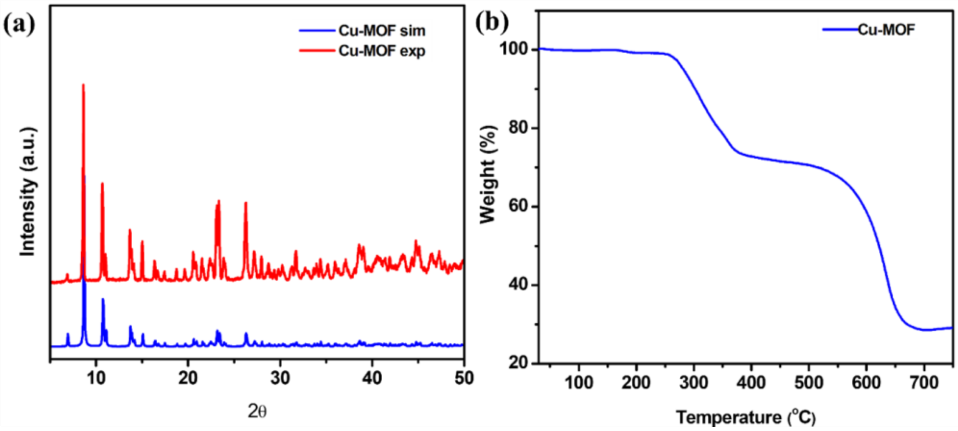

Fig. 3.8: (a) PXRD patterns of Simulated and experimental **Cu-MOF** (b) TGA curve of **Cu-MOF**

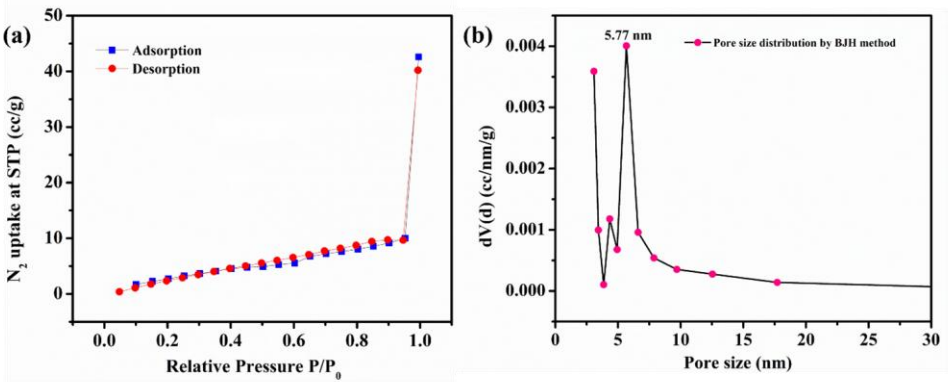

Fig. 3.9: (a) BET (b) BJH of **Cu-MOF**

Moreover, elemental mapping analysis confirms the uniform distribution of elements over the surface, indicating a consistent composition (F**ig. 3.10d-3.10g**). Transmission electron microscopic (TEM) images also confirmed the formation of agglomerated nano-particles of sizes ranging from 100 to 800 nm, with shades of darker color in a single particle which could show the extent of accumulation (F**ig. 3.10h-3.10i**). The selected area electron diffraction (SAED) pattern indicates rings corresponding to different diffraction planes present in **Cu-MOF**, suggesting the crystalline nature of **Cu-MOF** (F**ig. 3.10j**).

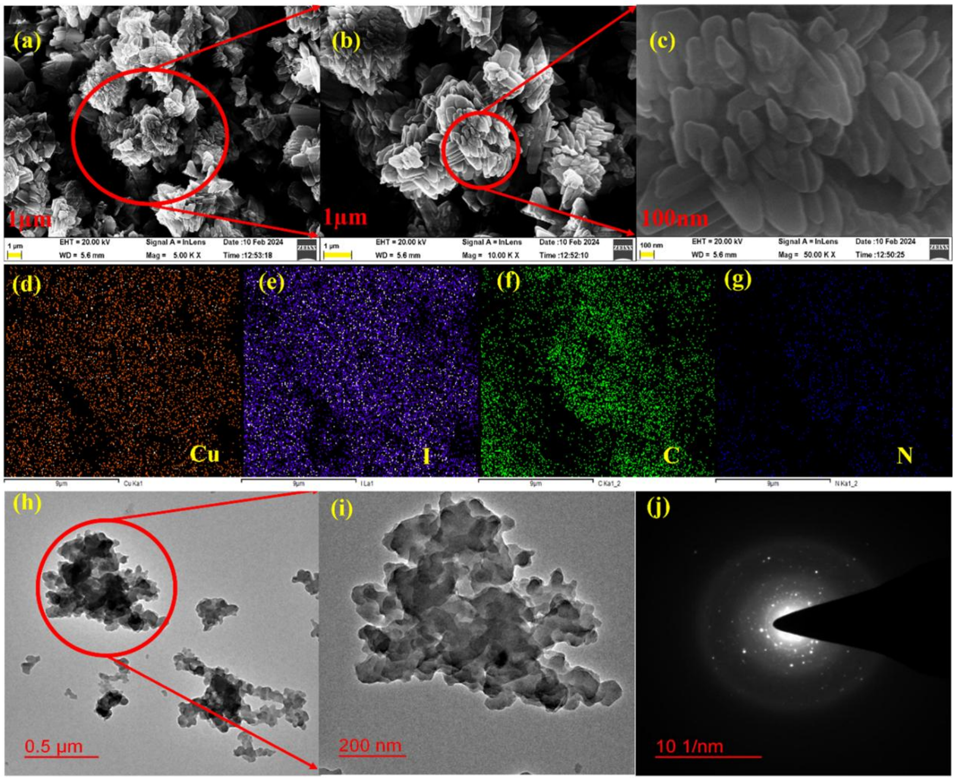

Fig. 3.10: (a-c) FE-SEM images of **Cu-MOF** (d-g) Elemental mapping of elements present in **Cu-MOF** (h-i) TEM images of **Cu-MOF** (j) SAED patterns from TEM.

The optical band gap of **Cu-MOF** was measured from ultraviolet-visible diffuse reflectance spectroscopy (UV-Vis DRS) using the Tauc plot function (F**ig. 3.12**). Band gap (E_g) of 2.04 eV, suggesting the semiconducting nature of **Cu-MOF**. Further, the electrical conductivity of the pressed pellet of **Cu-MOF** was measured using a Keithley 6517B electrometer across a voltage range of -10V to +10V. The electrical conductivity was found to be 3.3×10^{-7} S cm^{-1}, confirming the semiconductor characteristics of **Cu-MOF** (F**ig. 3.13**).

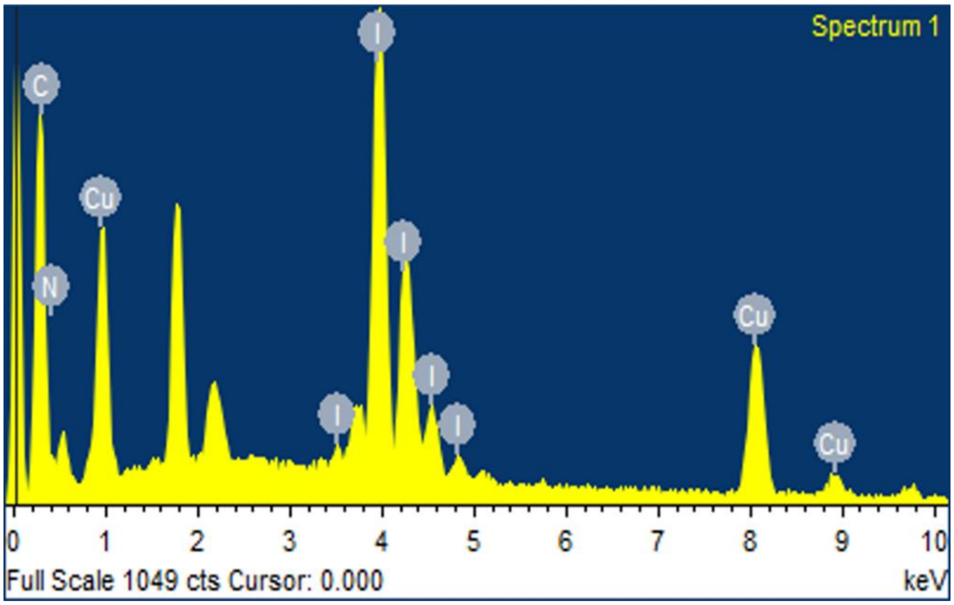

Fig. 3.11: Energy Dispersive X-ray of **Cu-MOF**

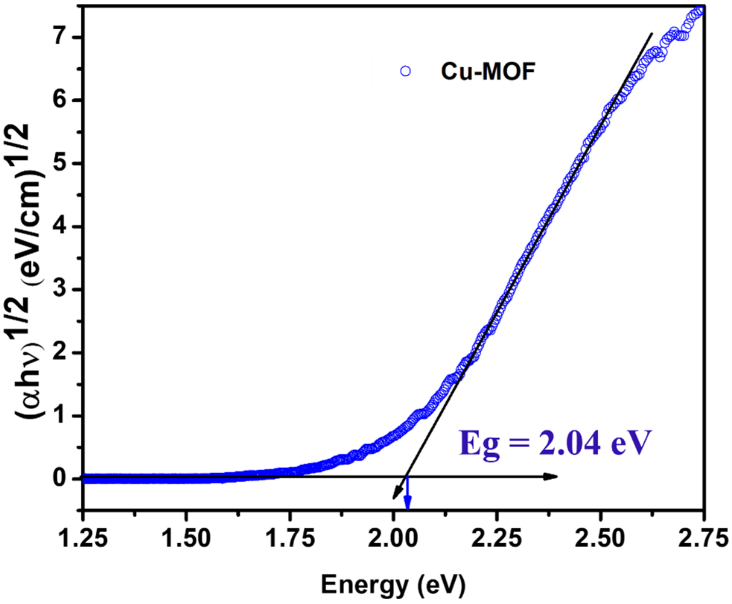

Fig. 3.12: Tauc-Plot of **Cu-MOF**

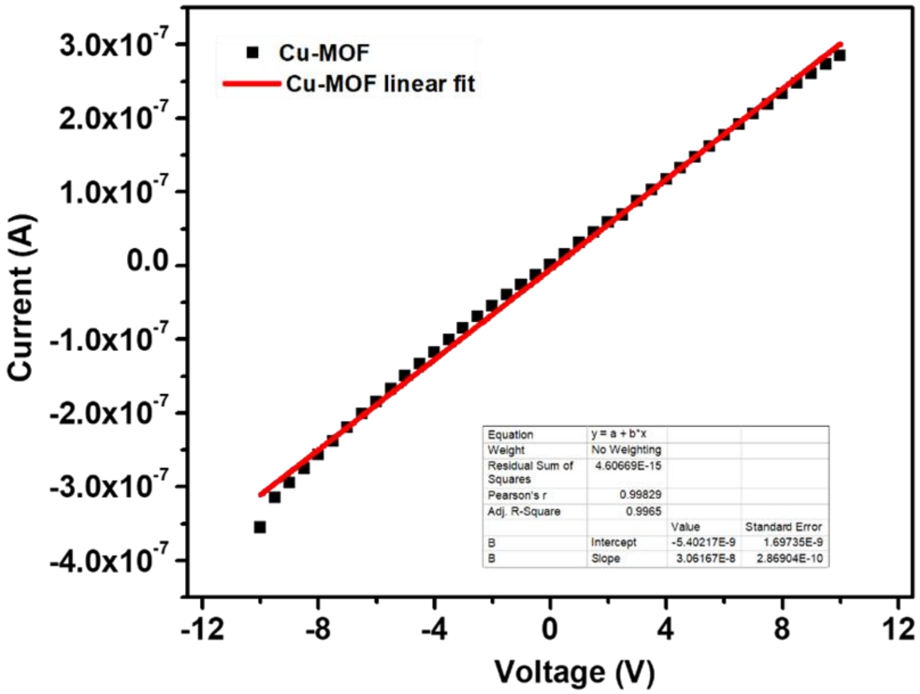

Equation	y = a + b*x		
Weight	No Weighting		
Residual Sum of Squares	4.60669E-15		
Pearson's r	0.99829		
Adj. R-Square	0.9965		
		Value	Standard Error
B	Intercept	-5.40217E-9	1.69735E-9
B	Slope	3.06167E-8	2.86904E-10

Fig. 3.13: Electrical Conductivity of **Cu-MOF**

3.4.1. Gas Sensing Measurements:

The 2D structure with accessible voids, favorable nanostructure morphology with mesoporous nature of the material and semiconducting behavior of **Cu-MOF** prompted us to explore its chemiresistive gas sensing behavior. **Cu-MOF** was mixed in ethanol, drop-casted onto interdigitated electrodes (IDEs, 1.5 × 1 cm) and then dried in the oven for 12 hours. This sensing device was kept inside the sensing chamber to perform the sensing experiment at 27 °C.

Initially, the responses of the **Cu-MOF** sensor toward different reducing and oxidizing gases were investigated (F**ig. 3.14a**). The **Cu-MOF** sensor shows response values of -80%, 630%, -48%, 220%, 110%, 60%, -64% and -49% to interfering gases such as H_2S (100 ppm), NO_2 (100 ppm), MeOH (100 ppm), SO_2 (100 ppm), CO_2 (200 ppm), CH_4 (500 ppm), NH_3 (100 ppm) and CO (200 ppm) respectively. The selectivity factors of the **Cu-MOF** sensor for 100 ppm of NO_2 are calculated to be SNO_2/SH_2S =

7.8, $SNO_2/SMeOH$ = 13.1, SNO_2/SSO_2 = 2.9, SNO_2/SCO_2 = 5.7, SNO_2/SCH_4 = 10.5, SNO_2/SNH_3 = 9.49 and SNO_2/SCO = 12.8 representing a significantly high selectivity toward NO_2 compared to other oxidizing and reducing gases. Afterward, the dynamic sensing performance of the **Cu-MOF** sensor at different concentrations of NO_2 was investigated at 27 °C (F**ig. 3.14b**). As the concentration of NO_2 decreases from 100 ppm to 100 ppb, the response value of **Cu-MOF** sensors also decreases from 630 to 98%. Most importantly, the **Cu-MOF** sensor exhibited a quick response/recovery time of only 11.6/13 seconds and 9.1/10.8 seconds at 10 ppm and 100 ppm NO_2 concentration, respectively (F**ig. 3.14c**). These transient times are the quickest among the MOF-based NO_2 sensors (F**ig. 3.16a** and **Table 3.3**). Furthermore, the LOD and LOQ values of the **Cu-MOF** sensor were found to be 3.5 and 11.7 ppb, respectively, highlighting its excellent sensitivity (F**ig. 3.14d**). The repeatability of the sensor was also studied up to 11 cycles, and complete consistency was observed with no significant drop in performance (F**ig. 3.14e**). To evaluate the quality and selectivity of the devices toward NO_2 under varying relative humidity (RH) conditions, we measured the response of four different devices A, B, C, and D, prepared similarly. The response was recorded at room temperature with RH levels of 36%, 51%, 71%, 84%, and 98.3% (F**ig. 3.14f**).

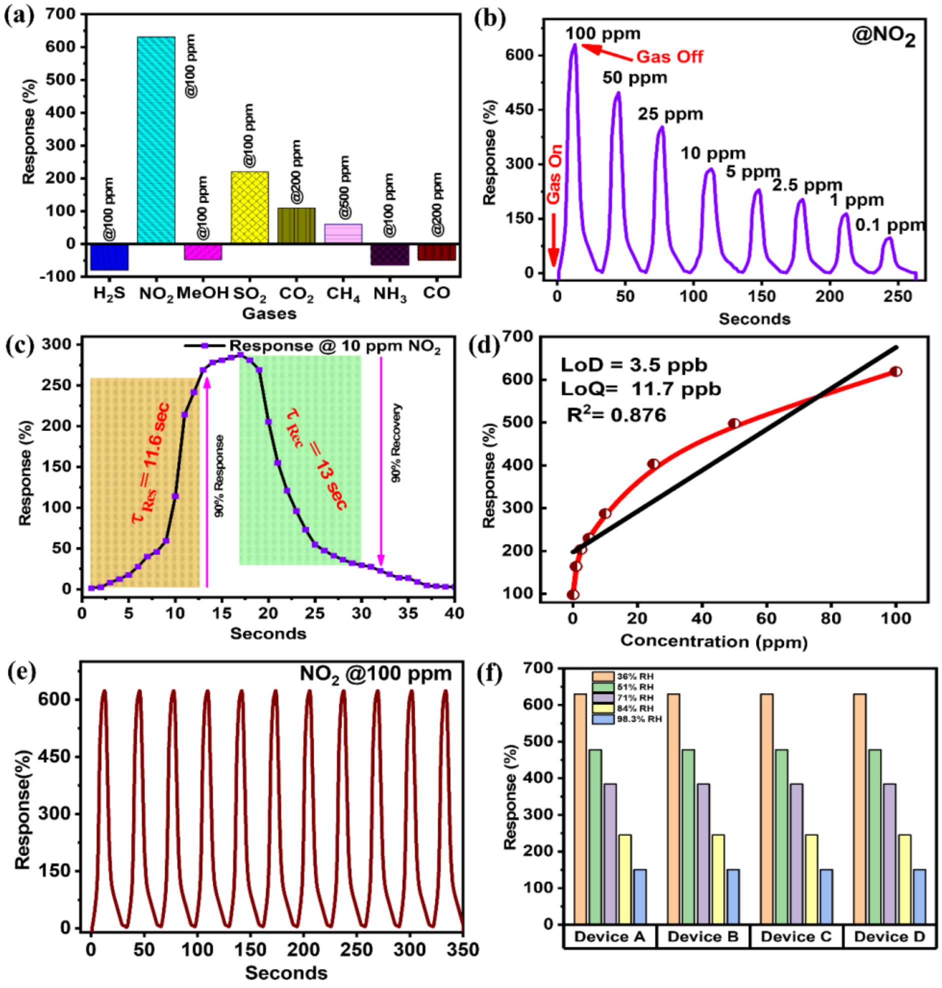

Fig. 3.14: (a) Sensor selectivity analysis for the **Cu-MOF** sensor with interfering gases, (b) **Cu-MOF** sensor response for various NO$_2$ concentrations at room temperature, (c) Transient profile of the **Cu-MOF** (d) LOD and LOQ of **Cu-MOF** (e) Repeatability of the **Cu-MOF** sensor performance for six consecutive (f) Changes in response with increasing humidity and reproducibility.

All four devices showed minimal variation in response, with only a small deviation in performance. However, as RH increased from 36% to 98%, the response of the **Cu-MOF** sensor gradually decreased from 630% to 151%. Despite this, the sensor maintained a significant response, demonstrating its robustness. The decline in response can be attributed to the reduced availability of active sites for analyte interaction.

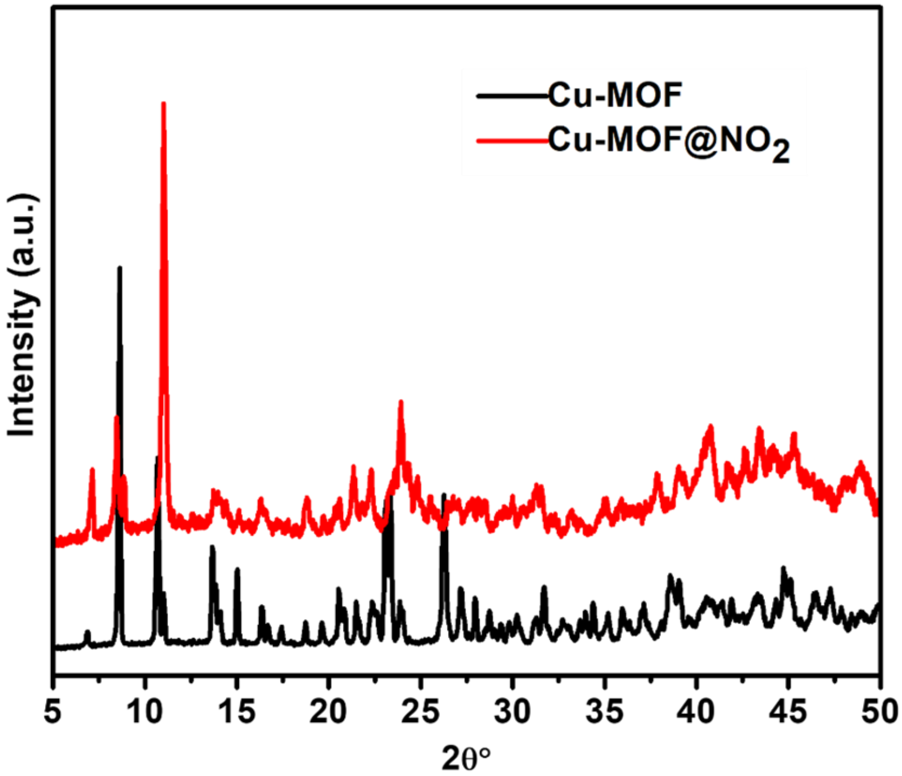

Fig. 3.15: Comparison of PXRD patterns of **Cu-MOF** before and after exposure to NO_2

To understand the sensing mechanism, we first recorded the ex-situ PXRD and ATR-IR of the **Cu-MOF** sensor after exposure to NO_2 gas over the powder sample. After exposure to NO_2, ATR-IR analysis revealed a new absorption peak at 1643 cm^{-1}, which corresponds to molecularly adsorbed NO_2 *[41,42]*. Additionally, a slight shift in the rest of the spectra confirms the interaction between the analyte and the sensing material (F**ig. 3.16b**). The sharp PXRD patterns confirmed the structural integrity of the **Cu-MOF** even after NO_2 exposure (F**ig. 3.15**). Additionally, for deeper insight into the changes in surface chemistry, oxidation states, and material-analyte interaction, XPS analysis was conducted before and after gas exposure (F**ig. 3.17**). Peaks at 952.08 eV and 932.08 eV, indicating the the presence of Cu(I) (Cu2p), 618.88 eV and 630.28 eV correspond to iodine (I3d), while peaks at 400.28 eV and 284.28 eV correspond to nitrogen (N1s) and carbon (C1s), respectively (F**ig. 3.18**). After exposing the material to NO_2, two distinct peaks at 934 and 932 eV, indicating the presence of both Cu^{2+} and Cu^{+} (F**ig. 3.16c-3.16d**) *[12,43–45]*.

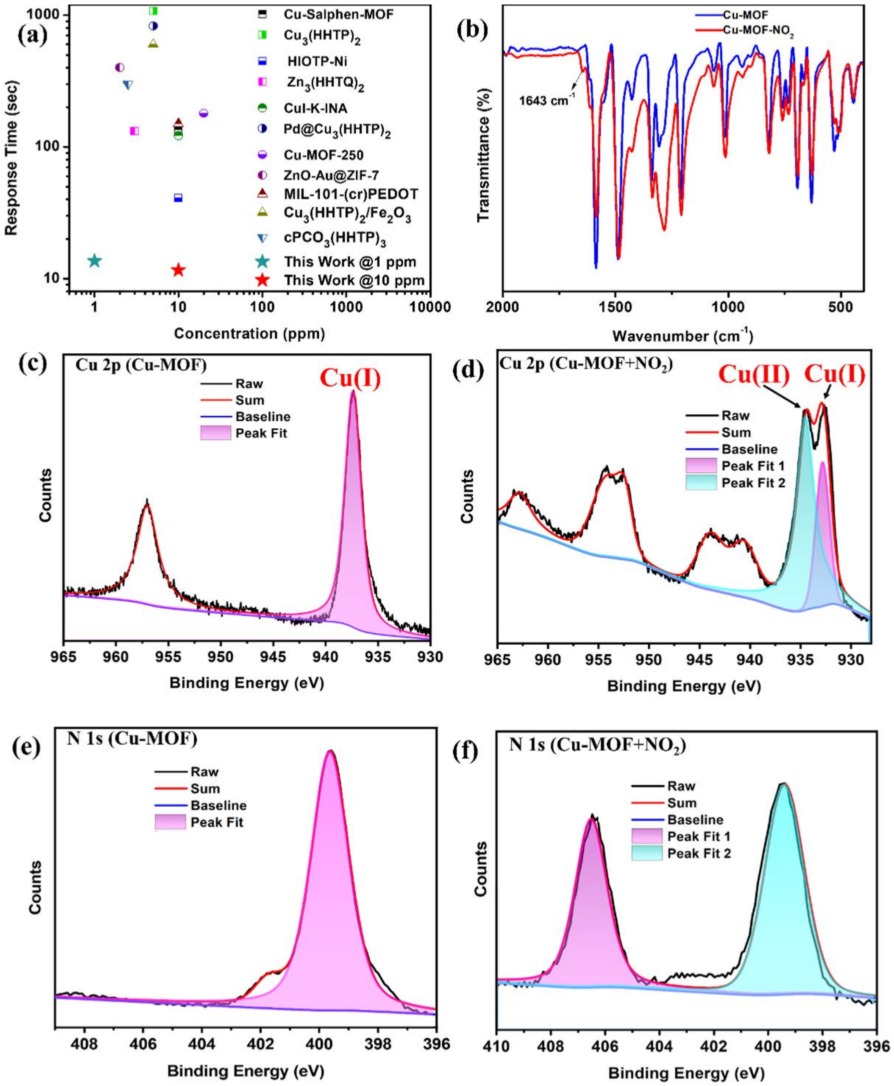

Fig. 3.16: (a) Response time comparison of **Cu-MOF** sensor with the reported MOFs and hybrid MOF-bases NO_2 sensors at room temperature (Table 3.3). (b) IR-spectra of **Cu-MOF** sensor before and after NO_2 exposure. High-resolution XPS spectra of Cu2p (c) before NO_2 exposure (d) after NO_2 exposure; High-resolution XPS spectra of N1s (e) before NO_2 exposure (f) after NO_2 exposure.

Moreover, a new peak at 406.7 eV in the N1s spectrum suggests the presence of metal-coordinated NO_2 molecules(F**ig. 3.16e-3.16f**) *[12,18]*. This observation suggests that NO_2 accepts an electron from Cu(I) and oxidizes it to Cu(II) during the interaction, leading to a change in electrical response.

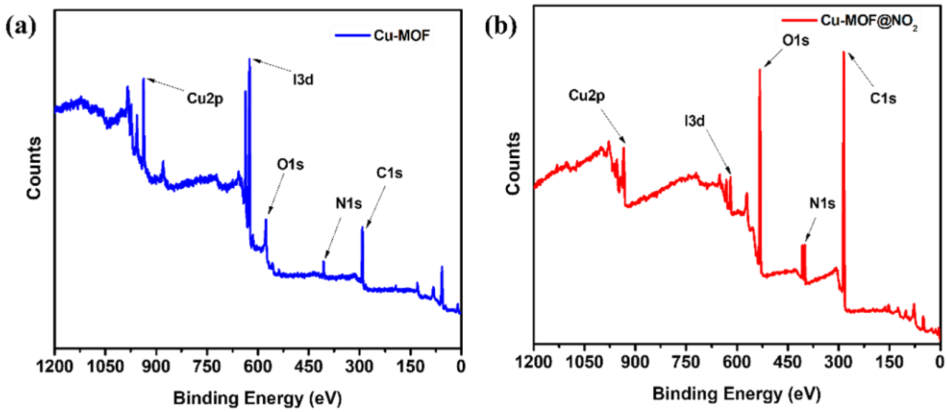

Fig. 3.17: (a) XPS survey before NO_2 exposure (b) XPS survey after NO_2 exposure.

To elucidate the experimental findings, we conducted density functional theory (DFT) calculations to simulate the adsorption of NO_2 on a 2D model of **Cu-MOF**. DFT calculations were performed for structural optimization and electronic property analysis. Structural optimizations were performed using the Linear Combination of Atomic Orbitals (LCAO) basis set as implemented in the QuantumATK software *[46]*. All other calculations such as adsorption energy, electronic properties and charge density were calculated using the plane wave basis Quantum Espresso code suite for enhanced accuracy *[47,48]*. The exchange-correlation interactions were addressed using the revised Perdew-Burke-Ernzerhof (RPBE) functional, which was designed to describe the adsorption process more accurately, within the Generalized Gradient Approximation (GGA) framework *[49,50]*. A 2x2x1 k-point mesh was employed during the structural optimization process and all subsequent calculations utilized a denser 4x4x1 k-point mesh in sampling the Brillouin zone for enhanced accuracy. Long-range interactions were accounted for using the Grimme-D3 dispersion correction method *[51,52]*. Mulliken population analysis was calculated using the QuantumATK code suite which provided insights into the system's charge distribution.

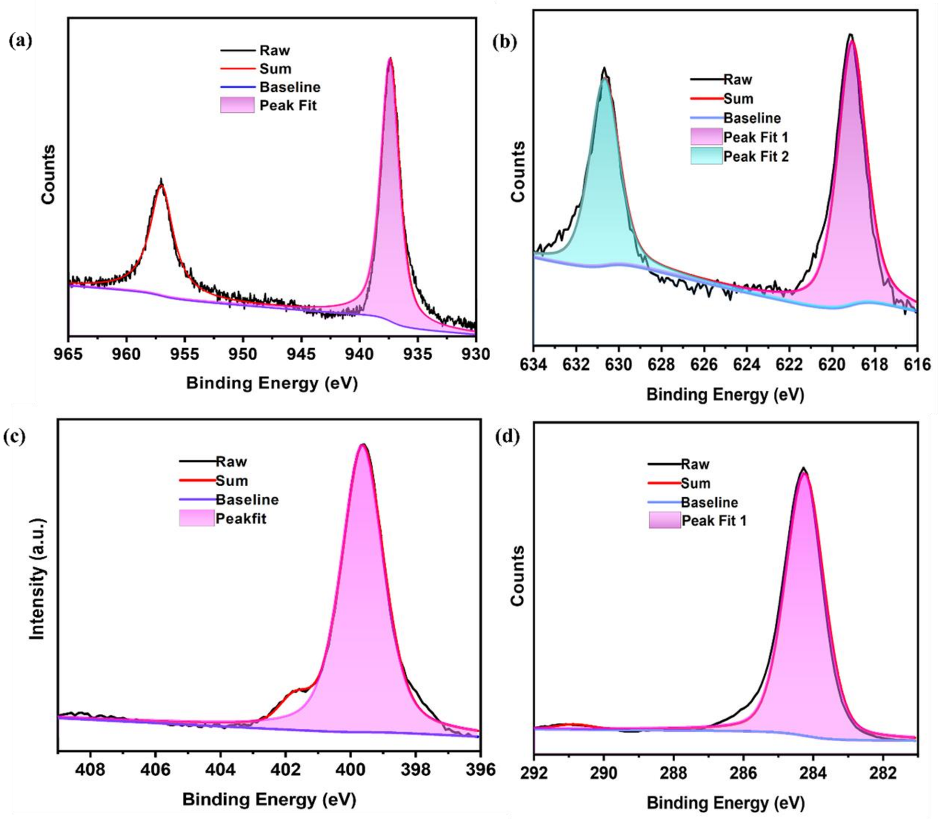

Fig. 3.18: High-resolution XPS spectra of **Cu-MOF** (a) Cu2p (b) I3d (c) N1s (d) C1s.

The experimental findings from XPS suggested the adsorption of NO$_2$ molecules onto the Cu atom. Based on this observation, the optimization was done with initial configurations positioning the NO$_2$ molecule at a distance of 2.00 Å above the cubane tetramer (Cu$_4$I$_4$) cluster. This starting point was chosen to reflect the likely interaction between the analyte and the substrate.

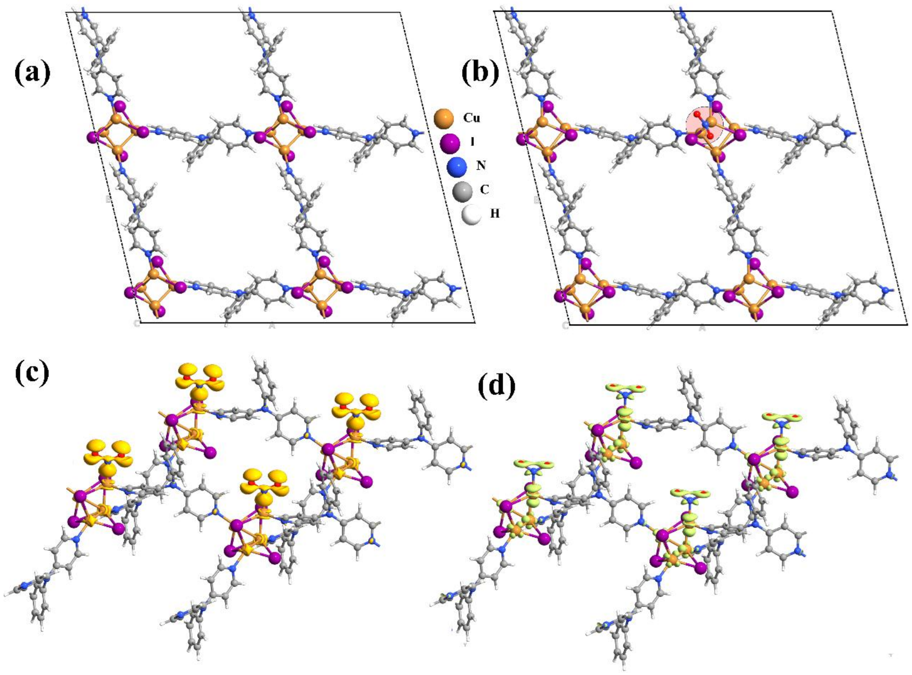

Fig. 3.19: The equilibrium structures of (a) pristine **Cu-MOF** and (b) NO_2-**Cu-MOF**. Electronic charge density difference plot with (c) accumulation region (golden yellow) and (d) depletion region (light green).

The post-optimization analysis elucidated that the NO_2 gas was effectively adsorbed onto a Cu atom of the cubane tetramer complex. Furthermore, enhanced stability was observed when the N atom of the analyte interacts with the Cu atom compared to the O atom of the analyte. The distance between the adsorbed NO_2 molecules and the Cu atom was found to be 2.74 Å. Therefore, our structural optimization studies further support that the NO_2 analyte exhibits a preferential binding affinity towards the Cu sites within the cubane tetramer complex of the **Cu-MOF** framework. The structure of bare as well as most stable NO_2 adsorbed 2D **Cu-MOF** (NO_2-**Cu-MOF**) are depicted in F**ig. 3.19a-3.19b**. The calculated adsorption energy of -0.286 eV for the most stable adsorbed configuration substantiates the energetic feasibility of the adsorption process. To elucidate the charge transfer characteristics, we conducted a comprehensive Mulliken charge population analysis. **Table 3.2** presents the calculated Mulliken charges of atoms within the Cu_4I_4 cubane tetramer and the adsorbate NO_2 molecule. The analysis reveals that the Cu atom directly interacts with the NO_2 gas with a subtle reduction in electron density, while the NO_2 acquires a marginally increased electron population compared to its molecular form. This observation suggests a minor charge transfer from the **Cu-MOF** framework to the NO_2 molecule upon adsorption. To further corroborate these findings, we plotted the charge density difference, comparing the electronic charge distribution before and after NO_2 adsorption, as illustrated in F**ig. 3.19**. In the plot, regions of charge accumulation are depicted in golden yellow (F**ig. 3.19c**), while areas of charge depletion are represented in light green (F**ig. 3.19d**). The plot unambiguously demonstrates electron transfer from the Cu atom to the NO_2 gas, providing compelling evidence for the redistribution of charge occurring during the adsorption process.

We further investigated the electronic structure modifications induced by NO_2 adsorption by calculating the density of states for both the pristine **Cu-MOF** and NO_2-**Cu-MOF** (NO_2 adsorbed **Cu-MOF**), as illustrated in **Fig. 3.20**. Upon NO_2 adsorption, a notable shift in the Fermi level (E_F) towards the valence band states was observed. This downward shift of Fermi level is characteristic of p-type doping in semiconductor materials. Consequently, the adsorption of NO_2 on the **Cu-MOF** framework appears to introduce hole carriers into the system. This observation suggests that the electrical response in the NO_2-**Cu-MOF** would predominantly governed by hole conductivity. Overall, the theoretical study provides valuable insights into the preferential binding mechanism of NO_2 on the properties, which corroborates the experimental results.

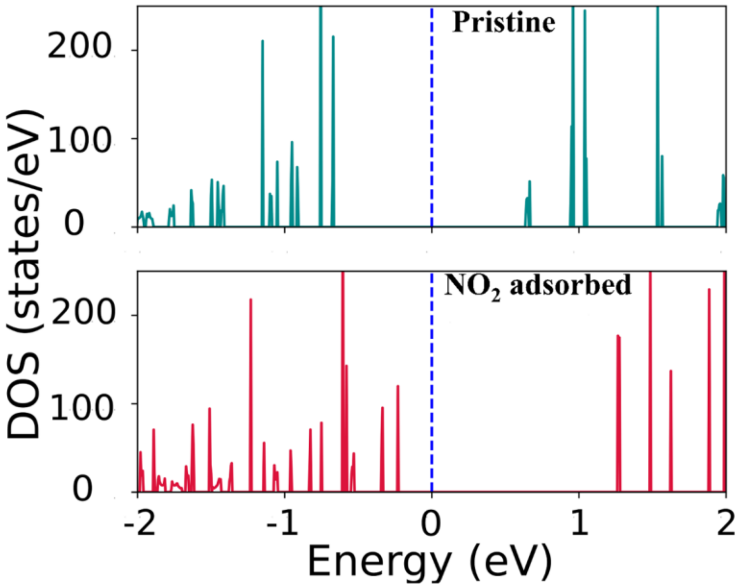

Fig. 3.20: DOS of prinstine and adsorbed NO_2 on **Cu-MOF**

Table 3.2. The calculated Mulliken charges (in e) before and after adsorption on NO_2 molecule and Cu-I complex of **Cu-MOF**

	Atom	Before adsorption	After Adsorption
Cu-MOF	Cu1	18.744	18.582
	Cu2	18.750	18.682
	Cu3	18.739	18.694
	Cu4	18.750	18.758
	I1	7.317	7.280
	I2	7.338	7.332
	I3	7.336	7.291
	I4	7.310	7.283
Adsorbate NO_2 molecule	N	4.897	5.002
	O	6.050	6.231
	O	6.053	6.225

Table 3.3. Comparison table for NO_2 gas sensing with MOF-based sensor at room temperature.

Sensing material	**Conc. (ppm)**	**Res /Rec time (s)**	**LOD**	**References**
Cu-Salphen-MOF	10	135/412.2	0.28 ppm	*Angew. Chem. Int. Ed.*, 2023, **62**, e202302645
$Cu_3(HHTP)_2$	1	1080/--	--	*Adv. Sci.*, 2019, **6**, 1900250
HIOTP-Ni	10	101.4/619.2	0.21 ppm	*Angew. Chem.*, 2023, **135**, e202306224
$Zn_3(HHTQ)_2$	3	132/594	0.269 ppm	*Angew. Chem. Int. Ed.*, 2024, **35**, e202408189
CuI-K-INA	10	121.8/312.6	14.12 ppb	*J. Am. Chem. Soc.*, 2023, **145**, 19293–19302
$Cu_3(HHTP)_2$ powder	3	1038/--	1 ppm	*Nat. Commun.*, 2021, **12**, 4294
PCN-222-Cu	0.02	67/261	0.93 ppb	*ACS Sens.*, 2023, **8**, 4353–4363
PCN-222-Ni	0.15	82/159	5.98 ppb	*ACS Sens.*, 2023, **8**, 4353–4363
Cu-MOF	**10**	**11.6/13**	**3.5 ppb**	**This Work**

3.5. Summary:

In this study, we have successfully demonstrated the potential of semiconducting Cu(I) MOF as a chemiresistive gas sensor for NO_2 detection. The **Cu-MOF**, constructed from Cu_4I_4 SBUs and the **L_3** ligand forms a 2D network which was thoroughly characterized by IR, SCXRD, PXRD, FE-SEM, TEM, and XPS. The mesoporous properties and semiconducting behavior of **Cu-MOF** offer distinct advantages for chemiresistive gas sensing. The sensor exhibited excellent performance in detecting NO_2 at room temperature, achieving a LOD of 3.5 ppb and exceptionally fast response and recovery times of less than 15 seconds. This performance surpasses that of many current state-of-the-art NO_2 sensors, making the **Cu-MOF** a strong candidate for practical sensing applications. The sensing mechanism was further investigated through IR, PXRD, XPS, and DFT analyses, suggesting electron transfer from the Cu(I) center to NO_2 during adsorption, resulting in a distinct and measurable change in electrical response. The straightforward synthesis and the outstanding performance of the **Cu-MOF**-based sensor in selective NO_2 detection, highlight its potential for industrial and environmental gas monitoring.

3.6. References

1. Xie, L.S., Skorupskii, G., and Dincă, M. (2020). Electrically Conductive Metal–Organic Frameworks. Chem. Rev. 120, 8536–8580. (DOI: 10.1021/acs.chemrev.9b00766)
2. Sun, L., Campbell, M.G., and Dincă, M. (2016). Electrically Conductive Porous Metal–Organic Frameworks. Angew. Chem. Int. Ed. 55, 3566–3579. https://doi.org/10.1002/anie.201506219.
3. Medina, D.D., Mähringer, A., and Bein, T. (2018). Electroactive Metalorganic Frameworks. Isr. J. Chem. 58, 1089–1101. (DOI: 10.1002/ijch.201800110)

4. Ko, M., Mendecki, L., and Mirica, K.A. (2018). Conductive two-dimensional metal–organic frameworks as multifunctional materials. Chem. Commun. 54, 7873–7891. (DOI: 10.1039/C8CC02871K)
5. Banda, H., Dou, J.-H., Chen, T., Libretto, N.J., Chaudhary, M., Bernard, G.M., Miller, J.T., Michaelis, V.K., and Dincă, M. (2021). High-Capacitance Pseudocapacitors from Li^+ Ion Intercalation in Nonporous, Electrically Conductive 2D Coordination Polymers. J. Am. Chem. Soc. 143, 2285–2292. (DOI: 10.1021/jacs.0c10849)
6. Park, C., Baek, J.W., Shin, E., and Kim, I.-D. (2023). Two-Dimensional Electrically Conductive Metal–Organic Frameworks as Chemiresistive Sensors. ACS Nanosci. Au 2023, 3, 5, 353–374 (DOI: 10.1021/acsnanoscienceau.3c00024)
7. Wang, M., Dong, R., and Feng, X. (2021). Two-dimensional conjugated metal–organic frameworks (2D c-MOFs): chemistry and function for MOFtronics. Chem. Soc. Rev. 50, 2764–2793. (DOI: 10.1039/D0CS01160F)
8. Lu, Y., Samorì, P., and Feng, X. (2024). Rational Construction of Two-Dimensional Conjugated Metal–Organic Frameworks (2D c-MOFs) for Electronics and Beyond. Acc. Chem. Res. 57, 1985–1996. (DOI: 10.1021/acs.accounts.4c00305)
9. Liu, W., Yuan, G., Jiang, S., Shi, Y., and Pang, H (2024). Two-Dimensional (2D) Conductive Metal-Organic Framework Thin Films: The Preparation and Applications in Electrochemistry. Chem. Eur. J. 34, e202402747. https://doi.org/10.1002/chem.202402747.
10. Mishra, S., Singh, M.K., Pandey, D., Rai, D.K., and Raghuvanshi, A. (2024). A two-dimensional semiconducting Cu(i)-MOF for binder and conductive additive-free supercapattery. J. Mater. Chem. A 12, 4534–4543. (DOI: 10.1039/D3TA04708C)

11. Yan, X., Chen, J., Su, X., Zhang, J., Wang, C., Zhang, H., Liu, Y., Wang, L., Xu, G., and Chen, L. (2024). Redox Synergy: Enhancing Gas Sensing Stability in 2D Conjugated Metal–Organic Frameworks via Balancing Metal Node and Ligand Reactivity. Angew. Chem. Int. Ed. 63, e202408189. (DOI: 10.1002/anie.202408189)
12. Chen, P., Su, X., Wang, C., Zhang, G., Zhang, T., Xu, G., and Chen, L. (2023). Two-Dimensional Conjugated Metal-Organic Frameworks with Large Pore Apertures and High Surface Areas for NO_2 Selective Chemiresistive Sensing. Angew. Chem. Int. Ed. 62, e202306224. (DOI: 10.1002/anie.202306224)
13. Jo, Y., Jo, Y.K., Lee, J., Jang, H.W., Hwang, I., and Yoo, D.J. (2023). MOF-Based Chemiresistive Gas Sensors: Toward New Functionalities. Adv. Mater. 35, 2206842. (DOI: 10.1002/adma.202206842)
14. Koo, W.-T., Jang, J.-S., and Kim, I.-D. (2019). Metal-Organic Frameworks for Chemiresistive Sensors. Chem 5, 1938–1963. (DOI: 10.1016/j.chempr.2019.04.013)
15. Sharma, A., Eadi, S.B., Noothalapati, H., Otyepka, M., Lee, H.-D., and Jayaramulu, K. (2024). Porous materials as effective chemiresistive gas sensors. Chem. Soc. Rev. 53, 2530–2577. (DOI: 10.1039/D2CS00761D)
16. Mohan, B., Virender, Gupta, R.K., Pombeiro, A.J.L., Solovev, A.A., and Singh, G (2024). Advancements in Metal-Organic, Enzymatic, and Nanocomposite Platforms for Wireless Sensors of the Next Generation. Adv. Funct. Mater. 34, 2405231. (DOI: 10.1002/adfm.202405231)
17. Campbell, M.G., Sheberla, D., Liu, S.F., Swager, T.M., and Dincă, M. (2015). $Cu_3(hexaiminotriphenylene)_2$: An Electrically Conductive 2D Metal–Organic Framework for Chemiresistive

Sensing. Angew. Chem. Int. Ed. 54, 4349–4352. (DOI: 10.1002/anie.201411854)

18. Wu, Z.-F., Wang, C., Liu, X., Tan, K., Fu, Z., Teat, S.J., Li, Z.-W., Hei, X., Huang, X.-Y., Xu, G., et al. (2023). Confinement of 1D Chain and 2D Layered CuI Modules in K-INA-R Frameworks via Coordination Assembly: Structure Regulation and Semiconductivity Tuning. J. Am. Chem. Soc. 145, 19293–19302. (DOI: 10.1021/jacs.3c05095)

19. Campbell, M.G., Liu, S.F., Swager, T.M., and Dincă, M. (2015). Chemiresistive Sensor Arrays from Conductive 2D Metal–Organic Frameworks. J. Am. Chem. Soc. 137, 13780–13783. (DOI: 10.1021/jacs.5b09600)

20. Pandey, D., Patel, C., Mishra, S., Mukherjee, S., and Raghuvanshi, A. (2024). Semiconducting 2D Copper(I) Framework for Sub-ppb-Level Ammonia Sensing. ACS Appl. Nano Mater. 7, 15833–15840. (DOI: 10.1021/acsanm.4c03199)

21. Mishra, S., Patel, C., Pandey, D., Mukherjee, S., and Raghuvanshi, A. (2024). Semiconducting 2D Copper(I) Iodide Coordination Polymer as a Potential Chemiresistive Sensor for Methanol. Small 20, 2311448. (DOI: 10.1002/smll.202311448)

22. Pandey, D., Mishra, A., Kharabe, L.S., Maurya, S.K., and Raghuvanshi, A. (2024). Semiconducting Copper(I) Iodide 2D-Coordination Polymers for Efficient Sunlight-Driven Photocatalysis in Dye Degradation. Cryst. Growth Des. 24, 6051–6059. (DOI: 10.1021/acs.cgd.4c00699)

23. Pandey, D., Singh, M.K., Mishra, S., Rai, D.K., and Raghuvanshi, A. (2024). A 2D layered semiconducting $(LCu_3I_3)_n$ coordination polymer for energy storage through dual ion intercalation. J. Mater. Chem. A 12, 27355–27363. (DOI: 10.1039/D4TA04301D)

24. Cariati, E., Lucenti, E., Botta, C., Giovanella, U., Marinotto, D., and Righetto, S. (2016). Cu(I) hybrid inorganic–organic materials with intriguing stimuli responsive and optoelectronic properties. Coord. Chem. Rev. 306, 566–614. (DOI: 10.1016/j.ccr.2015.03.004)

25. Troyano, J., Zamora, F., and Delgado, S. (2021). Copper(i)–iodide cluster structures as functional and processable platform materials. Chem. Soc. Rev. 50, 4606–4628. (DOI: 10.1039/D0CS01470B)

26. Raghuvanshi, A., Strohmann, C., Tissot, J., Clément, S., Mehdi, A., Richeter, S., Viau, L., and Knorr, M. (2017). Assembly of Coordination Polymers Using Thioether-Functionalized Octasilsesquioxanes: Occurrence of $(CuX)_n$ Clusters (X=Br and I) within 3D-POSS Networks. Chem. Eur. J. 23, 16479–16483. (DOI: 10.1002/chem.201704911)

27. Stokinger, H.E. (1958). Evaluation of the Hazards of Ozone and Oxides of Nitrogen Factors Modifying Acute Toxicity. J. Air Pollut. Control Assoc. 8, 129–137. (DOI: 10.1080/00966665.1958.10467839)

28. Zhang, J., Liu, X., Neri, G., and Pinna, N. (2016). Nanostructured Materials for Room-Temperature Gas Sensors. Adv. Mater. 28, 795–831. (DOI: 10.1002/adma.201503825)

29. Guidotti, T.L. (1978). The higher oxides of nitrogen: Inhalation toxicology. Environ. Res. 15, 443–472. (DOI: 10.1016/0013-9351(78)90125-1)

30. Ren, C., and Tong, S. (2008). Health effects of ambient air pollution – recent research development and contemporary methodological challenges. Environ. Health 7, 56. (DOI: 10.1186/1476-069X-7-56)

31. Li, Q., Zeng, W., and Li, Y. (2022). Metal oxide gas sensors for detecting NO_2 in industrial exhaust gas: Recent developments. Sens. Actuators B Chem. 359, 131579. (DOI: 10.1016/j.snb.2022.131579)

32. Kosaka, H., Uozumi, M., and Tyuma, I. (1989). The interaction between nitrogen oxides and hemoglobin and endothelium-derived relaxing factor. Free Radic. Biol. Med. 7, 653–658. (DOI: 10.1016/0891-5849(89)90146-9)
33. Timmons, A.J., and Symes, M.D. (2015). Converting between the oxides of nitrogen using metal–ligand coordination complexes. Chem. Soc. Rev. 44, 6708–6722. (DOI: 10.1039/C5CS00269A)
34. Wright, A.M., Sun, C., and Dincă, M. (2021). Thermal Cycling of a MOF-Based NO Disproportionation Catalyst. J. Am. Chem. Soc. 143, 681–686. (DOI: 10.1021/jacs.0c12134)
35. Roh, H., Kim, D., Cho, Y., Jo, Y., Del Alamo, J.A., Kulik, H.J., Dincă, M., and Gumyusenge, A. (2024). Robust Chemiresistive Behavior in Conductive Polymer/MOF Composites. Adv. Mater. 36, 2312382. (DOI: 10.1002/adma.202312382)
36. Pandey, D., Mishra, A., Kharabe, L.S., Maurya, S.K., and Raghuvanshi, A. (2024). Semiconducting Copper(I) Iodide 2D-Coordination Polymers for Efficient Sunlight-Driven Photocatalysis in Dye Degradation. Cryst. Growth Des. 24, 6051–6059. (DOI: 10.1021/acs.cgd.4c00699)
37. Mishra, S., Pandey, D., Mishra, K., Viau, L., and Raghuvanshi, A. (2023). Copper(i) iodide coordination polymers with triazole substituted pyridine ligands: photophysical and electrical conductivity properties. New J. Chem. 47, 19751–19759. (DOI: 10.1039/D3NJ02303F)
38. Sun, D., Yuan, S., Wang, H., Lu, H.-F., Feng, S.-Y., and Sun, D.-F. (2013). Luminescence thermochromism of two entangled copper-iodide networks with a large temperature-dependent emission shift. Chem. Commun. 49, 6152. (DOI: 10.1039/c3cc42741b)
39. Khatua, S., Goswami, S., Biswas, S., Tomar, K., Jena, H.S., and Konar, S. (2015). Stable Multiresponsive Luminescent MOF for

Colorimetric Detection of Small Molecules in Selective and Reversible Manner. Chem. Mater. 27, 5349–5360. (DOI: 10.1021/acs.chemmater.5b01773)

40. Fan, H.-C., Xia, X., Zeng, Y.-B., Wang, Q.-F., Chen, D., Qin, S.-C., Wang, C.-Q., Cao, Q.-E., and Zheng, L.-Y. (2022). Various Dimensional CuI–DPA Coordination Polymers Based on the Same Components for Different Electronic and Photothermal Properties. Small Struct. 3, 2200030. (DOI: 10.1002/sstr.202200030)

41. Schulz, M., Gehl, A., Schlenkrich, J., Schulze, H.A., Zimmermann, S., and Schaate, A. (2018). A Calixarene-Based Metal–Organic Framework for Highly Selective NO_2 Detection. Angew. Chem. Int. Ed. 57, 12961–12965. https://doi.org/10.1002/anie.201805355.

42. Nakamoto, K. (2001). Infrared and R aman Spectra of Inorganic and Coordination Compounds. In Handbook of Vibrational Spectroscopy, J. M. Chalmers and P. R. Griffiths, eds. (Wiley). (DOI: 10.1002/0470027320.s4104)

43. Su, X., Zhong, Z., Yan, X., Zhang, T., Wang, C., Wang, Y.-X., Xu, G., and Chen, L. (2023). Facile Synthesis of Metallosalphen-Based 2D Conductive Metal-Organic Frameworks for NO_2 Sensing: Metal Coordination Induced Planarization. Angew. Chem. Int. Ed. 62, e202302645. (DOI: 10.1002/anie.202302645)

44. Park, C., Koo, W., Chong, S., Shin, H., Kim, Y.H., Cho, H., Jang, J., Kim, D., Lee, J., Park, S., et al. (2021). Confinement of Ultrasmall Bimetallic Nanoparticles in Conductive Metal–Organic Frameworks via Site-Specific Nucleation. Adv. Mater. 33, 2101216. (DOI: 10.1002/adma.202101216)

45. Lim, H., Kwon, H., Kang, H., Jang, J.E., and Kwon, H.-J. (2023). Semiconducting MOFs on ultraviolet laser-induced graphene with a hierarchical pore architecture for NO_2 monitoring. Nat. Commun. 14, 3114. (DOI: 10.1038/s41467-023-38918-3)

46. Smidstrup, S., Markussen, T., Vancraeyveld, P., Wellendorff, J., Schneider, J., Gunst, T., Verstichel, B., Stradi, D., Khomyakov, P.A., Vej-Hansen, U.G., et al. (2020). QuantumATK: an integrated platform of electronic and atomic-scale modelling tools. J. Phys. Condens. Matter 32, 015901. (DOI: 10.1088/1361-648X/ab4007).

47. Giannozzi, P., Baroni, S., Bonini, N., Calandra, M., Car, R., Cavazzoni, C., Ceresoli, D., Chiarotti, G.L., Cococcioni, M., Dabo, I., et al. (2009). QUANTUM ESPRESSO: a modular and open-source software project for quantum simulations of materials. J. Phys. Condens. Matter 21, 395502. (DOI: 10.1088/0953-8984/21/39/395502)

48. Giannozzi, P., Andreussi, O., Brumme, T., Bunau, O., Buongiorno Nardelli, M., Calandra, M., Car, R., Cavazzoni, C., Ceresoli, D., Cococcioni, M., et al. (2017). Advanced capabilities for materials modelling with Quantum ESPRESSO. J. Phys. Condens. Matter 29, 465901. (DOI: 10.1088/1361-648X/aa8f79)

49. Hammer, B., Hansen, L.B., and Nørskov, J.K. (1999). Improved adsorption energetics within density-functional theory using revised Perdew-Burke-Ernzerhof functionals. Phys. Rev. B 59, 7413–7421. (DOI: 10.1103/PhysRevB.59.7413)

50. Perdew, J.P., Burke, K., and Ernzerhof, M. (1996). Generalized Gradient Approximation Made Simple. Phys. Rev. Lett. 77, 3865–3868. (DOI: 10.1103/PhysRevLett.77.3865)

51. Grimme, S., Antony, J., Ehrlich, S., and Krieg, H. (2010). A consistent and accurate ab initio parametrization of density functional dispersion correction (DFT-D) for the 94 elements H-Pu. J. Chem. Phys. 132, 154104. (DOI: 10.1063/1.3382344)

52. Grimme, S., Ehrlich, S., and Goerigk, L. (2011). Effect of the damping function in dispersion corrected density functional theory. J. Comput. Chem. 32, 1456–1465. (DOI: 10.1002/jcc.21759)

Chapter 4

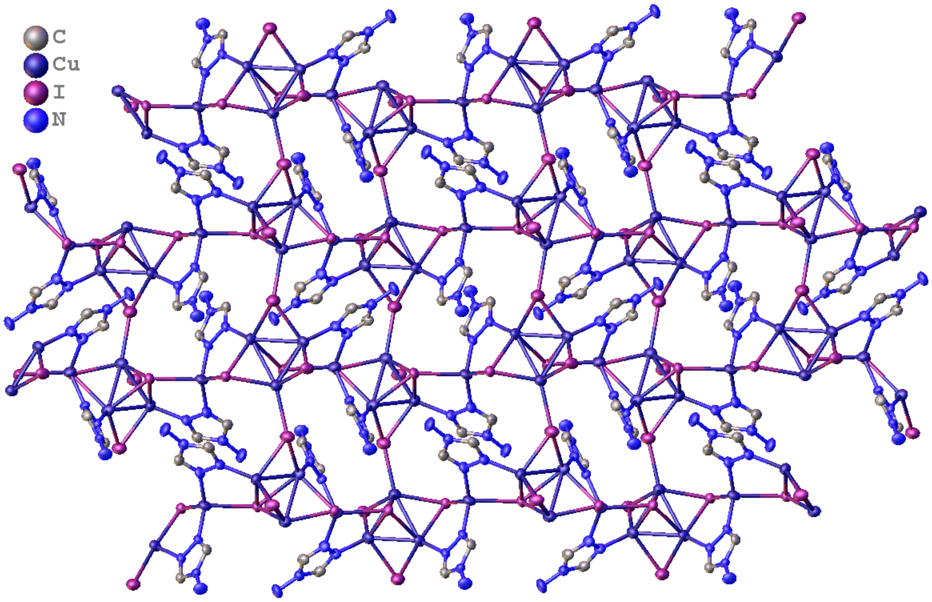

Semiconducting 2D copper(I) framework for ammonia sensing

4.1 Introduction

Conducting 2D coordination polymers (CPs)/metal-organic frameworks are an emerging class of materials because of their unique properties and have found potential applications in energy storage devices, electrocatalysis, gas sensors, etc *[1–6]*. Especially for the development of efficient room temperature chemiresistive gas sensors and volatile organic compound (VOC) sensors these materials present an ideal option. Chemiresistive gas sensing materials have drawn considerable attention due to their simplicity, cost-effectiveness, ease of use, and rapid nature. Copper(I) iodide CPs have gained significant interest because of their unique structural and photophysical properties *[7,8]*. Recently, there has been a growing exploration of Cu(I) CP as chemiresistive sensors for various gases and volatile organic compounds because of its high stability and semiconducting nature along with low-cost synthesis *[9–12]*. We have recently reported a Cu(I) CP chemiresistive sensor with excellent methanol sensing capabilities, while Wu *et al.* have designed Cu(I) CPs for NO_2 sensing *[11,12]*. The rapid surge in ammonia (NH_3) concentration, due to its extensive usage in pharmaceuticals, chemical, fertilizer industries and others, has raised serious concerns regarding environmental and human safety, owing to the inherent toxicity, flammability, and corrosiveness of NH_3 *[13–15]*. Three primary sources that contribute to both direct and indirect exposure to NH_3 in the environment are atmospheric deposition, nitrification, and combustion *[16–19]*. Prolonged exposure to NH_3 poses a risk of causing severe life-threatening diseases, while higher concentrations can even result in fatality *[20]*. Additionally, exhaled NH_3 serves as a critical biomarker for kidney and liver diseases *[21]*. Consequently, there is an urgent need for a low-cost, stable, sensitive, selective, and room-temperature gas sensor with rapid and precise NH_3 detection. Among different materials explored for NH_3 sensing, metal oxide-based NH_3 sensors offer high sensitivity and long-term stability *[22]*. However, their poor selectivity and high operating temperature hinder their commercialization potential *[23]*. In recent years, some coordination polymers (CPs)/metal-organic frameworks (MOFs) have also been explored for chemiresistive ammonia sensing. However, these sensors demonstrate moderate sensitivity and selectivity with lower response and higher response time. Some of the recent reports include Mg-MOF[24] (87s), Co-Porphyrin[25] (180s), NDC-Y-fcu-MOF[26] (250s) & $Cu_3(HHTP)_2$[14] (81s) Zn-MOF[27] (60s) etc., which could sense ammonia at lower concentrations at room temperature. Unfortunately, most of these materials exhibit response times in the range of several minutes. Inspired by these findings, we aimed to synthesize Cu(I)-MOF to achieve improved performance with improved response and lower response time.

Herein, we report two CPs of different dimensionalities **CuTz1** (2D) and **CuTz2** (1D), which can be conveniently synthesized using different ratios of CuI and 4-amino-1,2,4-triazole (**L_4**). **CuTz1** and **CuTz2** could easily be converted into each other in the presence of excess CuI and Ligand. Moreover, **CuTz1** was found to be green emissive and interestingly, was able to sense ammonia and show yellow-orange emission in the presence of aqueous ammonia vapor. Intrigued with this result, we have further used the semiconducting property of **CuTz1** to study ammonia-sensing behavior by measuring electrical resistivity. It was found that the chemiresistive sensor designed from **CuTz1** could sense ammonia at room temperature with an excellent response (R_g/R_a) of 21. Lower response and recovery time (29.5/39.5 s) with a detection limit of 73 ppb outperformed the reported MOFs/CPs and metal oxide-based ammonia sensors (**Tables 4.2-4.3**).

4.2. Experimental section

4.2.1. General Information

4.2.1.1. Materials

4-amino-1,2,4-triazole (**L4**) (>99%), bought from Spectrochem (India), CuI (>99%) from Loba Chemie Pvt. Ltd., and used without further purification. Acetonitrile (HPLC grade) and other solvents were bought from Advent Chembio Pvt. Ltd.

4.2.1.2. Characterisation

Rigaku Smart X-ray diffractometer with monochromatic Cu Kα (0.1540 nm) radiation in 2θ range of 5-50 degrees was utilized to check phase purity of the coordination polymer, which is further characterized by single crystal X-Ray using dual source Super Nova CCD, Agilent Technologies (Oxford Diffraction) System using Mo-Kα = 0.71073 at 293 K. The structure solution was done on OLEX software. The Brunauer-Emmett-Teller (BET) surface area and pore size on an Autosorb iQ, Quantachrome instruments by using Asiquin software. The attenuated total reflectance infrared spectroscopy (ATR-IR) was performed on Bruker Alpha II spectrophotometer of the powdered sample in the range of 4000-400 cm^{-1}. Morphological characterisation and its elemental mapping was done using field emission scanning electron microscope (FE-SEM) on JEOL JSM-7400F. The thermogravimetric analysis was performed on Mettler Toledo TGA/DSC 1 star e- system in the temperature range of 30-800 °C.

4.3. Synthesis

4.3.1. Synthesis of CuTz1:

To a solution of **L4** (4-amino-1,2,4-triazole) (9 mg, 0.10 mmol) in acetonitrile (5 mL) was added an acetonitrile solution of CuI (38 mg, 0.20 mmol). After stirring for 2h at room temperature, a white precipitate was obtained which was washed three times with hot acetonitrile. Further white powder was redissolved by heating in acetonitrile. The solution was cooled to room temperature and then kept at room temperature for a few days to get needle-shaped crystals, which were filtered off and air-dried to give **CuTz1** (62 mg, 67% yield). **IR (ATR)**: 3300, 1608, 1528, 1327, 1204, 1068, 952, 852, 609, and 420 cm^{-1}. Anal. Calc. for $C_4H_8Cu_4I_4N_8$ (927.42): C, 5.17; H, 0.87; N, 12.05. Found: C, 5.25; H, 0.91; N, 12.37 %.

4.3.2. Synthesis of CuTz2:

To a solution of **L$_4$** (4-amino-1,2,4-triazole) (20 mg, 0.24 mmol) in acetonitrile (5 mL) was added an acetonitrile solution of CuI (23 mg, 0.12 mmol). After stirring for 2h at room temperature, a white precipitate was obtained which was washed three times with hot acetonitrile. Further white powder was redissolved by heating in acetonitrile. The solution was cooled to room temperature and then kept at room temperature for a few days to get needle-shaped crystals, which were filtered off and air-dried to give **CuTz2** (70 mg, 56% yield). **IR (ATR)**: 3266, 3210, 3162, 3108, 1596, 1527, 1405, 1206, 1072, 1015, 986, 850, 665, and 609 cm^{-1}. Anal. Calc. for $C_4H_8Cu_2I_2N_8$ (547.75): C, 8.75; H, 1.47; N, 20.41. Found: C, 8.84; H, 1.52; N, 20.49 %.

4.4. Results and discussion

Self-assembly reaction between CuI and 4-amino-1,2,4-triazole (**L**) in acetonitrile solvent at room temperature produces two different coordination polymers (CPs): two-dimensional CP **CuTz1**, and one-dimensional CP **CuTz2** (**Scheme 4.1**). The reaction of CuI and **L** in a 2:1 molar ratio yielded $[Cu_4(\mu_2\text{–}I)(\mu_3\text{–}I)_2(\mu_4\text{–}I)(\mu_2\text{–}\mathbf{L_4})_2]_n$ (**CuTz1**), while reaction in 1:2 molar ratio yielded $[Cu_2(\mu_2\text{–}I)_2(\mu_2\text{–}\mathbf{L_4})_2]_n$ (**CuTz2**). These CPs can also be interconverted into one another. When the ligand was added in excess to an acetonitrile solution of **CuTz1** at 70 °C, **CuTz2** was obtained. On the other hand, when CuI is added in excess to an acetonitrile solution of **CuTz2** at 70°C, the formation of **CuTz1** is observed (**Scheme 4.1**). Both CPs exhibit high stability and can be stored at room temperature in an open atmosphere for several months without any noticeable degradation which was confirmed by the powder X-ray diffraction (PXRD) analysis.

4.4.1. Structural analysis

The compounds were dissolved in boiling acetonitrile and left undisturbed for a few days to obtain colorless needle-shaped crystals suitable for single-crystal X-ray diffraction analysis. **CuTz1** crystallizes in monoclinic space group $P2_1/n$ with Z = 4 (**Table 4.1**). The asymmetric unit contains two units of ligand, four Cu atoms, and four iodide atoms. The grown structure suggests the formation of a 2D coordination polymer with Cu_4I_4 secondary building units (SBUs) (**Fig. 4.1**). In addition to frequently observed cubane and staircase arrangements of Cu_4I_4 SBUs, some rarely observed arrangements are flower-basket, fused cubane, open and closed cubane tetramer *[28-31]*.

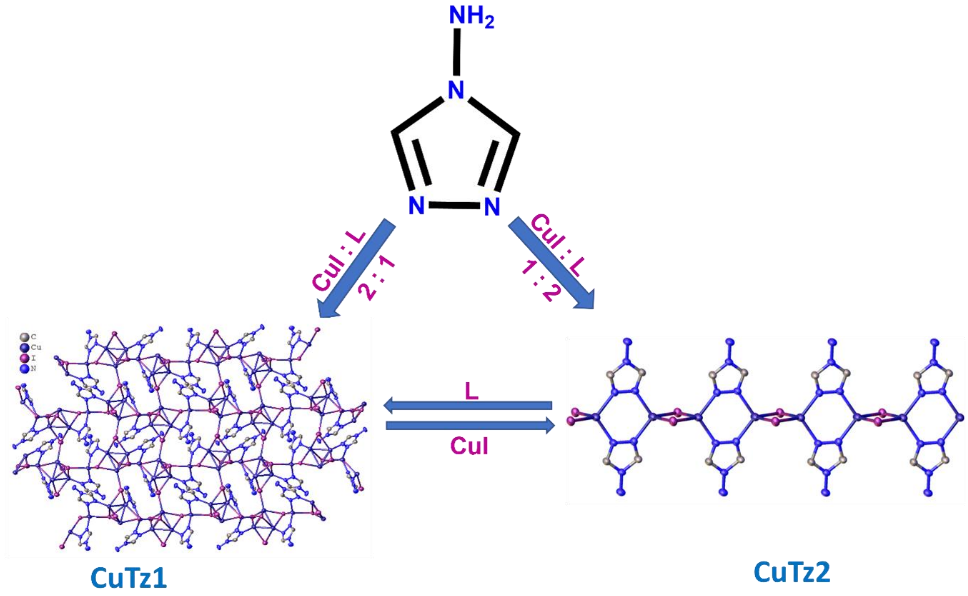

Scheme 4.1: Synthesis of **CuTz1** and **CuTz2**.

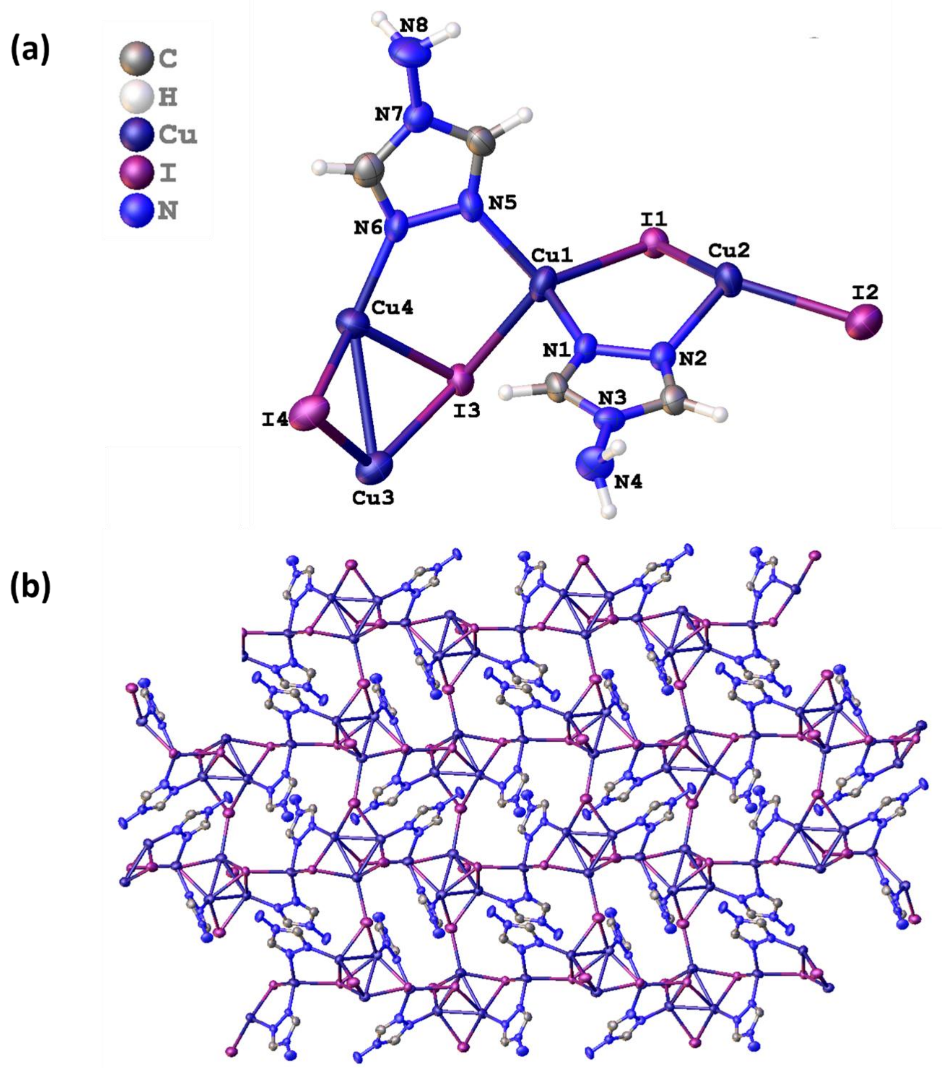

Fig. 4.1: (a) Individual motif of **CuTz1** (b) Polymeric structure of the 2D coordination polymer **CuTz1**.

However, in the case of **CuTz1** a hitherto unknown arrangement of Cu_4I_4 SBU is observed, which could be described as Cu_3I_4 clusters bridged by a Cu atom (**Fig. 4.2**). Three copper in the Cu_3I_4 units are arranged in a triangular fashion with Cu-Cu distances ranging from 2.64 to 2.82 Å. This Cu triangle is bridged by four iodine atoms. Interestingly, three different bridging modes of iodines are present in a single molecule. Out of four iodines, one is doubly bridging (μ_2-I), two are triply bridging (μ_3-I) and one is quarterly bridging (μ_4-I), generating the unique Cu_3I_4 cluster (**Fig. 4.2**).

To the best of our knowledge, **CuTz1** is the second example of CuI cluster having three different bridging modes of iodines in a single System *[32]*. Further, the

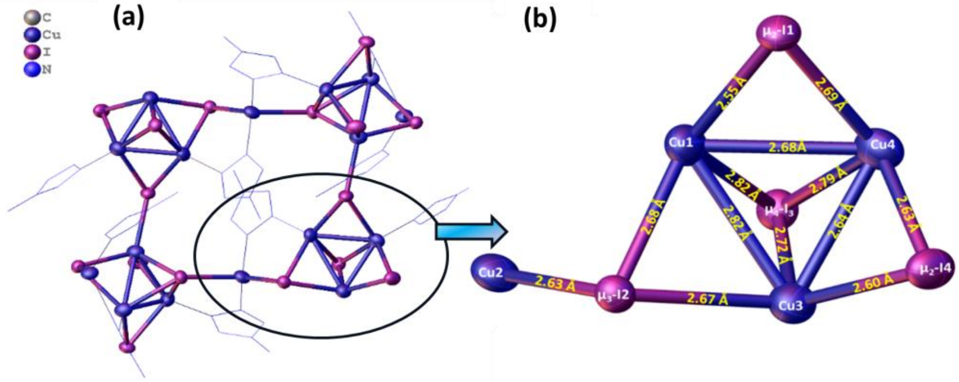

Fig. 4.2: (a) Individual motif of **CuTz1** (b) Cu_4I_4 cluster structure of the 2D coordination polymer **CuTz1**.

nitrogen's of the 4-aminotriazole ligand are bridged with Cu atoms to satisfy the electronic requirement of the Cu atoms. Two copper atoms have the same coordination environment, including one nitrogen atom of the ligand and three iodine atoms. The coordination environment around the third copper atom is entirely distinct, consisting of four iodide atoms while the fourth copper is coordinated to two nitrogen's of different ligands and two iodines. All the copper centers have distorted tetrahedral arrangements with Cu−I and Cu−N distances in the range of 2.56−2.82 Å and 2.09−2.04 Å, respectively (**Fig. 4.2b**). The unit-cell packing diagrams in **CuTz1** reveal the presence of a densely packed structure (**Fig. 4.3**).

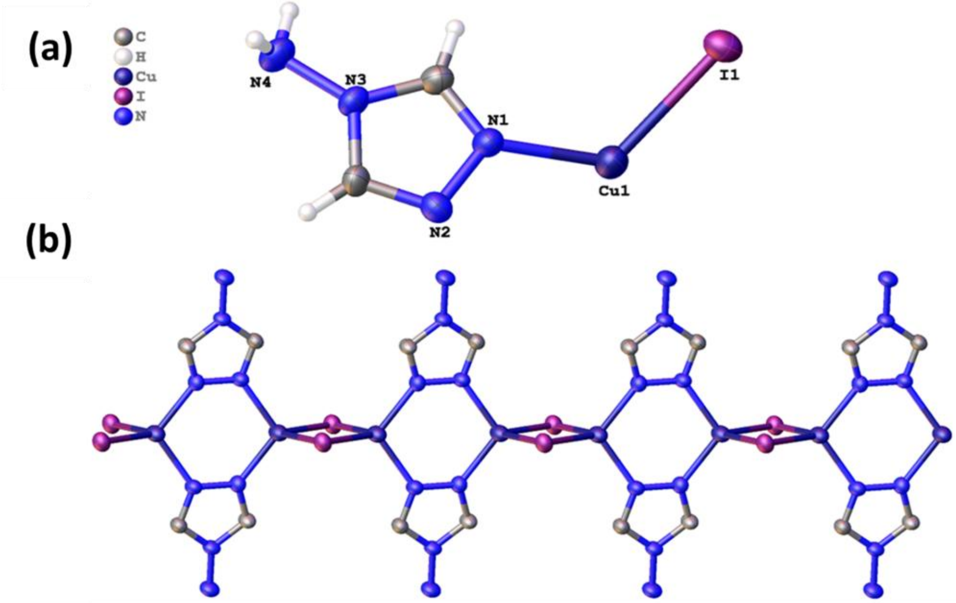

Fig. 4.3: (a) Individual motif of **CuTz2** (b) Polymeric structure of the 1D coordination polymer **CuTz2**.

CuTz2 crystallizes in the triclinic space group $P\bar{1}$(**Table 4.1**). The asymmetric unit consists of one Cu atom, one iodide and one ligand unit. **CuTz2** is built from a one-dimensional Cu_2I_2 rhomboid SBU anchored with amino triazole ligands (**Fig. 4.3**). Cu_2I_2 SBU is the most commonly observed unit in CuI CPs *[33]*. Cu(I) is coordinated with two μ_2–I and two N atoms of different ligand units in a distorted tetrahedral fashion. The distances of Cu−I and Cu−N are in the range of 2.62−2.72 Å and 2.02−2.05 Å, respectively, which is similar to corresponding bond lengths in **CuTz1**. The diagonal Cu−Cu distance in Cu_2I_2 rhomboid chain is 2.95 Å, which is quite longer than the sum of the van der Waals radii (2.80 Å) and in the range of similarly reported Cu_2I_2 rhomboid CPs *[34-36]*.

Table 4.1. Crystallographic parameters of **CuTz1** and **CuTz2**

Compound	**CuTz1**	**CuTz2**
CCDC No.	2283962	2283961
Formula	$C_4H_8Cu_4I_4N_8$	$C_4H_8Cu_2I_2N_8$
Formula Weight	929.94	549.06
Wavelength	0.71073 Å	0.71073 Å
Crystal System	monoclinic	triclinic
Space group	$P2_1/n$	P-1
a/Å	10.8898(15)	6.5596(5)
b/ Å	13.9053(18)	6.5954(3)
c/ Å	11.8940(14)	7.7719(5)
α /°	90	111.635(5)
β/°	104.128(14)	90.391(6)
γ/°	90	93.530(5)
V/ $Å^3$	1746.6(4)	311.67(4)
Z	4	1
ρ_{calcd} (g/cm^3)	3.537	2.925
Temperature/K	293.00	293.00
GOF	1.149	1.033
2θ range for data collection	5.832 to 54.97	6.662 to 58.01
Reflections collected	16305	2906
Independent reflections	3960 [R_{int} =0.0488]	1434 [R_{int} = 0.0472]
Completeness to θ=25.242	99.9	99.6
Final R indices [I>2σ(I)]	R_1 = 0.0625, wR_2 = 0.1777	R_1 = 0.0413, wR_2 = 0.1004
Final R indices [all data]	R_1 = 0.0724, wR_2 = 0.1834	R_1 = 0.0454, wR_2 = 0.1048
Largest diff. peak/hole/ e $Å^{-3}$	1.59/-4.86	1.64/-1.53

Powder X-ray diffraction studies were performed at room temperature to validate the phase purity of **CuTz1** and **CuTz2** (**Fig. 4.4a-4.4b**) We may infer that the bulk material and the crystals are homogeneous since the experimental PXRD patterns correlate well with the simulated data generated from X-ray single-crystal data. The thermal stability of copper-based **CuTz1** and **CuTz2** was assessed, as thermal stability is a crucial factor for the application of materials in different fields. The temperature gradient analysis (TGA) experiments were performed with heating at a rate of 10 °C min^{-1} under an N_2 atmosphere. The thermogravimetric curve **Fig. 4.4c** demonstrates that **CuTz1** and **CuTz2** are stable up to 228 and 211 °C, respectively, and have a similar two-step decomposition curve.

The initial decomposition of 20% in **CuTz1** and 24% in **CuTz2** suggests the loss of ligands. These values are in good agreement with the theoretical values of 18% and 25%, respectively. Subsequently, a second decomposition step is observed at 341°C and 360°C, with a loss of 46% and 45%, respectively for **CuTz1** and **CuTz2**. The remaining residues can be attributed to the formation of copper oxide (CuO), supported by a good agreement in experimental (37% and 29%) and theoretical values (34% and 31%). The higher stability of **CuTz1** is probably due to the formation of a higher nuclearity 2D CP than **CuTz2**.

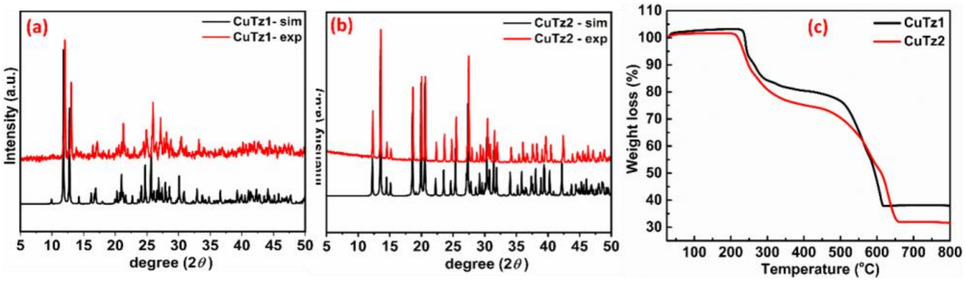

Fig. 4.4: (a) PXRD pattern of **CuTz1 and** (b) **CuTz2 (c)** TGA curve of **CuTz1** and **CuTz2**.

4.4.2. Photoluminiscent Propperties of CuTz1 and CuTz2

We examined the photoluminescent properties of the synthesized CPs in the solid state at room temperature (**Fig. 4.5**). **CuTz1** appeared off-white solid in visible light but emitted green light when exposed to UV light of 365 nm. In contrast, **CuTz2** was found to be weekly emissive with no observable color under UV light by the naked eye. The emission spectra of both **CuTz1** and **CuTz2** displayed three emission peaks with λ_{max} = 372, 396, and 532 nm for **CuTz1** (**Fig. 4.5a**) and 372, 396, and 513 nm for **CuTz2** (**Fig. 4.6**), respectively. Very strong emission bands at λ_{max} = 396 and 532 nm in **CuTz1** are characteristics of a high nuclearity CuI cluster *[37]*. The high-energy band at 396 nm can be assigned to a ^{3}XLCT/^{3}MLCT mixed transition, while the low-energy emission at 532 nm has been attributed to a combination of halide-to-copper charge transfer (XMCT) transition and cluster-centered transition (CC*), which largely depends on the Cu----Cu distances *[8,31,39]*. This is supported by the small average Cu----Cu distance of 2.71 Å, less than twice the van der Waals radii of Cu (2.8 Å). The intense peak at 532 nm in **CuTz1** gives green emission to the complex. Corresponding peaks in **CuTz2** at 396 and 513 nm are very weak. Moreover, the weak emission at 372 nm, in both CPs, can be assigned to intra-ligand (π–π*) charge transfer in the amino triazole ligand *[28,40]*. These observations are consistent with the previously reported high nuclearity CuI clusters *[8]*.

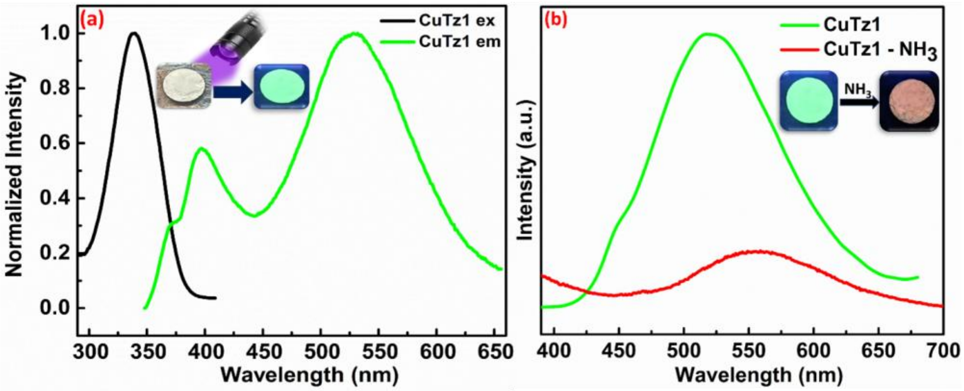

Fig. 4.5: (a) Excitation (338 nm) and emission spectra of **CuTz1** (b) Emission spectra of **CuTz1** with and without ammonia vapor, excited at 338 and 370 nm respectively.

To investigate the vapor-responsive characteristics, the powder form of **CuTz1** was exposed to different volatile compounds such as methanol, ethanol, acetone, ammonia, triethylamine, acid vapors, etc. Remarkably, **CuTz1** shows selectivity towards ammonia vapors only, as illustrated in **Fig. 4.5b**. When aqueous ammonia vapor came into contact with **CuTz1**, the emission color red shifted from its original bright green (532 nm) to yellow-orange (567 nm).

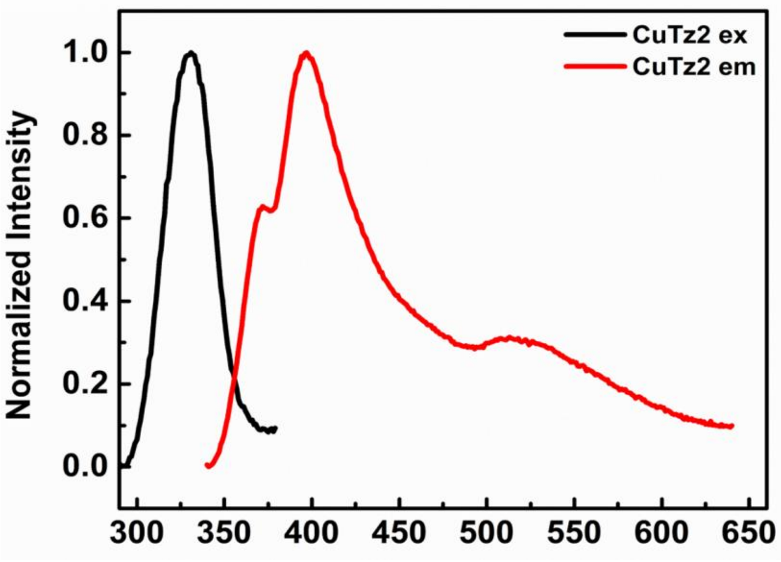

Fig. 4.6: Excitation (330 nm) and emission spectra of **CuTz2**.

This significant change in emission color confirms that **CuTz1** exhibits selective vapochromic behavior in response to the presence of ammonia vapor. In contrast, **CuTz2** did not show any change in response to different gas vapors.

4.4.3. Gas Sensor Fabrication and Measurement:

The electrical conductivity measurements suggest the semiconducting nature of **CuTz1** with an electrical conductivity value of 6.52 × 10^{-7} S cm^{-1} (**Fig. 4.7**). A continuous CuI cluster with small average Cu-Cu (2.71 Å) and Cu-I (2.67 Å) distances leads to better overlapping of orbitals for the propagation of charge carriers *[35,36,41]*. To improve the practical applicability of a gas sensor, a chemiresistive sensor was fabricated from the coordination polymer **CuTz1**. First, it is blended with an ethanol solution. Subsequently, 5μL of this mixture is drop-casted onto the active area of the device using a micropipette. The active area of the device is

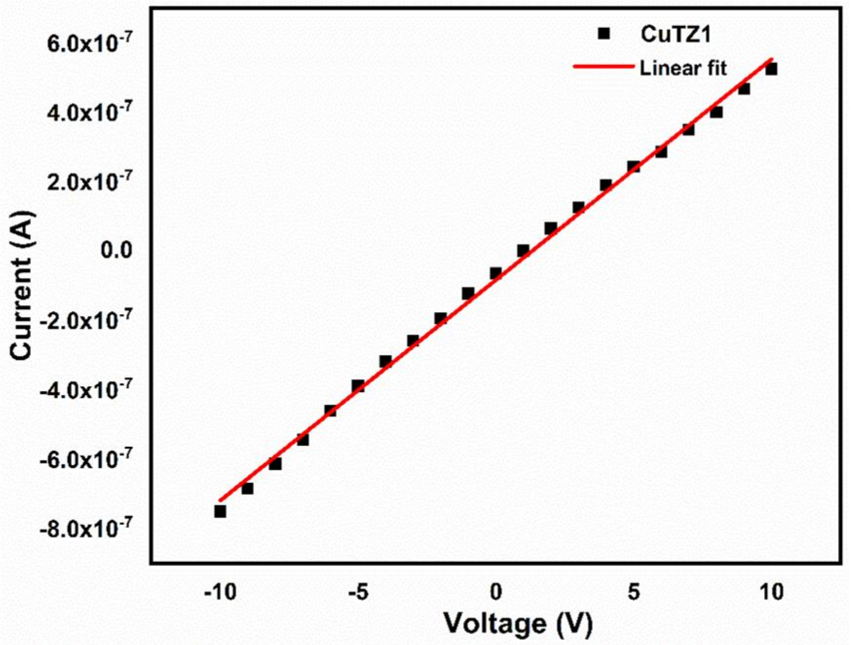

Fig. 4.7: Electrical conductivity of (a) **CuTz1**.

Constructed with Ti/Pt (20/200 nm) interdigitated electrodes (IDEs) on a glass substrate measuring (5.5 mm × 6 mm). The sensing performance of the fabricated **CuTz1** sensor is investigated under a dynamic flow gas sensing setup *[42]*.

The fabricated **CuTz1** sensor response was evaluated across a broad range of NH_3 concentrations, ranging from 500 ppm to 10 ppm, under ambient conditions in a dynamic flow gas sensing setup, as depicted in **Fig. 4.8a**. **CuTz1** sensor exhibits a relatively higher response (R) of 21 for the higher concentration (500 ppm) of NH_3 exposure. As the concentration of NH_3 decreases to 10 ppm, the response of the sensor comes down to 5.9. It is noteworthy to mention here no external stimuli are employed during the recovery of the sensor to its base value. Notably, the **CuTz1** sensor exhibits a substantial response (5.9) even at a 10 ppm NH_3 concentration. This enhanced sensing ability or greater sensing capability owing to the the small charge transfer caused by low concentration of gas molecules *[44,45]*. Moreover, the transient profile of the **CuTz1** sensor towards 500 ppm NH_3 exposure at room temperature is depicted in **Fig. 4.8b**. Response and recovery time values suggest the potential of the developed sensor for real-time deployment. The response (τ_{res}) and recovery time (τ_{rec}) of the **CuTz1** sensor are 29.5 sec and 39.2 sec, respectively. Response and recovery times are less than a minute, which highlights the quick response of the **CuTz1** sensor toward NH_3 sensing. Compared to previously reported MOFs/Metal oxide-based ammonia sensors which have poor response and higher response time (in minutes) (**Tables 4.2-4.3**), **CuTz1** sensors offers a significant advantage for industrial and commercial applications. The selective behavior of the fabricated **CuTz1** sensor is examined by exposing the **CuTz1** sensing material to various toxic gases, including NO_2 (100 ppm), H_2S (100 ppm), SO_2 (100 ppm), and CO_2 (500 ppm), at room temperature, as depicted in **Fig. 4.8c**. The **CuTz1** sensor demonstrates notable selectivity towards NH_3 (15.5) in comparison to other interfering gases such as NO_2 (7), H_2S (5), SO_2 (11), and CO_2 (3.8). The higher sensitivity, selectivity, room temperature operation, and lower transient time of the developed **CuTz1** sensor exhibit wide applicability for various commercial and industrial applications.

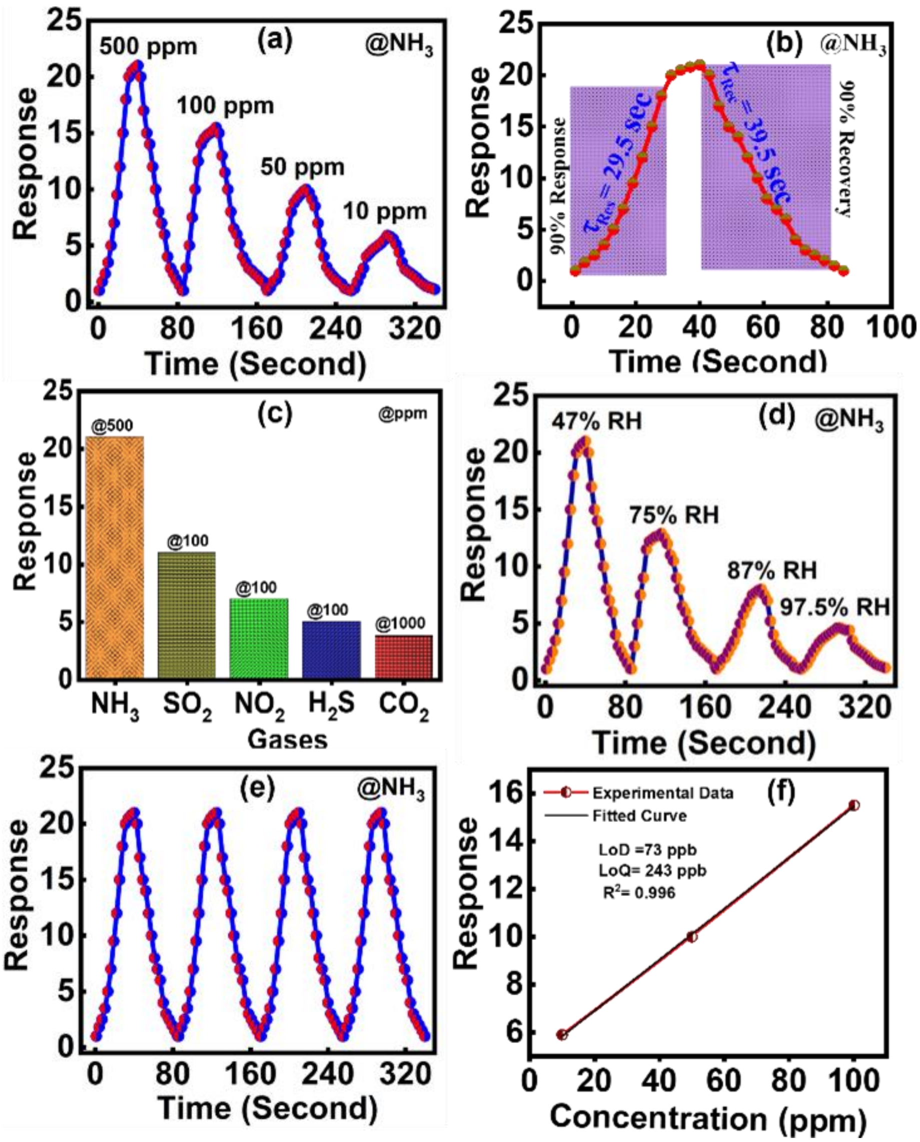

Fig. 4.8: (a) **CuTz1** sensor response for varying NH$_3$ concentrations at room temperature, (b) transient performance of the **CuTz1** sensor, (c) selectivity analysis for the **CuTz1** sensor with interfering gases, (d) Stability of ammonia detection for **CuTz1** upon exposure to 500 ppm of NH$_3$ at variable relative humidity (RH) %, (e) repeatability of the **CuTz1**

Furthermore, the examination of sensor performance in varying relative humidity (RH) is essential humidity serves as a significant limiting factor in the operation of the sensor under environmental conditions, affecting the modulation of active sites on the sensing surface through the adsorption of water molecules. The response of **CuTz1** is assessed under various RH conditions, ranging from 47% to 97.5%, with exposure to 500 ppm of NH_3 (**Fig. 4.8d**). As the RH within the sensing chamber varies from 47% to 97.5%, the sensor response decreases from approximately 21 to about 4.6, respectively. The lower response is probably due to less availability of active sites at higher RH. It is noteworthy to mention that even under extremely humid conditions (RH = 97.5%), the sensor response remains at 4.6, demonstrating the durability of the sensor in harsh humid environmental conditions.

After performing the sensor response with varying concentrations of NH_3, the repeatability of the **CuTz1** sensor performance was examined by exposing 500 ppm of NH_3 for four consecutive cycles as shown in **Fig. 4.8e**. The sensor significantly recovered to its base value in each cycle without any drift, which signifies the highly repetitive nature of the **CuTz1** sensor. The limit of detection (LoD) and limit of quantification (LoQ) for the fabricated **CuTz1** sensor are 73 ppb and 243 ppb as shown in **Fig. 4.8f**. The range of LoD and LoQ is in the sub-ppb level, highlighting the ultra-selective nature of the **CuTz1** sensor towards NH_3 gas at room temperature.

A comparison of all MOF/CP and metal oxide-based chemiresistive ammonia sensors are provided in **Tables 4.2-4.3**, which highlights the superiority of the **CuTz1** sensor in terms of response, transient time along with LoD and LoQ.

The reproducibility of the **CuTz1** sensor is investigated for four fabricated devices (A, B, C and D) of the **CuTz1** sensor keeping the synthesis and fabrication process of **CuTz1** and interdigitated electrode device (IDEs) constant. These four devices (A, B, C and D) are tested in a similar sensing environment as employed in the earlier device sensing performance depicted in **Fig. 4.9a**. Interestingly, no significant deviation was observed

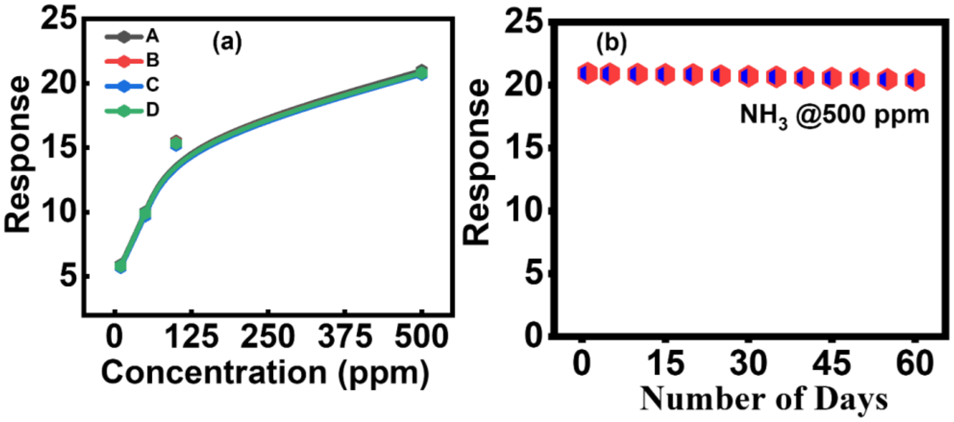

Fig. 4.9: (a) Reproducibility of the **CuTz1** sensor response for varying NH_3 concentrations at room temperature and (d) long-term stability of the **CuTz1** sensor.

in the sensing performance of these four devices. This highlights the excellent reproducibility of the fabricated **CuTz1** sensor. Further, the long-term operation/performance of the fabricated **CuTz1** sensor is investigated. Fabricated **CuTz1** sensor was kept in ambient conditions for 60 day observation period and the sensing performance of the **CuTz1** sensor was measured repeatedly. As shown in **Fig. 4.9b**, no degradation is observed in the sensing performance of the fabricated **CuTz1** sensor during this observation period, which highlights the durability of the fabricated **CuTz1** sensor.

Surface morphology and elemental composition of the synthesized **CuTz1** material is investigated by using scanning electron microscopy (SEM) and elemental mapping depicted in **Fig. 4.10**. **CuTz1** exhibits flake-like morphology with varying lengths in the 1-2 µm range while the thickness of the nano flakes is in the 100-200 nm range. **Fig. 4.10a-4.10b** depicts the magnified image of **CuTz1** confirming flakes-like morphology. As depicted in **Fig. 4.10a**, the flakes exhibit various shapes, such as hexagonal, rectangular, and circular. Furthermore, the magnified image in **Fig. 4.10b** reveals that these flakes are adorned with small nano-particles, enhancing the active surface area of the synthesized **CuTz1** material and subsequently improving its sensing performance at room temperature. The aspect ratio, being less than 1, indicates a high surface-to-volume ratio of the synthesized material. These microstructural parameters contribute to the efficient sensing performance of the synthesized **CuTz1** sensor. Elemental mapping images of Cu, I, N and C elements highlight the uniform distribution and significant presence of these elements in the synthesized **CuTz1** material as depicted in **Fig. 4.10c-4.10f**.

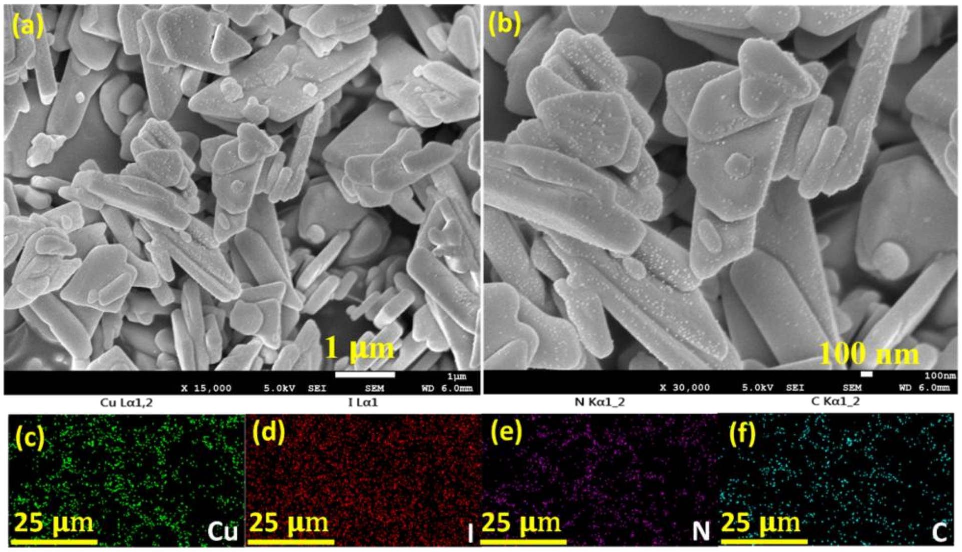

Fig. 4.10: FESEM images of **CuTz1** (a-b), and elemental mapping of **CuTz1** (c) – (f).

Though the mechanism for gas sensing on MOFs and CPs is not clearly understood, it is proposed that ligands as well as metal nodes can be involved in the interaction depending on the nature of the analyte.[45] In case of **CuTz1**, the change in emission, which is particularly due to cluster-centered transitions, clearly suggests the interaction of ammonia with the Cu_4I_4 cluster. In-situ PXRD and FT-IR measurements under ammonia vapor were not possible so the ex-situ FT-IR and PXRD of the **CuTz1** sensor was recorded immediately after the ammonia gas exposure over the powdered sample. However, even after exposure to ammonia vapors, there is no significant change in PXRD data (**Fig. 4.11**), which suggests no change in lattice arrangements on gas exposure. A similar observation was reported by Xu and co-workers *[46]*. Further, ATR-IR spectroscopy was used to show the interactions between the **CuTz1** sensor and the ammonia gas. Nakamoto thoroughly studied the metal interaction with ammonia through IR spectroscopy *[47]*. He has reported that for ammonia, antisymmetric and symmetric stretching, degenerate deformation, symmetric deformation, and rocking vibrations appear in the regions of 3400–3000, 1650–1550, 1370–1000, and 950–590 cm^{-1}, respectively.

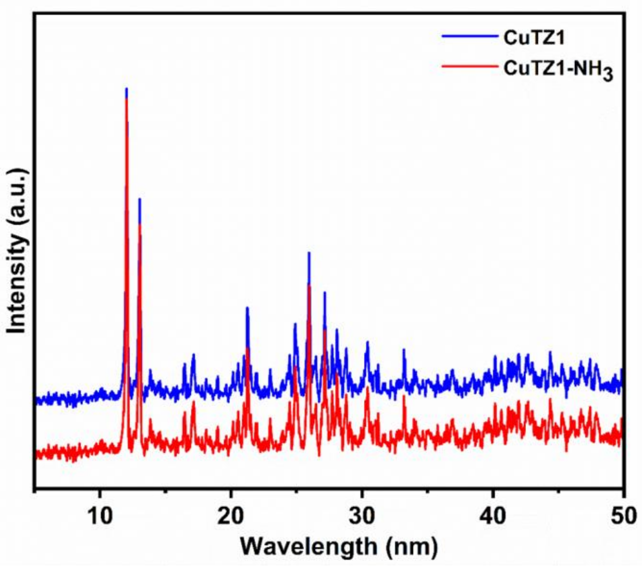

Fig. 4.11: PXRD patterns of **CuTz1** sensor before and after ammonia exposure.

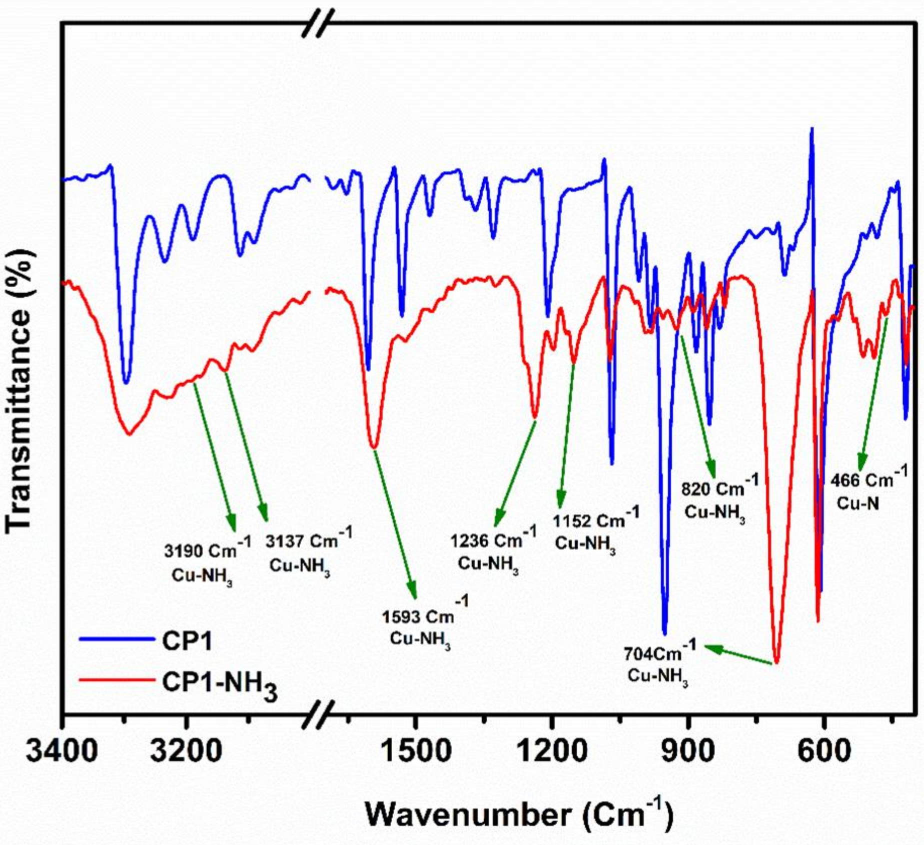

Fig. 4.12: IR spectra of and **CuTz1** sensor, before and after ammonia exposure.

Coordination with metal leads to weakening of the N-H bonds and shifting of NH_3 stretching frequencies to lower energy regions *[47]*. The ex-situ IR of the **CuTz1** sensor was recorded with and without ammonia gas exposure over the powdered sample. The ammonia-exposed sample clearly shows new peaks at 3190, 3137, 1593, 1152, 820, 704, and 466 cm^{-1} (**Fig. 4.12**). The appearance of these peaks in the reported region confirms the interaction of metal with ammonia. Further, a new peak at 466 cm^{-1} confirms the Cu-N bond. Similar changes in the IR bands with the ammonia interactions were also explained by Mircea and Yao *et al [2,16,49]*. These results clearly suggest the interaction of ammonia gas with the Cu(I) cluster (**Fig. 4.13**).

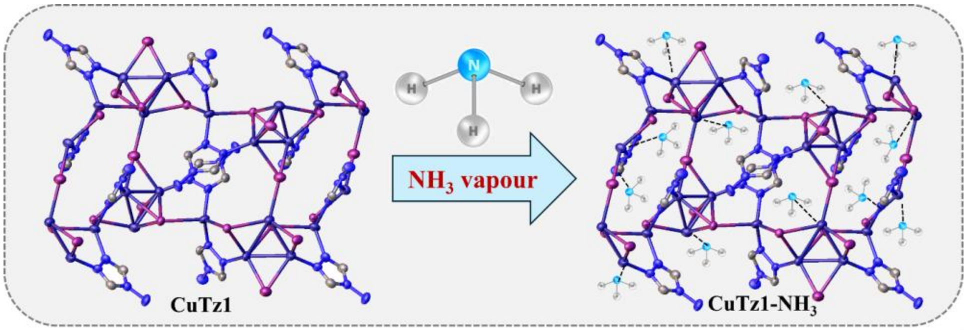

Fig. 4.13: Ammonia gas sensing mechanism with **CuTz1**.

It has been proposed that the increased resistance of the device in the presence of n-type gas vapors (such as NH_3) are due to the interaction of lone pair of analyte with the p-type material *[2,42]*. We propose a similar phenomenon: a p-type semiconductor (**CuTz1** sensor) undergoes n-type (NH_3) doping and during this process, the recombination between the holes in the **CuTz1** and the doped electrons from the ammonia reduces the carrier concentration and increases the sensor's resistance. To confirm this, we conducted UV-Visible diffuse reflectance spectra (DRS) analysis of the **CuTz1** sensor before and after ammonia exposure. The band gap of **CuTz1** was estimated using the Tauc-plot method. As shown in Figure S12, the energy band gap (Eg) values were 2.93 eV for the bare sample and 3.09 eV after ammonia exposure (**Fig. 4.14**). This increase in band gap energy after ammonia exposure suggests a rise in the Fermi energy level, leading to an increase in resistance. Moreover, it is suggested that the electron-rich metal centre plays a pivotal role in enhancing the chemiresistive response of MOFs/CPs *[45]*. The superior response of **CuTz1** compared to other MOFs and CPs may be attributed to the presence of electron-rich Cu(I) clusters.

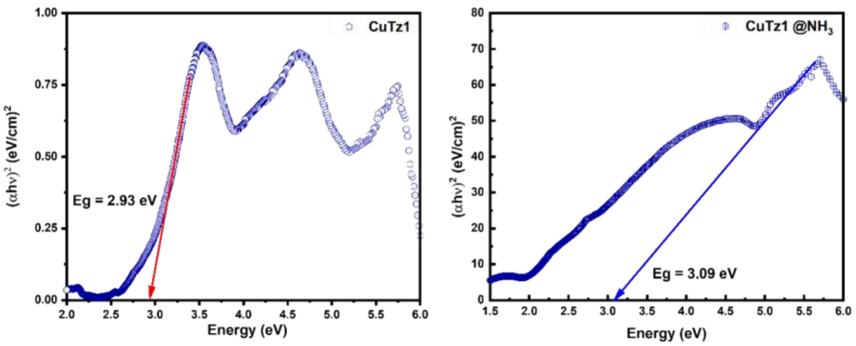

Fig.4.14: The Taut plots of **CuTz1** sensor (a) before and (b) after ammonia exposure.

Table 4.2. Comparison table for ammonia sensing with MOF-based sensor

Sensing material	**Conc. (ppm)**	**Response**	**Res/Rec time (s)**	**LOD**	**Ref.**
NDC-Y-fcu-MOF	100	0.025%	250/NA	92 ppb	*[50]*
$Cu_3(HHTP)_2$	100	129%	81/546	0.5 ppm	*[51]*
$Cu_3(HHTP)_2$THQ	100	800%	99/154	0.025 ppm	*[52]*
$Cu_3(HITP)_2$	10	0.045	NA	0.5 ppm	*[53]*
Co-Porphyrin	20	85%	180/10	1 ppm	*[54]*
Mg-MOF	50	2.4	87/127	1.5 ppm	*[55]*
ZIF-8	100	9	67/54	NA	*[56]*
DPA-Ph-DBPzDCN	100	73%	36/15	2 ppm	*[57]*
Zn-ICP	100	1.5	8.8/54.8	NA	*[58]*
CuTz1	**500**	**21**	**29.5/39.5**	**73 ppb**	**This Work**

Table 4.3. Comparison table for ammonia sensing with Metal oxide-based sensors.

Sensing material	**Conc. (ppm)**	**Response**	**Res/Rec time (s)**	**LOD**	**Ref.**
WS_2/SnO_2	10	850%	2700/3600	0.5 ppm	*[59]*
Cu_2O /MOS_2	100	268%	269/NA	NA	*[60]*
Cu_2O /rGO	200	104%	28/206	NA	*[61]*
α-Fe_2O_3/graphene	10	13.5%	152/648	NA	*[62]*
CuO–rGO	50	6.3%	16/10	12 ppm	*[63]*
SnO_2 Nanosheets	100	106.5%	8/55	0.064 ppb	*[64]*
PPy/ZnO	100	76%	45/NA	1 ppm	*[65]*
CuTz1	**500**	**21**	**29.5/39.5**	**73 ppb**	**This Work**

4.5. Summary:

This study demonstrates the synthesis of two coordination polymers of different dimensionality by varying the concentration of CuI and 4-amino-

1,2,4-triazole. **CuTz1**, characterized by a distinctive Cu_4I_4 SBU (Cu_3I_4 clusters bridging with a Cu), exhibited green luminescence in the solid state, while the 1D chain of **CuTz2** was non-emissive. Further, **CuTz1** was found to have 2D nano-flakes like morphology decorated with small nano-particles. Notably, exposure to aqueous ammonia vapors induced a remarkable change in the solid-state emission color of the **CuTz1** from green to yellow-orange. The change in emission color clearly suggests an interaction of ammonia with Cu_4I_4 cluster, which is also confirmed by the significant shifts in vibrational frequencies by ATR-IR spectroscopy. Further, a chemiresistive sensor developed with **CuTz1** by a convenient drop-casting method shows exceptional sensing capabilities towards ammonia vapors over other gases. The sensor exhibited a remarkable response of 21 at 500 ppm, coupled with rapid response and recovery time (29.5s/39.5s) and very high sensitivity (LoD 73 ppb, LoQ 243 ppb) for ammonia vapors at room temperature. Moreover, the chemiresistive sensor shows long-term stability and high response even in highly humid conditions. The introduction of an n-type gas into a p-type semiconductor leads to the recombination of the hole-electron pair and decreases the charge carriers consequently leading to increased resistance. The readily available reagents, facile synthesis, long-term stability and dual-mode sensing capability combined with excellent sensitivity and selectivity of room temperature chemiresistive sensors make **CuTz1** as one of the prominent ammonia sensors for real-world application. To the best of our knowledge, this work presents the first Cu(I) CP chemiresistive ammonia sensor with superior sensing performance than the reported MOF/CP-based sensors. This could be a significant step towards the development of practical and affordable sensors for a wide range of applications in environmental monitoring, industrial safety and healthcare.

4.6. References

1. Nam, K.W., Park, S.S., dos Reis, R., Dravid, V.P., Kim, H., Mirkin, C.A., and Stoddart, J.F. (2019). Conductive 2D metal-organic framework for high-performance cathodes in aqueous rechargeable zinc batteries. Nat. Commun. 10, 4948. (DOI: 10.1038/s41467-019-12857-4)
2. Wada, K., Sakaushi, K., Sasaki, S., and Nishihara, H. (2018). Multielectron-Transfer-based Rechargeable Energy Storage of Two-Dimensional Coordination Frameworks with Non-Innocent Ligands. Angew. Chem. Int. Ed. 57, 8886–8890. . (DOI: 10.1002/anie.201802521)
3. Pomerantseva, E., Bonaccorso, F., Feng, X., Cui, Y., and Gogotsi, Y. (2019). Energy storage: The future enabled by nanomaterials. Science 366, eaan8285. (DOI: 10.1126/science.aan8285)
4. Wang, H., Zhu, Q.-L., Zou, R., and Xu, Q. (2017). Metal-Organic Frameworks for Energy Applications. Chem 2, 52–80. (DOI: 10.1016/j.chempr.2016.12.002)
5. Feng, D., Lei, T., Lukatskaya, M.R., Park, J., Huang, Z., Lee, M., Shaw, L., Chen, S., Yakovenko, A.A., Kulkarni, A., et al. (2018). Robust and conductive two-dimensional metal−organic frameworks with exceptionally high volumetric and areal capacitance. Nat. Energy 3, 30–36. (DOI: 10.1038/s41560-017-0044-5)
6. Stassen, I., Burtch, N., Talin, A., Falcaro, P., Allendorf, M., and Ameloot, R. (2017). An updated roadmap for the integration of metal–organic frameworks with electronic devices and chemical sensors. Chem. Soc. Rev. 46, 3185–3241. (DOI: 10.1039/C7CS00122C)
7. Artem'ev, A.V., Davydova, M.P., Hei, X., Rakhmanova, M.I., Samsonenko, D.G., Bagryanskaya, I.Yu., Brylev, K.A., Fedin, V.P., Chen, J.-S., Cotlet, M., et al. (2020). Family of Robust and Strongly Luminescent CuI-Based Hybrid Networks Made of Ionic and Dative

Bonds. Chem. Mater. 32, 10708–10718. (DOI: 10.1021/acs.chemmater.0c03984)

8. Cariati, E., Lucenti, E., Botta, C., Giovanella, U., Marinotto, D., and Righetto, S. (2016). Cu(I) hybrid inorganic–organic materials with intriguing stimuli responsive and optoelectronic properties. Coord. Chem. Rev. 306, 566–614. (DOI: 10.1016/j.ccr.2015.03.004)
9. Zhang, Y., Xu, P., Xu, J., Li, H., and Ma, W. (2011). NH_3 Sensing Mechanism Investigation of CuBr: Different Complex Interactions of the Cu^+ Ion with NH_3 and O_2 Molecules. J. Phys. Chem. C 115, 2014–2019. (DOI: 10.1021/jp108732j)
10. Wolpert, B., Leitl, M., Pfitzner, A., and Mirsky, V.M. (2008). Chemosensitive properties of electrically conductive Cu(I) compounds at room temperature. Sens. Actuators B Chem. 134, 839–842. (DOI: 10.1016/j.snb.2008.06.047)
11. Wu, Z.-F., Wang, C., Liu, X., Tan, K., Fu, Z., Teat, S.J., Li, Z.-W., Hei, X., Huang, X.-Y., Xu, G., et al. (2023). Confinement of 1D Chain and 2D Layered CuI Modules in K-INA-R Frameworks via Coordination Assembly: Structure Regulation and Semiconductivity Tuning. J. Am. Chem. Soc. 145, 19293–19302. (DOI: 10.1021/jacs.3c05095)
12. Mishra, S., Patel, C., Pandey, D., Mukherjee, S., and Raghuvanshi, A (2024). Semiconducting 2D Copper(I) Iodide Coordination Polymer as a Potential Chemiresistive Sensor for Methanol. Small 20, 2311448. (DOI: 10.1002/smll.202311448)
13. A. Travlou, N., Singh, K., Rodríguez-Castellón, E., and J. Bandosz, T. (2015). Cu–BTC MOF–graphene-based hybrid materials as low concentration ammonia sensors. J. Mater. Chem. A 3, 11417–11429. (DOI: 10.1039/C5TA01738F)
14. Yao, M.-S., Lv, X.-J., Fu, Z.-H., Li, W.-H., Deng, W.-H., Wu, G.-D., and Xu, G. (2017). Layer-by-Layer Assembled Conductive Metal–Organic Framework Nanofilms for Room-Temperature

Chemiresistive Sensing. Angew. Chem. Int. Ed. 56, 16510–16514. (DOI: 10.1002/anie.201709558)

15. Behera, S.N., Sharma, M., Aneja, V.P., and Balasubramanian, R. (2013). Ammonia in the atmosphere: a review on emission sources, atmospheric chemistry and deposition on terrestrial bodies. Environ. Sci. Pollut. Res. 20, 8092–8131. (DOI: 10.1007/s11356-013-2051-9)
16. Mushtaq, M.A., Kumar, A., Liu, W., Ji, Q., Deng, Y., Yasin, G., Saad, A., Raza, W., Zhao, J., Ajmal, S., et al. (2024). A Metal Coordination Number Determined Catalytic Performance in Manganese Borides for Ambient Electrolysis of Nitrogen to Ammonia. Adv. Mater. 36, 2313086. (DOI: 10.1002/adma.202313086)
17. Zhang, H., Wang, H., Cao, X., Chen, M., Liu, Y., Zhou, Y., Huang, M., Xia, L., Wang, Y., Li, T., et al. (2024). Unveiling Cutting-Edge Developments in Electrocatalytic Nitrate-to-Ammonia Conversion. Adv. Mater. 36, 2312746. (DOI: 10.1002/adma.202312746)
18. Ouyang, L., Liang, J., Luo, Y., Zheng, D., Sun, S., Liu, Q., Hamdy, M.S., Sun, X., and Ying, B. (2023). Recent advances in electrocatalytic ammonia synthesis. Chin. J. Catal. 50, 6–44. (DOI: 10.1016/S1872-2067(23)64464-X)
19. Liang, J., Li, Z., Zhang, L., He, X., Luo, Y., Zheng, D., Wang, Y., Li, T., Yan, H., Ying, B., et al. (2023). Advances in ammonia electrosynthesis from ambient nitrate/nitrite reduction. Chem 9, 1768–1827. (DOI: 10.1016/j.chempr.2023.05.037)
20. Dai, M.-Z., Lin, Y.-L., Lin, H.-C., Zan, H.-W., Chang, K.-T., Meng, H.-F., Liao, J.-W., Tsai, M.-J., and Cheng, H. (2013). Highly Sensitive Ammonia Sensor with Organic Vertical Nanojunctions for Noninvasive Detection of Hepatic Injury. Anal. Chem. 85, 3110–3117. (DOI: 10.1021/ac303100k)

21. Davies, S., Spanel, P., and Smith, D. (1997). Quantitative analysis of ammonia on the breath of patients in end-stage renal failure. Kidney Int. 52, 223–228. (DOI: 10.1038/ki.1997.324)
22. Bai, J., Shen, Y., Zhao, S., Li, A., Kang, Z., Cui, B., Wei, D., Yuan, Z., and Meng, F. (2023). Room-Temperature NH_3 Sensor Based on SnO_2 Quantum Dots Functionalized SnS_2 Nanosheets. Adv. Mater. Technol. 8, 2201671. (DOI: 10.1002/admt.202201671)
23. Barsan, N., Koziej, D., and Weimar, U. (2007). Metal oxide-based gas sensor research: How to? Sens. Actuators B Chem. 121, 18–35. (DOI: 10.1016/j.snb.2006.09.047)
24. Li, Y.-P., Li, S.-N., Jiang, Y.-C., Hu, M.-C., and Zhai, Q.-G. (2018). A semiconductor and fluorescence dual-mode room-temperature ammonia sensor achieved by decorating hydroquinone into a metal–organic framework. Chem. Commun. 54, 9789–9792. (DOI: 10.1039/C8CC05459B)
25. Shah, M.N., Pathipati, S.R., Mehmood, S., Kahn, F.U., Sohail, M., Ullah, B., Yang, Y., and Pan, X. (2021). Stable Cobalt Porphyirn Ometed Type Small Molecule Sensor for the Sensitive and Selective Detection of Ammonia Gas at Room Temperature. Adv. Mater. Technol. 6, 2100147. (DOI: 10.1002/admt.202100147)
26. Assen, A.H., Yassine, O., Shekhah, O., Eddaoudi, M., and Salama, K.N. (2017). MOFs for the Sensitive Detection of Ammonia: Deployment of fcu-MOF Thin Films as Effective Chemical Capacitive Sensors. ACS Sens. 2, 1294–1301. (DOI: 10.1021/acssensors.7b00304)
27. Mohan Reddy, A.J., Katari, N.K., Nagaraju, P., and Manabolu Surya, S. (2020). ZIF-8, Zn(NA) and Zn(INA) MOFs as chemical selective sensors of ammonia, formaldehyde and ethanol gases. Mater. Chem. Phys. 241, 122357. (DOI: 10.1016/j.matchemphys.2019.122357)

28. Zhao, Z.-G., Yu, R.-M., Wu, X.-Y., Zhang, Q.-S., Xie, Y.-M., Wang, F., Weng Ng, S., and Lu, C.-Z. (2009). One-pot synthesis of two new copper(i) coordination polymers : in situ formation of different ligands from 4-aminotriazole. CrystEngComm 11, 2494–2499. (DOI: 10.1039/B821491C)
29. Schlachter, A., Tanner, K., and Harvey, P.D. (2021). Copper halide-chalcogenoether and -chalcogenone networks: Chain and cluster motifs, polymer dimensionality and photophysical properties. Coord. Chem. Rev. 448, 214176. (DOI: 10.1016/j.ccr.2021.214176)
30. Wang, S., Morgan, E.E., Panuganti, S., Mao, L., Vishnoi, P., Wu, G., Liu, Q., Kanatzidis, M.G., Schaller, R.D., and Seshadri, R. (2022). Ligand Control of Structural Diversity in Luminescent Hybrid Copper(I) Iodides. Chem. Mater. 34, 3206–3216. (DOI: 10.1021/acs.chemmater.1c04408)
31. Harvey, P.D., and Knorr, M. (2010). Luminescent Coordination Polymers Built Upon Cu_4X_4 (X=Br,I) Clusters and Mono- and Dithioethers. Macromol. Rapid Commun. 31, 808–826. (DOI: 10.1002/marc.200900893)
32. Troyano, J., Zapata, E., Perles, J., Amo-Ochoa, P., Fernández-Moreira, V., Martínez, J.I., Zamora, F., and Delgado, S. (2019). Multifunctional Copper(I) Coordination Polymers with Aromatic Mono- and Ditopic Thioamides. Inorg. Chem. 58, 3290–3301. (DOI: 10.1021/acs.inorgchem.8b03364)
33. Liu, W., Fang, Y., and Li, J. (2018). Copper Iodide Based Hybrid Phosphors for Energy-Efficient General Lighting Technologies. Adv. Funct. Mater. 28, 1705593. (DOI: 10.1002/adfm.201705593)
34. Lucenti, E., Cariati, E., Previtali, A., Marinotto, D., Forni, A., Bold, V., Kravtsov, V.Ch., Fonari, M.S., Galli, S., and Carlucci, L. (2019). Versatility of Cyclic Triimidazole to Assemble 1D, 2D, and 3D Cu(I)

Halide Coordination Networks. Cryst. Growth Des. 19, 1567–1575. (DOI: 10.1021/acs.cgd.8b01199)

35. Mishra, S., Pandey, D., Mishra, K., Viau, L., and Raghuvanshi, A. (2023). Copper(i) iodide coordination polymers with triazole substituted pyridine ligands: photophysical and electrical conductivity properties. New J. Chem. 47, 19751–19759. (DOI: 10.1039/D3NJ02303F)
36. López, J., Platas, J.G., Rodríguez-Mendoza, U.R., Martínez, J.I., Delgado, S., Lifante-Pedrola, G., Cantelar, E., Guerrero-Lemus, R., Hernández-Rodríguez, C., and Amo-Ochoa, P. (2021). Cu(I)–I-2,4-diaminopyrimidine Coordination Polymers with Optoelectronic Properties as a Proof of Concept for Solar Cells. Inorg. Chem. 60, 1208–1219. (DOI: 10.1021/acs.inorgchem.0c03347)
37. Schlachter, A., and D. Harvey, P. (2021). Properties and applications of copper halide-chalcogenoether and -chalcogenone networks and functional materials. J. Mater. Chem. C 9, 6648–6685. (DOI: 10.1039/D1TC00585E)
38. Raghuvanshi, A., Strohmann, C., Tissot, J.-B., Clément, S., Mehdi, A., Richeter, S., Viau, L., and Knorr, M. (2017). Assembly of Coordination Polymers Using Thioether-Functionalized Octasilsesquioxanes: Occurrence of (CuX)n Clusters (X=Br and I) within 3D-POSS Networks. Chem. – Eur. J. 23, 16479–16483. (DOI: 10.1002/chem.201704911)
39. Troyano, J., Zamora, F., and Delgado, S. (2021). Copper(i)–iodide cluster structures as functional and processable platform materials. Chem. Soc. Rev. 50, 4606–4628. (DOI: 10.1039/D0CS01470B)
40. Yeh, C.-W., Chang, W.-J., Suen, M.-C., Lee, H.-T., Tsai, H.-A., and Tsou, C.-H. (2013). Roles of the anion in the self-assembly of silver(I) complexes containing 4-amino-1,2,4-triazole. Polyhedron 61, 151–160. (DOI: 10.1016/j.poly.2013.05.044)

41. Givaja, G., Amo-Ochoa, P., J. Gómez-García, C., and Zamora, F. (2012). Electrical conductive coordination polymers. Chem. Soc. Rev. 41, 115–147. (DOI: 10.1039/C1CS15092H)
42. Patel, C., Singh, R., Dubey, M., Pandey, S.K., Upadhyay, S.N., Kumar, V., Sriram, S., Than Htay, M., Pakhira, S., Atuchin, V.V., et al. (2022). Large and Uniform Single Crystals of MoS_2 Monolayers for ppb-Level NO_2 Sensing. ACS Appl. Nano Mater. 5, 9415–9426. (DOI: 10.1021/acsanm.2c01701)
43. Patel, C., Chaudhary, S., Verma, V.K., Dubey, M., Sriram, S., and Mukherjee, S. (2023). Photoactivated Pd-Loaded WO_3 for Enhanced H2 S Sensing. IEEE Sens. J. 23, 12552–12558. (DOI: 10.1109/JSEN.2023.3272229)
44. Yuan, H., Li, N., Fan, W., Cai, H., and Zhao, D. (2022). Metal-Organic Framework Based Gas Sensors. Adv. Sci. 9, 2104374. (DOI: 10.1002/advs.202104374)
45. Park, C., Baek, J.W., Shin, E., and Kim, I.-D. (2023). Two-Dimensional Electrically Conductive Metal–Organic Frameworks as Chemiresistive Sensors. ACS Nanosci. Au 3, 353–374. (DOI: 10.1021/acsnanoscienceau.3c00024)
46. Yao, M.-S., Lv, X.-J., Fu, Z.-H., Li, W.-H., Deng, W.-H., Wu, G.-D., and Xu, G. (2017). Innentitelbild: Layer-by-Layer Assembled Conductive Metal–Organic Framework Nanofilms for Room-Temperature Chemiresistive Sensing (Angew. Chem. 52/2017). Angew. Chem. 129, 16638–16638. (DOI: 10.1002/ange.201712049)
47. Nakamoto, K. (2009). Infrared and Raman Spectra of Inorganic and Coordination Compounds, Part B: Applications in Coordination, Organometallic, and Bioinorganic Chemistry (John Wiley & Sons).
48. Yao, M.-S., Zheng, J.-J., Wu, A.-Q., Xu, G., Nagarkar, S.S., Zhang, G., Tsujimoto, M., Sakaki, S., Horike, S., Otake, K., et al. (2020). A Dual-Ligand Porous Coordination Polymer Chemiresistor with Modulated

Conductivity and Porosity. Angew. Chem. Int. Ed. 59, 172–176. (DOI: 10.1002/anie.201909096)

49. Stolz, R.M., Mahdavi-Shakib, A., Frederick, B.G., and Mirica, K.A. (2020). Host–Guest Interactions and Redox Activity in Layered Conductive Metal–Organic Frameworks. Chem. Mater. 32, 7639–7652. (DOI: 10.1021/acs.chemmater.0c01007)
50. Assen, A.H., Yassine, O., Shekhah, O., Eddaoudi, M., and Salama, K.N. (2017). MOFs for the Sensitive Detection of Ammonia: Deployment of fcu-MOF Thin Films as Effective Chemical Capacitive Sensors. ACS Sens. 2, 1294–1301. (DOI: 10.1021/acssensors.7b00304)
51. Yao, M.-S., Lv, X.-J., Fu, Z.-H., Li, W.-H., Deng, W.-H., Wu, G.-D., and Xu, G. (2017). Layer-by-Layer Assembled Conductive Metal–Organic Framework Nanofilms for Room-Temperature Chemiresistive Sensing. Angew. Chem. Int. Ed. 56, 16510–16514. (DOI: 10.1002/anie.201709558)
52. Yao, M.-S., Zheng, J.-J., Wu, A.-Q., Xu, G., Nagarkar, S.S., Zhang, G., Tsujimoto, M., Sakaki, S., Horike, S., Otake, K., et al. (2020). A Dual-Ligand Porous Coordination Polymer Chemiresistor with Modulated Conductivity and Porosity. Angew. Chem. Int. Ed. 59, 172–176. (DOI: 10.1002/anie.201909096)
53. Campbell, M.G., Sheberla, D., Liu, S.F., Swager, T.M., and Dincă, M. (2015). Cu_3(hexaiminotriphenylene)$_2$: An Electrically Conductive 2D Metal–Organic Framework for Chemiresistive Sensing. Angew. Chem. Int. Ed. 54, 4349–4352. (DOI: 10.1002/anie.201411854)
54. Shah, M.N., Pathipati, S.R., Mehmood, S., Kahn, F.U., Sohail, M., Ullah, B., Yang, Y., and Pan, X. (2021). Stable Cobalt Porphyirn Ometed Type Small Molecule Sensor for the Sensitive and Selective Detection of Ammonia Gas at Room Temperature. Adv. Mater. Technol. 6, 2100147. (DOI: 10.1002/admt.202100147)

55. Li, Y.-P., Li, S.-N., Jiang, Y.-C., Hu, M.-C., and Zhai, Q.-G. (2018). A semiconductor and fluorescence dual-mode room-temperature ammonia sensor achieved by decorating hydroquinone into a metal–organic framework. Chem. Commun. 54, 9789–9792. (DOI: 10.1039/C8CC05459B)

56. Mohan Reddy, A.J., Katari, N.K., Nagaraju, P., and Manabolu Surya, S. (2020). ZIF-8, Zn(NA) and Zn(INA) MOFs as chemical selective sensors of ammonia, formaldehyde and ethanol gases. Mater. Chem. Phys. 241, 122357. (DOI: 10.1016/j.matchemphys.2019.122357)

57. He, J., Yan, X., Liu, A., You, R., Liu, F., Li, S., Wang, J., Wang, C., Sun, P., Yan, X., et al. (2019). A rapid-response room-temperature planar type gas sensor based on DPA-Ph-DBPzDCN for the sensitive detection of NH_3. J. Mater. Chem. A 7, 4744–4750. (DOI: 10.1039/C8TA10840D)

58. Zhao, Y., Shao, L., Li, L., Wang, S., Song, G., Gao, Z., Zhang, X., Wang, T., Li, Y., Zhang, L., et al. (2020). Novel Zinc-Based Infinite Coordination Polymer for Highly Selective Ammonia Gas Sensing at Room Temperature. Bull. Chem. Soc. Jpn. 93, 1070–1073. (DOI: 10.1246/bcsj.20200132)

59. Dai, M.-Z., Lin, Y.-L., Lin, H.-C., Zan, H.-W., Chang, K.-T., Meng, H.-F., Liao, J.-W., Tsai, M.-J., and Cheng, H. (2013). Highly Sensitive Ammonia Sensor with Organic Vertical Nanojunctions for Noninvasive Detection of Hepatic Injury. Anal. Chem. 85, 3110–3117. (DOI: 10.1021/ac303100k)

60. Ding, Y., Guo, X., Du, B., Hu, X., Yang, X., He, Y., Zhou, Y., and Zang, Z. (2021). Low-operating temperature ammonia sensor based on Cu_2O nanoparticles decorated with p-type MoS_2 nanosheets. J. Mater. Chem. C 9, 4838–4846. (DOI: 10.1039/D1TC00391G)

61. Meng, H., Yang, W., Ding, K., Feng, L., and Guan, Y. (2014). Cu_2O nanorods modified by reduced graphene oxide for NH_3 sensing at

room temperature. J. Mater. Chem. A 3, 1174–1181. (DOI: 10.1039/C4TA06024E).

62. Haridas, V., Sukhananazerin, A., Mary Sneha, J., Pullithadathil, B., and Narayanan, B. (2020). α-Fe2O3 loaded less-defective graphene sheets as chemiresistive gas sensor for selective sensing of NH_3. Appl. Surf. Sci. 517, 146158. (DOI: 10.1016/j.apsusc.2020.146158)
63. Sivalingam, M.M., Olmos-Asar, J.A., Vinoth, E., Tharmar, T., Shkir, Mohd., Said, Z., and Balasubramanian, K. (2021). Copper Oxide Nanorod/Reduced Graphene Oxide Composites for NH3 Sensing. ACS Appl. Nano Mater. 4, 12977–12985. (DOI: 10.1021/acsanm.1c01831)
64. Verma, M., Bahuguna, G., Singh, S., Kumari, A., Ghosh, D., Haick, H., and Gupta, R. (2024). Porous SnO_2 nanosheets for room temperature ammonia sensing in extreme humidity. Mater. Horiz. 11, 184–195. (DOI: 10.1039/D3MH01078C)
65. Singh, P., Kushwaha, C.S., Singh, V.K., Dubey, G.C., and Shukla, S.Kr. (2021). Chemiresistive sensing of volatile ammonia over zinc oxide encapsulated polypyrrole based nanocomposite. Sens. Actuators B Chem. 342, 130042. (DOI: 10.1016/j.snb.2021.130042)

Chapter 5

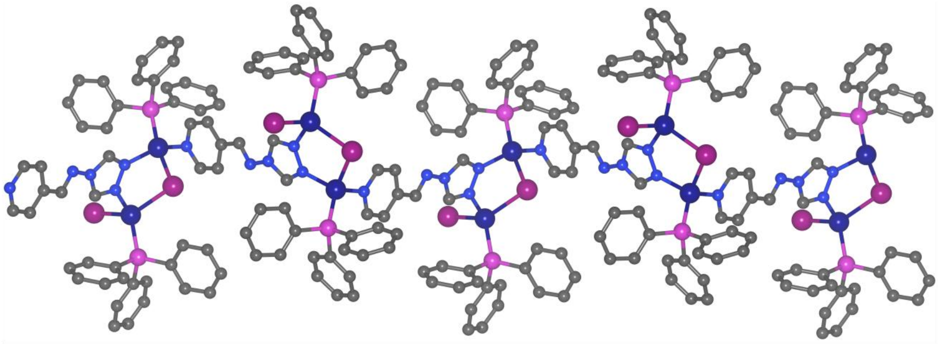

Semiconducting Cu(I) framework for room temperature NO_2 sensing via efficient charge transfer

5.1. Introduction

Due to the advancements in industrialization and urbanization, the increased discharge of harmful gases and volatile organic compounds into our environment causes severe consequences to human health and ecological systems *[1–3]*. In particular, nitrogen dioxide (NO_2) is a major air pollutant which is generated by burning fossil fuels, automobile emissions, etc. Several reports suggest that NO_2 accounts for 2% of all cardiovascular deaths, Parkinson's disease and even accounts for several respiratory diseases *[4–6]*. Therefore, there is a pressing need to develop highly efficient NO_2 sensors that offer rapid response and high selectivity to ensure human safety from this hazardous gas. Chemiresistive gas sensing has revolutionized the field of gas sensors due to its simplicity, low power requirements, precise sensitivity and potential for miniaturization. These sensors operate on the principle of change in electrical resistivity or conductivity upon the interaction of gas molecules with the sensing material *[7–11]*. Traditional chemiresistive sensors based on metal oxides and carbon have been extensively studied. However, high operating temperature to achieve satisfactory sensitivity and selectivity is a major drawback, which increases power consumption and limits their applicability. Additionally, these materials often lack systematic design strategies and methods for tailoring sensor properties *[12–14]*.

Conducting coordination polymers (CPs)/Metal-organic frameworks (MOFs) present a promising class of hybrid materials for next-generation electronic devices *[15–19]*. The vast structural diversity and adjustable properties by altering the molecular building blocks make them particularly attractive for gas sensing applications. It is observed that organic ligands, redox-active metal centers, or both can be involved in the interaction with the analyte *[7,20–23]*. So, the sensing properties can be easily altered by modifying the organic ligands and metal centers. While several MOF and hybrid MOF materials have shown promising results for NO_2 sensing, challenges such as prolonged transient time and irreversible sensing remain for room temperature operation. These issues are primarily due to the strong binding of NO_2 to metal ions, resulting in the formation of stable complexes *[24–30]*.

In recent years, various semiconducting copper(I) CPs have been identified as promising materials in gas sensing applications. Additionally, the high abundance, low cost and lower toxicity of copper further enhance their acceptability *[31,32]*. Li *et al.* have introduced the first semiconducting Cu(I) organic-inorganic framework for chemiresistive NO_2 gas sensing but with a response time of 121 seconds *[32]*. We have recently reported semiconducting CuI frameworks for chemiresistive gas sensing of methanol and ammonia *[33,34]*. In continuation of our work on the exploration of Cu(I) materials towards gas sensing application, herein, we report two 1D Cu(I) CPs using (pyridin-4-yl)-N-(4H-1,2,4-triazol-4-yl)methanimine and triphenylphosphine ligands. Both compounds consist of unique secondary building units and show semiconducting behavior. It is proposed that an electron-rich system leads to efficient charge transfer between the material and the analyte to give a better response *[35,36]*. Triphenylphosphine as a co-ligand along with nitrogen donor ligand is utilized in the synthesis to make the system more electron-rich, aiming to improve charge transfer with the analyte for efficient sensing properties. Moreover, the 1D nature of materials has the advantage of exposed metal centers that provide more interaction sites to the analytes compared to 2D and 3D materials *[37]*. Because of these properties, **CP5** was found to be an efficient chemiresistive gas sensor for NO_2 gas with excellent sensitivity (LOD 1.3ppb), response (1250 % @ 10 ppm), and ultrafast response (15.5 seconds) at room temperature. The observed chemiresistive NO_2 sensing performance is one of the best among MOF/CP-based sensors (**Table 5.2**). The detailed experimental and theoretical studies have been performed to understand the gas sensing mechanism.

5.2. Experimental Section:

5.2.1. General Information

5.2.1.1. Materials

All the synthesis was performed in an oven-dried two-neck round bottom flask kept at 80 °C, a day before use and the reactions were performed using the Schlenk line technique under N_2 atmosphere. Materials required for the synthesis of **CP5** and **CP6**; 4-amino-1,2,4-triazole, 4-pyridine carboxaldehyde, triphenylphosphine, and CuBr (>99%) bought from Spectrochem (India), CuI (>99%) from Loba Chemie Pvt. Ltd., and used without further purification. Solvents like chloroform, methanol and acetonitrile (HPLC grade) were bought from Advent Chembio Pvt. Ltd.

5.2.1.2. Physiochemical Characterisation

The phase purity of the coordination polymer was confirmed using a Rigaku Smart X-ray diffractometer with monochromatic Cu Kα (0.1540 nm) radiation in 2θ range of 5-50 degrees. The attenuated total reflectance infrared spectroscopy (ATR-IR) was performed on Bruker Alpha II spectrophotometer of the powdered sample in the range of 4000-400 cm^{-1}. We have used a field emission scanning electron microscope (FE-SEM) on JEOL JSM-7400F for morphological characterization and its elemental mapping. The thermogravimetric analysis was performed on Mettler Toledo TGA 1-star e-system in the temperature range of 30-600 °C. The resistance of the fabricated sensing device was monitored on the Keithley-2612A source meter by applying a constant voltage of +1 V.

The characterization of ligand is done on a Bruker Avance Neo spectrometer operating at 400 MHz and Bruker-Daltonic-Micro-TOF-QII mass spectrometer for exact mass and isotopic measurement. Dual source Super Nova CCD (Agilent Technologies (Oxford Diffraction) is used for

Single crystal X-Ray data using Mo-Kα= 0.71073 at 293 K. The structure solution was obtained by using OLEX software. The Brunauer-Emmet-Teller (BET) surface area and Barrett-Joyner-Halenda (BJH) pore size distribution were calculated using N_2 gas adsorption-desorption on an Autosorb iQ, Quantachrome Instruments and the data was collected using AsiQwin software.

5.2.1.3. Theory and Computational Details

Vienna *Ab initio* Simulation Package (VASP) has been used to perform all the density functional theory (DFT) and generalized gradient approximation (GGA) functionals Perdew–Burke–Ernzerhof (PBE) calculations *[38–40]*. The weak dispersion effects were taken into account in the present calculations; i.e., semiempirical Grimme's 3rd order dispersion corrections (noted by -D3) have been incorporated in order to consider weak van der Waals (vdW) dispersion interactions in the subject materials contemplated in the present investigation *[41–43]*. The dispersion-corrected DFT and PBE methods have been shown to give quite accurate thermochemistry for both covalently bonded systems and systems dominated by dispersion forces. To study the NO_2 sensing of both the **CP5** and **CP6**, we have employed the PBE-D3 method with spin-polarized calculations. The equilibrium structure and electronic properties, i.e., the electronic band structures and total density of states (DOS) of the **CP5** material, were computed by employing the projected augmented wave (PAW) method with a given pseudopotential *[44]*. To describe the exchange and correlation effects, the Perdew-Burke-Ernzerhof (PBE) method, which is a form of generalized gradient approximation (GGA) functionals, was used in the present investigation *[45–47]*. A plane-wave cutoff energy of 550 eV was included during the calculations, and the convergence energy was set to $1\text{x}10^{-4}$ eV. The pseudopotential basis sets used for carbon (C), hydrogen (H), nitrogen (N), phosphorus (P), copper

(Cu), iodine (I), and oxygen (O) atoms were PAW_PBE C_GW 28Sep2005, PAW_PBE H_GW 21Apr2008, PAW_PBE N_GW 10Apr2007, PAW_PBE P_GW 19Mar2012, PAW_PBE Cu_GW 19 May 2006, PAW_PBE I_GW 12Mar2012, and PAW_PBE O_GW 28Sep2005; which are implemented in VASP suite code. The PBE-D3 calculation utilized a 4x1x1 Monkhorst-Pack k-point grid with Gaussian smearing of 0.05 eV *[48]*. We have calculated the Gibbs free energy of the studied CPs (i.e., **CP1** and **CP2**) and the change in free energy (ΔG) after the NO_2 adsorption on the **CP1** and **CP2** materials. The change of Gibbs free energy (ΔG) has been calculated by employing the following equation.

$$\Delta G = G_{NO_2-CP1} - (G_{CP1} + G_{NO_2}) \qquad (1)$$

$$\Delta G = G_{NO_2-CP2} - (G_{CP2} + G_{NO_2}) \qquad (2)$$

In the above equations (1) and (2),G_{NO_2-CP1} and G_{NO_2-CP2} represents the change of Gibbs free energy of NO_2 adsorbed on both the **CP1** and **CP2**. Whereas G_{CP1}, G_{CP2} and G_{NO_2} represent the free energy of **CP**, **CP2**, and the NO_2 molecule. We have used VESTA software to visualize the equilibrium structure of the studied CPs *[49]*.

The adsorption energy of the NO_2 molecule is calculated using the following equation (3)

$$\Delta \mathrm{E} = E_{[\mathrm{CP} + NO_2]} + \boldsymbol{E}_{[\mathrm{CP}]} + \mathbf{E}_{[NO_2]} \qquad (3)$$

Where $E_{[\mathrm{CP} + NO_2]}$, $\boldsymbol{E}_{[\mathrm{CP}]}$, and $\mathbf{E}_{[NO_2]}$ correspond to the NO_2 adsorbed CP system, CP system (adsorbent), and NO_2 molecule (adsorbate), respectively.

5.2.2. Ligand synthesis

5.2.2.1. Synthesis of ligand (L_5)

In a two-neck round bottom flask, 4-amino-1,2,4-triazole (1.26 g, 15 mmol) was dissolved in 8 ml of toluene. To this solution, 4-pyridine carboxaldehyde (1.61 g, 15 mmol) was added with 1 ml of acetic acid. The reaction mixture was stirred for 6 hours under reflux. Upon completion of the reaction period, an off-white product was formed. The mixture was cooled, and the resulting mixture was then washed with dichloromethane (5 ml) two to three times and once with ethanol (5 ml), then dried in a vacuum. The white solid was recrystallized in ethanol to get the pure product. (Yield: 2.09 g, ~80%). **^{1}H NMR** (500 MHz, DMSO-d_6) δ(ppm) 9.20 (s, 2H), 9.13 (s, 1H), 8.77 (s, 2H), 7.75 (s, 2H). **^{13}C{^{1}H} NMR** (126 MHz, DMSO-d_6) δ(ppm) 156.16, 150.77, 139.19, 121.86.

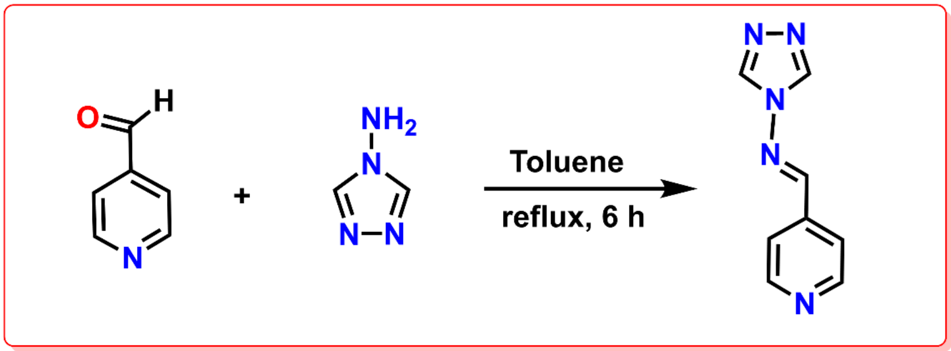

Scheme 5.1: Synthesis of Ligand (**L$_5$**)

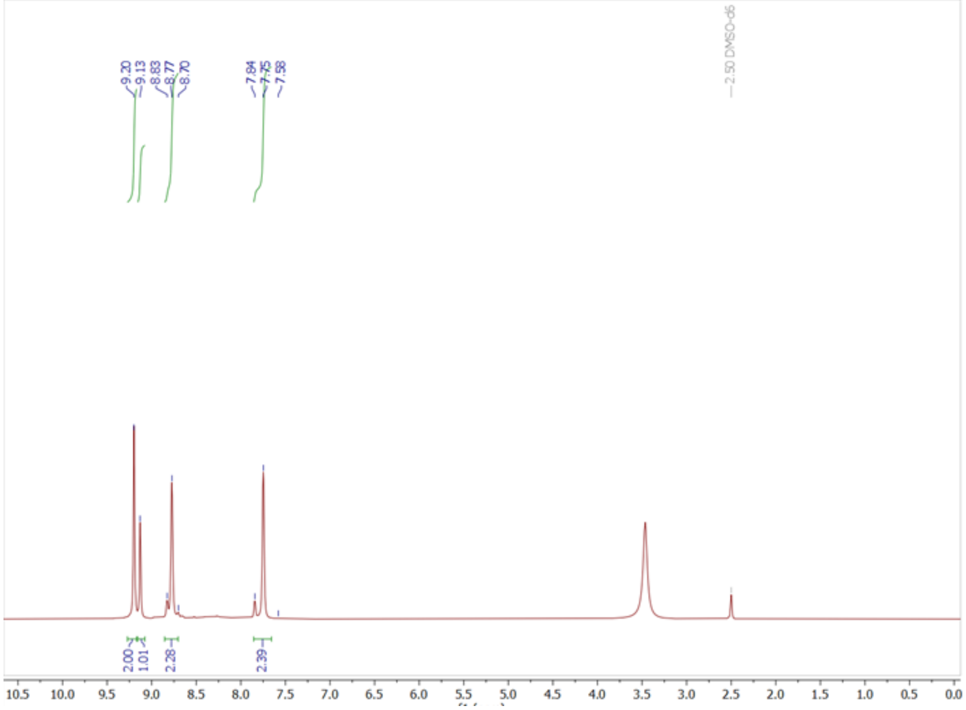

Fig. 5.1: ^{1}H NMR of ligand (**L**$_5$)

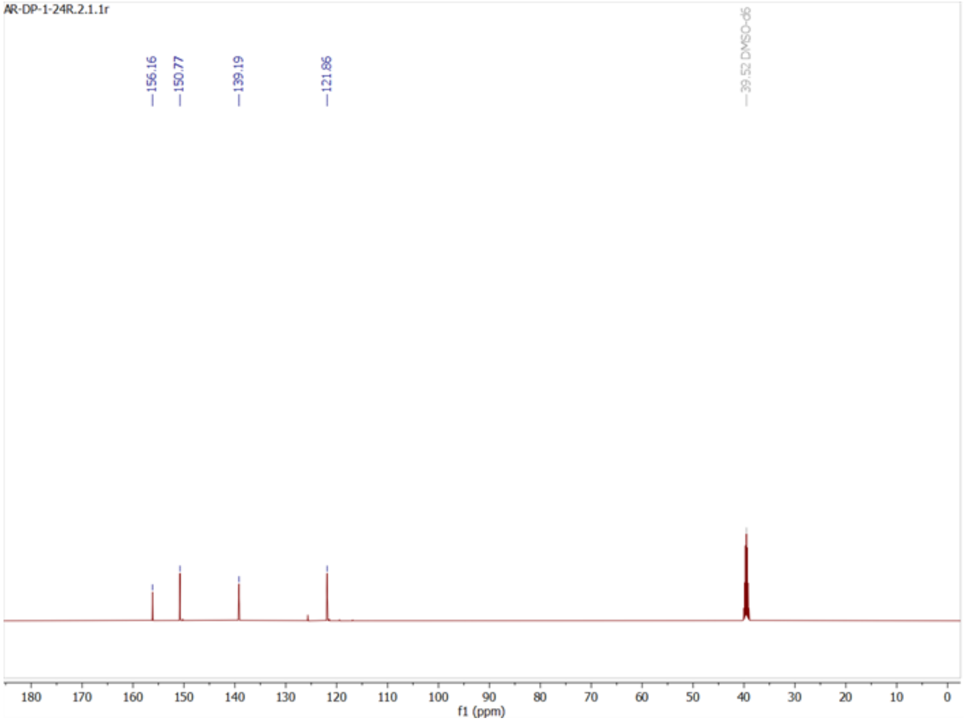

Fig. 5.2: ^{13}C{^{1}H} NMR of ligand (**L**$_5$)

5.2.3. Synthesis of CPs

5.2.3.1. Synthesis of CP5:

CuI (40 mg, 0.20 mmol) was added to a solution of triphenylphosphine (PPh_3) (109 mg, 0.41 mmol) in a mixture of MeOH (1 mL) and $CHCl_3$ (2 mL). After stirring for 15 min at room temperature, the bridging ligand, $\mathbf{L_5}$ (36 mg, 0.20 mmol) was added and the reaction mixture was stirred for another 1 hour at room temperature. After this, an orange microcrystalline product was obtained which was washed three times with a mixture of MeOH (1 mL) and $CHCl_3$ (2 mL) to remove the unreacted insoluble materials. Subsequently, the orange product was dissolved in acetonitrile solution and then kept at room temperature for two days to get orange needle-shaped crystals, which were filtered off and air-dried to give **CP5** [$Cu_2I_2(PPh_3)_2(\mathbf{L_5})$ MW 1078.66] (136 mg, 61 % yield). IR (ATR): 3063, 1513, 1478, 1425, 1307, 1161, 995, 821, 612, and 433 cm^{-1}. Anal. Calc. for $C_{44}H_{37}Cu_2I_2N_5P_2$ (1078.66): C, 48.99; H, 3.46; N, 6.49. Found: C, 48.97; H, 3.49; N, 6.48 %.

5.2.3.2. Synthesis of CP6:

CuBr (30 mg, 0.20 mmol) was added to a solution of triphenylphosphine (PPh_3) (109 mg, 0.41 mmol) in a mixture of MeOH (1 mL) and $CHCl_3$ (2 mL). After stirring for 15 min at room temperature, the bridging ligand, $\mathbf{L_5}$ (36 mg, 0.20 mmol) was added, and the reaction mixture was stirred for another 1 hour at room temperature. After this, a yellow-orange microcrystalline product was obtained which was washed three times with a mixture of MeOH (1 mL) and $CHCl_3$ (2 mL) to remove the unreacted insoluble materials. Subsequently, the orange product was dissolved in acetonitrile solution and then kept at room temperature for two days to get orange needle-shaped crystals, which were filtered off and air-dried to give **CP6** [$Cu_2Br_2(PPh_3)_2(\mathbf{L_5})$ MW 980.95] (120 mg, 60 % yield). IR (ATR): 3045, 1515, 1480, 1427, 1309, 1164, 995, 821, 694, and 437 cm^{-1}. Anal.

Calc. For $C_{44}H_{37}Br_2Cu_2N_5P_2$ (980.95): C, 53.67; H, 3.79; N, 7.11. Found: C, 53.62; H, 3.76; N, 7.10 %.

5.3. Results and discussion:

Ligand (pyridin-4-yl)-N-(4H-1,2,4-triazol-4-yl)methenamine **(L_5)** was synthesized by the Schiff-base condensation reaction of 4-pyridine carboxaldehyde and 4-amino-1,2,4-triazole in 80% yield following the reported procedure *[50]* (**Scheme 5.1 and Fig. 5.1-5.2**). Subsequently, the synthesized ligand was reacted with CuX (X = I; **CP5** and X = Br; **CP6**) and PPh_3 in a 1:1:2 ratio to obtain two new Cu(I) 1D CPs with 61 and 60% yields (**Scheme 5.2**). The synthesized CPs were characterized by single-crystal X-ray diffraction (SCXRD), powder X-ray diffraction (PXRD), and X-ray photoelectron spectroscopy (XPS) techniques.

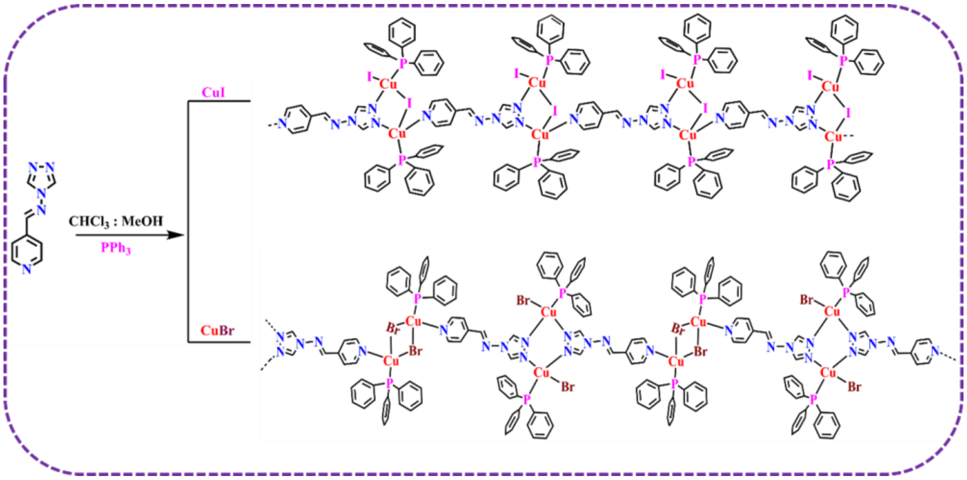

Scheme 5.2: Synthesis of **CP5** and **CP6**.

5.3.1. Structural analysis:

SCXRD analysis confirms the formation of **CP5** with triclinic space group $P2_1$ and **CP6** with monoclinic space group $P\bar{1}$ (**Table 5.1**). **Fig. 5.3** shows the molecular structure of **CP5** and **CP5**. The 1D **CP5** features two crystallographically independent copper atoms with an unusual open $[Cu_2(\mu_2\text{-}I)I(PPh_3)_2]$ secondary building unit (SBU). One iodine bridges the two copper atoms, while the other iodine coordinates with only one Cu. The triazolyl nitrogens coordinate with the two copper atoms of an SBU to form a five-membered Cu_2N_2I ring, while the pyridine nitrogen coordinates with the copper atom of another SBU to form a polymeric structure (**Fig. 5.3a**). Average Cu–I, Cu–N and Cu–P distances are 2.62, 2.34 and 2.22 Å, respectively, which is similar to the other iodo-bridged Cu(I) polymers with N heteroaromatic ligands and PPh_3 [51–54].

In contrast to **CP5**, the polymeric structure of **CP6** consists of two distinct cluster cores: a closed $[Cu_2(\mu_2\text{-}Br)_2(PPh_3)_2]$ rhomboid and an open $[Cu_2Br_2(PPh_3)_2]$ SBU (**Fig. 5.3b**). These SBUs are alternately arranged in XYXY pattern along the 1-D polymeric chain. The $[Cu_2(\mu_2\text{-}Br)_2(PPh_3)_2]$ rhomboid is coordinated to the pyridine N atom of the ligand, while the

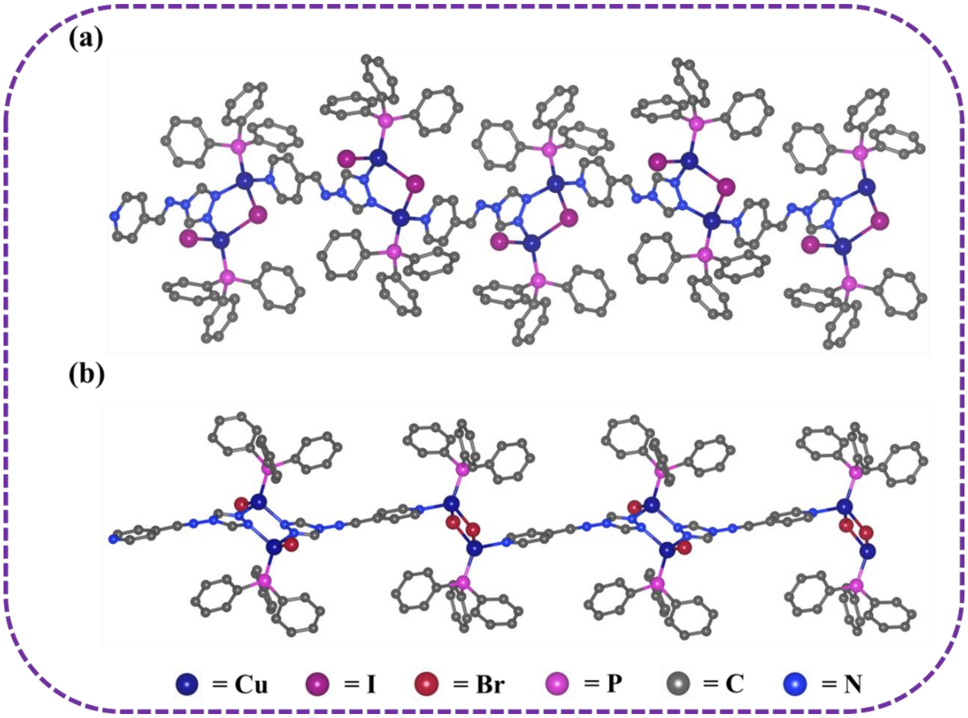

Fig. 5.3: The Polymeric structure of the 1D coordination polymer (a) **CP5** and (b) **CP6**.

Table 5.1. Crystallographic parameters of **CP5** and **CP6**

Compound	**CP5**	**CP6**
CCDC No.	2310728	2310729
Formula	$C_{44}H_{37}Cu_2I_2N_5P_2$	$C_{44}H_{37}Br_2Cu_2N_5P_2$
Formula Weight	1078.60	984.62
Wavelength	0.71073 Å	0.71073 Å
Crystal System	monoclinic	triclinic
Space group	$P2_1$	$P\bar{1}$
a/Å	9.2405(11)	9.2431(5)
b/ Å	17.6751(19)	13.6120(7)
c/ Å	13.3599(15)	18.2551(9)
α /°	90	99.296(4)
β/°	106.185(3)	99.283(4)
γ/°	90	107.388(5)
V/ Å^3	2095.5(4)	2108.8(2)
Z	2	2
ρ_{calcd} (g/cm^3)	1.709	1.551
Temperature/K	298.00	298.00
GOF	1.029	1.115
2θ range for data collection	3.922 to 56.702	6.662 to 58.01
Reflections collected	37146	26656
Independent reflections	10450 [R_{int} =0.0433]	9918[R_{int} = 0.0496]
Completeness to θ=25.242	100	99.6
Final R indices [I>2σ(I)]	R_1 = 0.0279, wR_2 = 0.0474	R_1 = 0.0522, wR_2 = 0.1212
Final R indices [all data]	R_1 = 0.0331, wR_2 = 0.0490	R_1 = 0.0705, wR_2 = 0.1312
Largest diff. peak/hole/ e Å^{-3}	0.86/-0.52	0.77/-0.50

open [$Cu_2Br_2(PPh_3)_2$] SBU is coordinated with the two triazolyl nitrogens to form the polymeric structure. Average Cu–Br, Cu–N and Cu–P distances are 2.62, 2.34 and 2.22 Å, respectively, aligning with reported Cu_2Br_2 CPs *[55–57]*. Further, the Cu-Cu distance in 1D **CP5** was found to be 3.01 Å, whereas in **CP6**, the distances were 3.20 and 3.84 Å. Both compounds consist of analogous $[Cu_2X_2(PPh_3)_2(\mathbf{L_5})]_n$ chemical formula but with distinct secondary building units (SBUs). To our knowledge, structural arrangements of copper halide clusters similar to **CP5** or **CP6** have not been reported.

The phase purity of **CP5** and **CP6** was confirmed by comparing the experimental Powder X-ray diffraction (PXRD) pattern with the simulated data derived from SCXRD analysis (**Fig. 5.4a-5.4b**). Both CPs exhibit high stability in ambient conditions, allowing them to be stored for several months without any deterioration. Further, temperature gradient analysis (TGA) was conducted under a nitrogen atmosphere from 30 to 800 °C, which indicates that both CPs are thermally stable up to 210 °C (**Fig. 5.4c**). In **CP5**, initial decomposition begins at 220 °C, involving the removal of two phosphine units and one ligand, accounting for 65% of the mass loss and the second decomposition step at 441 °C results in the loss of two iodines from the Cu_2I_2 cluster, contributing to 24% mass loss. Similarly, **CP6** undergoes two degradations at 214 and 444 °C, which corresponds to the loss of organic ligands and bromides, respectively. The observed weight loss closely matches the theoretical values. The TGA profiles demonstrate high thermal stability, making these materials suitable for applications in electronic devices requiring high-temperature resilience.

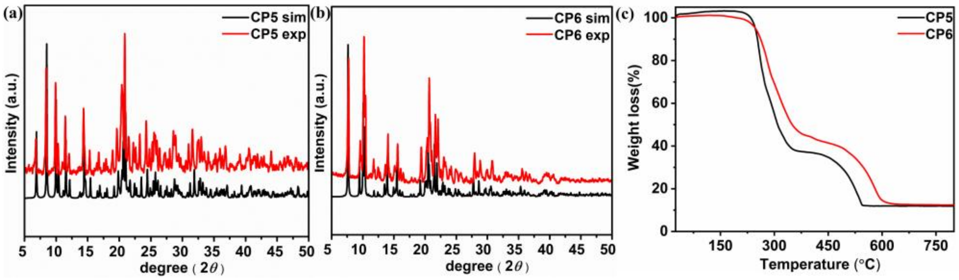

Fig. 5.4: (a) PXRD pattern of **CP5** (b) PXRD pattern of **CP6** (c) TGA curve of **CP5** and **CP6**.

The electrical conductivity of **CP5** and **CP6** was measured at room temperature using the two-probe direct current method. The microcrystalline samples were pressed into pallets at a pressure of 5.0 GPa for 10 minutes.

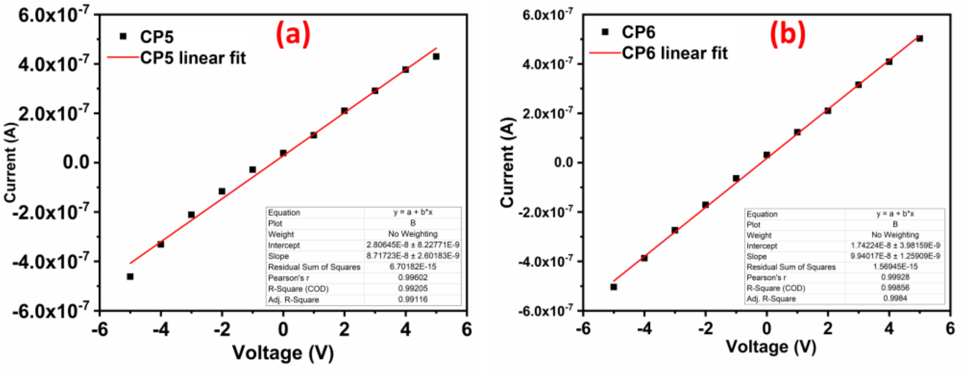

Equation	y = a + b*x
Plot	B
Weight	No Weighting
Intercept	2.80645E-8 ± 8.22771E-9
Slope	8.71723E-8 ± 2.60183E-9
Residual Sum of Squares	6.70182E-15
Pearson's r	0.99602
R-Square (COD)	0.99205
Adj. R-Square	0.99116

Equation	y = a + b*x
Plot	B
Weight	No Weighting
Intercept	1.74224E-8 ± 3.98159E-9
Slope	9.94017E-8 ± 1.25909E-9
Residual Sum of Squares	1.56945E-15
Pearson's r	0.99928
R-Square (COD)	0.99856
Adj. R-Square	0.9984

Fig. 5.5: Electrical conductivity of (a) **CP5** (b) **CP6**.

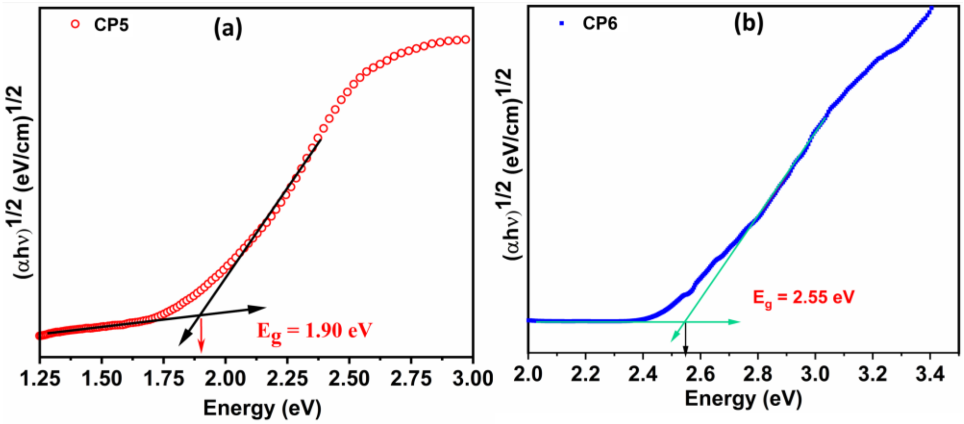

Fig. 5.6: The Tauc plot of (a) **CP5** and (b) **CP6**.

Further, the silver paste was used to make contact with the pressed pallets and a Keithley model 6517B electrometer voltage source to measure conductivity within a voltage range of -5V to +5V. **CP5** and **CP6** exhibited a conductivity value of 4.8 × 10^{-7} S cm^{-1} and 6.8 × 10^{-8} S cm^{-1}, respectively (**Fig. 5.5**), suggesting the semiconducting nature of the synthesized CPs. Additionally, band gaps of 1.90 eV for **CP5** and 2.55 eV for **CP6** were measured using Tauc plots from their UV/Vis reflectance spectra (**Fig. 5.6**).

This optical band gap further confirms the semiconducting nature of both CPs.

5.3.2. Gas Sensor Fabrication and Measurement:

The semiconducting nature of CPs encouraged us to investigate their gas-sensing performance. CPs were dissolved in ethanol, drop-casted on an interdigitated electrode (IDE) device ($1.5 \times 1\ cm^2$) and dried in the hot air oven for 24h.

CP5 and **CP6** chemiresistive sensor's performance were initially observed for various toxic gases such as NO_2, CO_2, SO_2, H_2S, and NH_3 for 100 ppm concentration at atmospheric pressure and room temperature. Interestingly, both sensors exhibit a notably higher response to NO_2 than other toxic gases. An increase in sensor resistance was observed upon NO_2 gas exposure, and it came back to its initial value when purged with dry air. However, **CP5** exhibited approximately 2.5 times better response than **CP6** (**Fig. 5.7a**); therefore, all further studies were performed with the **CP5** sensor. The selectivity of the **CP5** sensor was assessed by exposing different toxic gases such as NO_2 (100 ppm), CO_2 (100 ppm), SO_2 (100 ppm), H_2S (100 ppm), and NH_3 (500 ppm) to the sensing material at the room temperature as shown in **Fig. 5.7d**. Interestingly, the **CP5** sensor exhibits a remarkable selectivity toward NO_2 (25) compared to other interfering gases CO_2 (6.2), SO_2 (3.6), NH_3 (-5), and H_2S (-5.7).

Since NO_2 is hazardous to humans even at smaller concentrations, the dynamic sensing performance of the sensor was investigated from 100 ppm to 100 ppb NO_2 concentrations (**Fig. 5.7b**). **CP5** sensor exhibited a response of 2400%, ($R_g/ R_a = 25$) at 100 ppm, which decreased to 480%, ($R_g/ R_a = 6.36$) at 1 ppm and 280% ($R_g/ R_a = 4.40$) at 100 ppb. This value (1250% @10 ppm) is approximately 10^4 times higher than the response of pristine CuI (-0.0098% ppm^{-1}) towards NO_2 at 240 °C *[58]*. The high response values and excellent selectivity suggest that using a coordinating assembly to confine CuI significantly enhances the gas-sensing performance. After assessing the sensor response to varying NO_2 concentrations, the repeatability of **CP5** performance by exposing it to 100 ppm of NO_2 for 5 consecutive cycles was explored (**Fig. 5.9**). The sensor consistently returned to its base resistance in each cycle without any drift, indicating its highly repetitive nature. Subsequently, the **CP5** sensor demonstrated a swift response, with a response time (τ_{res}) of 15.5 seconds and a recovery time (τ_{rec}) of 21 seconds toward 10 ppm NO_2 (**Fig. 5.7c**). The sensor response was measured on five different devices under varying relative humidity (RH) levels (from 47% to 97.5%) with exposure of 100 ppm of NO_2. As RH increased from 47% to 97.5%, the sensor response gradually decreased from 25 to 7.5 (**Fig. 5.7e**). This decline in response is attributed to the reduced availability of active sites at higher RH levels. Notably, even under extreme humidity conditions (RH = 97.5%), the sensor maintained a response of 7.5, indicating its durability and robustness.

The limit of detection (LoD) and limit of quantification (LoQ) for the **CP5** sensor were calculated to be 1.3 ppb and 4.3 ppb, respectively (**Fig. 5.7f**). The **CP5** sensor's high response, excellent sensitivity and selectivity, room temperature operation with ultrafast response and recovery time in seconds make it an excellent NO_2 sensor. The performance is found to be one of the best in terms of response and response time among the MOF/CP-based room temperature NO_2 sensors (**Fig. 5.8 and Tables 5.2-5.3**). Moreover, the convenient synthesis of **CP5** using cost-effective and non-toxic material makes the sensor ideal for various commercial and industrial applications.

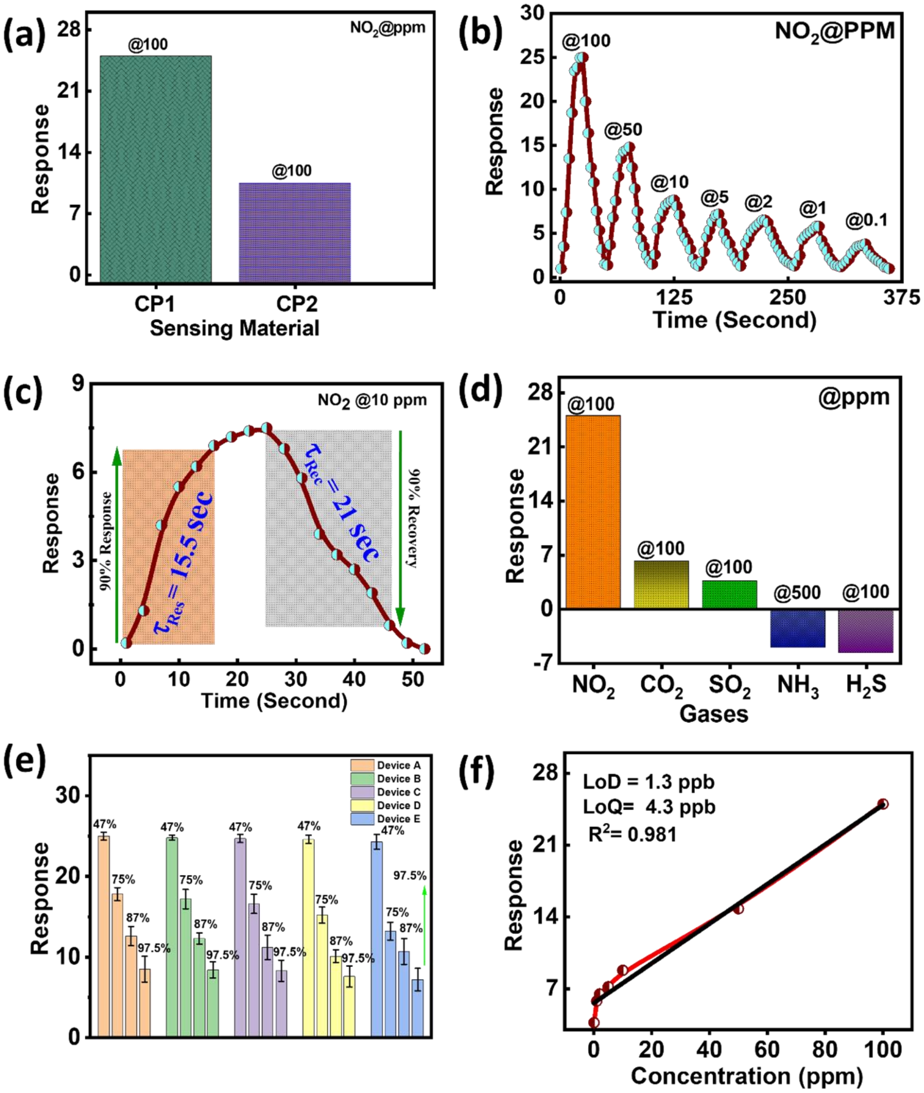

Fig. 5.7: (a) **CP5** and **CP6** sensor response for NO_2 at room temperature, (b) response and recovery of NO_2 at various concentrations of the **CP5** sensor, (c) transient performance of the **CP5** sensor, (d) selectivity analysis for the **CP5** sensor with interfering gases, (e) stability of **CP5** sensor for NO_2 with different RH concentrations for all the five devices, (f) LoD and LoQ analysis for **CP5** sensor.

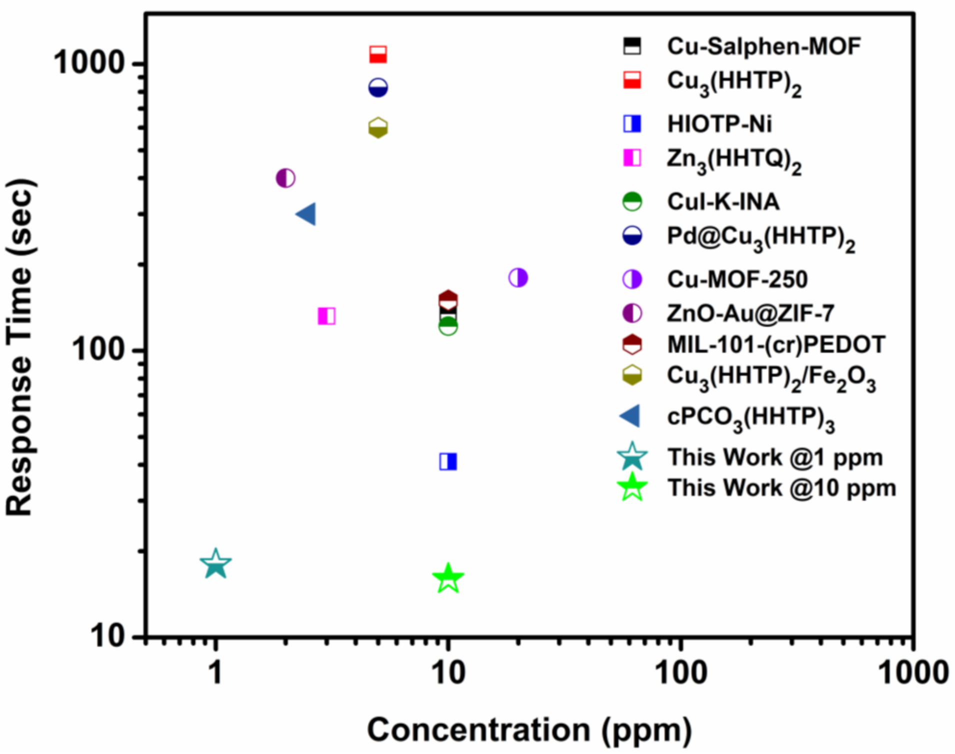

Fig. 5.8: Response time comparison of **CP1** with the reported MOFs and hybrid MOF-bases NO_2 sensors at room temperature [see references top to bottom *9,26,27,27,29-31,34,59-61]*.

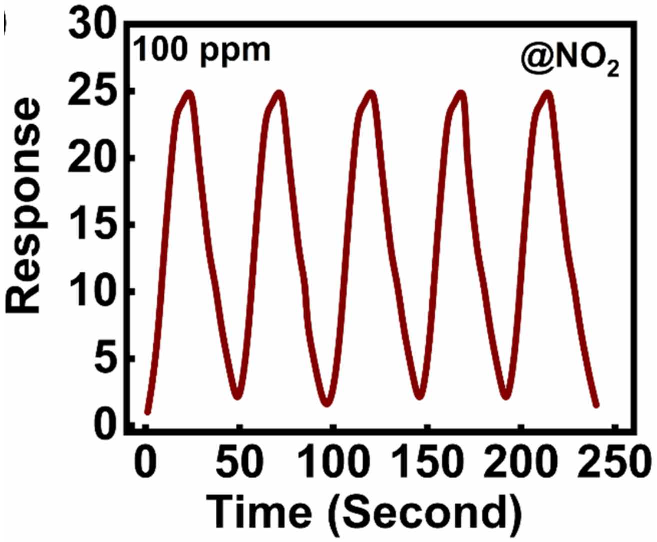

Fig. 5.9: Repeatability of the **CP5** sensor after 5 cycles.

5.3.3. Sensing Mechanism:

To understand the sensing behavior, first of all, the surface morphology and elemental composition of the synthesized **CP5** and **CP6** material were investigated using scanning electron microscopy (SEM) and elemental mapping (**Fig. 5.10-5.11**). The low magnification SEM image reveals that **CP5** has irregular 2D rod-like morphology with a cross-sectional area of about 2–4 μm and a length of 20–30 μm (**Fig. 5.10a-5.10b**). High-magnification FE-SEM images provide a detailed view of this 2D microrod structure (**Fig. 5.10b**). However, **CP6** exhibits irregular plate-like morphology with different shapes and sizes (**Fig. 5.11**). The EDS analysis indicates the presence of Cu, I, Br, C, P, and N in appropriate proportions (**Fig. 5.10c and Fig. 5.12**). Additionally, elemental mapping analysis highlights the uniform distribution of these elements, indicating a consistent composition throughout the material (**Fig. 5.10d and Fig. 5.11c**). The low and high-magnification TEM images of **CP5** also suggest the formation of a well-separated crystalline 2D structure with an average length of 450 nm (**Fig. 5.10e-5.10g**). At 77 K, N_2 sorption isotherm shows that the Brunauer–Emmett–Teller (BET) surface areas for **CP5** and **CP6** are 27.32 and 10.23 m^2g^{-1}, respectively (**Fig. 5.13a and 5.13c**), suggesting type IV isotherm and a mesoporous structure. Further, the pore volume of **CP5** and **CP6** were calculated using the Barrett-Joyner-Halenda (BJH) method and found to be 3.44 and 2.39 nm, respectively (**Fig. 5.13b and-5.13d**). A higher surface area, pore volume, and favorable morphology favor **CP5** over **CP6** as a better material for gas sensing applications.over **CP2** as a better material for gas sensing applications.

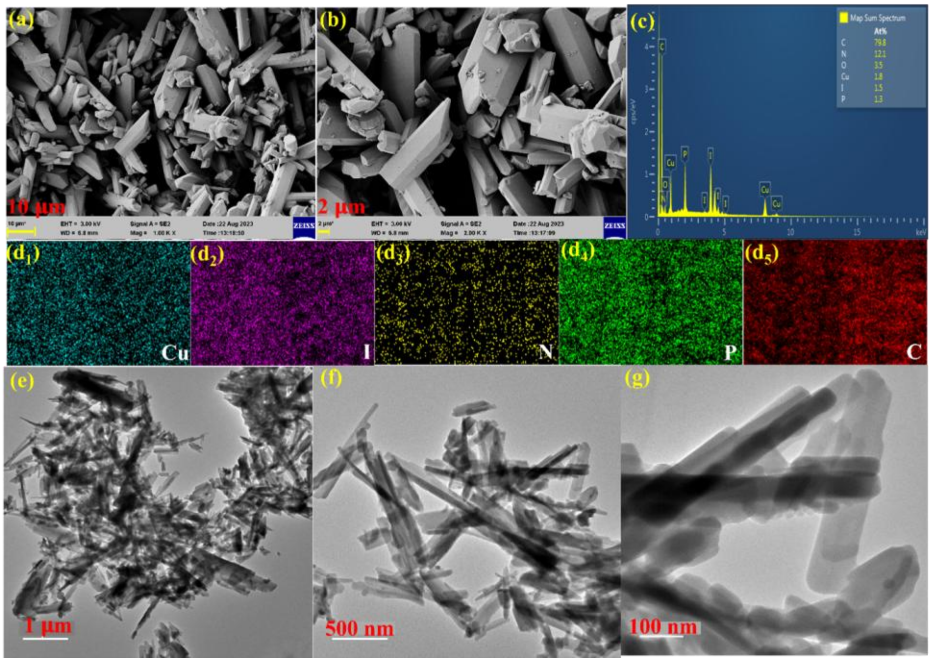

Fig. 5.10: Morphological and elemental analysis of **CP5**. (a) SEM image at 10 µm (b) SEM image at 2 µm (c) EDX of **CP5** (d_1-d_5) elemental mapping of Cu, I, N, P and C (e) TEM images of **CP5** at 20 nm (e) TEM images of **CP5** obtained at 1 µm (f) TEM images of **CP5** obtained at 500 nm (g) TEM images of **CP5** obtained at 100 nm.

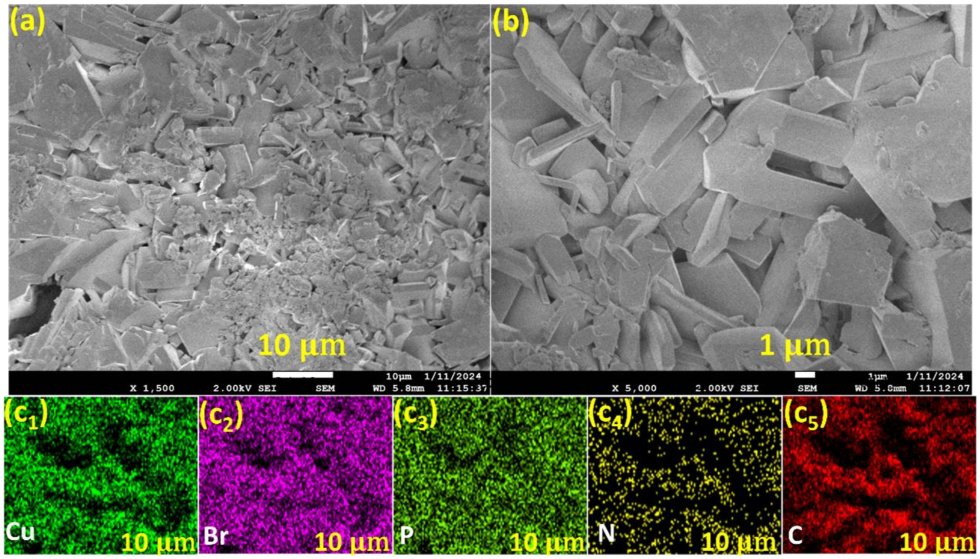

Fig. 5.11: FE-SEM (a) and (b); (C_1-C_5) elemental analysis of **CP6**.

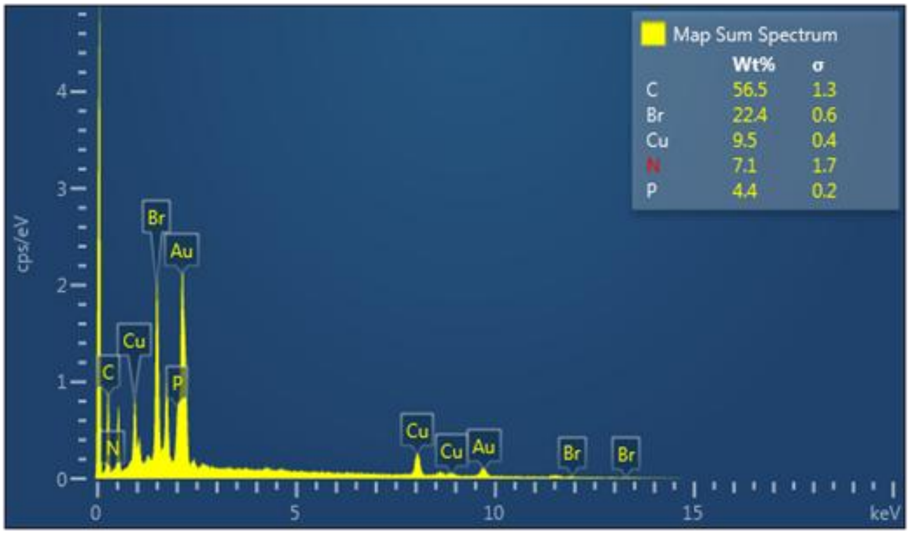

Fig. 5.12: EDS spectrum of **CP6**.

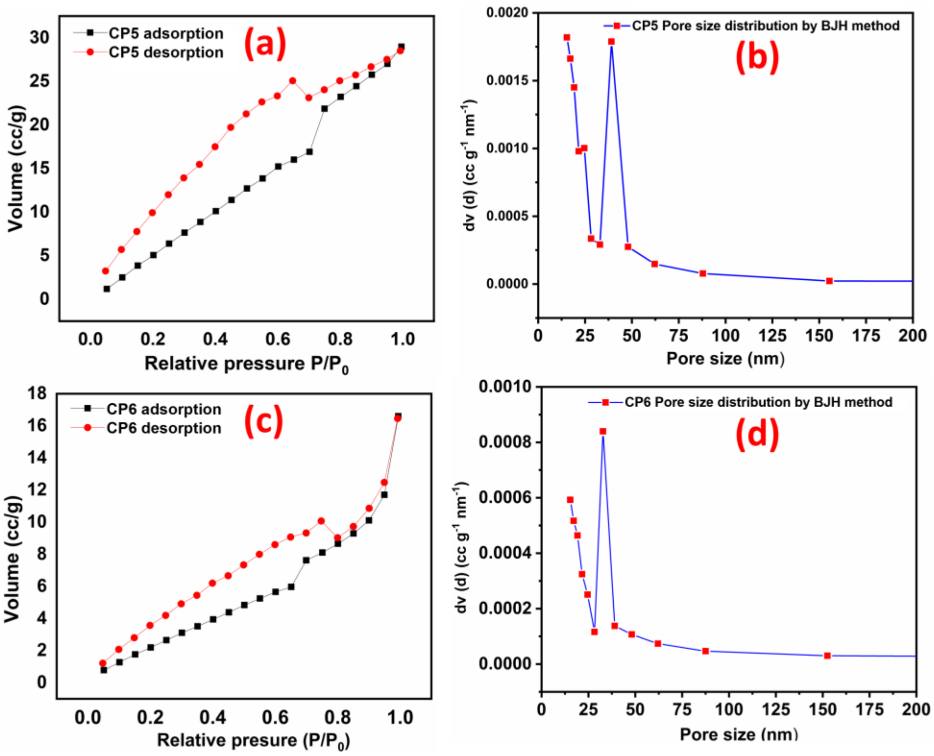

Fig. 5.13: BET surface area analysis of (a) **CP1** and (c) **CP2**; Pore size distribution of (b) **CP1** and (d) **CP2**.

Next, the ATR-IR and PXRD of the samples of the **CP1** were compared before and after ex-situ NO_2 exposure over the powder sample. In the IR spectrum, a new peak at 1640 cm^{-1} corresponds to adsorbed NO_2 (**Fig. 5.14**) *[2,62]*.

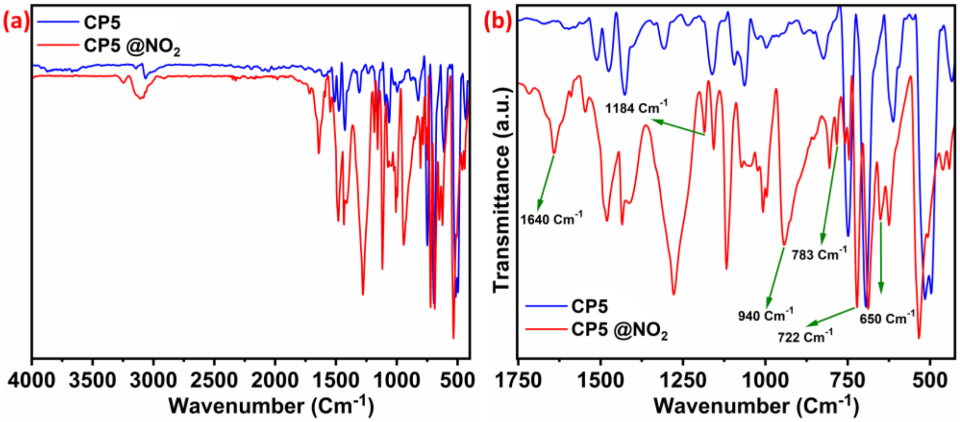

Fig. 5.14: IR-spectra of **CP5** sensor before and after NO_2 exposure (a) full spectra (b) zoomed spectra.

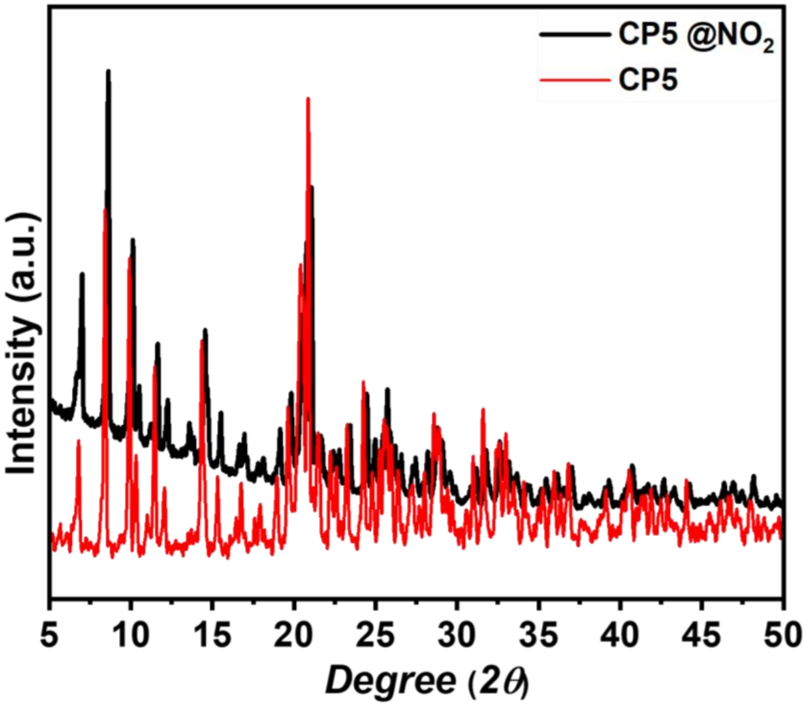

Fig. 5.15: PXRD patterns of **CP5** sensor before and after NO_2 exposure.

The structural integrity of the **CP5** after exposure (**Fig. 5.15**). To understand the changes in surface chemistry, oxidation states, and material-analyte interaction, X-ray photoelectron spectroscopy (XPS) analysis was conducted before and after gas exposure. The XPS analysis revealed the presence of Cu, I, P, N, and C elements before and after exposure. The high-resolution spectra for I3d, P2p, and C1s remained unchanged after NO_2 exposure to **CP5**. Significant changes were observed in the Cu2p and N1s peaks after exposure. The XPS spectrum for the **CP5** before gas exposure shows only one peak at 932, which corresponds to Cu(I). After exposing the material to NO_2, two distinct peaks at 935 and 932 eV, indicating the presence of both Cu(II) and Cu(I) (**Fig. 5.16a and 5.16d**) *[1,8,27,28]*. Additionally, a new peak at 406.7 eV in the N1s spectrum indicates the presence of metal-coordinated NO_2 molecules (**Fig. 5.16b and 5.16e**), which is consistent with previous reports *[27,32]*. These observations suggest a reversible charge transfer between NO_2 and Cu(I) of **CP5** takes place during gas sensing. Further, the resistance of the **CP5** sensor increases upon exposure to the NO_2 gas. This is a typical phenomenon when p-type doping occurs in a n-type semiconductor. NO_2 is known to behave as a p-type dopant, confirming the n-type semiconducting property of **CP5**. The recombination between the electrons in the **CP5** sensor and the holes from analytes decreases carrier concentration and increases the resistance of the sensor. It was also observed that the band gap (E_g) of NO_2 adsorbed **CP5** has increased to 2.14 eV from 1.90 eV of pristine **CP5** (**Fig. 5.16c and 5.16f**). The higher band gap results in increased resistance of material after gas exposure.

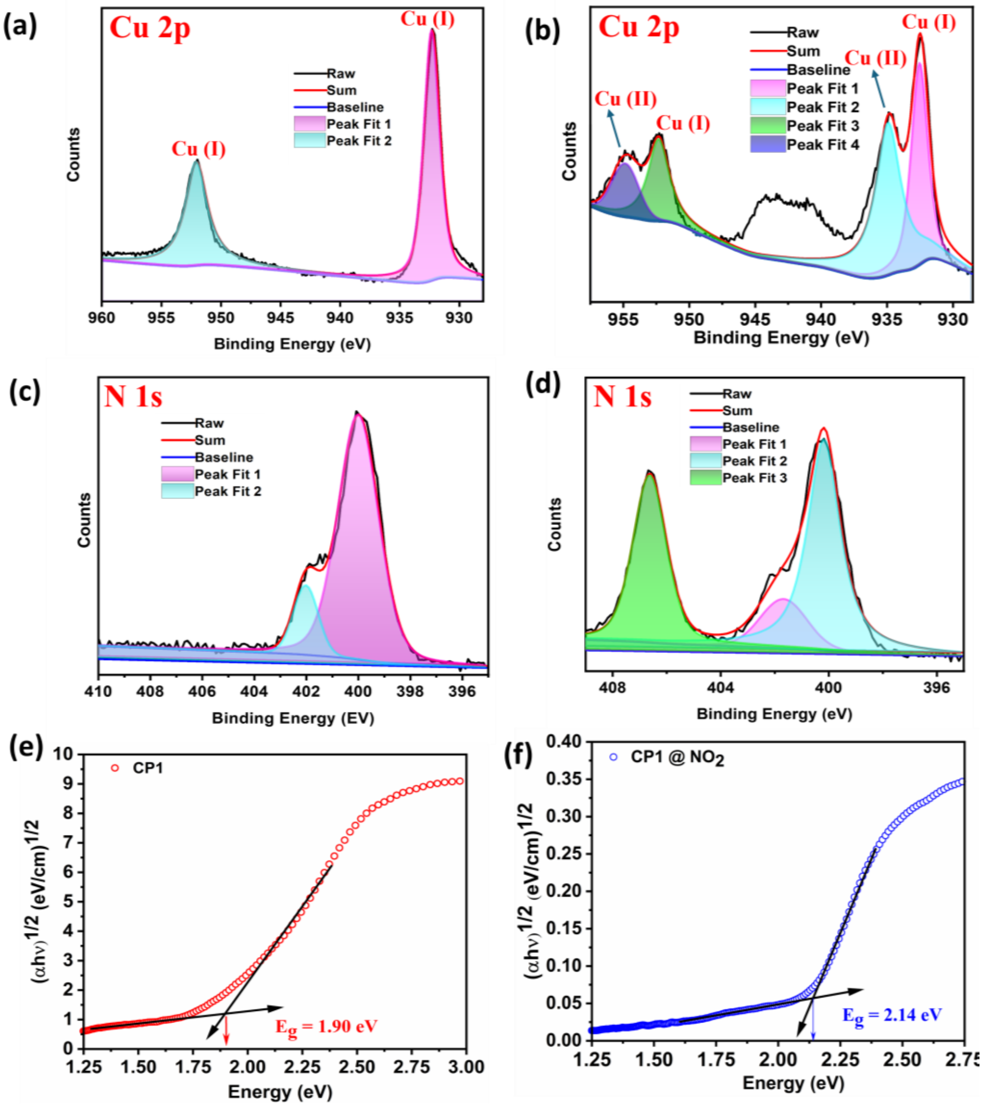

Fig. 5.16: (a) XPS spectra of Cu 2p before NO_2 exposure (b) XPS spectra of Cu 2p after NO_2 exposure (c) XPS spectra of N 1s before NO_2 exposure (d) XPS spectra of N 1s after NO_2 exposure (e) The Tauc plot of **CP1** before NO_2 exposure and (f) The Tauc plot of **CP1** after NO_2 exposure.

Overall, experimental results suggest that the sensing performance is due to the adsorption of NO_2 and reversible charge transfer between the analyte and Cu(I).

To support the experimental observations, computational analysis was done using PBE-D3 GGA calculations. The equilibrium structure of both the **CP5** and **CP6** for NO_2 sensing was obtained by PBE-D3 method using Vienna *Ab initio* Simulation Package (VASP) suite code *[63–65]*. This study investigated the potential of **CP5** and **CP6** for NO_2 sensing by optimizing their structures and calculating the change in Gibbs free energy (ΔG) after NO_2 adsorption. The change in Gibbs free energy (ΔG) was calculated after NO_2 adsorption for both the **CP5** and **CP6** to assess their NO_2 sensing capabilities. The results revealed that the change in the values of Gibbs free energy for the **CP5** is lower than the **CP6**. Specifically, the values of ΔG were determined to be -2.5 eV for **CP5** and -2.0 eV for **CP6**. Further, the adsorption energy of NO_2 molecules on **CP5** and **CP6** material was found to be -2.48 eV and -2.21 eV. These values suggest that the NO_2 adsorption on the **CP5** is energetically more favorable than the **CP6**. Moreover, We performed a Bader charge analysis to calculate the charge on the atoms of the CPs (**Fig. 5.17**) *[66]*. In case of the **CP5**, the Cu atom acquired a 0.24e charge, while the charge acquired by the Cu atom in **CP2** was -0.30e. A small positive charge on the Cu atom of **CP5** material indicates that it is electron-rich and would be more favorable to interact with π−accepting NO_2 than **CP6**.

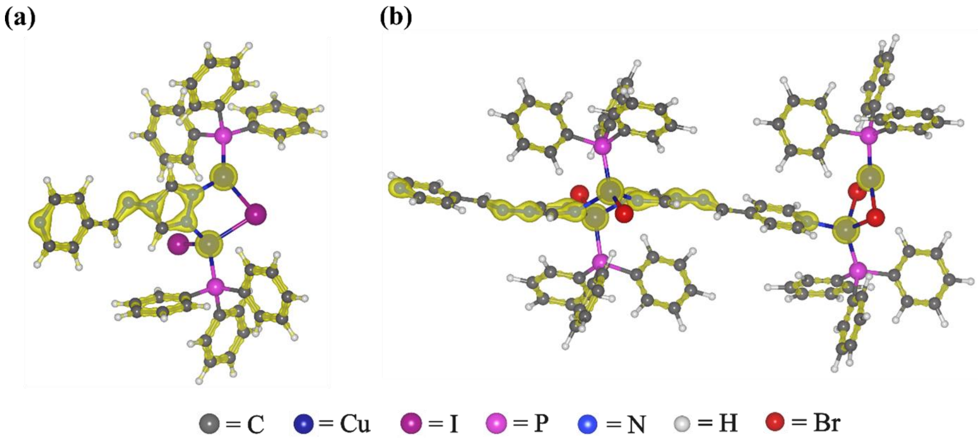

Fig. 5.17: The charge density distribution of (a) **CP5** and (b) **CP6** material, in yellow, shows the charge accumulation.

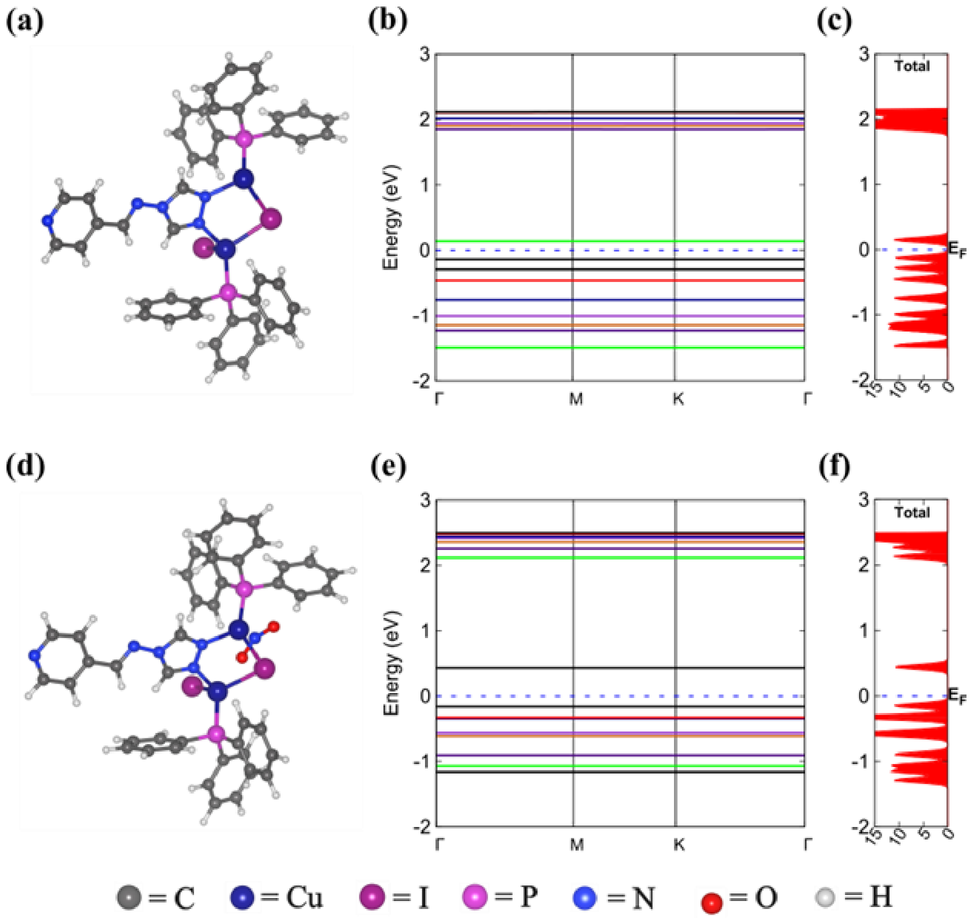

Fig. 5.18: Presents the following: (a) The equilibrium structure of the pristine **CP5**, (b) The electronic band structure of the pristine **CP5**, (c) The total DOS of the pristine **CP5**, (d) The equilibrium structure of the NO_2-CP5, (e) The electronic band structure of the NO_2-CP5, and (f) The total DOS of the NO_2-CP5.

This higher activity of **CP5** towards NO_2 sensing can be attributed to its superior electronic properties and structural characteristics. So, we have exclusively focused on the **CP5** for further investigation because it has demonstrated superior NO_2 sensing capabilities compared to the **CP6**; The optimized structures of both the **CP5** and NO_2-CP5 (where NO_2 is considered with the pristine **CP5**) are shown in **Fig. 5.18a and 5.18d**, respectively. We further analyzed the electronic properties of both the pristine **CP1** and NO_2-CP5. The electronic band structure calculations show that the pristine **CP5** has a direct band gap of 0.28 eV, as shown in **Fig. 5.18b**. The normalized band structure of **CP5** has been computed with respect to the Fermi level (E_F) using the k-vector Γ-M-K-Γ path. This finding is confirmed by the total density of states (DOS) calculations, illustrated in **Fig. 5.18c**. The small energy band gap of the pure **CP5** material suggests that there is a possibility of higher electronic conductivity and a more efficient charge transfer during NO_2 adsorption. Furthermore, we have used the same PBE-D3 GGA method to obtain the equilibrium structure of the NO_2-CP5 after sensing the NO_2. Our calculations reveal that the NO_2 molecule adsorbs at the Cu site of the **CP5**. The weak bond length between Cu and the adsorbed NO_2 molecule has been calculated to be approximately 2.37 Å. The electronic band structures and the total DOS of the NO_2-CP5 are shown in **Fig. 5.18e** and 7f, respectively. A highly symmetric k-vector Γ-M-K-Γ direction has been used to compute the normalized band structure of NO_2-CP5. The electronic band structure calculations of NO_2-CP5 reveal a band gap of about 0.59 eV. This observation is further confirmed by the DOS calculations presented in **Fig. 5.18f**, where we have observed almost negligible electron density of states around the Fermi energy level (E_F). We have also analyzed the Fermi energy (E_F) level shift after the NO_2 adsorption on **CP5** material. The Fermi energy of **CP5** (before NO_2 adsorption) was –3.23 eV and the Fermi energy of NO_2-CP5 (after NO_2 adsorption) was –3.80 eV. The Fermi energy level shift was found to be –0.57 eV which means the Fermi energy (E_F) level has shifted downwards by 0.57 eV after the NO_2 adsorption on **CP5**. The increase in the band gap suggests that the strong electron-withdrawing nature of the NO_2 group significantly alters the electronic properties of the NO_2-CP5, potentially enhancing its sensitivity towards NO_2 detection. Our study demonstrates that **CP5** is a promising candidate for NO_2 sensing applications due to its higher activity and better electronic properties than **CP5**. These findings provide valuable insights for designing and developing advanced NO_2 sensors based on the organic-inorganic framework.

Table 5.2. Comparison table for NO_2 gas sensing with room temperature MOF-based sensors.

Sensing material	Conc. (ppm)	Response	Res/Rec time (s)	LOD	References
Cu-Salphen-MOF	10	766 %	135/412.2	0.28 ppm	*Angew. Chem. Int. Ed.* **2023**, *62*, e202302645
$Cu_3(HHTP)_2$	5	29.95 %	1080/--	--	*Adv. Sci.* **2019**, *6*, 1900250
HIOTP-Ni	10	405 %	41.4/619.2	0.21 ppm	*Angew. Chem.* **2023**, *135*, e202306224
$Zn_3(HHTQ)_2$	10	168 %	132/594	0.269 ppm	*Angew. Chem. Int. Ed.* **2024**, *63*, e202408189
CuI-K-INA	10	1434 %	121.8/312.6	14.12 ppb	*J. Am. Chem. Soc.* **2023**, *145*, 19293–19302
$Cu_3(HHTP)_2$ powder	3	11.8 %	840/--	1 ppm	*Nat. Commun.* **2021**, *12*, 4294
PCN-222-Cu	0.02	44.18 %	67/261	0.93 ppb	*ACS Sens.* **2023**, *8*, 4353–4363
PCN-222-Ni	0.15	18.15 %	82/159	5.98 ppb	*ACS Sens.* **2023**, *8*, 4353–4363
CP5	**10**	**1250%**	**15.5/21**	**1.3 ppb**	**ThisWork**

Table 5.3. Comparison table for NO_2 gas sensing with hybrid room temperature MOF-based sensors.

Sensing material	**Conc. (ppm)**	**Response**	**Res /Rec time (s)**	**LOD**	**References**
$Ni_3(HHTP)_2$/ polyimide (PI), tape (PET)	1	215 %	--/--	56 ppb	*ACS Sens*. **2024**, *9*, 1916–1926
Au/ZIF-8-film	10	46 %	7.2/ > 600	0.19 ppm	*ACS Appl. Mater. Interfaces* **2019**, *11*, 13624–13631
$Cu_3(HHTP)_2$-NFs	5	68.9 %	~ 600/~ 600	--	*ACS Cent. Sci.* **2021**, *7*, 1176–1182
$Cu_3(HHTP)_2/Fe_2O_3$	5	63.5 %	~ 600/~ 600	11 ppb	*ACS Cent. Sci.* **2021**, *7*, 1176–1182
Pt@$Cu_3(HHTP)_2$	3	89.9 %	492/492	1 ppm	*Nat. Commun.* **2021**, *12*, 4294
MIL-101(Cr)⊃ PEDOT	10	46 %	150/Irr.	0.06 ppm	*J. Am. Chem. Soc.* **2016**, *138*, 10088–10091
LIG@$Cu_3(HHTP_2)$	0.001	--	16/15	0.168 ppb	*Nat. Commun.* **2023**, *14*, 3114
Pd@$Cu_3(HHTP)_2$	5	62.1 %	828/--	1ppm	*Adv. Sci.* **2019**, *6*, 1900250
Thin film Pt@$Cu_3(HHTP)_2$	3	89.9 %	492/--	0.1 ppm	*Nat. Commun.* **2021**, *12*, 4294
cP@ $Co_3(HHTP)_2$	2.5	2863 %	300/600	0.25 ppm	*Adv. Mater*. **2024**, *36*, 2312382
cP@ $Ni_3(HITP)_2$	2.5	2282 %	--/--	0.25 ppm	*Adv. Mater*. **2024**, *36*, 2312382
CP5	**10**	**1250 %**	**15.5/21**	**1.3 ppb**	**This Work**

5.4. Summary:

We have demonstrated two new semiconducting 1D hybrid Cu(I) frameworks, $[Cu_2X_2(PPh_3)_2(\mathbf{L_5})]_n$ (X = I and Br for **CP5** and **CP6**, respectively) with distinct SBUs. While **CP5** has a repeating SBU with one terminal and one bridging iodine, **CP6** has two distinct SBUs arranged alternately throughout the 1D chain. Chemiresistive sensing devices fabricated using these semiconducting materials exhibit NO_2 sensing properties. **CP5**, in particular, exhibited superior sensing performance, with a response approximately three times higher than that of **CP6**. Room temperature operation and selective sensing for NO_2 gas coupled with a high response (1250%), and ultrafast response time (15.5 sec.) toward 10 ppm NO_2 gas highlights its potential as a highly efficient chemiresistive NO_2 sensor. The experimental and theoretical studies were performed to elucidate the mechanism, which suggests that the excellent performance is due to effective charge transfer between Cu(I) and adsorbed NO_2 on **CP5**. Further, the exposed active sites in a 1D framework and comparatively electron-rich metal center, make **CP5** an efficient NO_2 sensor whose sensing performance is comparable to the best room temperature MOF/CP based chemiresistive sensors reported so far. This work provides further insight into designing novel chemiresistive sensing materials using coordination complexes and holds great potential for the development of stable and efficient room temperature NO_2 sensors for applications in environmental monitoring and healthcare.

5.5. References

1. Lim, H., Kwon, H., Kang, H., Jang, J.E., and Kwon, H.-J. (2023). Semiconducting MOFs on ultraviolet laser-induced graphene with a hierarchical pore architecture for NO_2 monitoring. Nat. Commun. 14, 3114. (DOI: 10.1038/s41467-023-38918-3)

2. Schulz, M., Gehl, A., Schlenkrich, J., Schulze, H.A., Zimmermann, S., and Schaate, A. (2018). A Calixarene-Based Metal–Organic Framework for Highly Selective NO_2 Detection. Angew. Chem. Int. Ed. 57, 12961–12965. (DOI: 10.1002/anie.201805355)
3. Cao, P., Cai, Y., Pawar, D., Navale, S.T., Rao, Ch.N., Han, S., Xu, W., Fang, M., Liu, X., Zeng, Y., et al. (2020). Down to ppb level NO_2 detection by ZnO/rGO heterojunction based chemiresistive sensors. Chem. Eng. J. 401, 125491. (DOI: 10.1016/j.cej.2020.125491)
4. Kampa, M., and Castanas, E. (2008). Human health effects of air pollution. Environ. Pollut. 151, 362–367. (DOI: 10.1016/j.envpol.2007.06.012)
5. Driscoll, C.T., Whitall, D., Aber, J., Boyer, E., Castro, M., Cronan, C., Goodale, C.L., Groffman, P., Hopkinson, C., Lambert, K., et al. (2003). Nitrogen Pollution in the Northeastern United States: Sources, Effects, and Management Options. BioScience 53, 357–374. (DOI: 0.1641/0006-3568(2003)053[0357:NPITNU]2.0.CO;2)
6. Han, J., Kong, D., Zhou, W., Gao, Y., Gao, Y., Liu, G., and Lu, G. (2023). Interface-engineering in MOF-derived In_2O_3 for highly sensitive and dual-functional gas sensor towards NO_2 and triethylamine. Sens. Actuators B Chem. 395, 134491. (DOI: 10.1016/j.snb.2023.134491)
7. Jo, Y.-M., Jo, Y.K., Lee, J.-H., Jang, H.W., Hwang, I.-S., and Yoo, D.J. (2023). MOF-Based Chemiresistive Gas Sensors: Toward New Functionalities (Adv. Mater. 43/2023). Adv. Mater. 35, 2370308. (DOI: 10.1002/adma.202370308)
8. Park, C., Koo, W.-T., Chong, S., Shin, H., Kim, Y.H., Cho, H.-J., Jang, J.-S., Kim, D.-H., Lee, J., Park, S., et al. (2021). Confinement of Ultrasmall Bimetallic Nanoparticles in Conductive Metal–

Organic Frameworks via Site-Specific Nucleation. Adv. Mater. 33, 2101216. (DOI: 10.1002/adma.202101216)

9. Wang, S., Liu, J., Zhao, H., Guo, Z., Xing, H., and Gao, Y. (2018). Electrically Conductive Coordination Polymer for Highly Selective Chemiresistive Sensing of Volatile Amines. Inorg. Chem. 57, 541–544. (DOI: 10.1021/acs.inorgchem.7b02464)
10. Xue, Z., Zheng, J.-J., Nishiyama, Y., Yao, M.-S., Aoyama, Y., Fan, Z., Wang, P., Kajiwara, T., Kubota, Y., Horike, S., et al. (2023). Fine Pore-Structure Engineering by Ligand Conformational Control of Naphthalene Diimide-Based Semiconducting Porous Coordination Polymers for Efficient Chemiresistive Gas Sensing. Angew. Chem. Int. Ed. 62, e202215234. (DOI: 10.1002/anie.202215234)
11. Park, C., Baek, J.W., Shin, E., and Kim, I.-D. (2023). Two-Dimensional Electrically Conductive Metal–Organic Frameworks as Chemiresistive Sensors. ACS Nanosci. Au 3, 353–374. (DOI: 10.1021/acsnanoscienceau.3c00024)
12. Kumar, S., Pavelyev, V., Mishra, P., Tripathi, N., Sharma, P., and Calle, F. (2020). A review on 2D transition metal di-chalcogenides and metal oxide nanostructures based NO_2 gas sensors. Mater. Sci. Semicond. Process. 107, 104865. (DOI: 10.1016/j.mssp.2019.104865)
13. Koo, W.-T., Jang, J.-S., and Kim, I.-D. (2019). Metal-Organic Frameworks for Chemiresistive Sensors. Chem 5, 1938–1963. (DOI: 10.1016/j.chempr.2019.04.013)
14. Huang, Y., Jiao, W., Chu, Z., Ding, G., Yan, M., Zhong, X., and Wang, R. (2019). Ultrasensitive room temperature ppb-level NO 2 gas sensors based on SnS_2 /rGO nanohybrids with P–N transition and optoelectronic visible light enhancement performance. J. Mater. Chem. C 7, 8616–8625. (DOI: 10.1039/C9TC02436K)

15. Givaja, G., Amo-Ochoa, P., Gómez-García, C.J., and Zamora, F. (2011). Electrical conductive coordination polymers. Chem. Soc. Rev. 41, 115–147. (DOI: 10.1039/C1CS15092H)

16. Ko, M., Mendecki, L., and A. Mirica, K. (2018). Conductive two-dimensional metal–organic frameworks as multifunctional materials. Chem. Commun. 54, 7873–7891. (DOI: 10.1039/C8CC02871K)

17. Xie, L.S., Skorupskii, G., and Dincă, M. (2020). Electrically Conductive Metal–Organic Frameworks. Chem. Rev. 120, 8536–8580. (DOI: 10.1021/acs.chemrev.9b00766)

18. Banda, H., Dou, J.-H., Chen, T., Libretto, N.J., Chaudhary, M., Bernard, G.M., Miller, J.T., Michaelis, V.K., and Dincă, M. (2021). High-Capacitance Pseudocapacitors from Li^+ Ion Intercalation in Nonporous, Electrically Conductive 2D Coordination Polymers. J. Am. Chem. Soc. 143, 2285–2292. (DOI: 10.1021/jacs.0c10849)

19. Ding, L., Yu, Z.-D., Wang, X.-Y., Yao, Z.-F., Lu, Y., Yang, C.-Y., Wang, J.-Y., and Pei, J. (2023). Polymer Semiconductors: Synthesis, Processing, and Applications. Chem. Rev. 123, 7421–7497. (DOI: 10.1021/acs.chemrev.2c00696)

20. Aubrey, M.L., Kapelewski, M.T., Melville, J.F., Oktawiec, J., Presti, D., Gagliardi, L., and Long, J.R. (2019). Chemiresistive Detection of Gaseous Hydrocarbons and Interrogation of Charge Transport in $Cu[Ni(2,3\text{-pyrazinedithiolate})_2]$ by Gas Adsorption. J. Am. Chem. Soc. 141, 5005–5013. (DOI: 10.1021/jacs.9b00654)

21. Yao, M.-S., Li, W.-H., and Xu, G. (2021). Metal–organic frameworks and their derivatives for electrically-transduced gas sensors. Coord. Chem. Rev. 426, 213479. (DOI: 10.1016/j.ccr.2020.213479)

22. Yao, M.-S., Lv, X.-J., Fu, Z.-H., Li, W.-H., Deng, W.-H., Wu, G.-D., and Xu, G. (2017). Layer-by-Layer Assembled Conductive

Metal–Organic Framework Nanofilms for Room-Temperature Chemiresistive Sensing. Angew. Chem. Int. Ed. 56, 16510–16514. (DOI: 10.1002/anie.201709558)

23. Li, W., Zhu, Z., Chen, Q., Li, J., and Tu, M. (2023). Device fabrication and sensing mechanism in metal-organic framework-based chemical sensors. Cell Rep. Phys. Sci. 4. (DOI: 10.1016/j.xcrp.2023.101679)
24. Le Ouay, B., Boudot, M., Kitao, T., Yanagida, T., Kitagawa, S., and Uemura, T. (2016). Nanostructuration of PEDOT in Porous Coordination Polymers for Tunable Porosity and Conductivity. J. Am. Chem. Soc. 138, 10088–10091. (DOI: 10.1021/jacs.6b05552)
25. Koo, W.-T., Kim, S.-J., Jang, J.-S., Kim, D.-H., and Kim, I.-D. (2019). Catalytic Metal Nanoparticles Embedded in Conductive Metal–Organic Frameworks for Chemiresistors: Highly Active and Conductive Porous Materials. Adv. Sci. 6, 1900250. (DOI: 10.1002/advs.201900250)
26. Kim, J.-O., Koo, W.-T., Kim, H., Park, C., Lee, T., Hutomo, C.A., Choi, S.Q., Kim, D.S., Kim, I.-D., and Park, S. (2021). Large-area synthesis of nanoscopic catalyst-decorated conductive MOF film using microfluidic-based solution shearing. Nat. Commun. 12, 4294. (DOI: 10.1038/s41467-021-24571-1)
27. Chen, P., Su, X., Wang, C., Zhang, G., Zhang, T., Xu, G., and Chen, L. (2023). Two-Dimensional Conjugated Metal-Organic Frameworks with Large Pore Apertures and High Surface Areas for NO_2 Selective Chemiresistive Sensing. Angew. Chem. 135, e202306224. (DOI: 10.1002/ange.202306224)
28. Su, X., Zhong, Z., Yan, X., Zhang, T., Wang, C., Wang, Y.-X., Xu, G., and Chen, L. (2023). Facile Synthesis of Metallosalphen-Based 2D Conductive Metal-Organic Frameworks for NO_2 Sensing: Metal

Coordination Induced Planarization. Angew. Chem. Int. Ed. 62, e202302645. (DOI: 10.1002/anie.202302645)

29. Yan, X., Chen, J., Su, X., Zhang, J., Wang, C., Zhang, H., Liu, Y., Wang, L., Xu, G., and Chen, L. Redox Synergy: Enhancing Gas Sensing Stability in 2D Conjugated Metal–Organic Frameworks via Balancing Metal Node and Ligand Reactivity. Angew. Chem. Int. Ed. n/a, e202408189. (DOI: 10.1002/anie.202408189)

30. Zhang, Y., Liu, Q., Sun, Q., Li, H., Shen, J., Liu, H., Chen, W., Zhang, Y., and Chen, Y. (2023). Metalloporphyrin-Based Metal–Organic Frameworks for the Ultrasensitive Chemiresistive Detection of NO_2: Effect of the Central Metal on Tuning the Sensing Performance. ACS Sens. 8, 4353–4363. (DOI: 10.1021/acssensors.3c01740)

31. Im, T., Lee, J., Kim, S.-C., Randrianandraina, J., Lee, J.-W., Won Chung, M., Park, T., Low, K.-H., Lee, S., Ju Oh, S., et al. (2024). Single stranded 1D-helical Cu coordination polymer for ultra-sensitive ammonia sensing at room temperature. Mater. Horiz. (DOI: 10.1039/D4MH00651H)

32. Wu, Z.-F., Wang, C., Liu, X., Tan, K., Fu, Z., Teat, S.J., Li, Z.-W., Hei, X., Huang, X.-Y., Xu, G., et al. (2023). Confinement of 1D Chain and 2D Layered CuI Modules in K-INA-R Frameworks via Coordination Assembly: Structure Regulation and Semiconductivity Tuning. J. Am. Chem. Soc. 145, 19293–19302. (DOI: 10.1021/jacs.3c05095)

33. Mishra, S., Patel, C., Pandey, D., Mukherjee, S., and Raghuvanshi, A. (2024). Semiconducting 2D Copper(I) Iodide Coordination Polymer as a Potential Chemiresistive Sensor for Methanol. Small 20, 2311448. (DOI: 10.1002/smll.202311448)

34. Pandey, D., Patel, C., Mishra, S., Mukherjee, S., and Raghuvanshi, A. (2024). Semiconducting 2D Copper(I) Framework for Sub-ppb-

Level Ammonia Sensing. ACS Appl. Nano Mater. 7, 15833–15840. (DOI: 10.1021/acsanm.4c03199)

35. Campbell, M.G., Liu, S.F., Swager, T.M., and Dincă, M. (2015). Chemiresistive Sensor Arrays from Conductive 2D Metal–Organic Frameworks. J. Am. Chem. Soc. 137, 13780–13783. (DOI: 10.1021/jacs.5b09600)

36. Stassen, I., Burtch, N., Talin, A., Falcaro, P., Allendorf, M., and Ameloot, R. (2017). An updated roadmap for the integration of metal–organic frameworks with electronic devices and chemical sensors. Chem. Soc. Rev. 46, 3185–3241. (DOI: 10.1039/C7CS00122C)

37. Lippi, M., and Cametti, M. (2021). Highly dynamic 1D coordination polymers for adsorption and separation applications. Coord. Chem. Rev. 430, 213661. (DOI: 10.1016/j.ccr.2020.213661)

38. Bazhina, E.S., Bovkunova, A.A., Shmelev, M.A., Korlyukov, A.A., Pavlov, A.A., Hochvaldová, L., Kvítek, L., Panáček, A., Kopel, P., Eremenko, I.L., et al. (2023). Zinc(II) and copper(II) complexes with N-substituted imines derived from 4-amino-1,2,4-triazole: Synthesis, crystal structure, and biological activity. Inorganica Chim. Acta 547, 121359. (DOI: 10.1016/j.ica.2022.121359)

39. Kresse, G., and Furthmüller, J. (1996). Efficiency of ab-initio total energy calculations for metals and semiconductors using a plane-wave basis set. Comput. Mater. Sci. 6, 15–50. (DOI: 10.1016/0927-0256(96)00008-0)

40. Hafner, J. (2008). Ab-initio simulations of materials using VASP: Density-functional theory and beyond. J. Comput. Chem. 29, 2044–2078. (DOI: 10.1002/jcc.21057)

41. Kresse, G., and Hafner, J. (1994). Norm-conserving and ultrasoft pseudopotentials for first-row and transition elements. J. Phys. Condens. Matter 6, 8245. (DOI: 10.1088/0953-8984/6/40/015)

42. Grimme, S., Antony, J., Ehrlich, S., and Krieg, H. (2010). A consistent and accurate ab initio parametrization of density functional dispersion correction (DFT-D) for the 94 elements H-Pu. J. Chem. Phys. 132, 154104. (DOI: 10.1063/1.3382344)

43. Singh, A., and Pakhira, S. (2024). Synergistic Niobium Doped Two-Dimensional Zirconium Diselenide: An Efficient Electrocatalyst for O2 Reduction Reaction. ACS Phys. Chem. Au 4, 40–56. (DOI: 10.1021/acsphyschemau.3c00035)

44. Pakhira, S., Mandal, D., Mondal, B., and Das, A.K. (2012). Theoretical study of spectroscopy, interaction, and dissociation of linear and T-shaped isomers of RgClF (Rg = He, Ne, and Ar) van der Waals complexes. Struct. Chem. 23, 681–692. (DOI: 10.1007/s11224-011-9914-9)

45. Blöchl, P.E. (1994). Projector augmented-wave method. Phys Rev B 50, 17953–17979. (DOI: 10.1103/PhysRevB.50.17953)

46. Halba, D., and Pakhira, S. (2024). Unraveling the O_2 Reduction Reaction on 2D Monolayer LaNiO3 Perovskite. ACS Omega. (DOI: 10.1021/acsomega.4c03544)

47. Pakhira, S., Lucht, K.P., and Mendoza-Cortes, J.L. (2017). Iron Intercalation in Covalent–Organic Frameworks: A Promising Approach for Semiconductors. J. Phys. Chem. C 121, 21160–21170. (DOI: 10.1021/acs.jpcc.7b06617)

48. Patel, C., Mandal, B., Jadhav, R.G., Ghosh, T., Dubey, M., Das, A.K., Htay, M.T., Atuchin, V.V., and Mukherjee, S. (2022). S, N Co-Doped Carbon Dot-Functionalized WO_3 Nanostructures for NO_2 and H_2S Detection. ACS Appl. Nano Mater. 5, 2492–2500. (DOI: 10.1021/acsanm.1c04174)

49. Hu, K., Wu, M., Hinokuma, S., Ohto, T., Wakisaka, M., Fujita, J., and Ito, Y. (2019). Boosting electrochemical water splitting via

ternary NiMoCo hybrid nanowire arrays. J. Mater. Chem. A 7, 2156–2164. (DOI: 10.1039/C8TA11250A)

50. Momma, K., and Izumi, F. (2011). VESTA 3 for three-dimensional visualization of crystal, volumetric and morphology data. J. Appl. Crystallogr. 44, 1272–1276. (DOI: 10.1107/S0021889811038970)

51. Kobayashi, A., Fujii, M., Shigeta, Y., Yoshida, M., and Kato, M. (2019). Quantitative Solvent-Free Thermal Synthesis of Luminescent Cu(I) Coordination Polymers. Inorg. Chem. 58, 4456–4464. (DOI: 10.1021/acs.inorgchem.8b03641)

52. Kobayashi, A., Ehara, T., Yoshida, M., and Kato, M. (2020). Quantitative Thermal Synthesis of Cu(I) Coordination Polymers That Exhibit Thermally Activated Delayed Fluorescence. Inorg. Chem. 59, 9511–9520. (DOI: 10.1021/acs.inorgchem.0c00341)

53. Kobayashi, A., Yoshida, Y., Yoshida, M., and Kato, M. (2018). Mechanochromic Switching between Delayed Fluorescence and Phosphorescence of Luminescent Coordination Polymers Composed of Dinuclear Copper(I) Iodide Rhombic Cores. Chem. – Eur. J. 24, 14750–14759. (DOI: 10.1002/chem.201802532)

54. Liu, W., Zhu, K., Teat, S.J., Deibert, B.J., Yuan, W., and Li, J. (2017). A mechanochemical route toward the rational, systematic, and cost-effective green synthesis of strongly luminescent copper iodide based hybrid phosphors. J. Mater. Chem. C 5, 5962–5969. (DOI: 10.1039/C7TC00889A)

55. Tsuge, K., Chishina, Y., Hashiguchi, H., Sasaki, Y., Kato, M., Ishizaka, S., and Kitamura, N. (2016). Luminescent copper(I) complexes with halogenido-bridged dimeric core. Coord. Chem. Rev. 306, 636–651. (DOI: 10.1016/j.ccr.2015.03.022)

56. Takeda, H., Kobayashi, A., and Tsuge, K. (2022). Recent developments of photoactive Cu(I) and Ag(I) complexes with

diphosphine and related ligands. Coord. Chem. Rev. 470, 214700. (DOI: 10.1016/j.ccr.2022.214700)

57. Araki, H., Tsuge, K., Sasaki, Y., Ishizaka, S., and Kitamura, N. (2005). Luminescence Ranging from Red to Blue: A Series of Copper(I)−Halide Complexes Having Rhombic {Cu2(μ-X)2} (X = Br and I) Units with N-Heteroaromatic Ligands. Inorg. Chem. 44, 9667–9675. (DOI: 10.1021/ic0510359)

58. Wolpert, B., Wolfbeis, O.S., and Mirsky, V.M. (2009). Gas sensing properties of electrically conductive Cu(I) compounds at elevated temperatures. Sens. Actuators B Chem. 142, 446–450. (DOI: 10.1016/j.snb.2009.04.042)

59. Le Ouay, B., Boudot, M., Kitao, T., Yanagida, T., Kitagawa, S., and Uemura, T. (2016). Nanostructuration of PEDOT in Porous Coordination Polymers for Tunable Porosity and Conductivity. J. Am. Chem. Soc. 138, 10088–10091. (DOI: 10.1021/jacs.6b05552)

60. Jo, Y.-M., Lim, K., Yoon, J.W., Jo, Y.K., Moon, Y.K., Jang, H.W., and Lee, J.-H. (2021). Visible-Light-Activated Type II Heterojunction in Cu3(hexahydroxytriphenylene)2/Fe2O3 Hybrids for Reversible NO_2 Sensing: Critical Role of π–π* Transition. ACS Cent. Sci. 7, 1176–1182. (DOI: 10.1021/acscentsci.1c00289)

61. Roh, H., Kim, D.-H., Cho, Y., Jo, Y.-M., del Alamo, J.A., Kulik, H.J., Dincă, M., and Gumyusenge, A. (2024). Robust Chemiresistive Behavior in Conductive Polymer/MOF Composites. Adv. Mater. 36, 2312382. (DOI: 10.1002/adma.202312382)

62. Nakamoto, K. (2006). Infrared and Raman Spectra of Inorganic and Coordination Compounds. In Handbook of Vibrational Spectroscopy (John Wiley & Sons, Ltd). (DOI: 10.1002/0470027320.s4104)

63. Kresse, G., and Furthmüller, J. (1996). Efficiency of ab-initio total energy calculations for metals and semiconductors using a plane-

wave basis set. Comput. Mater. Sci. 6, 15–50. (DOI: 10.1016/0927-0256(96)00008-0)

64. Hafner, J. (2008). Ab-initio simulations of materials using VASP: Density-functional theory and beyond. J. Comput. Chem. 29, 2044–2078. (DOI: 10.1002/jcc.21057)

65. Kresse, G., and Hafner, J. (1994). Norm-conserving and ultrasoft pseudopotentials for first-row and transition elements. J. Phys. Condens. Matter 6, 8245. (DOI: 10.1088/0953-8984/6/40/015)

66. Tang, W., Sanville, E., and Henkelman, G. (2009). A grid-based Bader analysis algorithm without lattice bias. J. Phys. Condens. Matter *21*, 084204. (DOI: 10.1088/0953-8984/21/8/084204)

Chapter 6

General conclusion and future scope

6.1. Conclusions

In conclusion, this thesis demonstrates the design, synthesis, and application of copper-based coordination polymers (CPs) and metal-organic frameworks (MOFs) for effective gas sensing, with an emphasis on detecting toxic gases such as NO_2 and NH_3. Chapter 1 introduces the need for advanced materials in gas sensing and highlights copper(I) frameworks, especially those with N and S donor ligands, as promising alternatives. Chapter 2 explores copper(I) coordination polymers with unique emissive properties, including solvatochromism and mechanoluminescence, which support their potential for multifunctional sensor applications. Chapter 3 presents a 2D semiconducting copper(I)-MOF that exhibits mesoporosity, enabling highly selective and rapid NO_2 detection at room temperature, setting new benchmarks in MOF-based sensors. Chapter 4 investigates two copper(I) coordination polymers, **CuTz1** and **CuTz2**, focusing on the impact of framework dimensionality on gas sensing. **CuTz1**, in particular, shows excellent NH_3 selectivity, sensitivity, and response times, establishing it as a leading material for ammonia sensing. In Chapter 5, two 1D Cu(I)-based frameworks (**CP5** and **CP6**) are introduced, with **CP6** displaying an ultrafast, reversible NO_2 sensing response due to efficient charge transfer, along with straightforward synthesis and device fabrication. Collectively, these chapters present a cohesive study on copper(I)-based frameworks, showcasing their advantages over traditional materials and underscoring their potential in practical applications for environmental monitoring, industrial safety, and diagnostics. The work provides a promising pathway for future developments in MOF/CP-based gas sensing technologies.

6.2. Future Scopes:

6.2.1. Advancing Material Properties: The effectiveness of copper(I) CPs and MOFs in chemiresistive gas sensing hinges on critical parameters such as surface area, porosity, stability, and conductivity. Enhancing these aspects through the strategic design of conjugated ligands and stable molecular frameworks will improve charge transfer efficiency and enable more precise and reliable sensing performance.

6.2.2. Improved Fabrication Techniques: Drop-casting methods often result in uneven material distribution, which compromises sensor uniformity and repeatability. Employing advanced techniques like spin coating, spray coating, in-situ growth, or layer-by-layer deposition can create uniform, high-quality films, leading to enhanced sensitivity and consistent sensing outcomes.

6.2.3. Optimizing Analyte Interaction: Engineering surface-active sites to enhance selective interactions with target gases will significantly improve sensitivity and reduce cross-reactivity, enabling more efficient and accurate detection of specific analytes. Scalable

6.2.4. Production and Integration: Developing scalable and cost-effective methods for producing chemiresistive sensors can facilitate their adoption in diverse applications such as environmental monitoring, industrial safety, and healthcare. These advancements will enable the integration of sensors into portable and real-time monitoring devices.

6.2.5. Robust Performance in Diverse Conditions: Addressing challenges like humidity and temperature variations by incorporating durable materials and adaptable sensing protocols can ensure long-term operational stability, expanding chemiresistive sensors' utility across various environmental conditions.

6.2.6. Addressing Real-World Challenges: To further strengthen practical applicability, future studies should also focus on evaluating sensor stability under humid conditions, selectivity against complex mixtures of volatile organic compounds (VOCs), and challenges associated with scaling up device fabrication. Addressing these aspects will provide a more comprehensive and balanced understanding of the material and device performance in real-world scenarios.

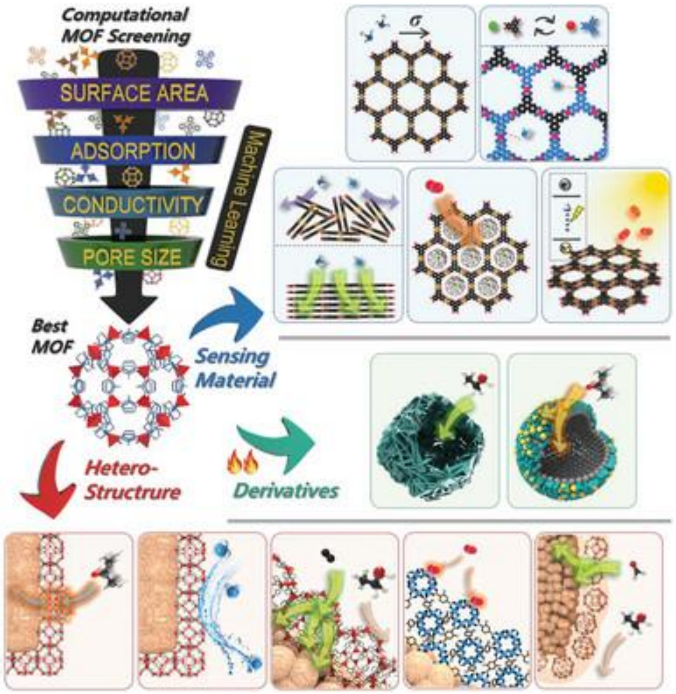

Fig. 6.1: Schematic illustration of different techniques for achieving improved sensing performance, reproduced with permission from John Wiley and Sons, ref *[1]*.

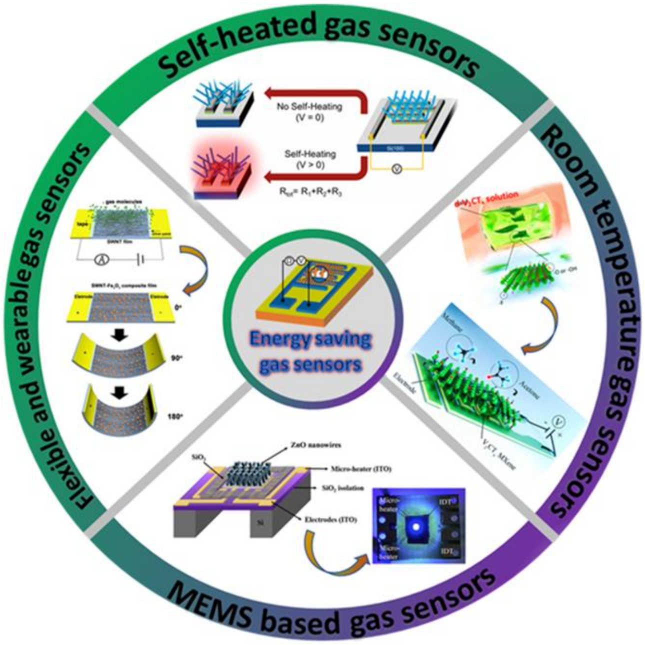

Fig. 6.2 An overview of the main techniques and applications of the energy-saving gas sensors, reproduces with permission from Elsevier, ref *[2]*. (Nano Energy 79 (2021) 105369)

6.3. Reference

1. Jo Y., Jo Y. K., Lee J., Jang H. W., Hwang I., Yoo D. J., (2023), MOF-Based Chemiresistive Gas Sensors: Toward New Functionalities, Adv Mater, 2206842 (DOI: 10.1002/adma.202206842)
2. Majhi, S.M., Mirzaei, A., Kim, H.W., Kim, S.S., and Kim, T.W. (2021). Recent advances in energy-saving chemiresistive gas sensors: A review. Nano Energy *79*, 105369. (DOI: 10.1016/j.nanoen.2020.105369)